Numerical and Experimental Investigation of CO_2 Hydrates on Injectivity Decline

John Alexander Riano Castaneda

Delft University of Technology

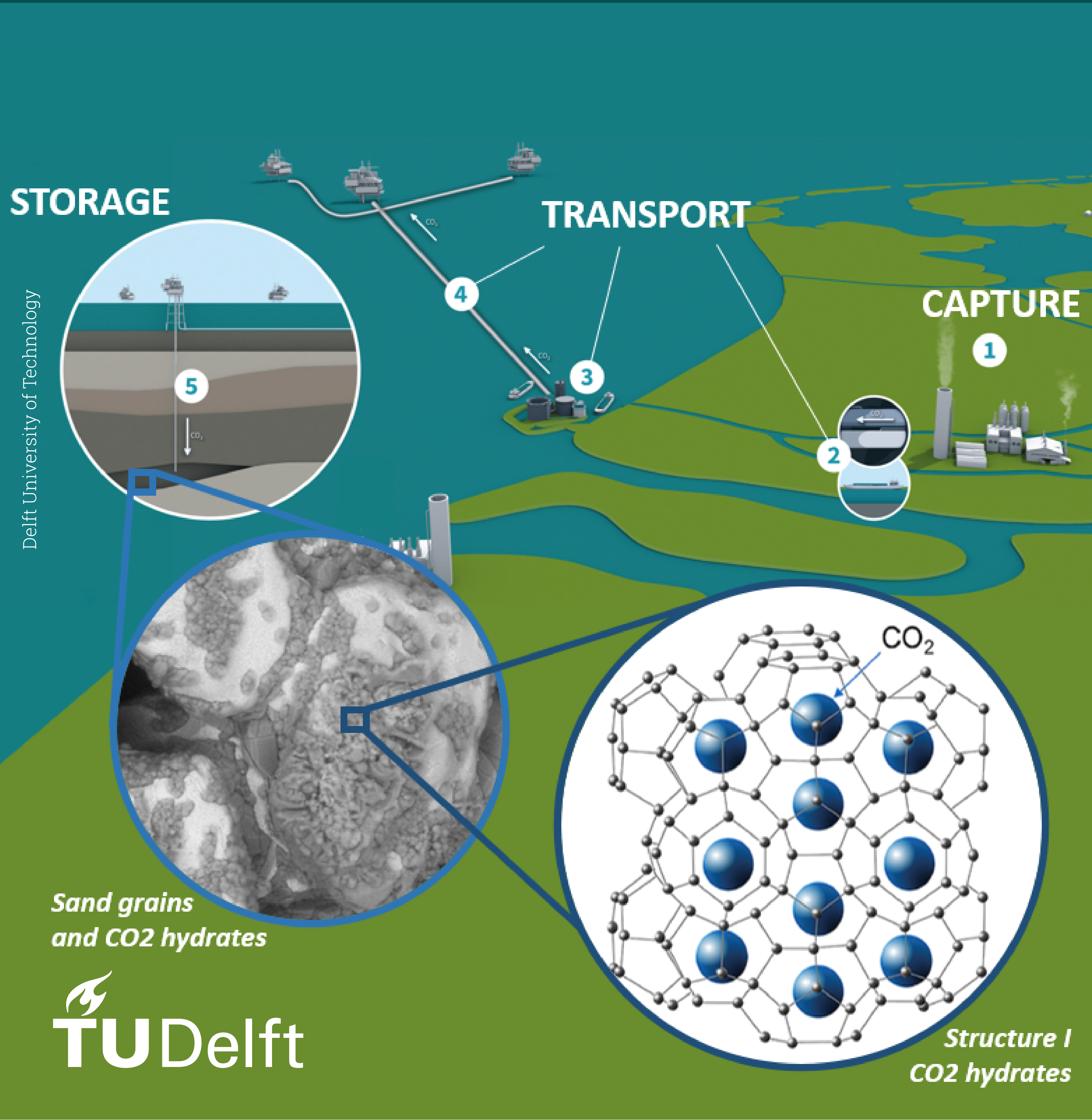

Sand grains and CO2 hydrates

Structure I CO2 hydrates

TUDelft

Numerical and Experimental Investigation of CO_2 Hydrates on Injectivity Decline

by

John Alexander Riano Castaneda

Student Number
5510783

Supervisor:	Rouhi Farajzadeh
Co-Supervisor:	Denis Voskov
Project Duration:	November, 2022 - August, 2023
Faculty:	Faculty of Civil Engineering and Geosciences, Delft

Cover:	Created by combining adaptations from (Rochelle et al., 2009), (Sa et al., 2017) and (TotalEnergies et al., 2023).

Numerical and Experimental Investigation of CO_2 Hydrates on Injectivity Decline

by

John Alexander Riano Castaneda

to obtain the degree of Master of Science in
Applied Earth Sciences track Geo-Energy Engineering
at the Delft University of Technology,
to be defended publicly on Thursday August 31, 2023 at 3:00 P.M.

Student number:	5510783	
Project duration:	November 15, 2022 – August 31, 2023	
Thesis committee:	Dr. Rouhi Farajzadeh,	TU Delft - Shell, supervisor
	Dr. Denis Voskov,	TU Delft, co-supervisor
	Dr. Auke Barnhoorn,	TU Delft
	Dr. Mahnaz Aghajanloo,	TU Delft
	Dr. Ali Fadili,	Shell
	Dr. Siavash Kahrobaei,	Shell

Cover: Created by combining adaptations from (Rochelle et al., 2009), (Sa et al., 2017) and (TotalEnergies et al., 2023).

Acknowledgments

I would like to express my heartfelt gratitude to all those who have contributed to the completion of this thesis. Special thanks go to Dr. Rouhi Farajzadeh, whose generous sharing of knowledge, boundless expertise, and unrelenting scrutiny played a crucial role in refining the procedures, interpreting the results, and analyzing the findings of this study. As the saying by Alexandra Trenfor goes, *“The best teachers are those who show you where to look but do not tell you what to see”.*

My sincere appreciation extends to Dr. Mahnaz Aghajanloo for providing insightful explanations on hydrate formation and dissociation processes, as well as for sharing the data from the additional laboratory experiments.

A sincere acknowledgment is due to Dr. Ali Fadili for his consistent guidance and assistance in understanding and developing the empirical model.

I am grateful to both Dr. Siavash Kahrobaei and Dr. Rouhi Farajzadeh for sharing the numerical model that served as the foundation for the empirical model developed in this study.

I extend my thanks to the entire laboratory team for their kind assistance and guidance throughout the execution of the experiments.

I would like to acknowledge Shell for providing me with the opportunity to undertake my master’s thesis as an intern within the company.

A special note of gratitude goes to Ecopetrol S.A. for their unwavering support and encouragement, contributing to my professional growth over the past nine years of service.

I am especially grateful to my friends, who have been a constant source of help, support, and companionship throughout the challenging yet rewarding journey of the past two years of study.

My deepest appreciation goes to my dear mother and beloved sister for their constant encouragement and unwavering belief in my dreams. Your presence has been my anchor during overwhelming times.

Lastly, I offer profound thanks to my father, whose teachings of perseverance and discipline have been my guiding light on the path to achieving my dreams. Your spirit continues to inspire and guide me in my journey, and I am forever grateful.

JohnRC
Delft, August 2023

Summary

The increasing levels of carbon dioxide (CO_2) emissions in the atmosphere are significantly contributing to climate change. One approach to mitigate this issue is through Carbon Capture and Storage (CCS) techniques, which involve storing CO_2 emissions underground. Depleted reservoirs are a potential option for subsurface CO_2 storage. However, a challenge arises due to the disparity between injection pressure and reservoir pressure. When CO_2 is injected into the reservoir, it undergoes expansion and cooling (known as the Joule-Thomson cooling effect), potentially leading to the risk of CO_2 hydrate formation when it interacts with connate water.

CO_2 hydrates pose a considerable threat to the success of CCS projects, as they can decrease injectivity near the wellbore, resulting in technical complications and increased costs. Thus, a thorough understanding of CO_2 hydrate formation is imperative for the planning of robust and sustainable CCS initiatives. This study aims to elucidate the specific conditions under which CO_2 hydrates are formed in a porous media and to assess their impact on injectivity decline.

The investigation begins with a core flooding experiment designed to delve into the physical processes involved in CO_2 hydrate formation and dissociation. It also explores potential methods for prevention, mitigation and remediation. In total, results from 13 experiments are presented, with nine conducted by the author and four provided by the Advanced Sub-Surface Energy Transition (ASSET) research team.

Subsequently, an empirical numerical reservoir simulator is developed to model the formation and dissociation of CO_2 hydrates within the reservoir. The empirical model facilitates a sensitivity analysis of the parameters that influence hydrate formation and allows for the assessment of the efficacy of prevention techniques examined in the laboratory setting.

The core flooding experiment helped to establish that hydrate formation is contingent upon specific pressure and temperature parameters within the hydrate stability zone. The experiment also delved into the impact of water saturation, connate water salinity, and the use of thermodynamic hydrate inhibitors (THIs) on the hydrate formation process. Furthermore, the experimental procedure facilitated the testing of prevention and remediation techniques after hydrate formation, including thermal stimulation and THIs injection.

The empirical model, developed based on an existing model shared by Kahrobaei and Farajzadeh (2022), served as a representation of the CO_2 injection process in a depleted gas reservoir. It enabled a sensitivity analysis to identify the main parameters that affect hydrate formation. Additionally, the model investigated the resulting reduction in permeability, which ultimately led to diminished injectivity and increased injection pressure due to hydrate formation.

Ultimately, both experimental and numerical approaches showed that the formation of hydrates leads to a reduction in permeability, thereby diminishing injectivity and elevating injection pressure.

Contents

List of Figures

List of Tables

Nomenclature

Abbreviations

Abbreviation	Definition
AAs	Anti-agglomerates
ASSET	Advanced Sub-Surface Energy Transition
BHP	Bottom Hole Pressure
$CaCl_2$	Calcium chloride
CCS	Carbon Capture and Storage
CH_4	Methane
CO_2	Carbon dioxide
Cont.	Continuation
G	Gaseous CO_2-rich phase
GHG	Greenhouse gases
H	Hydrates
H_2O	Water
HDHI	High dosage hydrate inhibitors
I	Ice
J-T	Joule–Thomson
KHIs	Kinetic hydrate inhibitors
L_{CO2}	Liquid CO_2-rich phase
LDHIs	Low dosage hydrate inhibitors
MeOH	Methanol
MoReS	Modular Reservoir Simulator
$Mtpa$	Million tonnes per annum
N_2	Nitrogen
NaCl	Sodium chloride
$P-T$	Pressure-temperature
$Q1$	Upper quadruple point $WHL_{CO2}G$
$Q2$	Lower quadruple point $IHWG$
SDE++	Stimulation of Sustainable Energy Production and Climate Transition
THIs	Thermodynamic hydrate inhibitors
W	Liquid water-rich phase

Symbols

Symbol	Definition	Unit
A	Area	[m^2]
C	Fitting parameter for Chen et al. model	[-]
F	Degrees of freedom	[-]
H_{cst}	Constant enthalpy	[J/kg]
J	Injectivity index	[$m^3/s/bar$]
k	Thermal Conductivity	[$W/m/K$]
k_b	Backward reaction rate coefficient	[-]
k_f	Forward reaction rate coefficient	[-]
K	Permeability	[mD]
K_0	Initial permeability	[mD]

Symbol	**Definition**	**Unit**
K/K_0	Normalized permeability	[-]
K_{rw}	Water relative permeability	[-]
K_{rg}	Gas relative permeability	[-]
L	Length	$[m]$
MRF	Mobility Reduction Factor	[-]
n	Hydration number	[-]
n_g	Gas exponent on relative permeability	[-]
n_w	Water exponent on relative permeability	[-]
N	Number of components	[-]
P	Pressure	$[bar]$
Pc	Capillary pressure	$[bar]$
P_{inj}	Injection pressure	$[bar]$
P_{res}	Reservoir pressure	$[bar]$
PV	Pore volume	$[ml]$
q_i	Injection rate	$[m^3/s]$
r_b	Backward reaction rate	$[kmol/m^3/s]$
r_f	Forward reaction rate	$[kmol/m^3/s]$
S_{gr}	Residual gas saturation	[-]
S_H	Hydrate saturation	[-]
S_w	Water saturation	[-]
S_{wc}	Connate water saturation	[-]
S_{wi}	Initial water saturation	[-]
t	Time	$[s]$
T	Temperature	$[°C]$
T_{inj}	Injection temperature	$[°C]$
T_{res}	Reservoir temperature	$[°C]$
[ ]	Concentration	$[wt\%]$
β	Constant for Pang-Sharma model	[-]
ΔP	Differential pressure	$[bar]$
ΔP_i	Initial differential pressure	$[bar]$
ΔT	Differential temperature	$[°C]$
Π	Number of phases	[-]
μ	Viscosity	$[cP]$
μ_{J-T}	Joule–Thomson coefficient	$[°C/bar]$

1

Introduction

1.1. CO_2 Emissions and CCS Context

Over the past 60 years, the world has experienced an increase in global temperature, Figure 1.1, a phenomenon commonly referred to as global warming (Shaftel et al., 2023). This continuous and long-term rise in global temperature impacts weather patterns, resulting in what is known as climate change (United Nations, n.d.). Climate change encompasses not only increments in temperature and variations in weather patterns but also devastating consequences for human life, such as severe droughts, water shortages, wildfires, flooding, rising sea levels, melting glaciers, disastrous storms, and biodiversity reduction (Masson-Delmotte et al., 2018).

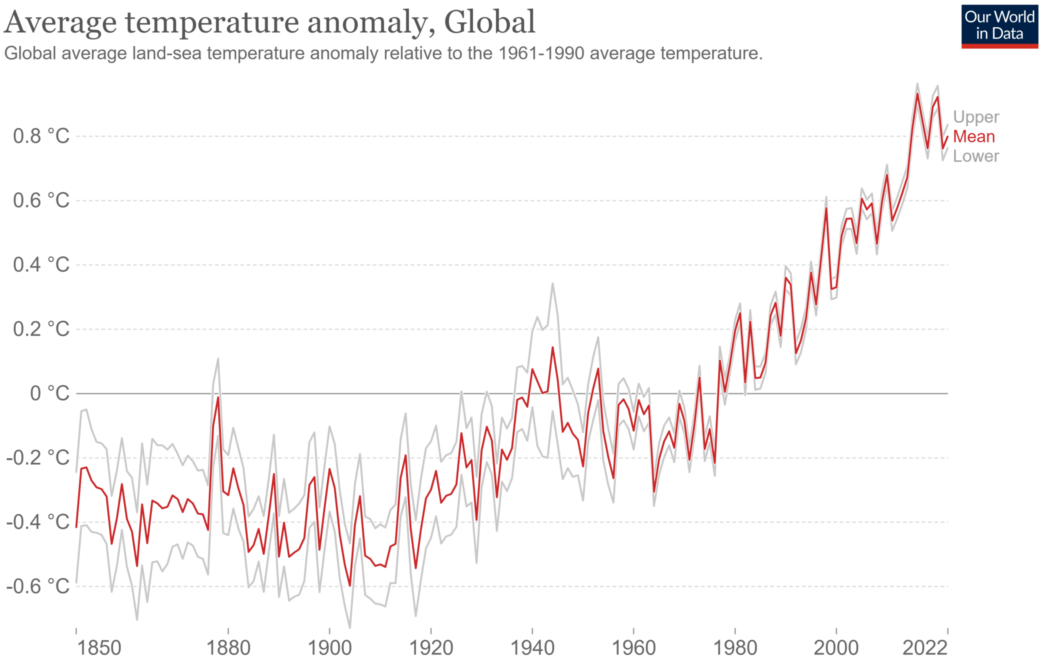

Figure 1.1: Global average land-sea temperature anomaly from 1850 to 2022 (Ritchie et al., 2020).

Climate change has been caused mainly by the continuous increment concentration of greenhouse gases (GHG) in the atmosphere, dominated primarily by carbon dioxide (CO_2) and methane (CH_4) (IPCC, 2023). This is illustrated in Figure 1.2, which depicts the increasing trend in atmospheric CO_2 concentrations over time. The excessive accumulation of CO_2 in the atmosphere retains the infrared radiation that the Earth's surface emits after absorbing sunlight, which warms the globe (Zandalinas et al., 2021).

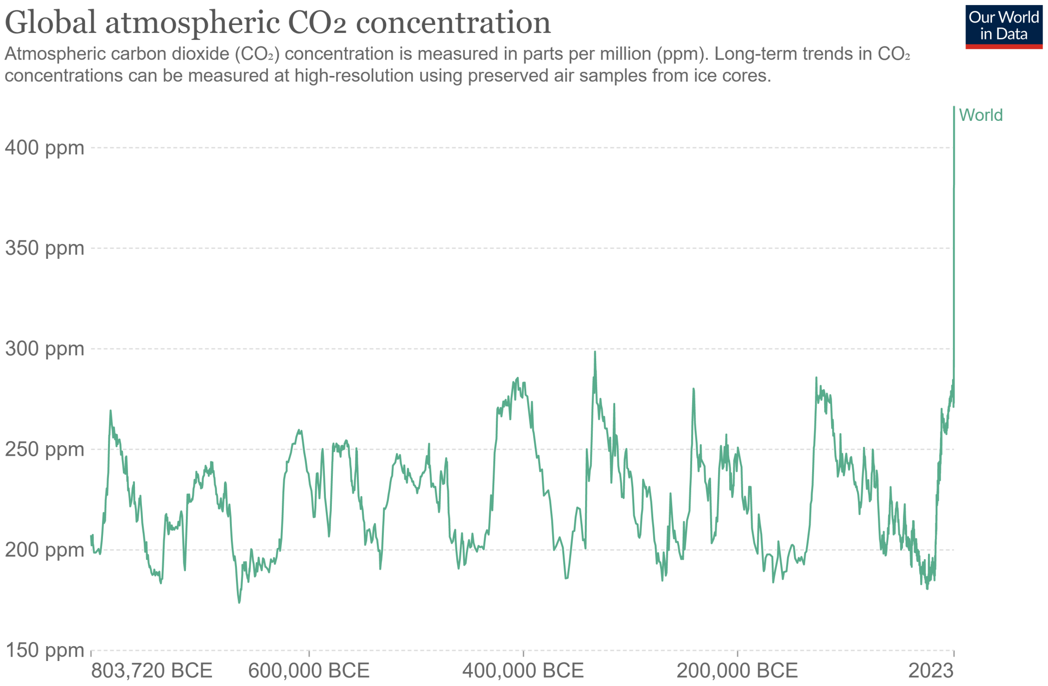

Figure 1.2: Atmospheric CO$_2$ concentration since 800 thousands of years before 2023 (Ritchie et al., 2020).

In order to limit global warming and cope with the catastrophic climate change consequences, governments around the world signed the Paris Agreement in 2015, with the goal of *"reducing the increase in the global average temperature to well below* $2^{\circ}C$ *above pre-industrial levels"* (United Nations, 2015). However, with the current world climate policies, the increment in the global temperature would be around $2.5 - 2.9^{\circ}C$, as shown in Figure 1.3. Therefore, it is required to keep developing solutions that help to reduce the increase in atmospheric CO$_2$ concentration and prevent climate change devastating outcomes.

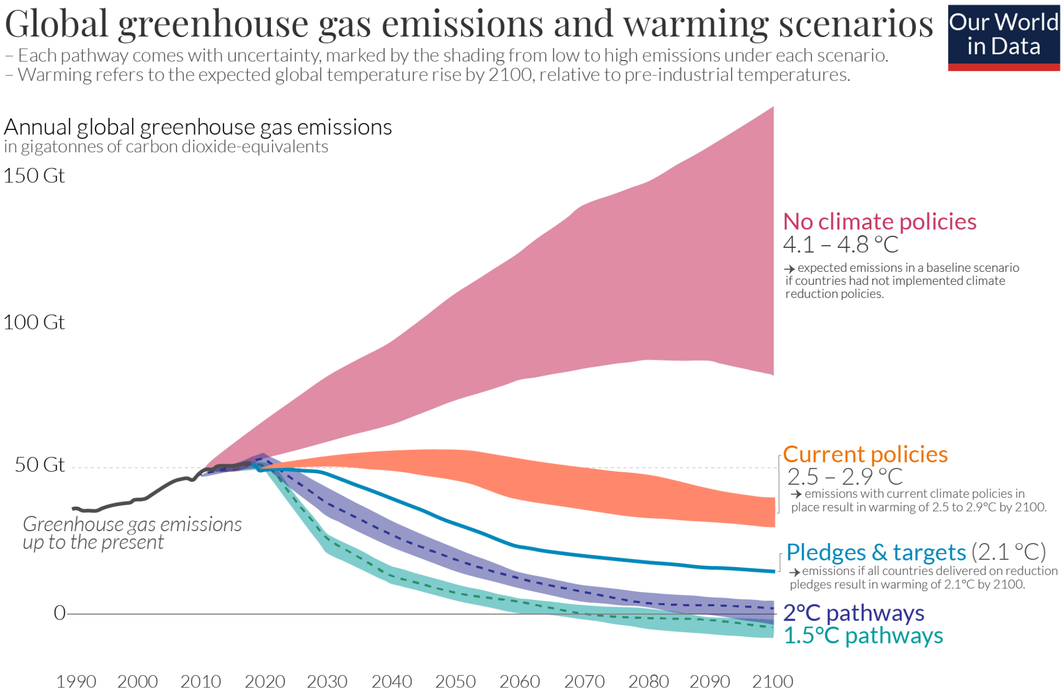

Figure 1.3: Global GHG emissions and warming scenarios according to climate policies (Ritchie et al., 2020).

CO_2 emissions sources cover several sectors, including energy generation, industrial, transport, agriculture, and residential sectors (EPA, 2023). Among these sectors, the most predominant sources of CO_2 emissions are the use of fossil fuels in power generation and transportation, and the industrial sector (IPCC, 2023). To reduce CO_2 emissions, options include reducing energy consumption, transitioning to less carbon-intensive fuels, expanding the use of renewable energy sources, and implementing CO_2 capture and storage technology (IPCC, 2005).

The Carbon Capture and Storage (CCS) technology has been verified and proven throughout the past several decades; being Norway, in 1996, the pioneer of the Sleipner project, first industrial-scale project that developed storage of CO_2 in a deep saline aquifer (Baklid et al., 1996; Eiken et al., 2011). Following the Sleipner project, CCS was pointed and recognized as a technology to reduce and stabilize CO_2 emissions (IPCC, 2005; Haszeldine, 2009).

Figure 1.4 depicts the four processes included in a CCS project: capture, transport, storage, and monitoring (Rochelle et al., 2009; English & English, 2022). Initially, CO_2 is captured in a source to produce a pure CO_2 stream. Prior to transport to the storage site via pipelines, trucks or ships, CO_2 is compressed, generally into a liquid state. Following, CO_2 is stored in a geological site. Finally, continuous monitoring of the geological site is imperative to ensure secure and long-term containment of CO_2, preventing, mitigating, and remediating any potential leakage.

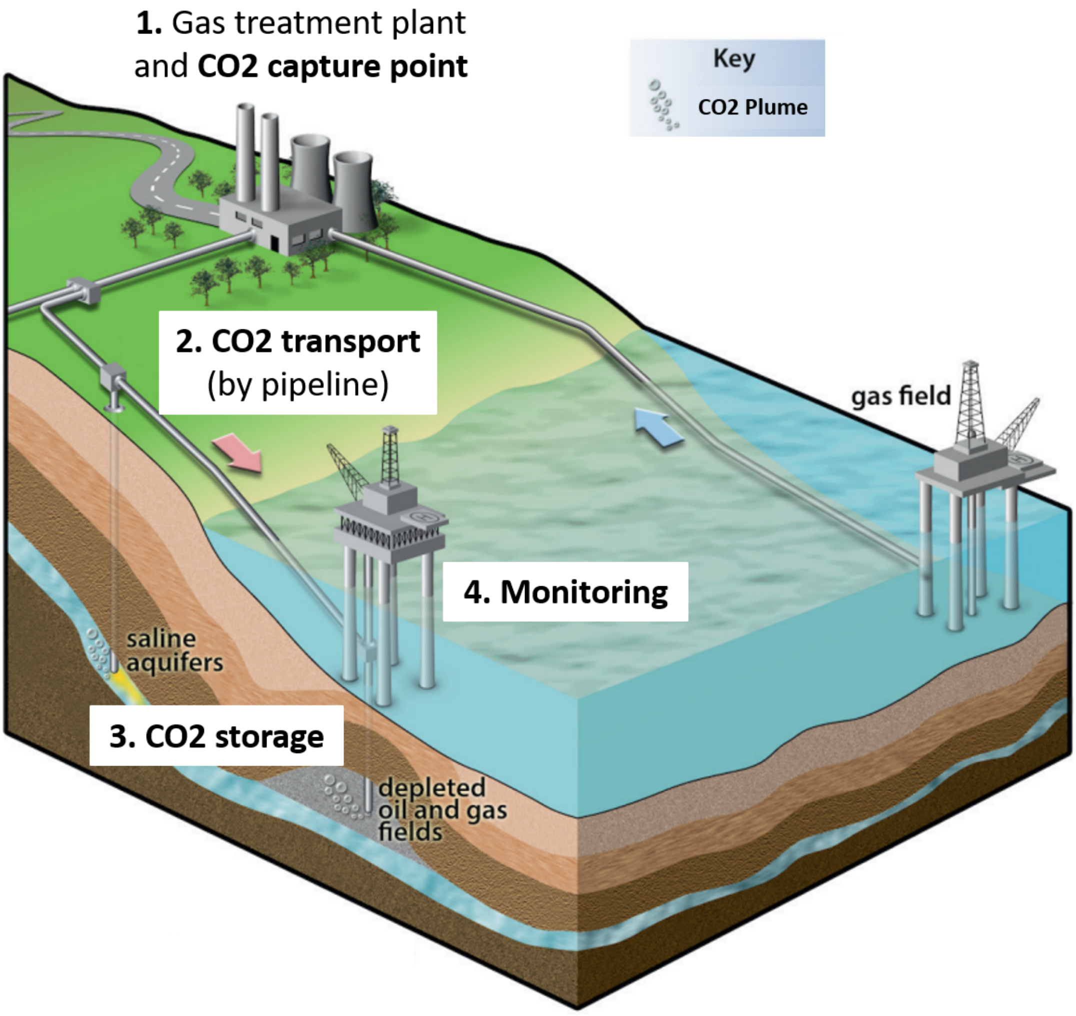

Figure 1.4: Processes included in a CCS project, modified from (SCCS, 2023).

Regarding the geological sites for CO_2 storage, several options are available. These include depleted oil and gas reservoirs, utilization of CO_2 for enhanced oil recovery, deep saline aquifers, deep unmineable coal seams, use of CO_2 for enhanced coal bed methane recovery, as well as other alternatives like caverns or basalt formations (IPCC, 2005). Figure 1.5 illustrates a visual representation of the geological storage options. The storage formation must be capped by a non-permeable unit to prevent any leakage, and it should also have adequate thickness and porosity, to provide storage capacity, and permeability, to facilitate injectivity of CO_2 (English & English, 2022).

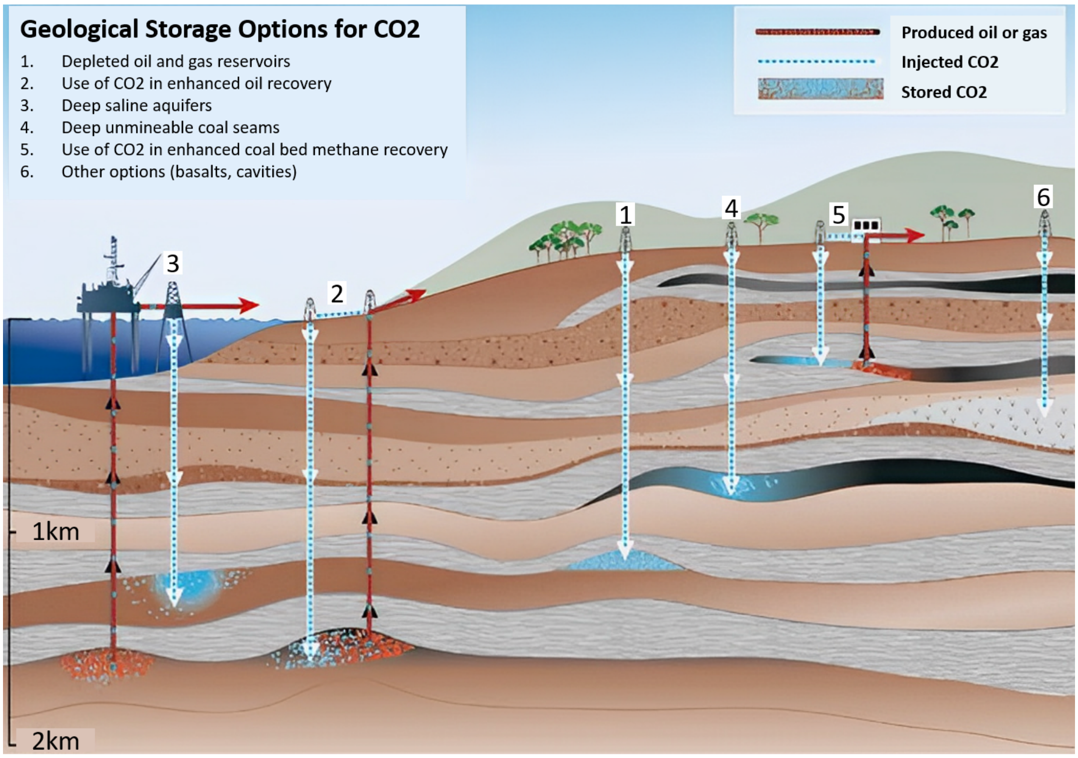

Figure 1.5: Geological storage options for CO_2 (IPCC, 2005).

Among the enunciated geological sites, depleted oil and gas reservoirs are especially attractive for CCS projects for several reasons (IPCC, 2005; Loizzo et al., 2010; Jenkins et al., 2012; Raza et al., 2018; English & English, 2022). Since the oil and gas originally in place did not escape, these formations have proven to be secure traps for storing CO_2. These reservoirs have been largely characterized while extracting hydrocarbons; therefore, there is a large amount of data available for any new development, including models to predict the movement of fluids in the reservoir. Moreover, production and injection history can give a solid indication of the CO_2 injection rate to be used, as well as the total amount of hydrocarbons produced allows to initially estimate the CO_2 storage capacity. Additionally, the existing infrastructure, including wells and facilities, may be suitable to be utilized by CCS projects. Furthermore, depleted reservoirs usually have sufficient CO_2 storage capacity, enabling the long-term storage of CO_2 emissions.

Despite the mentioned advantages, there are some potential challenges associated with storing CO_2 in depleted oil and gas reservoirs (IPCC, 2005; Oldenburg, 2007; Loizzo et al., 2010; English & English, 2022; Kirchin, 2023). Legacy well penetrations in depleted reservoirs can pose a potential risk of leakage. The utilization of existing infrastructure may be limited by the integrity of the materials not originally designed for CO_2 injection. In addition, the depletion status of the reservoirs can lead to a Joule-Thomson (J-T) cooling effect, as CO_2 expands from injection pressure to low reservoir pressure. This effect can lead to the formation of CO_2 hydrates in the reservoir, which can affect CO_2 injectivity. Furthermore, despite the proven storage capacity in depleted reservoirs, there remains uncertainty regarding the long-term behavior of the reservoir, specifically concerning reservoir integrity and containment aspects.

1.2. The Netherlands' Context

Climate change is a global concern; however, its consequences affect each country differently. In the case of The Netherlands, global warming poses specific threats, including sea-level rise and heat waves (IEA, 2022). Changes in temperature patterns can also disrupt energy systems due to shifts in heating and cooling demand, which may put stress on the electricity network. Additionally, the increase in precipitation is also alarming, since it can amplify the risk of floods (PBL, 2013).

The country has a significant industrial sector (OEC, 2022; World Steel Association, 2023), including energy-intensive industries such as petrochemicals and steel production, which contribute to a substantial portion of CO_2 emissions (Ritchie et al., 2020). Moreover, the Netherlands' history, as a significant gas producer, has resulted in a well-developed natural gas infrastructure, which may present potential for CCS projects (IEA, 2020).

In 2019, the Dutch government, represented by the Ministry of Economic Affairs and Climate Policy, introduced the National Climate Act as part of its efforts to address climate change. The Climate Act defined a goal of reducing GHG emissions by 49% by 2030, compared to 1990 levels, and by 95% by 2050 (Ministry of Economic Affairs and Climate Policy, 2019).

The Dutch government recognizes the importance of the CCS projects to achieve the goals defined by the Climate Act. In line with this, the government has established a subsidy program called *Stimulation of Sustainable Energy Production and Climate Transition* (SDE++). The SDE++ program aims to provide funding for projects that contribute to the reduction of CO_2 emissions (Ministry of Economic Affairs and Climate Policy, 2019).

Currently, in the Netherlands, there are two major CCS projects, namely Porthos and Aramis, which have the objective of storing CO_2 in depleted gas reservoirs in the North Sea. These projects are expected to become operational in 2026. Figure 1.6 depicts the location of the two projects. The Porthos project aims to store $2.5\ Mtpa$ of CO_2, while the Aramis project plans to store $5\ Mtpa$ of CO_2 (Porthos, 2023; TotalEnergies et al., 2023).

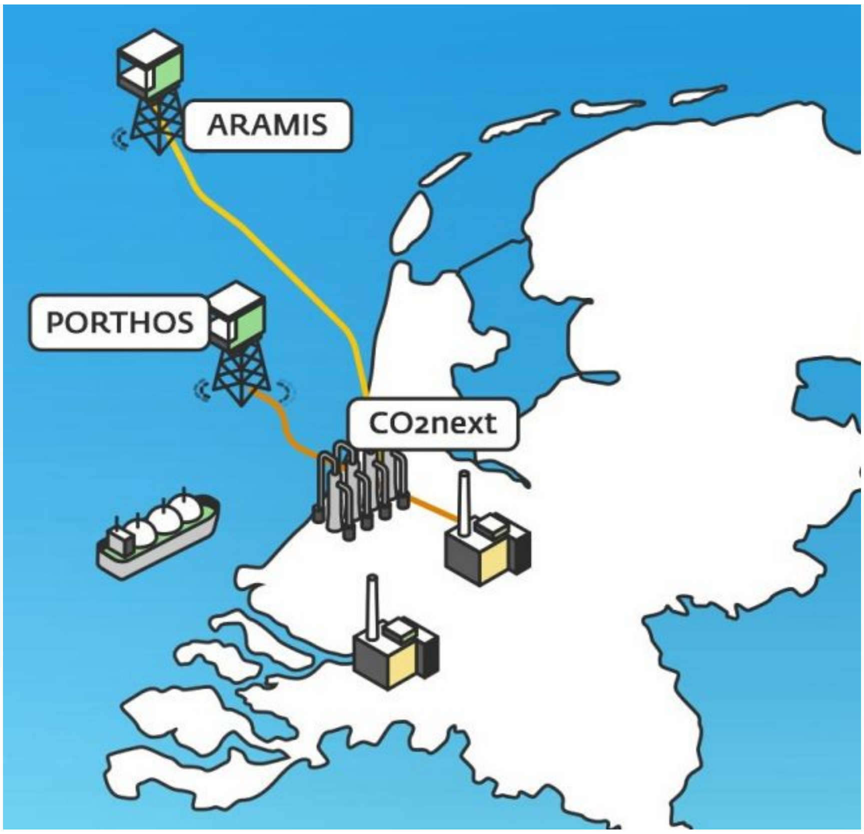

Figure 1.6: Location of Aramis and Porthos CCS projects (Gasunie, 2022).

1.3. Research Objectives

Knowing that the number of projects in the Netherlands and worldwide focusing on CO_2 storage in depleted gas reservoirs is increasing, it is crucial to assess the potential impact of CO_2 hydrates on injectivity decline. This study aims to investigate and evaluate the effect of CO_2 hydrates formation when injecting CO_2 in depleted gas reservoirs, employing a combination of experimental and modeling approaches.

Through conducting experiments, this study seeks to understand the behavior of CO_2 hydrates and their influence on the flow dynamics in porous media. The injectivity decline, resulting from the formation and accumulation of CO_2 hydrates, will be analyzed in detail. Experimental results will also be essential for calibration of the modeling approach.

Furthermore, this study aims to develop an empirical model to predict the formation of CO_2 hydrates in the reservoir and provide insights into their impact on flow dynamics, as well as potential prevention strategies. Understanding these factors will contribute to the development of robust and reliable guidelines for CCS projects in depleted gas reservoirs, ensuring the sustainability and efficiency of operations in the long term. The findings will contribute to the optimization of CO_2 storage strategies, facilitating the successful implementation of CCS projects and furthering the efforts to mitigate climate change.

In order to reach our goals, this study will focus on answering the main research question and also examining several sub-questions:

> What is the impact of hydrate formation on well injectivity during CO_2 injection in depleted gas reservoirs?
>
> - How does the formation of CO_2 hydrates impact permeability?
> - How is the injection pressure affected by the formation of CO_2 hydrates?
> - What prevention or mitigation mechanisms can be employed to address CO_2 hydrates formation?
> - What is the impact of variables such as capillary pressure, rock thermal conductivity, reaction rate coefficients, CO_2 injection rate and CO_2 injection temperature on hydrate formation?

1.4. Report Structure

This study is structured into eight chapters. Chapter 1 establishes the project's context, outlines the research objectives, and provides an overview of the report. In Chapter 2, the theoretical foundation is presented, covering topics such as CO_2 hydrates, their structure, formation and dissociation processes.

Chapter 3 focuses on the experimental setup, procedures, and results gathered at the lab. In total, results from 13 experiments are covered, with nine carried out by the author and four shared by the Advanced Sub-Surface Energy Transition (ASSET) research team. Chapter 4 is dedicated to the development and results of an empirical model, based on an existing model shared by Kahrobaei and Farajzadeh (2022). Following the model's construction, Chapter 5 describes the history match conducted using the model for selected experiments discussed in Chapter 3.

A comprehensive discussion is provided in Chapter 6, covering both experimental and modeling results. Chapter 7 presents the research conclusions based on the results and analysis presented throughout the study. Finally, Chapter 8 offers recommendations for further research to expand upon the findings and address any remaining gaps in knowledge.

2

CO_2 Hydrate Theory

The storage of CO_2 in depleted gas reservoirs has been recognized worldwide, including in the Netherlands, as a viable approach to mitigate the devastating consequences of global warming and climate change. However, several challenges arise when injecting CO_2 into depleted reservoirs, and one of these challenges is the formation of CO_2 hydrates (Kirchin, 2023).

This chapter aims to provide a comprehensive theoretical background on CO_2 hydrates. It will cover essential aspects such as the definition of CO_2 hydrates, their structural characteristics, the pressure-temperature ($P - T$) phase diagram, the processes involved in their formation and dissociation, the behavior of hydrates in porous media, as well as the mechanisms used to inhibit and remediate their formation.

By understanding the fundamental principles of CO_2 hydrates, it becomes possible to address their impact on the permeability of the reservoir and its effect on injectivity, allowing the development of effective prevention and mitigation strategies.

2.1. CO_2 Hydrate

CO_2 hydrate is part of the clathrate hydrates family, which are crystalline ice-like solid compounds (Nagashima et al., 2020). These compounds are formed when hydrogen-bonded water molecules act as a host, create a cavity, and encapsulate guest molecules, in this case CO_2, within their structure. The resulting CO_2 hydrate consist of a lattice of water molecules that trap and encage CO_2 molecules (Sa et al., 2017).

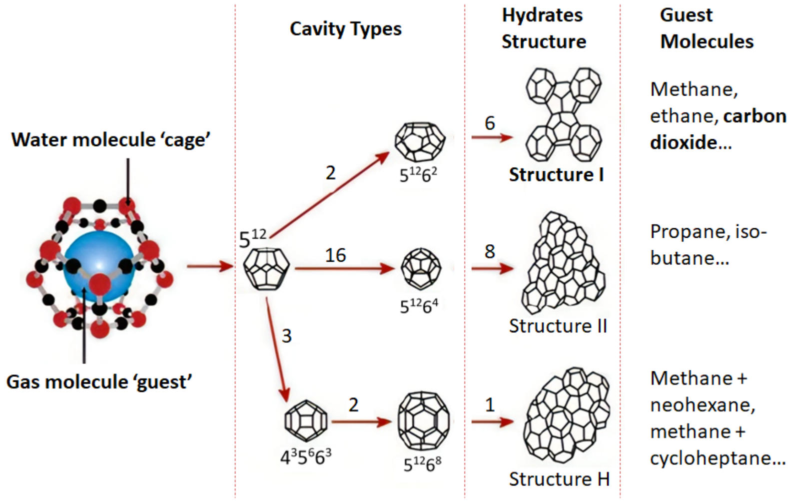

Figure 2.1: Hydrates structure (Jensen, 2010).

Clathrate hydrates are nonstoichiometric compounds that can form three types of structures: I, II, and H (Kang et al., 2008; Nagashima et al., 2020; Gaidukova et al., 2022; Aghajanloo, 2023). Figure 2.1 illustrates these types of structures. CO_2 hydrate belongs to the Structure I type, characterized by a cubic structure composed of tetrakaidecahedron ($5^{12}6^{2}$) and pentagonal dodecahedron (5^{12}) cages (Circone et al., 2003; Sloan & Koh, 2007).

2.2. Hydration Number

CO_2 hydrates can be described by Equation 2.1, where n is the hydration number, representing the ratio of the water (H_2O) molecules number to the CO_2 molecules number in a unit cell of hydrates (Nagashima et al., 2020). The hydration number indicates the amount of water molecules required to trap a guest gas molecule and is characterized by the occupation of structural cavities.

$$CO_2 + nH_2O \longleftrightarrow CO_2 \cdot nH_2O \tag{2.1}$$

Under the ideal assumption of full occupancy (100%) of the cages, n is equal to 5.75 (Circone et al., 2003; Sloan & Koh, 2007). However, it practically is impossible to completely fill the entire cages capacity, therefore, the hydration number is higher. In the literature, a commonly used reference hydration number is 7.67, which corresponds to approximately 75% occupancy of the hydrate cages (Ferdows & Ota, 2006), assuming that CO_2 fills only the large cavities (Lirio & Pessoa, 2013; Qorbani et al., 2017).

It is important to note that the occupancy of the cages in the hydrate structure is affected by thermodynamic conditions, specifically pressure and temperature. Changes in these conditions can impact the occupancy and stability of CO_2 hydrate (Uchida, 1998; Ferdows & Ota, 2006).

2.3. $P - T$ Phase Diagram for CO_2 Hydrate

Phase diagrams help to understand the thermodynamic behavior of a system when changing pressure (P) or temperature (T), or both.

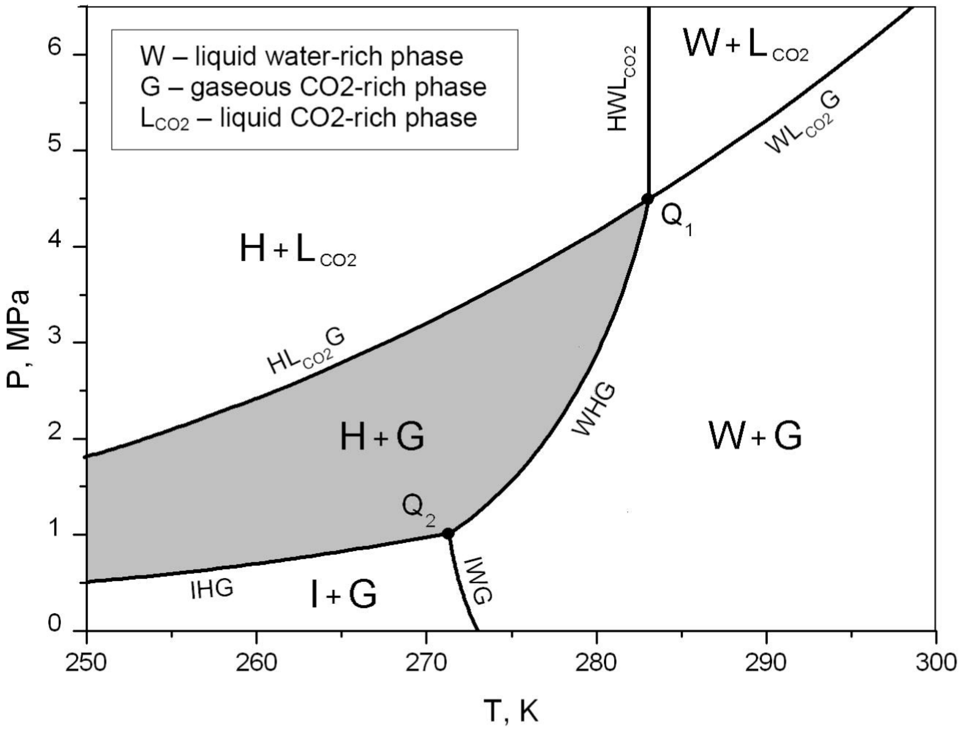

Figure 2.2: Pressure and temperature phase diagram for the binary water-CO_2 system (Voronov et al., 2016).

Figure 2.2 illustrates the $P-T$ phase diagram for the binary water and CO_2 system. The phases present in the phase diagram are hydrates (H), gaseous CO_2-rich phase (G), liquid water-rich phase (W), liquid CO_2-rich phase (L_{CO2}), and ice (I). In the phase diagram, the thick lines represent the three-phase equilibrium curves, the grey area is the two-phase hydrate-gas equilibrium region (also called hydrate stability zone), and the points $Q1$ and $Q2$ indicate the upper ($WHL_{CO2}G$) and lower ($IHWG$) quadruple points, respectively (Voronov et al., 2016).

Equation 2.2 presents the well-known Gibbs' phase rule (Gibbs, 1961), where F, N and Π are the degrees of freedom, number of components, and number of phases, respectively.

$$F = N - \Pi + 2 \tag{2.2}$$

The degrees of freedom are useful to determine the number of independent variables required to specify the condition of a system (Fegley, 2013). By applying Gibbs' phase rule to the binary water and CO_2 system, it is possible to see in the $P-T$ phase diagram that an area defines the presence of two phases, a line defines three phases, and a point defines four phases (Aghajanloo, 2023).

2.4. Hydrates Formation and Dissociation

The processes of hydrate formation and dissociation, described as time-dependent phenomena (Sloan & Koh, 2007), pose a greater challenge in terms of measurement and modeling compared to thermodynamic processes. As time-dependent processes are inherently more complex, the accuracy of measurements and models may decrease by at least one order of magnitude (Sloan & Koh, 2007).

Before explaining in detail the hydrates formation and dissociation processes, it is required to understand, when storing CO_2 in a depleted reservoir, how the thermodynamic conditions are met in order to locate the binary water-CO_2 system into the hydrates stability zone.

2.4.1. Joule–Thomson (J-T) Expansion Effect

Normally, when storing CO_2 in a depleted gas reservoir, CO_2 is compressed and transported to be injected from a high-pressure condition to a low-pressure condition (English & English, 2022). The specific pressure condition for injection depends on the status of the selected reservoir for storage. The expansion of the gas from high-pressure to low-pressure generates a temperature change, variation determined by the Joule–Thomson coefficient (μ_{J-T}), which is equal to the ratio of the temperature decrease to the pressure drop ($\frac{\partial T}{\partial p}$) at constant enthalpy ($H_{cst}$), according to Equation 2.3 (Ott & Boerio-Goates, 2000).

$$\mu_{J-T} = \left(\frac{\partial T}{\partial P}\right)_{Hcst} \tag{2.3}$$

The Joule–Thomson expansion can generate a cooling or heating effect, depending on the sign of the J-T coefficient (Tosun, 2021). Generally, if the J-T coefficient is positive, the J-T expansion generates a cooling effect, otherwise, a heating effect is produced when the J-T coefficient is negative, as shown in Figure 2.3.

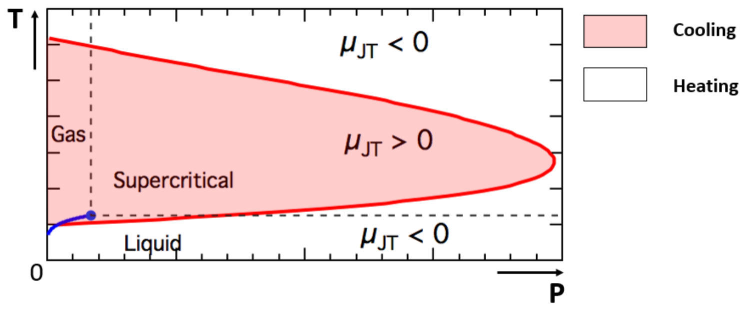

Figure 2.3: Sign of the J-T coefficient, modified from (Winterbone & Turan, 2015).

Figure 2.4 shows a schematic of the J-T cooling effect that is experienced when injecting CO_2 in a depleted gas reservoir.

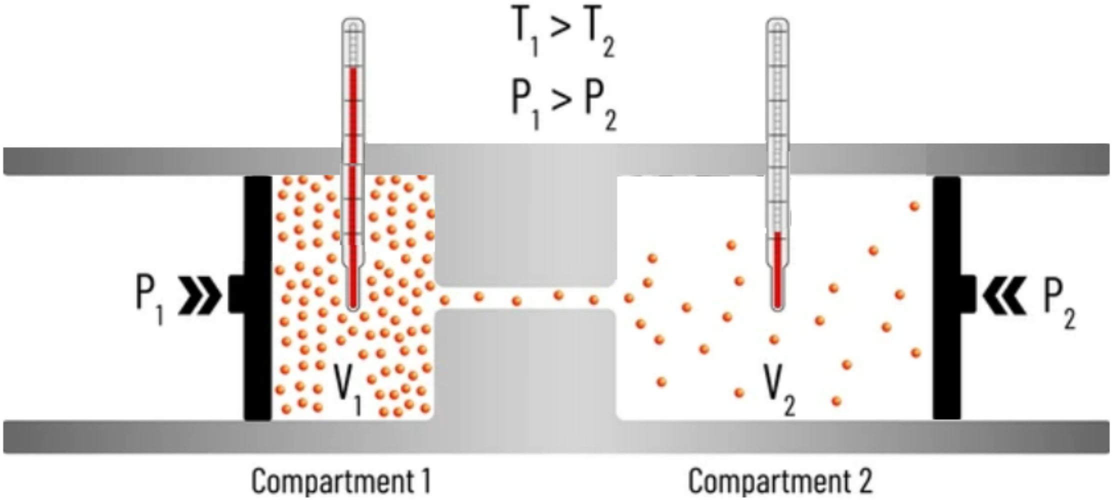

Figure 2.4: Schematic of the J-T cooling effect (RKTZ, n.d.).

Figure 2.5 illustrates the different conditions during the injection of CO_2 into a depleted reservoir, including the bottom hole injection, near wellbore, and reservoir conditions. It is important to mention that even though CO_2 is injected as pure and as dehydrated as possible, the reservoir is water saturated, situation that explains the use of a phase diagram for the binary water-CO_2 system. As mentioned before, usually, CO_2 is injected in liquid phase (represented by the orange star). However, due to the cooling generated by the J-T expansion, the system enters in the hydrate stability zone (indicated by the green star). Considering that the reservoir is depleted and has a normal geothermal gradient, the reservoir condition is represented by the blue star.

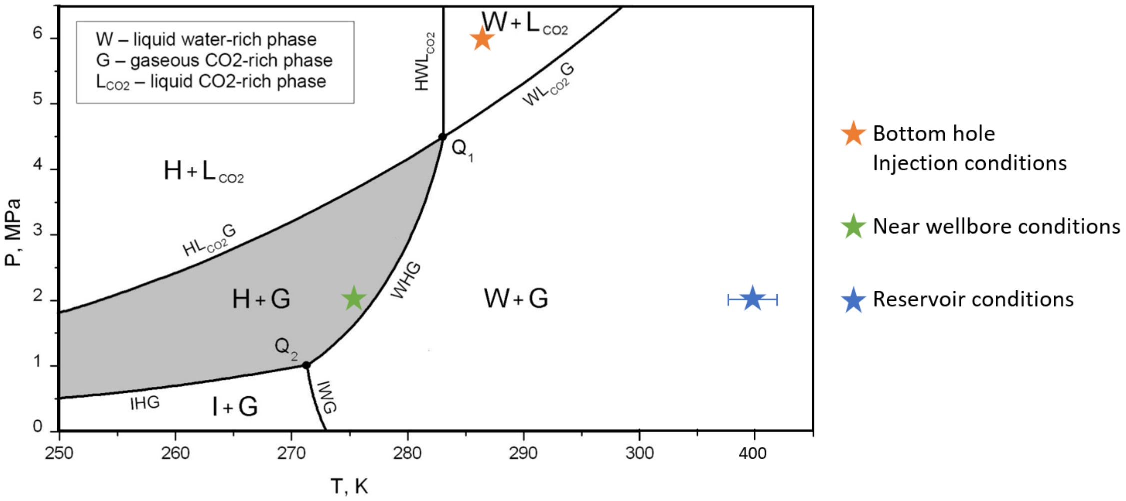

Figure 2.5: $P - T$ phase diagram for the binary system water-CO_2 and location of the bottom hole injection, near wellbore and reservoir conditions, modified from (Voronov et al., 2016).

2.4.2. Formation

Once the thermodynamic conditions have been achieved, and the binary water-CO_2 system is in the hydrates stability zone, hydrates formation takes place. It should be emphasized that hydrate formation technically qualifies as a phase transition because it does not result in the creation of new chemical bonds (Yin et al., 2018).

The hydrates formation kinetics can be divided into two stages, hydrate nucleation and hydrate growth (Sloan & Koh, 2007; Aghajanloo, 2023). The formation process can be explained by considering the gas consumption versus time in a cell containing water that is pressurized with gas and brought to P and T conditions within the hydrate stability zone. Gas is added to the cell to keep constant pressure. Hydrates form with time. The described process is shown in Figure 2.6, where the nucleation stage is depicted by *Region 1* (illustrated in green) and *Regions 2, 3* and *4* correspond to the hydrate growth stage (represented in red, yellow, and blue) (Sloan & Koh, 2007; Yin et al., 2018).

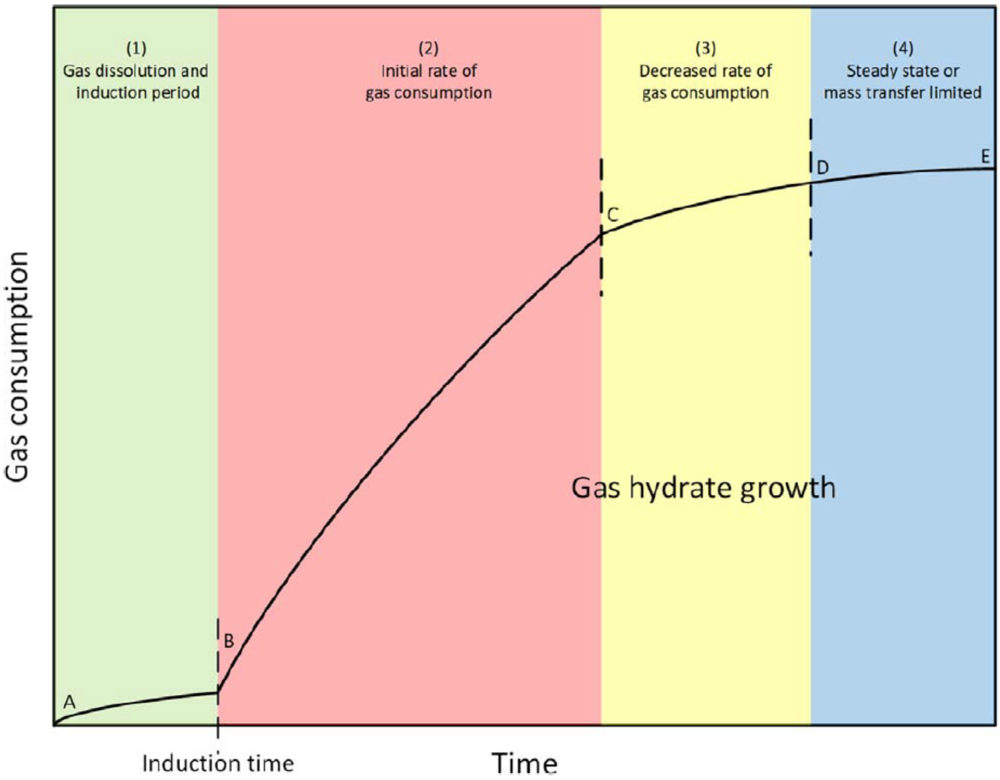

Figure 2.6: Gas consumption curve during gas hydrate formation in a stirred tank reactor (Yin et al., 2018).

2.4.2.1. Nucleation

The nucleation, characterized by a low gas consumption, is a microscopic and stochastic process that starts with the dissolution/adsorption of guest molecules into the aqueous phase. During the nucleation, small clusters of gas and water (hydrate nuclei) grow and spread until reaching a critical size that triggers the hydrate growth stage (Liu et al., 2022). Thus, the critical size is the hydrate nuclei size that must be reached before nuclei/clusters can grow spontaneously. Once hydrates can be detected macroscopically, the gas hydrate growth stage begins, moment defined as the induction time or induction period (Sloan & Koh, 2007; Hassanpouryouzband et al., 2020).

Nucleation can be homogeneous or heterogeneous, depending on the location at which hydrate nuclei form. The homogeneous nucleation happens at the nucleus of the hydrate phase emerging directly from the parent phase in the absence of impurities, whereas heterogeneous nucleation happens on the contact surface of gas (or liquid) and water or in the presence of an alien particle (Hassanpouryouzband et al., 2020; Aghajanloo, 2023).

The hydrate nucleation can be identified by a rapid decrease in pressure during the encapsulation of guest molecules within the crystalline hydrate cages, or a expeditious increase in temperature as a result of the exothermic reaction of the hydrate formation (Sloan & Koh, 2007; Hassanpouryouzband et al., 2020; Aghajanloo, 2023).

2.4.2.2. Hydrate Growth

After the nucleation stage, hydrate growth takes place. This represents a complex interfacial process where various components (water, gas, and hydrate) are dispersed within multiple phases (liquid, gas, and hydrate) on multiple scales (ranging from molecular to macroscopic). The growth period involves heat and mass transfer, fluids flow, and intrinsic kinetics of phase change. Although several models for hydrate growth have been described depending on the controlling mechanism (heat transfer, mass transfer, or reaction kinetics), hydrate growth is still a matter of research (Yin et al., 2018).

The hydrate growth period, shown in Figure 2.6, is characterized by three stages that are distinguished from one another based on the gas consumption. During the first stage, *Region 2* (illustrated in red), there is a quite fast hydrate growth and a relevant rise in gas consumption. In this stage, gas molecules are transferred from vapour to liquid phase and massively packed in the hydrate cages. Since water and gas molecules are consumed during hydrate formation, the rate of hydrate formation gradually declines with time to finally flatten at the end of the hydrate formation process, stage depicted by *Region 3* (shown in yellow). Finally, the steady state is reached, *Region 4* (colored in blue), due to maximum consumption of hydrate-forming components (water or gas) or the limitation of mass transfer or heat transfer (Sloan & Koh, 2007; Yin et al., 2018).

2.4.3. Dissociation

The dissociation of hydrates is a thermally driven process demanding an external provision of heat to disrupt the hydrogen bonds among water molecules and the van der Waals interaction forces existing between the guest and host water molecules within the hydrate structure. This disruption leads to the decomposition of the hydrate into water and gas. Thus, the dissociation process is dependent upon heat transfer (Sloan & Koh, 2007; Hassanpouryouzband et al., 2020; Zhao et al., 2021).

Depressurization, thermal stimulation, thermodynamic inhibitor injection, or a combination of these techniques can all be employed to dissociate hydrates (Sloan & Koh, 2007). Figure 2.7 presents a phase diagram showing the three common hydrate dissociation techniques. Depressurization is depicted as $\Delta T = 0$, thermal stimulation as $\Delta P = 0$, and inhibitor injection is illustrated by displacing the solid hydrate equilibrium curve to the dashed curve with the injection of $10wt\%$ methanol (MeOH) in the free water phase (Sloan & Koh, 2007).

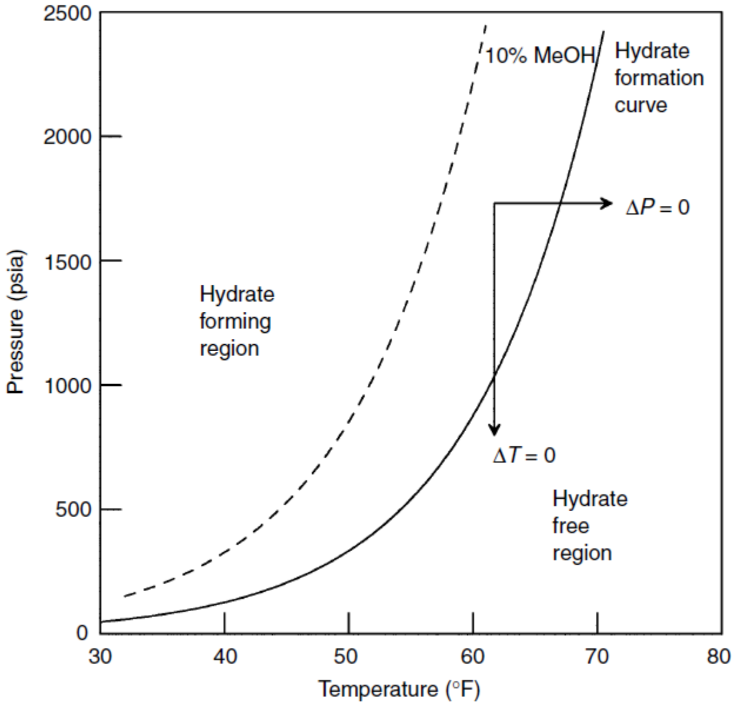

Figure 2.7: $P - T$ phase diagram showing the three common hydrate dissociation techniques (Sloan & Koh, 2007).

2.4.4. Memory Effect

It has been observed that the formation time for gas hydrates is reduced significantly for water that is decomposed from gas hydrates, in comparison with water that has never formed gas hydrates (Rossi et al., 2021). This phenomenon, called the memory effect, means that hydrates keep a memory of their structure when dissociated thermally at moderate temperatures (Wen et al., 2021). However, if the hydrate system is heated substantially above the temperature at which hydrates form at a given pressure, the memory effect will vanish (Sloan & Koh, 2007).

Two hypotheses explain the memory effect; however, research at the molecular level has been limited, still being unresolved which of the two hypotheses is the reason for this phenomenon (Sloan & Koh, 2007). The initial hypothesis suggests that the structure of hydrates, which cannot be discerned by the unaided eye, persists within the solution subsequent to the dissociation of hydrates (Sloan & Koh, 2007). The remaining hydrate structure can be either a residual structure (Takeya et al., 2000) or persistent hydrate crystallites (Buchanan et al., 2005). The second hypothesis states that once the hydrate has broken down, any dissolved gas continues to stay within the solution (Rodger, 2000). Nevertheless, in both cases, the formation time of hydrates is shortened due to a decrease in the induction period. This reduction is attributed to the presence of either hydrate structures or dissolved gas in the solution, particularly when the system has already formed hydrates (Aghajanloo, 2023).

When it comes to reservoirs and the memory effect, it is crucial to keep in mind that heating the reservoir or replacing the hydrate-forming water is not an option. Therefore, it is crucial to consider this phenomenon while executing CCS projects.

2.5. Hydrates in Porous Media

Depleted gas reservoirs are a porous media; therefore, it is crucial a comprehensive understanding of how the behavior of CO_2 hydrates is influenced by the conditions of the porous space.

While the morphology of hydrates is primarily controlled by environmental conditions (temperature and pressure) and the availability of the necessary chemical components (water and gas), the nature of the sediment host also influences hydrate formation (Gabitto & Tsouris, 2010). Grain size may play a significant role in hydrate formation, as fine-grained mud is unlikely to exhibit hydrate growth compared to coarser-grained sediments, with larger pores, that are more likely to act as hosts (Clennell et al., 1999; Henry et al., 1999).

Additionally, surface tension and the capillarity effect, created by the pores, have a direct impact on hydrate formation. They reduce water activity, making the hydrate formation conditions more demanding. In general, the hydrates equilibrium curve shifts to the low-temperature and high-pressure zone when considering a porous media (Kang et al., 2007; Kang et al., 2008; Wang et al., 2022; Aghajanloo, 2023). An example highlighting this phenomenon is the shift in the hydrates equilibrium curve that occurs on the ocean floor (Clennell et al., 1999).

Moreover, studies have shown that porous space also affects hydrate dissociation, revealing that dissociation is more easily accomplished within small pores than in large pores (Anderson et al., 2003; Llamedo et al., 2004; Aghajanloo, 2023). Therefore, hydrate breakdown may primarily take place in small pores, rather than in neighboring larger pores.

In general, porous media affects the kinetics of the hydrates formation process. Small particle sizes may enlarge the surface area for gas-water contact, increase the number of nucleating sites, and expedite hydrate growing rates (Wang et al., 2022).

Concerning the interaction of the fluids, CO_2 and water, in the porous space, CO_2 may be dissolved in water or as a separate component. Regardless, studies have shown that hydrates can be formed in both situations if the thermodynamic conditions are sufficient, and water is available. Thus, the guest CO_2 molecule that is captured by the water molecules to form hydrates may be dissolved in water or as a free-gas phase (Tohidi et al., 2001).

In porous media, water saturation plays an important role when it comes to the formation of hydrates. In environments with lower water saturation, water availability is a limiting factor for hydrate formation (Gabitto & Tsouris, 2010). In partially water-saturated formations, water tends to accumulate at grain contacts covering individual sand grains. This effect boosts the preferential growth of hydrates at grain contacts, which will act as cement between the rock grains. In fully water-saturated media, hydrates will tend to form at the gas-water interface that occurs in the pore space, becoming a pore-filling component (Kingston et al., 2008).

2.5.1. Impact of Hydrates on Injectivity

One of the challenges encountered during the storage of CO_2 in depleted gas reservoirs is the reduction in injectivity resulting from the formation of CO_2 hydrates within the reservoir formation due to the cooling effect caused by the J-T expansion. To address this challenge effectively, it is crucial to have a clear understanding of what injectivity entails, how it can be measured, and why the presence of hydrates diminishes it.

Injectivity can be defined as the ease with which the fluids can flow through a formation (Manjunath, 2022). Injectivity is quantified through the injectivity index (J), Equation 2.4, which is the ratio of fluid rate injected (q_i) to the differential pressure (ΔP) required to keep the injection of that rate.

$$J = \frac{q_i}{\Delta P} \tag{2.4}$$

It is known, from Darcy's law (Hubbert, 1957), that rate (q) is related to permeability (K), which refers to the capacity of a rock to enable the passage of fluids through it (NETL, 2010). Permeability is dependent on the flow paths through which fluid can flow; therefore, the presence of hydrates reducing or obstructing flow paths directly affects injectivity.

To assess the impact of hydrates on permeability, it is essential to quantify the extent to which the porous space is occupied by hydrates. This quantification is typically expressed as the parameter known as hydrate saturation (S_H).

Considering the hydrate saturation, several permeability models have been proposed to predict the dynamic permeability evolution of sediments containing hydrates. These models employ various methods, such as theoretical derivation or empirical fitting, and consider different assumptions, including the morphology and distribution of hydrates within the porous space (Xu et al., 2022). Figure 2.8 provides a schematic representation of gas hydrates morphology in porous media, illustrating the diverse ways in which hydrates can form and occupy the porous space, such as pore center, grain-coating, cementing, load-bearing, and patchy distribution. Each of these morphologies has a distinct impact on permeability and results in a different permeability model (Ren et al., 2020).

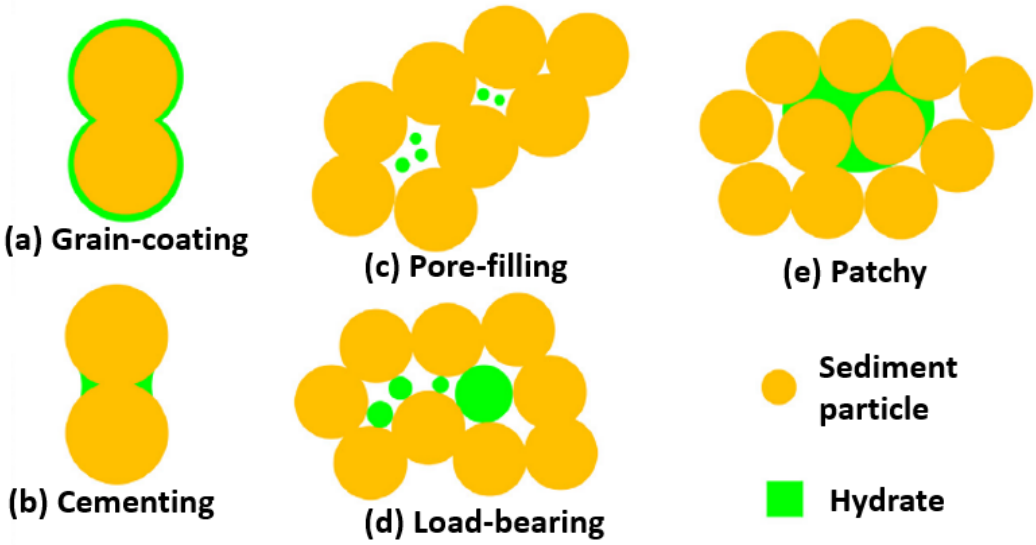

Figure 2.8: Hydrate morphology in porous media (Ren et al., 2020).

As mentioned, multiple models have been proposed to predict permeability as a function of hydrate saturation. However, there is no consensus on a universal model, necessitating a case-by-case examination. This lack of agreement is illustrated by Figure 2.9, which displays experimental data and various permeability models that are dependent on the morphology of gas hydrates within the porous space. In the figure, the normalized permeability (K/K_0) represents the ratio of current permeability to initial permeability.

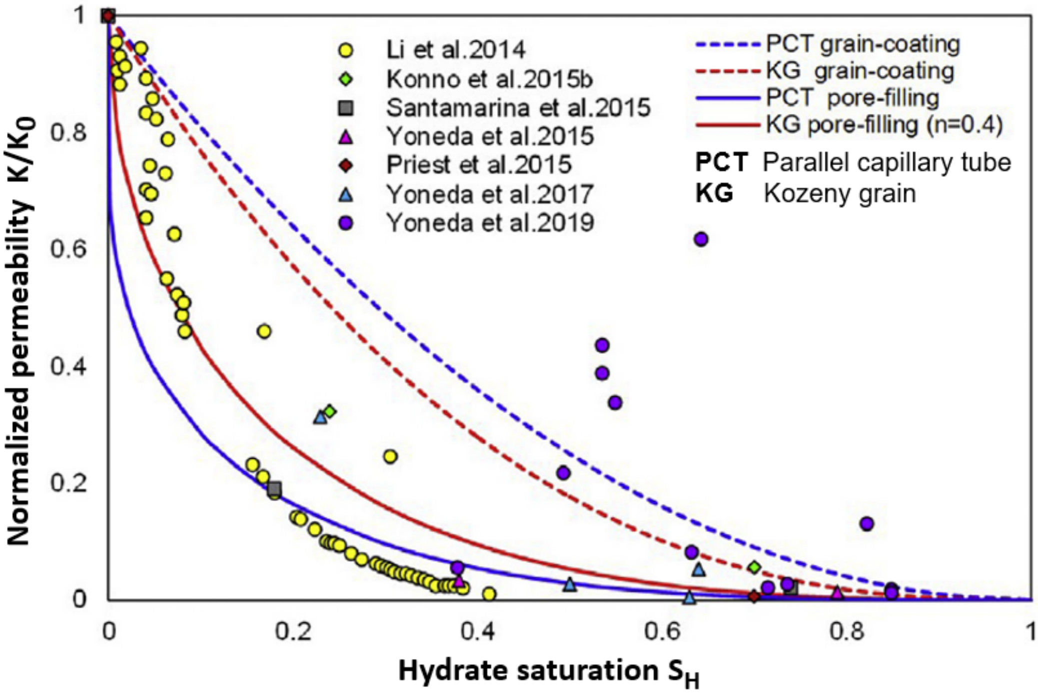

Figure 2.9: Data from pressure-core samples and permeability models versus hydrate saturation, modified from (Ren et al., 2020).

For this study, two well-known models will be used to predict the permeability reduction depending on hydrate saturation. The first model, introduced by Pang & Sharma in 1997, is a function of hydrate saturation (S_H) and a constant (β) that accounts for trapped particles deposit in the pores (Pang & Sharma, 1997). The Pang-Sharma model is presented in Equation 2.5.

$$\frac{K}{K_0} = \frac{1}{1 + \beta \cdot S_H} \tag{2.5}$$

The second model, defined by Chen et al. in 2018, proposes a modified Corey model with an exponential function of hydrate saturation (S_H), which includes a fitting parameter (C) that indicates the degree of crystal coarsening and patch size for a multiphase system (Xu et al., 2022). The Chen et al. model is depicted in Equation 2.6.

$$\frac{K}{K_0} = (1 - S_H) \cdot e^{-C \cdot S_H} \tag{2.6}$$

Figures 2.10a and 2.10b show two examples of the permeability prediction achieved with the mentioned models based on experimental data from (Kumar et al., 2010) and (Li et al., 2023), respectively.

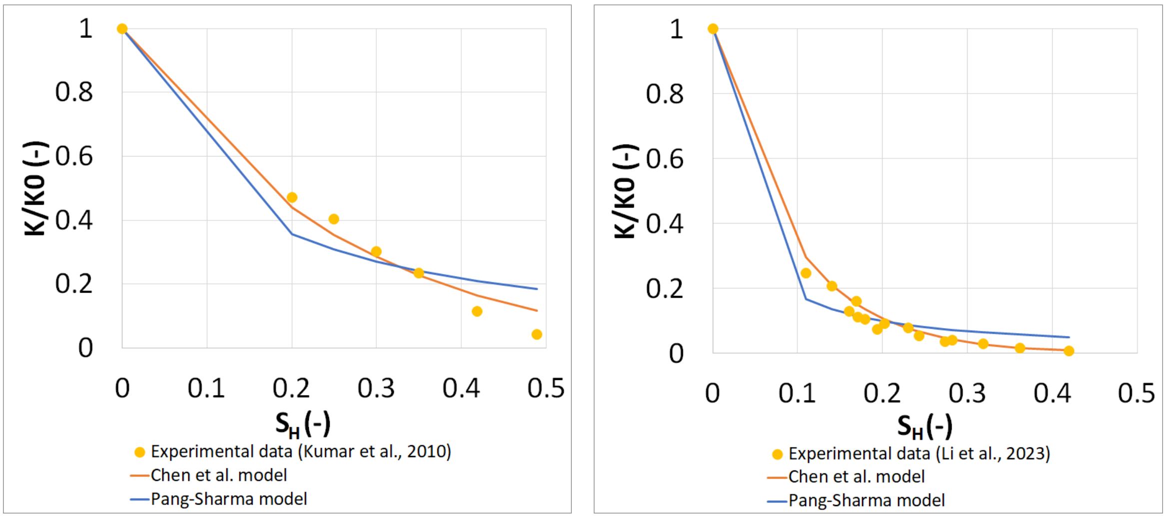

(a) Permeability prediction for data from (Kumar et al., 2010).

(b) Permeability prediction for data from (Li et al., 2023).

Figure 2.10: Permeability prediction as a function of hydrate saturation based on Pang-Sharma and Chen et al. models.

2.6. Inhibitors

Given that hydrates can reduce reservoir permeability and affect injectivity, chemical compounds can be employed to change the thermodynamic conditions of hydrate formation, thus preventing the formation of hydrates in the porous media. These chemical compounds are called inhibitors and are classified based on the necessary amount needed to prevent hydrates formation. The two classes of inhibitors are low dosage hydrate inhibitors (LDHIs) and high dosage hydrate inhibitors (HDHI) (Khan et al., 2020; Aghajanloo, 2023). LDHIs are effective at lower concentrations, while HDHIs require higher concentrations to achieve the desired inhibitory effect.

Thermodynamic hydrate inhibitors (THIs), which are based on alcohols like methanol (MeOH), glycols like MEG, or ordinary salts like sodium chloride (NaCl), make up the HDHI category. THIs work by shifting the hydrate equilibrium curve towards lower-temperature and higher-pressure areas which prevents the system from entering the hydrate stability zone (Nagashima et al., 2020). Figure 2.11 depicts the effect of THIs on the hydrate equilibrium curve for the system brine-CO_2. In this phase diagram, the equilibrium curve liquid-gas CO_2 has been omitted.

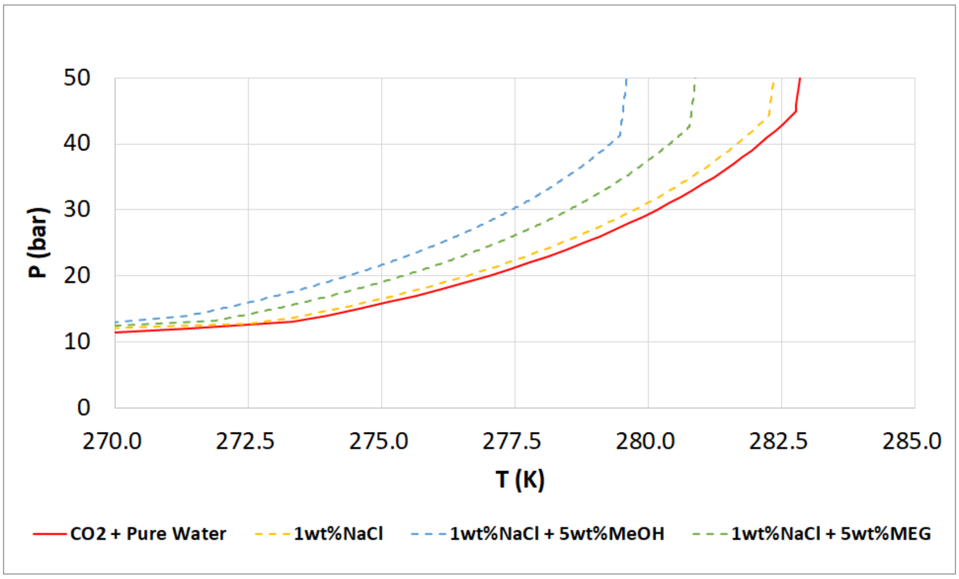

Figure 2.11: Shift on the hydrate equilibrium curve due to THIs, made with data from HydraFlash (thermodynamic software).

The group of LDHIs is formed by kinetic hydrate inhibitors (KHIs) and anti-agglomerates (AAs). KHIs work by delaying the hydrate formation through two mechanisms. Firstly, KHIs disrupt the local water structure via hydrophobic interactions, which inhibits hydrate nuclei particles from reaching the critical size required for spontaneous growth. Secondly, KHIs attach to newly formed hydrate crystals, preventing their further growth process. Regarding AAs, they avoid the agglomeration or clumping together of hydrate crystals by coating the hydrate nuclei, preventing them from sticking to each other and forming larger clusters (Sloan & Koh, 2007; Khan et al., 2020).

2.7. Remediation Techniques

As mentioned in Section 2.4.3, hydrates dissociation is possible via depressurization, thermal stimulation, inhibitor injection, or a combination of these techniques. However, in cases where hydrate formation occurs deep within the reservoir, depressurization and thermal stimulation may not be feasible options. In such scenarios, the injection of inhibitors becomes a viable solution.

Core-flooding experiments have shown that even when hydrates have already formed, the injection of THIs helps to dissociate gas hydrates. One notable advantage of THIs, such as MeOH, is their miscibility in water. This property enables MeOH to come into contact with the already-formed hydrates via preserved water channels, leading to the destabilization of the hydrate structure through the water phase. MeOH lowers the water activity and interacts with the water cages in the hydrate structure (Gauteplass et al., 2020). Therefore, the injection of THIs is a remediation technique that can assist in the dissociation of already-formed hydrates.

3

Experimental Approach

To gain a deeper understanding of CO_2 hydrates behavior, especially regarding formation and dissociation processes, several laboratory experiments were conducted using a specifically designed setup. The tests were based on a core-flooding experiment, where CO_2 was injected into a core sample with well-defined properties such as porosity and permeability. The objective was to investigate how various parameters, such as water saturation, brine salinity, and the use of thermodynamic inhibitors, impacted the hydrates formation and dissociation processes. The analysis includes examining factors like hydrate formation time and the preferential location of formed hydrates within the core.

This chapter presents a detailed review of the experimental setup, the procedures employed, and the outcomes obtained from the core-flooding experiments. The results provide valuable insights into the behavior of CO_2 hydrates in porous media and reveal the influence of different variables on hydrate formation and dissociation processes.

Although the author only performed the first nine experiments with high water saturation, the Advanced Sub-Surface Energy Transition (ASSET) research team shared their experimental results, four additional data sets, where they reduced the core water saturation previous injection of CO_2. This chapter will also present the experimental results shared by ASSET team, which serve as the foundation for the subsequent history match conducted with the empirical model built in Chapter 4. The outcomes of the history match will be presented in Chapter 5.

3.1. Lab setup

The lab setup was designed to perform a core flooding experiment maintaining thermodynamic conditions (P and T) within the hydrate stability zone to promote hydrate formation. The setup comprises three sections: the inlet section, the central section, and the outlet section. Figure 3.1 provides a schematic representation of the laboratory setup.

The inlet section comprehends the fluids that are injected in the core (brine, THIs, and CO_2) and the pumps that allow injection (Vindum Pump for liquids and mass flow control for gases). To ensure that fluids are at the desired experimental temperature, two springs are employed inside the cooler along the injection lines, which prolong the circulation time of the fluids in the lines and reduce the fluid temperature from room temperature.

The central section consists of the core holder and associated measurement equipment. The core holder is located inside a cooler, which allows to achieve the temperature required for hydrate formation. The measurement equipment includes two thermocouples, four pressure gauges, and two differential pressure gauges. The thermocouples are located one in the inlet and one in the outlet of the core holder. The schematic illustrates the placement of the pressure and temperature sensors.

The outlet section involves a valve that connects the outlet with the vacuum on one side and with the back pressure on the other side. The back pressure is used to ensure that the system maintains the necessary pressure conditions within the hydrate stability zone.

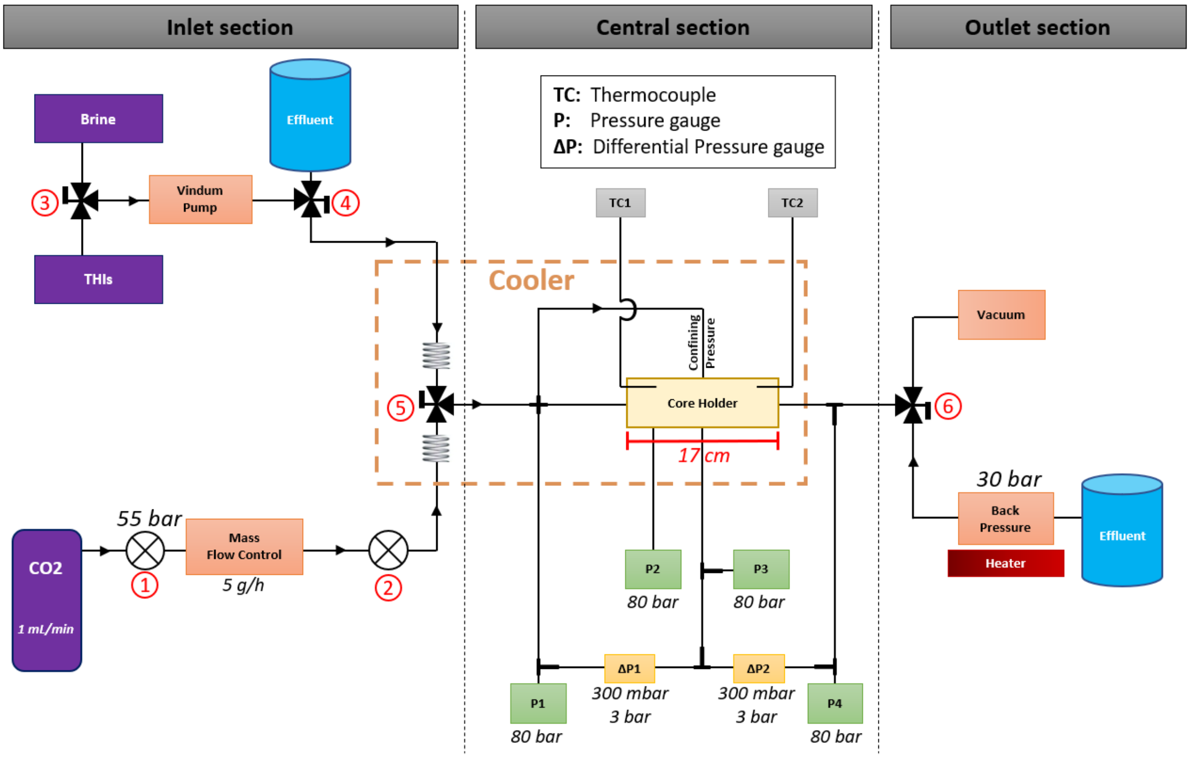

Figure 3.1: Schematic of the experimental setup.

3.1.1. Core description

The selected core consisted of Bentheimer sandstone (91.6% quartz, 2.5% kaolinite, 5.0% K-feldspar, 0.9% other) with average measured porosity and absolute permeability of 23% and $1.8\ D$, respectively (Peksa et al., 2015). The length of the core is $17\ cm$ and the diameter is $3.8\ cm$. The pore volume (PV) calculated is $44.3\ ml$. The dimensions of the core and location of the P and T sensors are shown in Figure 3.2.

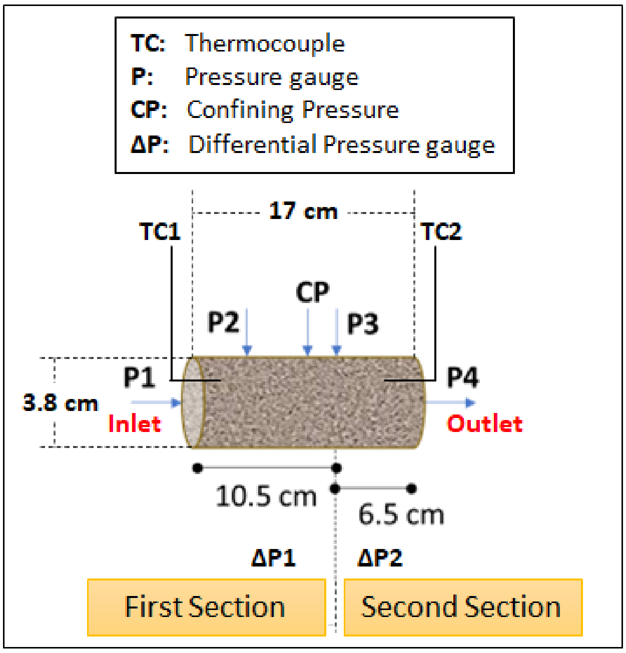

Figure 3.2: Schematic of the core dimensions and location of the measurement equipment in the core.

3.2. Procedure

After building the setup and testing the system against leakages, the experiment starts. Following, a general description of the procedure is described, however a few modifications are implemented if pre-injection of THIs is required or if water saturation (S_w) in the core is required to be less than 100%.

Initially, the core is vacuumed, and then several pore volumes of brine are injected into the core to ensure 100% water saturation. The core is then pressurized up to $30\ bar$ and the fridge temperature is set to $1°C$ resulting in an internal core temperature of $1.5 \pm 0.5°C$. A permeability test is conducted by varying the injection rate and measuring the core differential pressure for each selected rate. Once the permeability is determined, a base line is established by injecting at least $5\ PV$ of brine.

When the base line has been built, the injection of CO_2 starts at a constant rate of $5\ g/h$, which is equivalent to $1\ ml/min$. When the pressure starts to rise from the baseline, blockage is identified as a consequence of hydrate formation in the core. CO_2 injection continues until a maximum safety pressure is reached or steady-state is achieved. After this, CO_2 injection is stopped.

Subsequently, the injection of $30wt\%$ MeOH is initiated. The injection of MeOH is slow and conditioned by the safety pressure. After injecting MeOH, hydrates dissociation is expected, which results in pressure reduction. However, if MeOH injection does not dissociate the hydrates, thermal stimulation is performed by opening the door of the cooler. Finally, complete hydrates dissociation is inferred when pressure returns to the base line.

After each experiment the core is cleaned and vacuumed to remove air bubbles before starting a new experiment.

3.2.1. Permeability Test

The permeability test involves systematically altering the brine injection rate and recording the corresponding core differential pressure at various sections of the core. To determine permeability (K), Darcy's Law (Hubbert, 1957) is applied, expression that is rearranged according to Equation 3.1, where $q\ [m^3/s]$ is the flow rate, $A\ [m^2]$ represents the cross-sectional area, $\Delta P\ [Pa]$ is the pressure drop along the core length section, $L\ [m]$, and $\mu\ [Pa \cdot s]$ is the viscosity of the fluid. Through data plotting, the permeability can be inferred from the slope of the curve, which should pass through the origin point $(0, 0)$.

$$\frac{q}{A} = K\frac{\Delta P}{\mu L} \tag{3.1}$$

3.2.2. Mobility Reduction Factor

In order to analyze the decline in injectivity, it is necessary to understand the meaning of the mobility reduction factor (MRF). As defined by Equation 3.2, the MRF helps to assess the decrease in injectivity by comparing the current differential pressure (ΔP) required for injection versus the initial value (ΔP_i). MRF values higher than one reflect an injectivity loss.

$$MRF = \frac{\Delta P}{\Delta P_i} \tag{3.2}$$

3.3. Results

The results section involves a total of 13 experiments, with nine conducted by the author and four performed by the ASSET research team. Initially, a concise summary of all the results is provided. Subsequently, the chapter examines into detailed results from five selected experiments. For the remaining experiments not presented in this chapter, their analysis is provided in Appendix A.

3.3.1. Results Summary

The summary of the results is presented in Table 3.1. The results are organized based on initial water saturation, from highest to lowest.

Table 3.1 is structured into three distinct sections: Initial Condition, CO_2 Injection, and Inhibitor Injection (Remediation).

The Initial Condition comprises the initial water saturation, the salinity of the brine used to saturate the core, the base line condition, and the concentration of THI (if applicable) in case of pre-injection.

The CO_2 Injection section specifies the CO_2 injection rate, the CO_2 injected PV until breakthrough, the total CO_2 injected, the water saturation after CO_2 injection, the location of the hydrate-induced blockage if observed, and the PV at which hydrates are detected.

Lastly, the Inhibitor Injection section involves the remediation mechanism employed, the concentration of THI (if utilized), the inhibitor PV injected, and the temperature at which hydrates are dissociated.

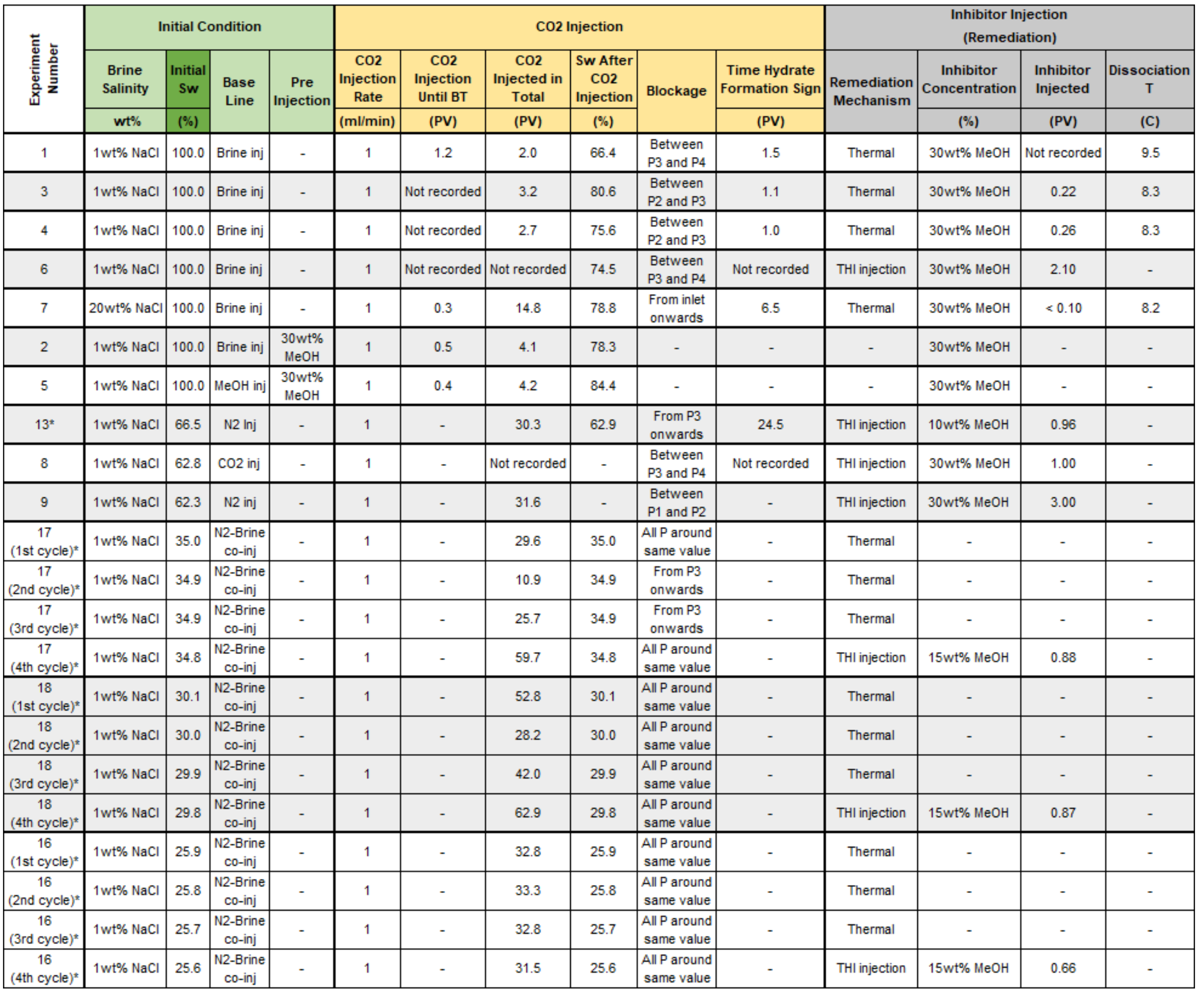

Experiment Number	Initial Condition				CO2 Injection						Inhibitor Injection (Remediation)			
	Brine Salinity	Initial Sw	Base Line	Pre Injection	CO2 Injection Rate	CO2 Injection Until BT	CO2 Injected in Total	Sw After CO2 Injection	Blockage	Time Hydrate Formation Sign	Remediation Mechanism	Inhibitor Concentration	Inhibitor Injected	Dissociation T
	wt%	(%)			(ml/min)	(PV)	(PV)	(%)		(PV)		(%)	(PV)	(C)
1	1wt% NaCl	100.0	Brine inj	-	1	1.2	2.0	66.4	Between P3 and P4	1.5	Thermal	30wt% MeOH	Not recorded	9.5
3	1wt% NaCl	100.0	Brine inj	-	1	Not recorded	3.2	80.6	Between P2 and P3	1.1	Thermal	30wt% MeOH	0.22	8.3
4	1wt% NaCl	100.0	Brine inj	-	1	Not recorded	2.7	75.6	Between P2 and P3	1.0	Thermal	30wt% MeOH	0.26	8.3
6	1wt% NaCl	100.0	Brine inj	-	1	Not recorded	Not recorded	74.5	Between P3 and P4	Not recorded	THI injection	30wt% MeOH	2.10	-
7	20wt% NaCl	100.0	Brine inj	-	1	0.3	14.8	78.8	From inlet onwards	6.5	Thermal	30wt% MeOH	< 0.10	8.2
2	1wt% NaCl	100.0	Brine inj	30wt% MeOH	1	0.5	4.1	78.3	-	-	-	30wt% MeOH	-	-
5	1wt% NaCl	100.0	MeOH inj	30wt% MeOH	1	0.4	4.2	84.4	-	-	-	30wt% MeOH	-	-
13*	1wt% NaCl	66.5	N2 Inj	-	1	-	30.3	62.9	From P3 onwards	24.5	THI injection	10wt% MeOH	0.96	-
8	1wt% NaCl	62.8	CO2 inj	-	1	-	Not recorded	-	Between P3 and P4	Not recorded	THI injection	30wt% MeOH	1.00	-
9	1wt% NaCl	62.3	N2 inj	-	1	-	31.6	-	Between P1 and P2	-	THI injection	30wt% MeOH	3.00	-
17 (1st cycle)*	1wt% NaCl	35.0	N2-Brine co-inj	-	1	-	29.6	35.0	All P around same value	-	Thermal	-	-	-
17 (2nd cycle)*	1wt% NaCl	34.9	N2-Brine co-inj	-	1	-	10.9	34.9	From P3 onwards	-	Thermal	-	-	-
17 (3rd cycle)*	1wt% NaCl	34.9	N2-Brine co-inj	-	1	-	25.7	34.9	From P3 onwards	-	Thermal	-	-	-
17 (4th cycle)*	1wt% NaCl	34.8	N2-Brine co-inj	-	1	-	59.7	34.8	All P around same value	-	THI injection	15wt% MeOH	0.88	-
18 (1st cycle)*	1wt% NaCl	30.1	N2-Brine co-inj	-	1	-	52.8	30.1	All P around same value	-	Thermal	-	-	-
18 (2nd cycle)*	1wt% NaCl	30.0	N2-Brine co-inj	-	1	-	28.2	30.0	All P around same value	-	Thermal	-	-	-
18 (3rd cycle)*	1wt% NaCl	29.9	N2-Brine co-inj	-	1	-	42.0	29.9	All P around same value	-	Thermal	-	-	-
18 (4th cycle)*	1wt% NaCl	29.8	N2-Brine co-inj	-	1	-	62.9	29.8	All P around same value	-	THI injection	15wt% MeOH	0.87	-
16 (1st cycle)*	1wt% NaCl	25.9	N2-Brine co-inj	-	1	-	32.8	25.9	All P around same value	-	Thermal	-	-	-
16 (2nd cycle)*	1wt% NaCl	25.8	N2-Brine co-inj	-	1	-	33.3	25.8	All P around same value	-	Thermal	-	-	-
16 (3rd cycle)*	1wt% NaCl	25.7	N2-Brine co-inj	-	1	-	32.8	25.7	All P around same value	-	Thermal	-	-	-
16 (4th cycle)*	1wt% NaCl	25.6	N2-Brine co-inj	-	1	-	31.5	25.6	All P around same value	-	THI injection	15wt% MeOH	0.66	-

Table 3.1: Experimental summary results. The results mark with an asterisk (*) were shared by the ASSET research team.

3.3.2. Experiment No. $6 : S_w = 100.0\%$, brine salinity $1wt\%$ NaCl

The conditions for experiment No. 6 considered an initial water saturation of 100% with brine salinity of $1wt\%$ NaCl.

Figure 3.3 illustrates the brine permeability test performed before hydrate formation and dissociation. According to the results, there was an intrinsic heterogeneity in the core, where the first section showed a permeability of $2.65\ D$ and the second section exhibited a permeability of $2.73\ D$.

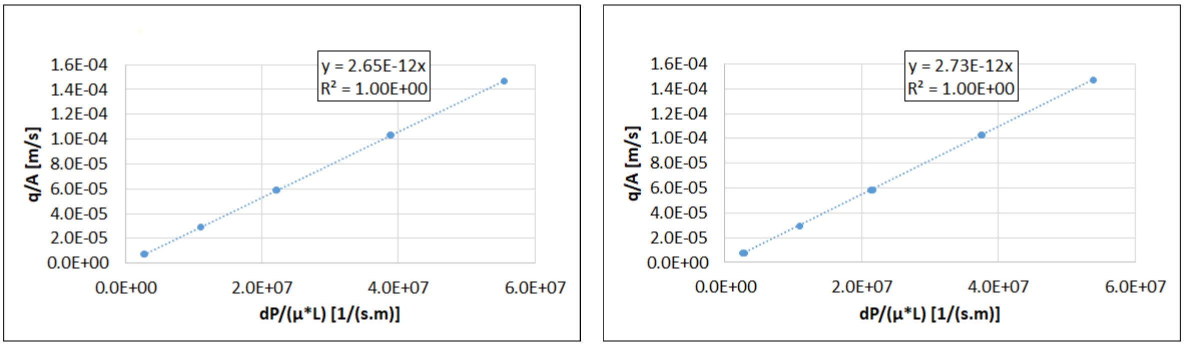

(a) Brine permeability before hydrates formation, core first section. **(b)** Brine permeability before hydrates formation, core second section.

Figure 3.3: Permeability test before hydrates formation, experiment No. 6.

Figure 3.4 presents the hydrate equilibrium curve and the experimental conditions for experiment No. 6. According to the $P-T$ phase diagram shown, hydrate formation was expected since the experimental conditions were in the hydrate stability zone. In this phase diagram, the equilibrium curve liquid-gas CO_2 was omitted.

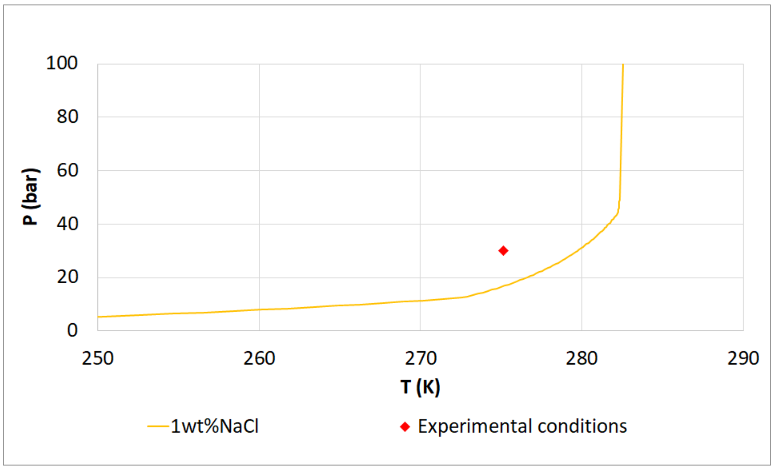

Figure 3.4: $P-T$ phase diagram depicting pressure-temperature conditions for experiment No. 6 and hydrate equilibrium curve for a binary system brine (salinity $1wt\%$ NaCl) and CO_2, made with data from HydraFlash (thermodynamic software).

Figure 3.5 shows the P and T results for experiment No.6. The first area (shown in green) corresponds to the base line of brine injection at $1\ ml/min$. CO_2 injection started at $181 \times 20\ s$ and extended until $600 \times 20\ s$ (illustrated in yellow). Hydrate-induced blockage was observed during CO_2 injection as pressure increased from $30\ bar$ to $35\ bar$. The hydrate-induced blockage was identified between $P3$ and $P4$ as $P4$ did not continue registering the same increase in pressure observed in the other pressure gauges.

Subsequently, $30wt\%$ MeOH injection began immediately after CO_2 injections was stopped (displayed in grey). Since the flow paths were already blocked inside the core, when MeOH was injected, the safety pressure was reached at $50\ bar$ (presented in orange), impeding further MeOH injection. While MeOH injection was not possible, MeOH soaking was allowed to promote hydrates dissociation. Finally, at $850 \times 20\ s$ pressure decreased and MeOH injection continued (depicted in grey). Hydrates were assumed to be dissociated since pressure returned to the base line after MeOH injection.

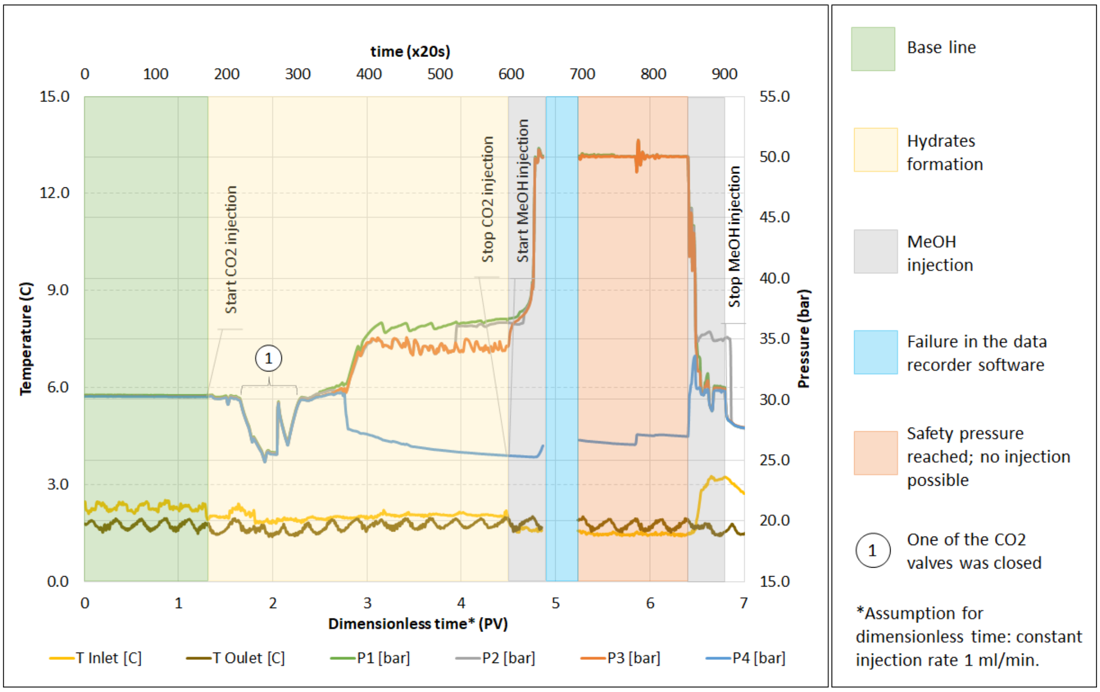

Figure 3.5: P and T history for experiment No. 6.

According to the P measurements for experiment No.6, the MRF is plotted in Figure 3.6 to address the injectivity decline due to hydrate formation. The MRF between $P3$ and $P4$ rose up to approximately 400, which corroborated the location of the hydrate-induced blockage identified in Figure 3.5.

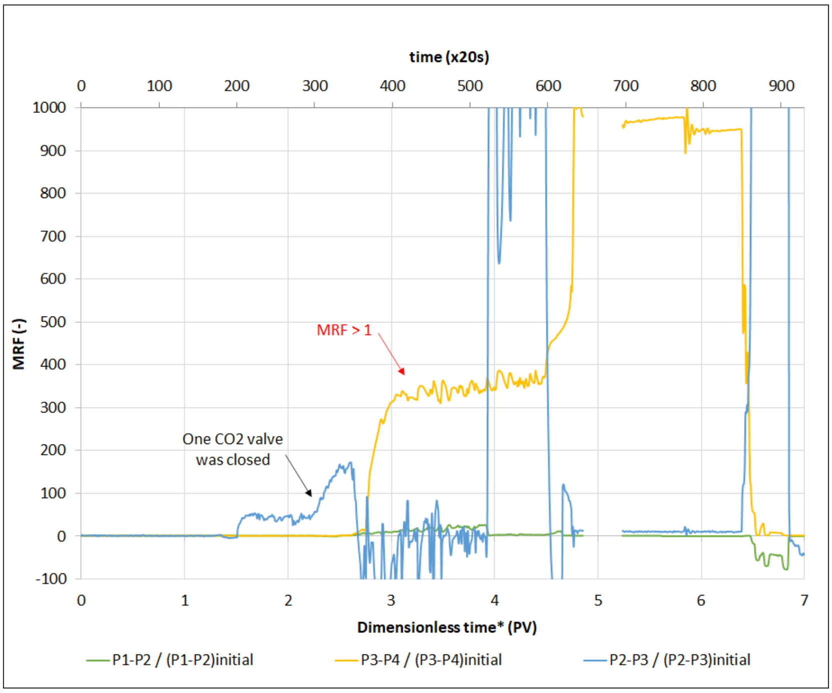

Figure 3.6: MRF for experiment No. 6.

After hydrates were dissociated, a brine permeability test was conducted. The results, presented in Figure 3.7, showed a reduction in the core permeability of 4% in the first section and 20% in the second section.

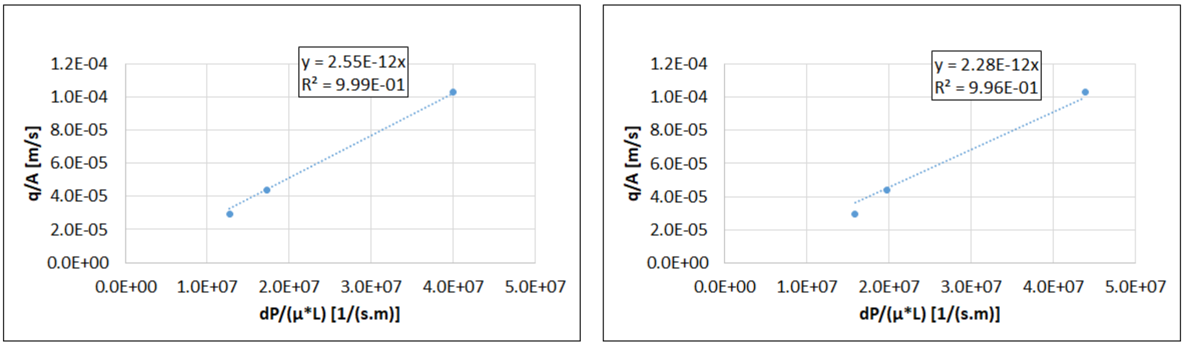

(a) Brine permeability after hydrates formation and dissociation, core first section.

(b) Brine permeability after hydrates formation and dissociation, core second section.

Figure 3.7: Permeability test after hydrates formation and dissociation, experiment No. 6.

3.3.3. Experiment No. $13 : S_w = 66.5\%$, brine salinity $1wt\%$ NaCl

For experiment No. 13, the specified conditions involved an initial water saturation of 66.5% using brine salinity $1wt\%$ NaCl. To reduce the initial water saturation from 100%, nitrogen (N_2) was injected into the core in a vertical position until breakthrough was reached, the volume of brine displaced was noted. Subsequently, the core was repositioned horizontally in the cooler to initiate CO_2 injection.

Figure 3.8 depicts the brine permeability test conducted prior to hydrate formation and dissociation. The results revealed an inherent heterogeneity in the core, with the first section exhibiting a permeability of $2.42\ D$ and the second section showing a permeability of $2.56\ D$.

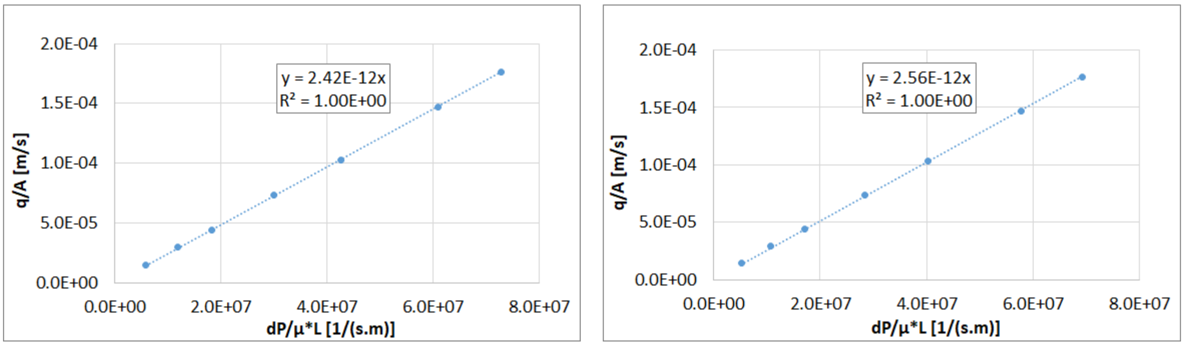

(a) Brine permeability before hydrates formation, core first section.

(b) Brine permeability before hydrates formation, core second section.

Figure 3.8: Permeability test before hydrates formation, experiment No. 13.

Figure 3.9 displays the hydrate equilibrium curve and the experimental parameters applied for experiment No. 13. Based on the $P-T$ phase diagram, hydrate formation was anticipated as the experimental conditions fell within the hydrate stability zone. It is worth noting that the equilibrium curve for liquid-gas CO_2 was excluded from this phase diagram.

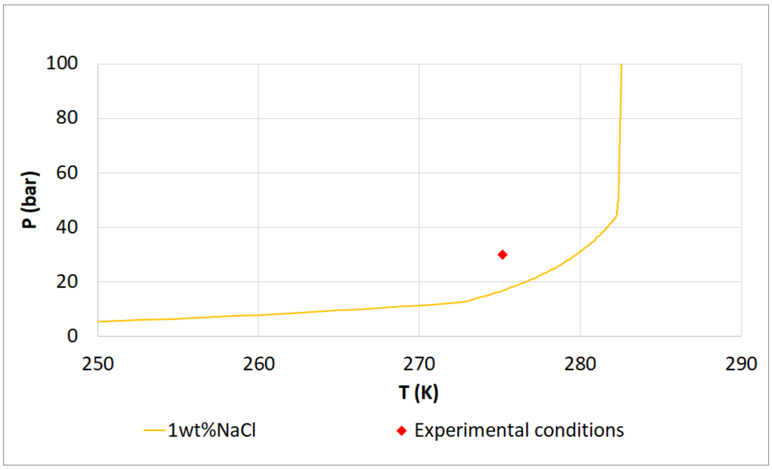

Figure 3.9: $P-T$ phase diagram depicting pressure-temperature conditions for experiment No. 13 and hydrate equilibrium curve for a binary system brine (salinity $1wt\%$ NaCl) and CO_2, made with data from HydraFlash (thermodynamic software).

Figure 3.10 illustrates the P and T outcomes for experiment No. 13. The initial phase (shown in green) represents the N_2 injection baseline at a rate of $1\ ml/min$. CO_2 injection started at $30 \times 100\ s$ and lasted until $833 \times 100\ s$ (depicted in yellow). During CO_2 injection, hydrate-induced blockage was observed as pressure rose from $30\ bar$ to $36\ bar$. The hydrate-induced blockage was identified to be partial between $P2$ and $P3$ as $P3$ and $P4$ did not continue registering the same increase in pressure observed in the other pressure gauges.

$10wt\%$ MeOH injection began immediately after halting CO_2 injection (shown in grey). Hydrates were presumed to be dissociated since the pressure returned to the baseline after MeOH injection.

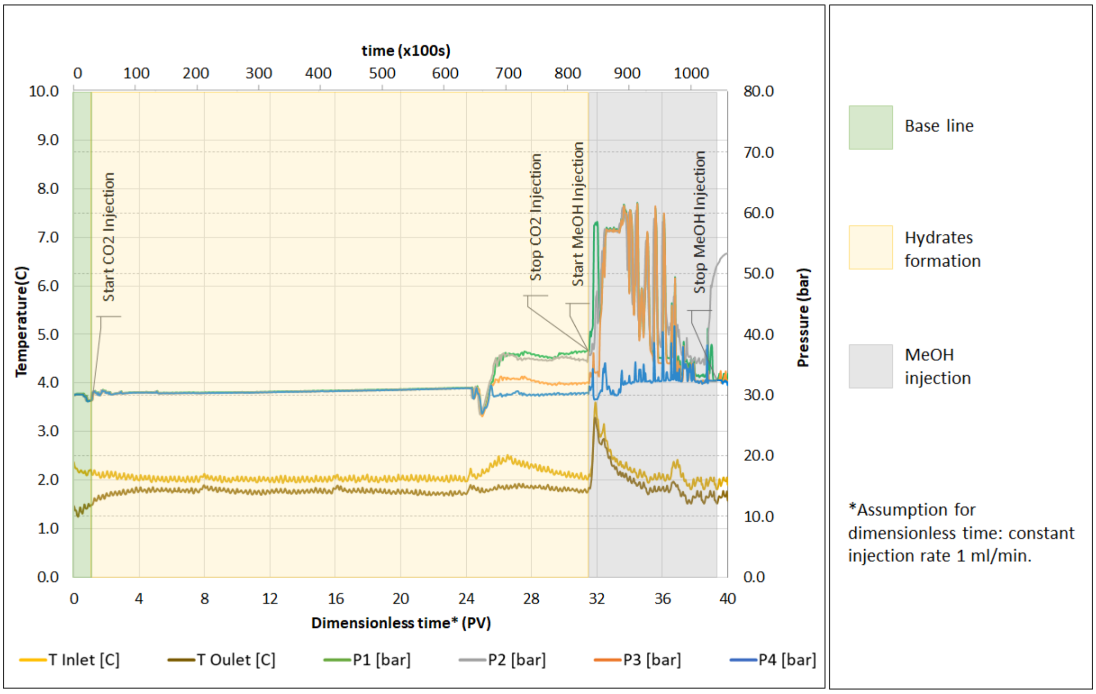

Figure 3.10: P and T history for experiment No. 13.

Based on the P measurements from experiment No. 13, Figure 3.11 displays the MRF, which is used to analyze the decrease in injectivity caused by hydrate formation. The MRF between $P2$ and $P3$ increased significantly, supporting the identified location of the partial hydrate-induced blockage shown in Figure 3.10.

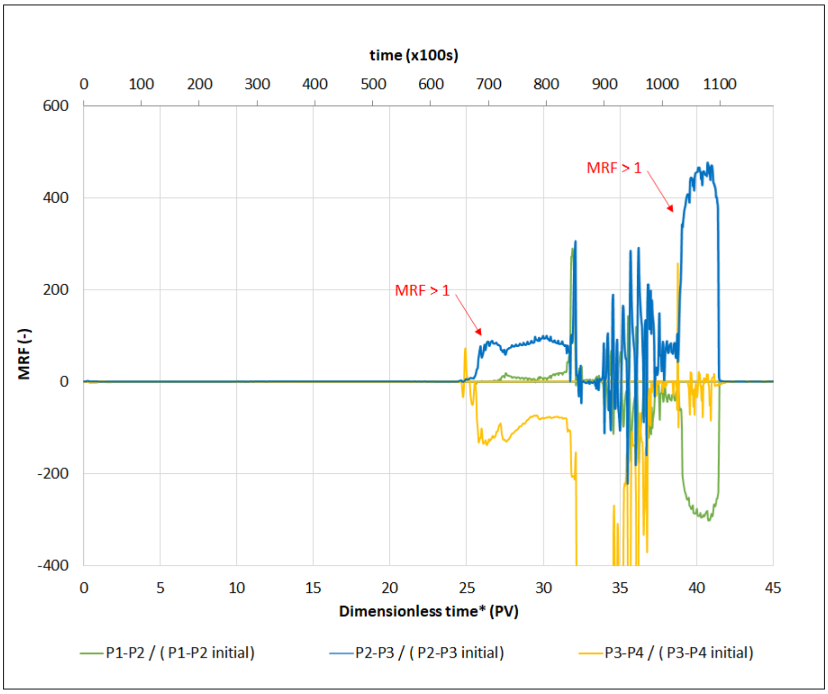

Figure 3.11: MRF for experiment No. 13.

Following the dissociation of hydrates, a brine permeability test was performed. The outcomes, depicted in Figure 3.12, indicated a decrease in core permeability of 1% in the first section and 2% in the second section.

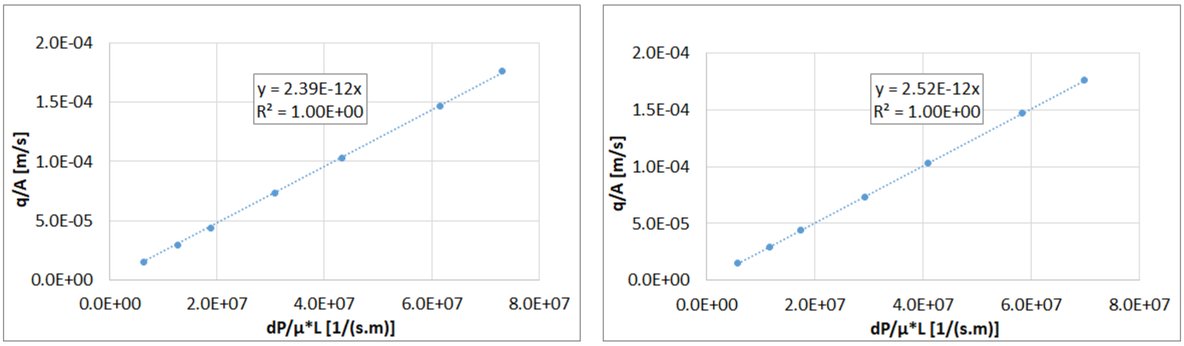

(a) Brine permeability after hydrates formation and dissociation, core first section.

(b) Brine permeability after hydrates formation and dissociation, core second section.

Figure 3.12: Permeability test after hydrates formation and dissociation, experiment No. 13.

3.3.4. Experiment No. 17 : $S_w = 35.0\%$, brine salinity $1wt\%$ NaCl

For experiment No. 17, the initial conditions involved an initial water saturation of 35.0% using brine salinity $1wt\%$ NaCl. To get the initial water saturation equal to 35.0%, brine and N_2 were co-injected into the core. The co-injection was carried out until brine was produced from the core. After this procedure, brine injection was stopped but N_2 injection continued for two hours at $1\ ml/min$ with the goal of drying the inlet line. Then, CO_2 injection started at $1\ ml/min$.

Figure 3.13 presents the hydrate equilibrium curve and the experimental conditions for experiment No. 17. According to the $P-T$ phase diagram shown, hydrate formation was expected since the experimental conditions were in the hydrate stability zone. In this phase diagram, the equilibrium curve liquid-gas CO_2 was omitted.

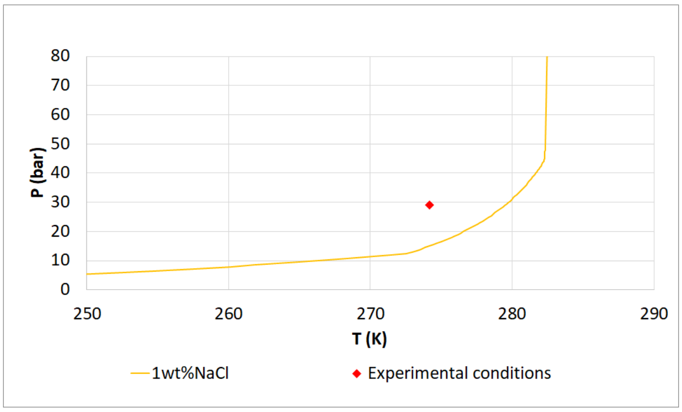

Figure 3.13: $P-T$ phase diagram depicting pressure-temperature conditions for experiment No. 17 and hydrate equilibrium curve for a binary system brine (salinity $1wt\%$ NaCl) and CO_2, made with data from HydraFlash (thermodynamic software).

Figure 3.14 shows the P and T results for experiment No.17, which consisted in four cycles of CO_2 injection followed by hydrate dissociation. CO_2 injection was stopped in each cycle after steady-state was reached. Each cycle of CO_2 injection was followed by a remediation technique (THIs injection or thermal stimulation). The graph utilizes different colors to represent distinct phases: the base line is shown in green, CO_2 injection and consequently hydrate formation in yellow, thermal dissociation in blue, and $15wt\%$ MeOH injection in grey.

In the yellow areas, hydrate formation is presumed based on the progressive build up in pressure. A pressure drop was identified systematically during the initial stage of hydrate formation in the last three cycles.

Regarding blockages caused by hydrate formation, the first and last cycles did not show hydrate-induced blockage. However, in the second and third cycles, the hydrate-induced blockage was located from $P3$ onwards, as $P4$ did not continue registering the same increase in pressure observed in the other pressure gauges.

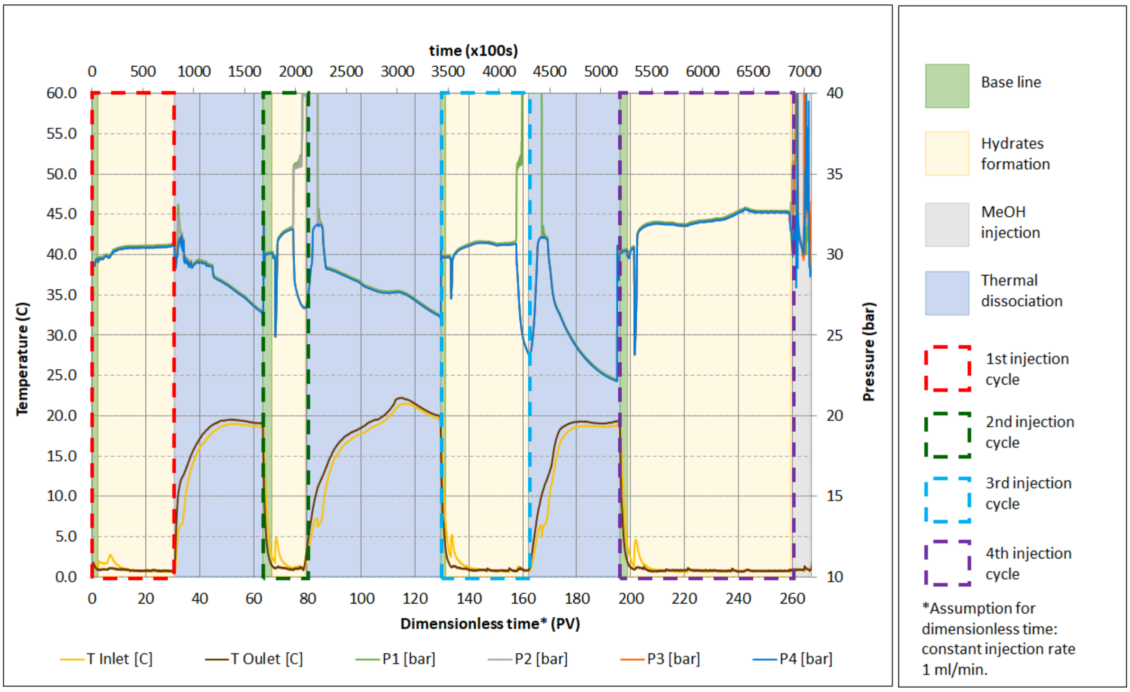

Figure 3.14: P and T history for experiment No. 17.

Figure 3.15 shows the history pressure for the first CO_2 injection cycle of experiment No. 17. Progressive increase in pressure was observed while injecting CO_2, which indicated hydrate formation. This data will be history matched in Chapter 5 using the empirical model from Chapter 4.

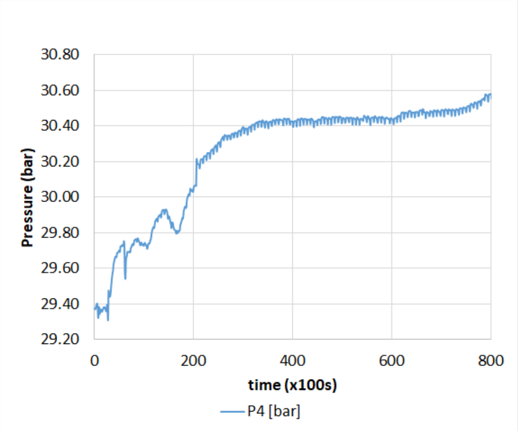

Figure 3.15: P history for experiment No. 17, first CO_2 injection cycle.

Figure 3.16 depicts the MRF for the first CO_2 injection cycle of experiment No. 17. The graph clearly demonstrates the decline in injectivity caused by hydrate formation, as indicated by the MRF higher than one between $P2$ and $P3$.

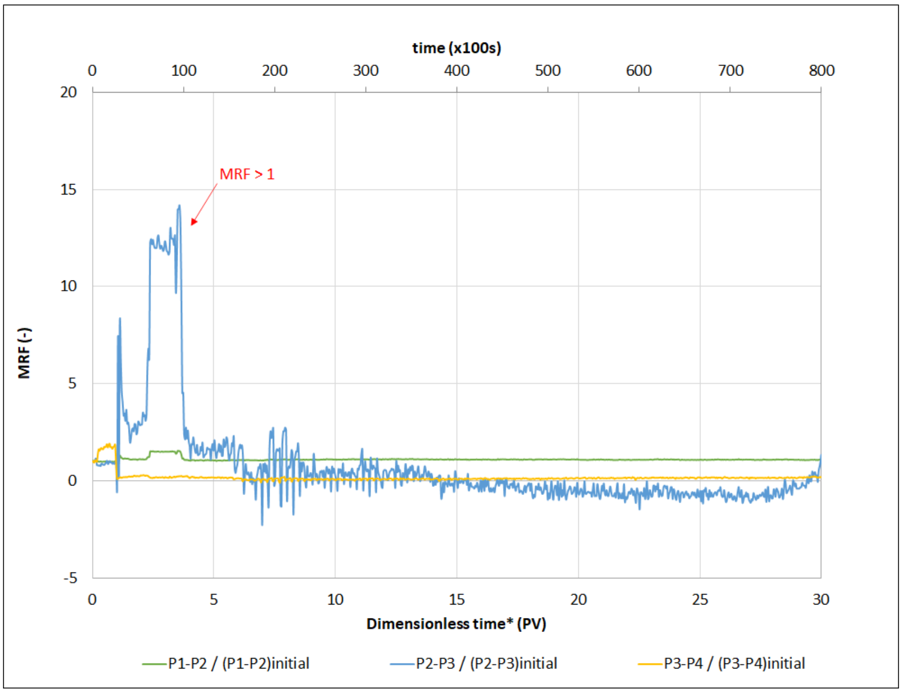

Figure 3.16: MRF for experiment No. 17, first CO_2 injection cycle.

3.3.5. Experiment No. $18 : S_w = 30.0\%$, brine salinity $1wt\%$ NaCl

For experiment No. 18, the initial conditions comprised an initial water saturation of 30.0% using brine salinity $1wt\%$ NaCl. To get the initial water saturation equal to 30.0%, brine and N_2 were co-injected into the core. The co-injection was carried out until brine was produced from the core. After this procedure, brine injection was stopped but N_2 injection continued for two hours at $1\ ml/min$ with the goal of drying the inlet line. Then, CO_2 injection started at $1\ ml/min$.

Figure 3.17 presents the hydrate equilibrium curve and the experimental conditions for experiment No. 18. According to the $P - T$ phase diagram shown, hydrate formation was expected since the experimental conditions were in the hydrate stability zone. In this phase diagram, the equilibrium curve liquid-gas CO_2 was omitted.

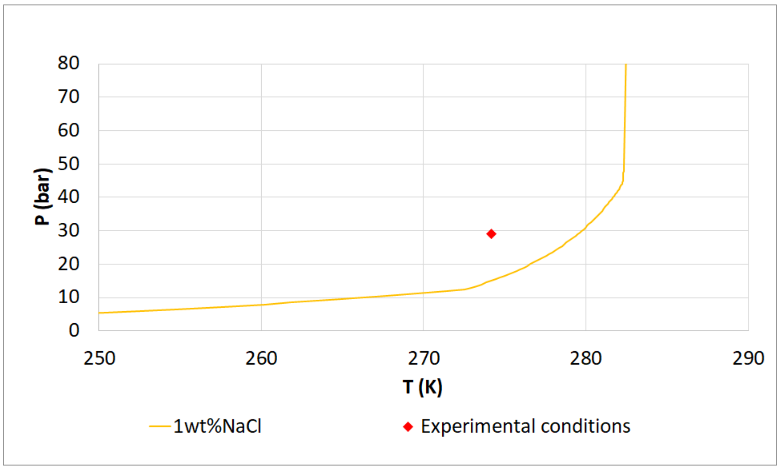

Figure 3.17: $P-T$ phase diagram depicting pressure-temperature conditions for experiment No. 18 and hydrate equilibrium curve for a binary system brine (salinity $1wt\%$ NaCl) and CO_2, made with data from HydraFlash (thermodynamic software).

Figure 3.18 displays the P and T outcomes for experiment No. 18, which involved four cycles of CO_2 injection followed by hydrate dissociation. CO_2 injection was stopped in each cycle after steady-state was reached. Each cycle of CO_2 injection was followed by a remediation technique (THIs injection or thermal stimulation). Different colors are used to represent distinct phases: the base line is presented in green, CO_2 injection and consequent hydrate formation in yellow, thermal dissociation in blue, and $15wt\%$ MeOH injection in grey.

The gradual increase in pressure indicates hydrate formation in the yellow areas. No hydrate-induced blockage ocurred based on P measurements, since pressure rose equally in all the pressure gauges. Once again, a systematic pressure drop was identified during the initial stage of hydrate formation in the last three cycles.

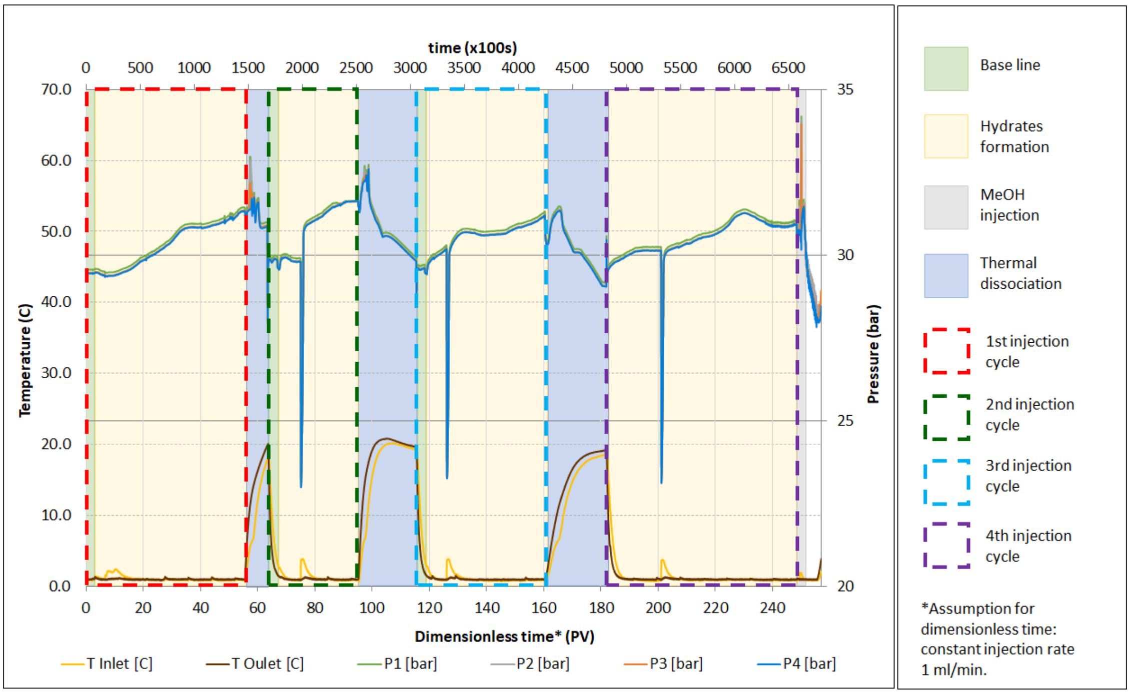

Figure 3.18: P and T history for experiment No. 18.

Figure 3.19 presents the pressure history during the first CO_2 injection cycle of experiment No. 18. A gradual and continuous rise in pressure was observed during CO_2 injection, which strongly suggested the occurrence of hydrate formation. This data will be used for history matching in Chapter 5 by using the empirical model from Chapter 4.

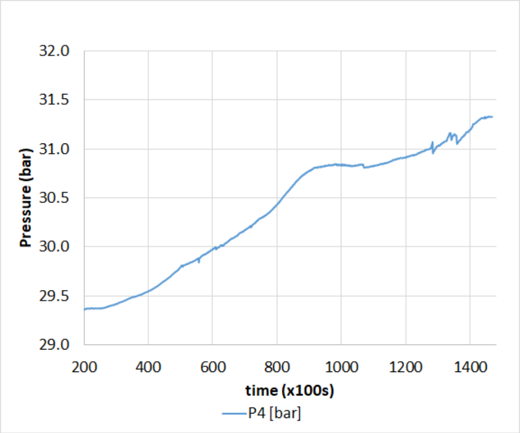

Figure 3.19: P history for experiment No. 18, first CO_2 injection cycle.

Figure 3.20 illustrates the MRF for the initial CO_2 injection cycle of experiment No. 18. The graph provides clear evidence of the reduced injectivity caused by hydrate formation, as indicated by the MRF value higher than one between $P2$ and $P3$.

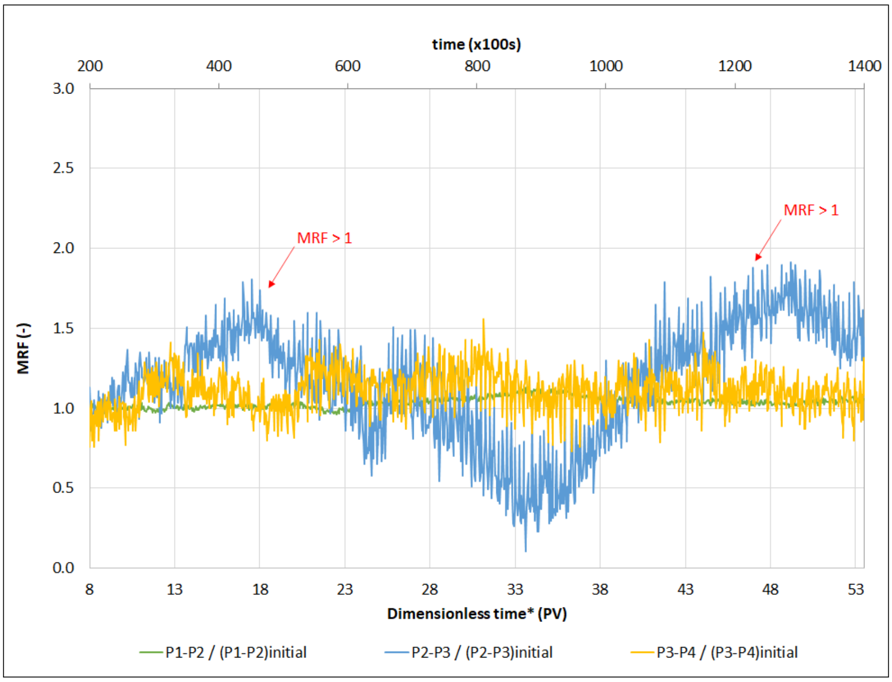

Figure 3.20: MRF for experiment No. 18, first CO_2 injection cycle.

3.3.6. Experiment No. $16 : S_w = 25.8\%$, brine salinity $1wt\%$ NaCl

For experiment No. 16, the initial conditions encompassed an initial water saturation of 25.8% using brine salinity $1wt\%$ NaCl. To get the initial water saturation equal to 25.8%, brine and N_2 were co-injected into the core. The co-injection was carried out until brine was produced from the core. After this procedure, brine injection was stopped but N_2 injection continued for two hours at $1\ ml/min$ with the goal of drying the inlet line. Then, CO_2 injection started at $1\ ml/min$.

Figure 3.21 illustrates the hydrate equilibrium curve and the experimental conditions for experiment No. 16. According to the $P - T$ phase diagram shown, hydrate formation was predicted since the experimental conditions were in the hydrate stability zone. In this phase diagram, the equilibrium curve liquid-gas CO_2 was omitted.

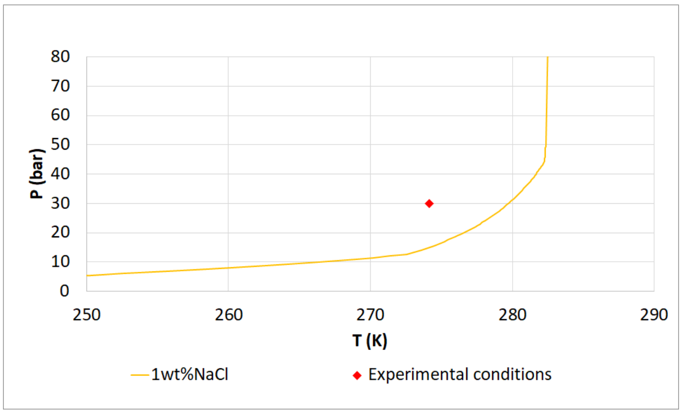

Figure 3.21: $P - T$ phase diagram depicting pressure-temperature conditions for experiment No. 16 and hydrate equilibrium curve for a binary system brine (salinity $1wt\%$ NaCl) and CO_2, made with data from HydraFlash (thermodynamic software).

Figure 3.22 presents the P and T results for Experiment No. 16, involving four cycles of CO_2 injection followed by hydrate dissociation. CO_2 injection was stopped in each cycle after steady-state was reached. Each cycle of CO_2 injection was followed by a remediation technique (THIs injection or thermal stimulation). Different colors are used to indicate distinct phases: the base line is represented in green, CO_2 injection and subsequent hydrate formation in yellow, thermal dissociation in blue, and $15wt\%$ MeOH injection in grey.

In the yellow regions, the pressure gradually increases, indicating hydrate formation. No hydrate-induced blockage ocurred based on P measurements, since pressure rose equally in all the pressure gauges. Furthermore, a systematic pressure drop was observed during the initial stage of hydrate formation in all the cycles.

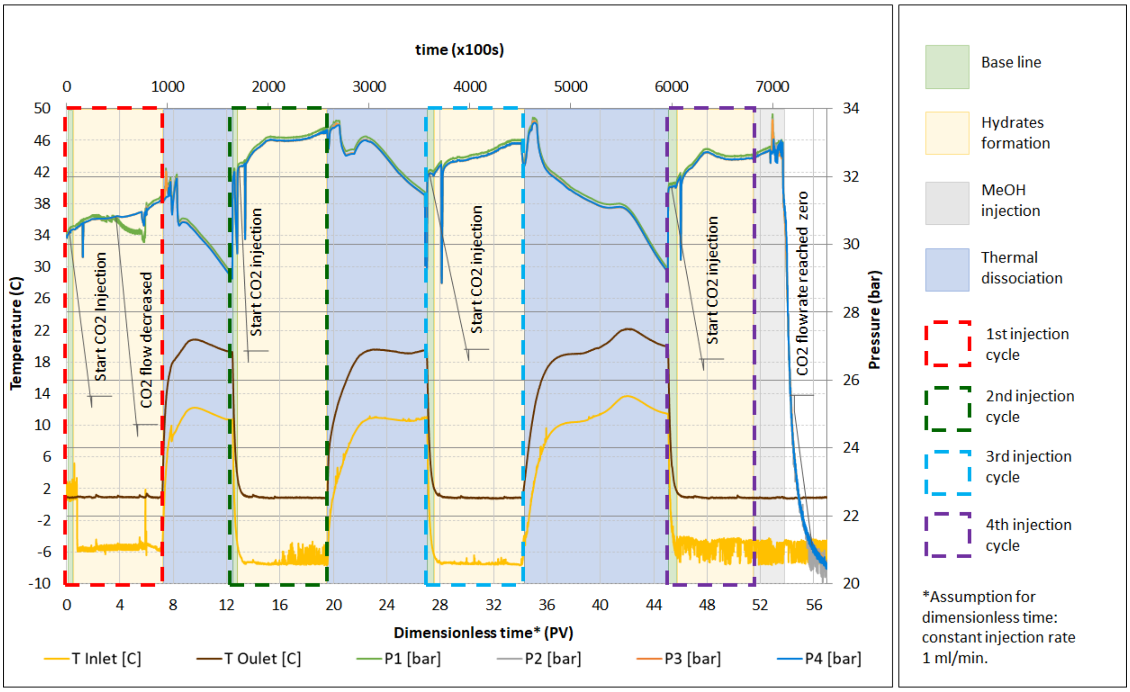

Figure 3.22: P and T history for experiment No. 16.

Figure 3.23 presents the pressure history during the first CO_2 injection cycle of experiment No. 16. During CO_2 injection, a progressive and consistent increase in pressure was noted, strongly indicating the presence of hydrate formation. This data will be employed for history matching in Chapter 5, utilizing the empirical model introduced in Chapter 4.

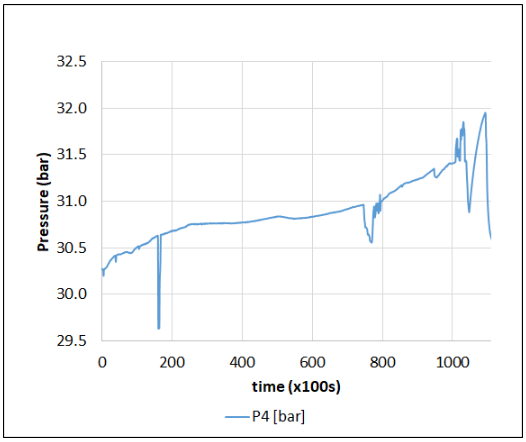

Figure 3.23: P history for experiment No. 16, first CO_2 injection cycle.

4

Modeling Approach

A model is a representation of reality built through a process of simplification and discretization of the actual system, with the main goal of resembling and understanding the physical processes occurring in the analyzed situation. Moreover, a model is useful not only for predicting physical behaviors but also for evaluating uncertainties associated with the data utilized in constructing the model.

The objective of this chapter is to illustrate the methodology used to create an empirical model, derived from an existing model, to reproduce hydrate formation and dissociation in porous media, aiming to achieve two primary purposes. The first goal is to assess the impact of gas hydrates on injectivity decline during CO_2 injection in depleted gas reservoirs. The second objective is to study the impact of several variables (i.e., number of cells, capillary pressure, rock thermal conductivity, reaction rate coefficients, CO_2 injection rate and CO_2 injection temperature) on hydrate formation through a sensitivity analysis.

The chapter commences with a description of the base model utilized, followed by a review on the CO_2 fluid properties and the J-T effect. After confirming the physics underlying the J-T effect, the chapter proceeds with a comprehensive review of the inclusions made in the empirical model. These additions cover the representation of hydrate formation and dissociation processes, as well as the reduction in permeability caused by hydrate formation in the porous space.

Once the empirical model is assembled, this chapter displays the results and sensitivity analysis for a conceptual case. Subsequently, two case studies are simulated using the model to explore hydrates formation scenarios. Finally, this chapter concludes presenting the findings on prevention techniques studied using the model, providing valuable insights into addressing the challenges posed by hydrates.

The empirical model developed in this chapter will be utilized in Chapter 5 to conduct a history matching process with some of the experimental results obtained through the procedure described in Chapter 3.

4.1. Base Model Description

The empirical model developed in this study was derived from an existing model (Kahrobaei & Farajzadeh, 2022). The base model reproduces the J-T effect resulting from the injection of CO_2 in a depleted gas reservoir.

The base model is a numerical model built in the Modular Reservoir Simulator (MoReS) version 2021.2, which is an in-house numerical simulator developed by Shell. In the following subsections, the key characteristics and features of the base model will be described in detail.

4.1.1. Geometry

The model's geometry is based on a radial configuration with 100 cells in the radial direction and one cell in the vertical direction, without any inclination. The absence of inclination means that the model is completely horizontal. Its dimensions consist of a radius of $1000\ m$ and a thickness of $90\ m$. Figure

4.1 depicts the geometry of the model and its dimensions from top and cross-section views. As usual in radial models, the resolution decreases with increasing distance from the well, as shown in Figure 4.2. The well is positioned at the center of the model.

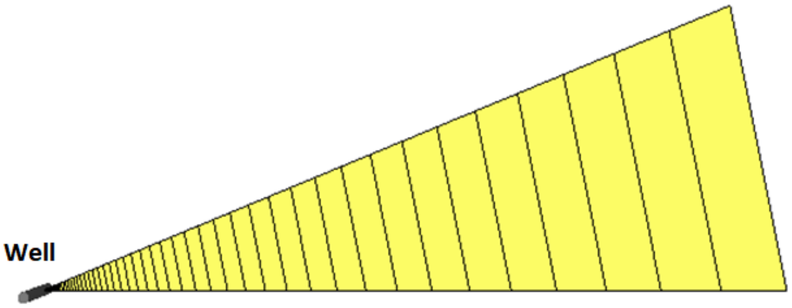

(a) Top view.

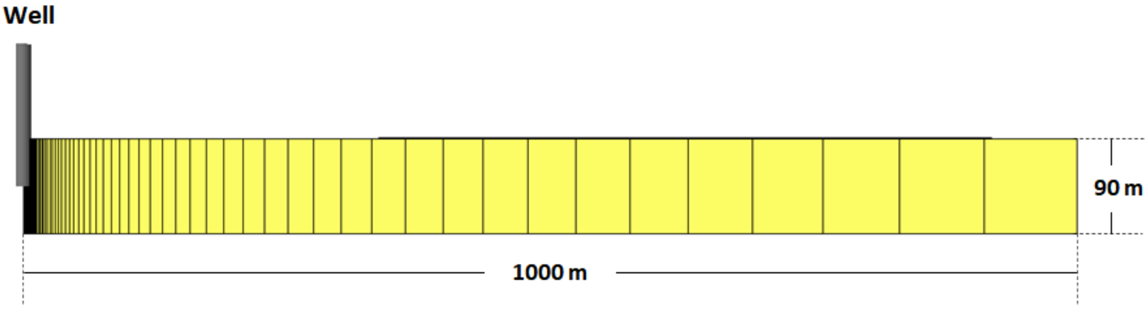

(b) Cross-section view.

Figure 4.1: Model's geometry and dimensions.

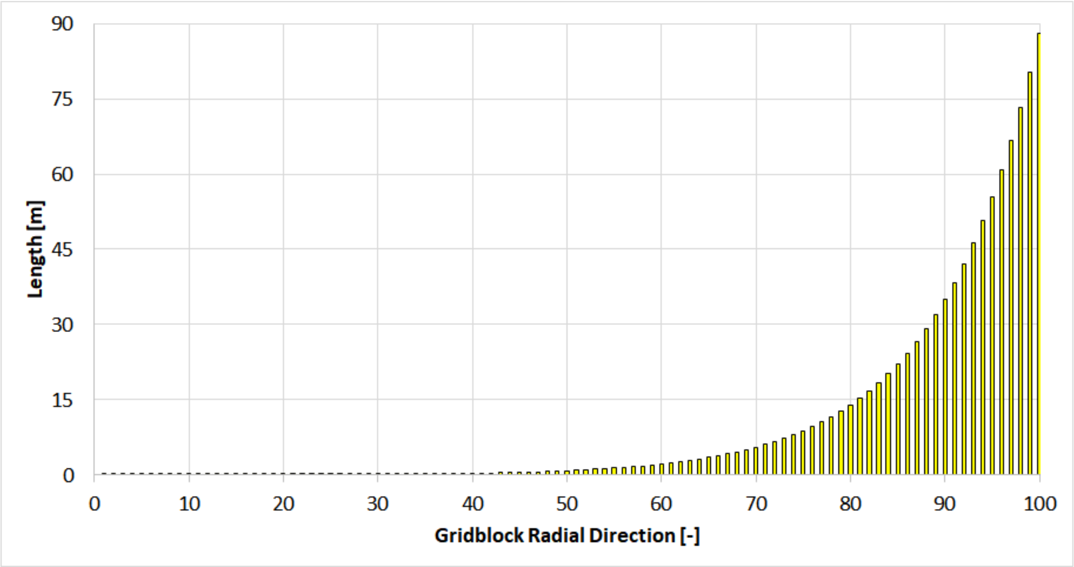

Figure 4.2: Resolution of the model per grid-block in the radial direction.

4.1.2. Phases and Components

The model represents a two-phase system comprising water and gas phases. The components in the system are water, CO_2, and CH_4. Water remains in a constant liquid state throughout the simulation, while CO_2 and CH_4 are consistently in a gaseous state. No phase transitions occur for any of the components during the simulation; they maintain their respective states throughout all the simulated time.

4.1.3. Thermal Model

The model operates in thermal mode, accounting for temperature-dependent fluid compositions, porosity, enthalpy, density, and viscosity. It also considers heat conductivity and rock heat capacity, which can be included if specified. Additionally, the model can incorporate heat loss to the overburden and underburden if necessary. This thermal approach ensures a comprehensive representation of the system, capturing the influence of temperature on fluid and rock properties.

In the base model, the temperature varies as a function of depth following a normal temperature gradient of $0.03\ °C/m$. The porosity remains constant and does not change with temperature. Heat conductivity is set to zero, and no heat gain is taken into account. However, enthalpy, density, and viscosity are all pressure and temperature dependent. The values of heat capacity for rock and each component are presented in Table 4.1.

Component	Heat Capacity [J/kg/K]
Rock (sandstone)	1,000
Water	4,037
CO2	798
CH4	3,265

Table 4.1: Heat capacities used in the model.

4.1.4. Rock Properties

The model is assumed to be a sandstone homogeneous and isotropic, with porosity of 11% and permeability of $20\ mD$. The rock density is $2600\ kg/m^3$, and the rock compressibility is $5.8 \times 10^{-7}\ bar^{-1}$.

4.1.5. Fluid properties

This section will offer a comprehensive and detailed examination of the fluid properties, including enthalpy, density, viscosity, and composition, for water, CO_2, and CH_4. Additionally, a brief explanation of the mixing rules employed in the model will be provided.

4.1.5.1. Water Fluid Properties

Although fluid properties are pressure and temperature dependent in the thermal mode, for water, the density and viscosity are treated as constant, with water density set at $992\ kg/m^3$ and water viscosity at $1\ cP$. For water enthalpy, its values are defined according to Table 4.2.

Enthalpy [J/kg]		
P [bar]	T [K]	
	273	473
1	1.13E+06	1.96E+06
1000	1.13E+06	1.96E+06

Table 4.2: Water enthalpy.

4.1.5.2. CO_2 and CH_4 Fluid Properties

As mentioned in Section 4.1.3, fluid properties are pressure and temperature dependent in thermal mode. The fluid properties for CO_2 are determined using tables obtained from the widely accepted

Span-Wagner equation of state, which is known for accurately modeling CO_2 fluid properties (Span & Wagner, 1996). The figures 4.3, 4.4, and 4.5 present the enthalpy, density, and viscosity of CO_2, respectively, providing a comprehensive illustration of how these properties vary with temperature and pressure.

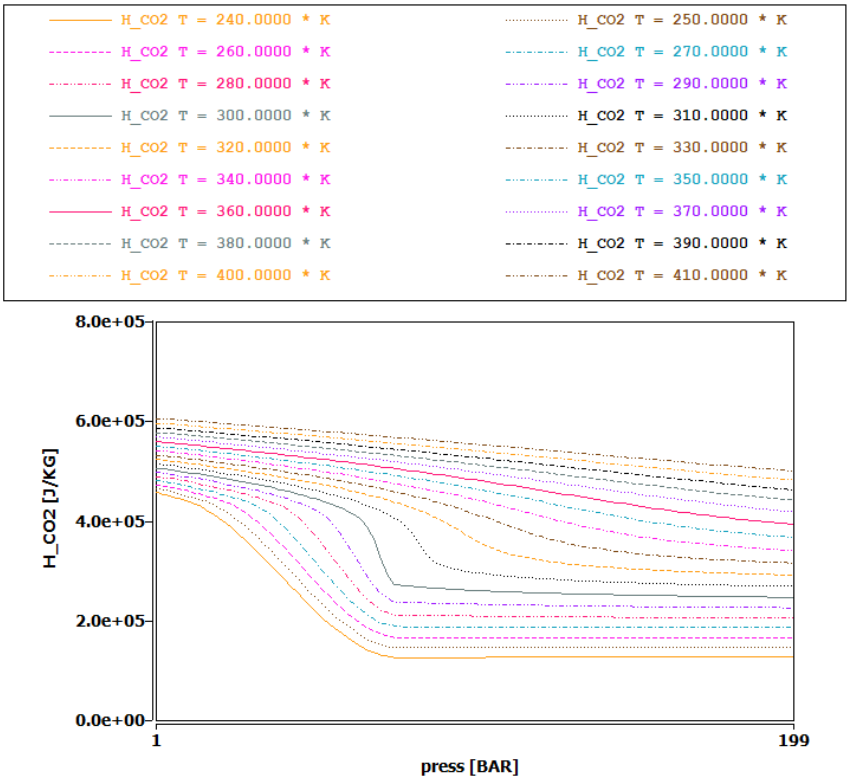

Figure 4.3: CO_2 enthalpy depending on pressure and temperature.

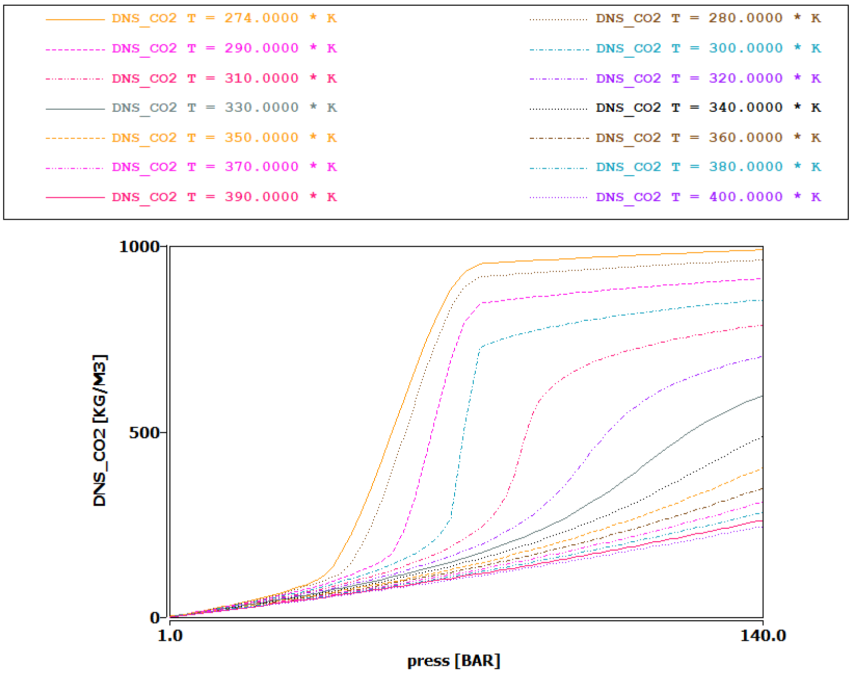

Figure 4.4: CO_2 density depending on pressure and temperature.

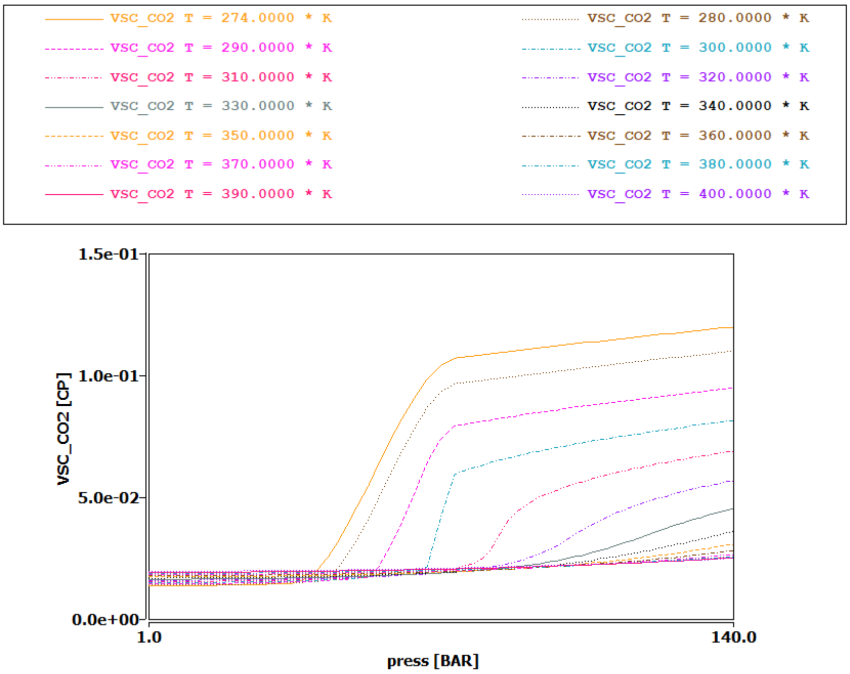

Figure 4.5: CO_2 viscosity depending on pressure and temperature.

Regarding CH_4 fluid properties, enthalpy, density, and viscosity data are shown in figures 4.6, 4.7 and 4.8, respectively.

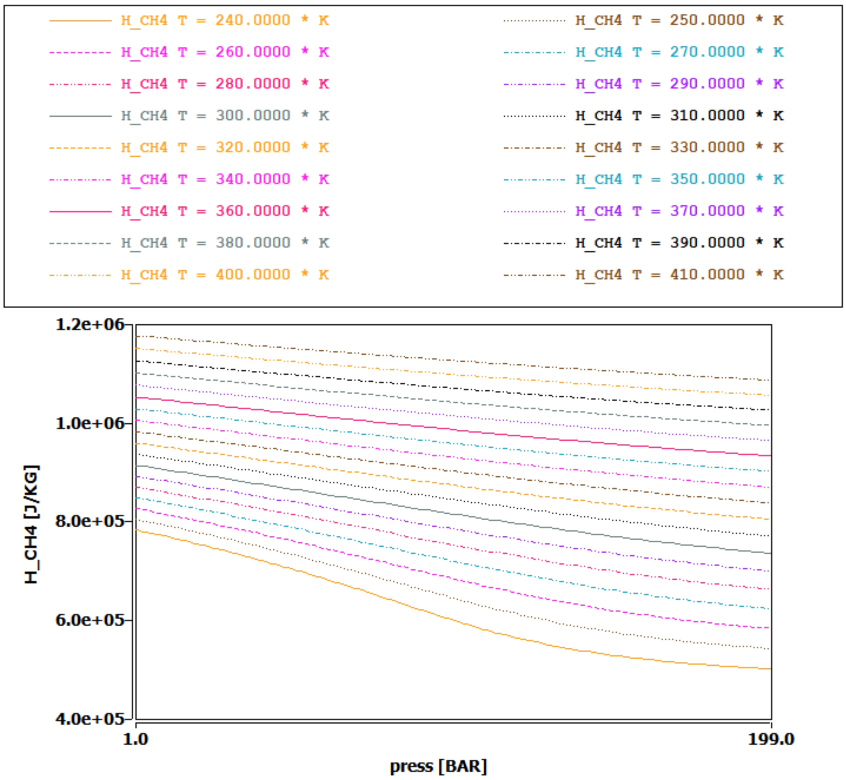

Figure 4.6: CH_4 enthalpy depending on pressure and temperature.

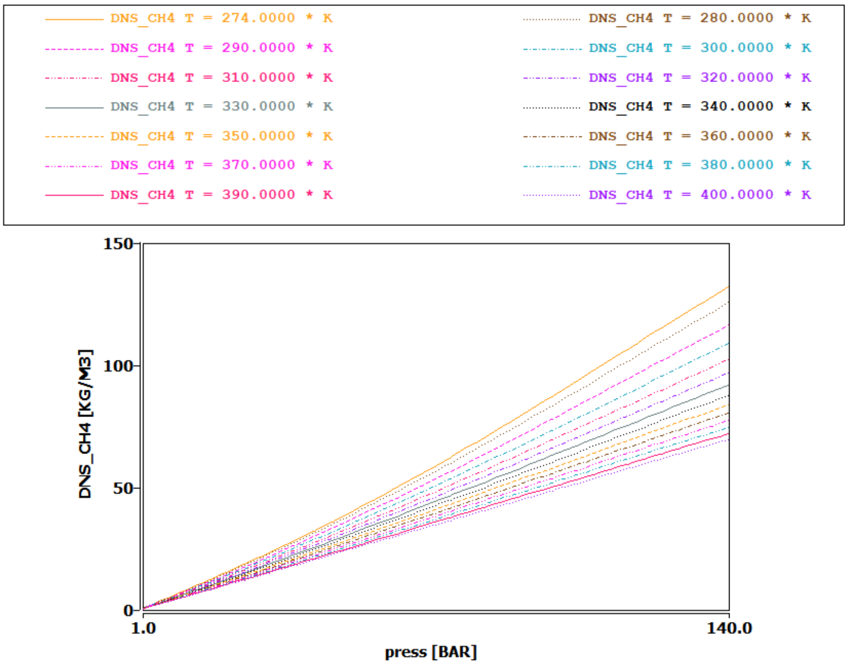

Figure 4.7: CH_4 density depending on pressure and temperature.

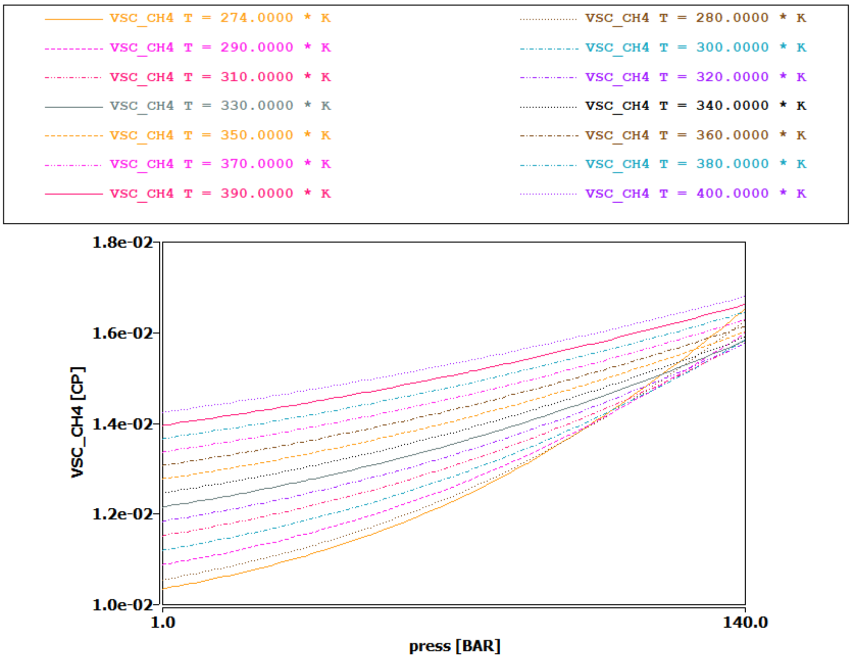

Figure 4.8: CH_4 viscosity depending on pressure and temperature.

4.1.5.3. Composition and Molecular Weight

In the base model operating in the thermal mode, the fluid composition is determined by K-values. As discussed in Section 4.1.2, there are no phase transitions for any component, and all components exist in a single phase without partitioning. Consequently, the K-value for each component is 1, reflecting that each component remains in its only possible phase, as shown in Table 4.3.

	Phase	
Component	**Liquid**	**Gas**
Water	1	0
CO2	0	1
CH4	0	1

Table 4.3: K-values per component.

Concerning molecular weight, the values for each component are provided in Table 4.4.

Component	Molecular Weigth [g/mol]
Water	18
CO2	44
CH4	16

Table 4.4: Molecular weight per component.

4.1.5.4. Mixing Rule

In the base model, as it represents a depleted gas reservoir, some grid-blocks will contain a mixture of CO_2 and CH_4 when CO_2 is injected. In such cases, the gas fluid properties are determined based on the fraction of each component present in that cell. An illustration of this scenario is depicted in Figure 4.9, where three different situations are depicted.

In Situation A, the grid-block contains a fraction of 1 for CO_2. Situation B illustrates a grid-block with a mixture of CO_2 and CH_4. In this case, the gas fluid properties are determined by calculating the fluid properties of the grid-block based on the properties of each component and their respective fraction in the mixture. Lastly, Situation C shows a grid-block with a fraction of 1 for CH_4. This approach ensures that the fluid properties accurately reflect the mixture of components in the grid-blocks, enabling a realistic simulation of fluid behavior during CO_2 injection into the reservoir.

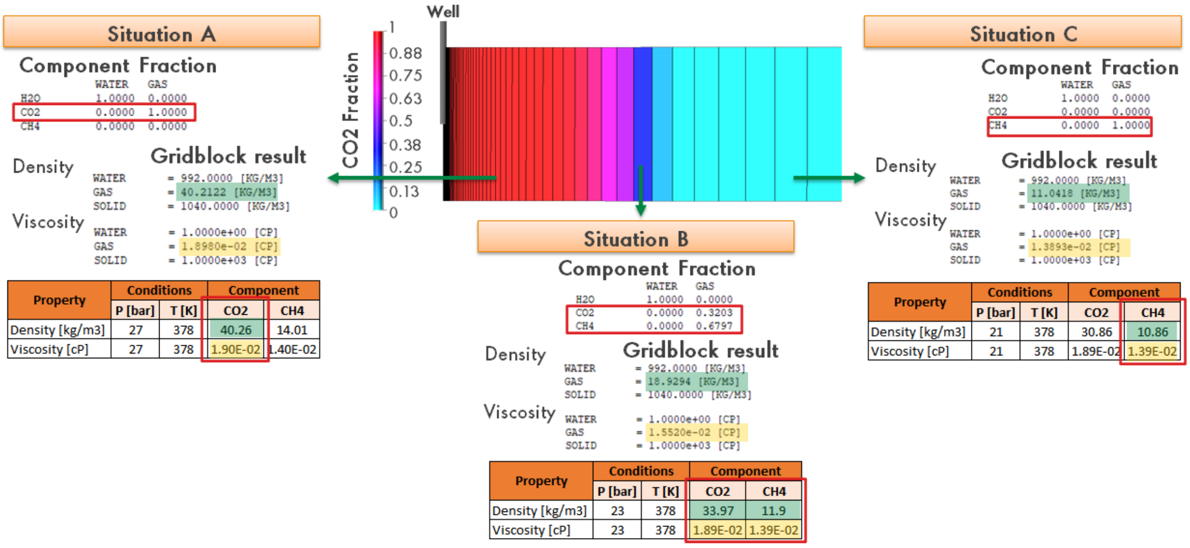

Situation A

```
        WATER   GAS
H2O     1.0000  0.0000
CO2     0.0000  1.0000
CH4     0.0000  0.0000
```

```
WATER      = 992.0000 [KG/M3]
GAS        = 40.2122 [KG/M3]
SOLID      = 1040.0000 [KG/M3]

WATER      = 1.0000e+00 [CP]
GAS        = 1.8980e-02 [CP]
SOLID      = 1.0000e+03 [CP]
```

Property	Conditions		Component	
	P [bar]	T [K]	CO2	CH4
Density [kg/m3]	27	378	40.26	14.01
Viscosity [cP]	27	378	1.90E-02	1.40E-02

Situation B

```
        WATER   GAS
H2O     1.0000  0.0000
CO2     0.0000  0.3203
CH4     0.0000  0.6797
```

```
WATER      = 992.0000 [KG/M3]
GAS        = 18.9294 [KG/M3]
SOLID      = 1040.0000 [KG/M3]

WATER      = 1.0000e+00 [CP]
GAS        = 1.5520e-02 [CP]
SOLID      = 1.0000e+03 [CP]
```

Property	Conditions		Component	
	P [bar]	T [K]	CO2	CH4
Density [kg/m3]	23	378	33.97	11.9
Viscosity [cP]	23	378	1.89E-02	1.39E-02

Situation C

```
        WATER   GAS
H2O     1.0000  0.0000
CO2     0.0000  0.0000
CH4     0.0000  1.0000
```

```
WATER      = 992.0000 [KG/M3]
GAS        = 11.0418 [KG/M3]
SOLID      = 1040.0000 [KG/M3]

WATER      = 1.0000e+00 [CP]
GAS        = 1.3893e-02 [CP]
SOLID      = 1.0000e+03 [CP]
```

Property	Conditions		Component	
	P [bar]	T [K]	CO2	CH4
Density [kg/m3]	21	378	30.86	10.86
Viscosity [cP]	21	378	1.89E-02	1.39E-02

Figure 4.9: Example of mixing rule for fluid properties.

4.1.6. Capillary Pressure and Relative Permeabilities

The base model does not take into account capillary pressure (Pc), and the relative permeability curves are constructed using the Corey definition (Corey, 1954), utilizing generic gas-water values, as indicated in Table 4.5. Figure 4.10 displays the relative permeability curve for the gas-water system. It is important to highlight that the model is at connate water saturation conditions. Consequently, there is no water displacement when CO_2 is injected into the reservoir.

Water			Gas		
Swc [-]	Krw [-]	nw [-]	Sgr [-]	Krg [-]	ng [-]
0.20	1	2	0.01	1	2

Table 4.5: Corey parameters for the relative permeability model of a generic gas-water system.

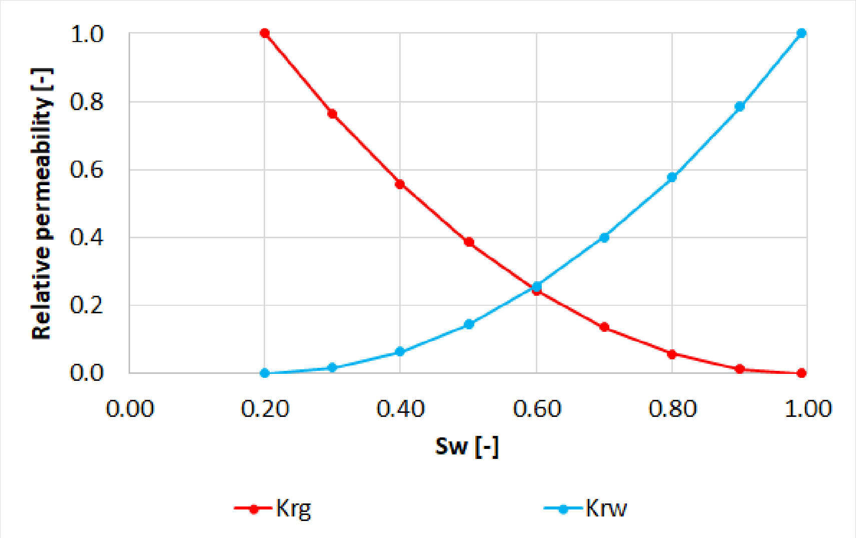

Figure 4.10: Relative permeability curves for gas-water system.

4.1.7. Initialization

The initial condition of the model aims to represent the current state of a depleted gas reservoir. The model is initialized with an initial pressure of $20\ bar$ and an initial temperature of $105°C$. At this stage, the reservoir is at connate water saturation conditions, where gas saturation is 80%, and water saturation is 20%. The gas present in the reservoir is 100% CH_4.

The initialization is conducted under isothermal conditions, in accordance with the specified initial temperature, which increases with depth based on the thermal gradient defined in Section 4.1.3.

The model does not incorporate a gas-water contact, and a closed boundary condition is assumed.

4.1.8. Well Parameters

The injection well is perforated in the only vertical cell of the model, and it injects CO_2 at a constant rate of $30\ kg/s$ ($\sim 1\ Mtpa$), which is a commercial rate commonly used in similar CCS projects. CO_2 is injected at a temperature of $12°C$.

4.2. Base Model Review

This section focuses on the quality control of CO_2 fluid properties and base model results for the J-T effect, comparing them with relevant literature. The J-T effect is crucial in creating the thermodynamic conditions necessary for hydrate formation, making it essential to verify that the base model accurately represents this phenomenon.

It is essential to emphasize that, in CCS projects, CO_2 is typically injected into the reservoir in its liquid phase. Consequently, the model needs to consider three phases (water, gas, and liquid) to accurately simulate the phase transition of CO_2 from liquid to gas. However, despite the initial attempt to configure the base model as a three-phase model, numerical challenges were encountered. As a result, the decision was made to proceed with a the simplified two-phase base model that includes water and gas phases exclusively.

4.2.1. CO_2 Fluid Properties Quality Control

A quality control of the fluid properties for CO_2 is conducted to ensure that the values fall within the expected theoretical ranges. Figure 4.11 provides an illustrative example of three data points, demonstrating that the model accurately represents the CO_2 fluid properties.

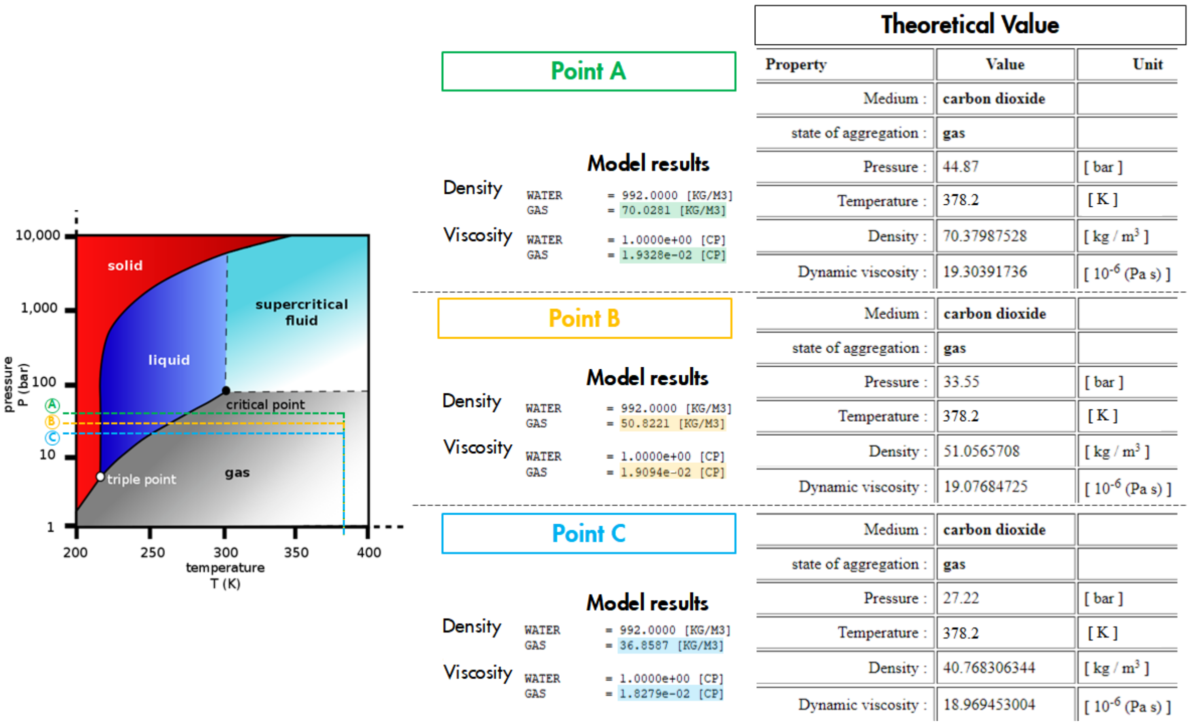

Point A

Model results

```
Density    WATER   = 992.0000 [KG/M3]
           GAS     = 70.0281 [KG/M3]
Viscosity  WATER   = 1.0000e+00 [CP]
           GAS     = 1.9328e-02 [CP]
```

Point B

Model results

```
Density    WATER   = 992.0000 [KG/M3]
           GAS     = 50.8221 [KG/M3]
Viscosity  WATER   = 1.0000e+00 [CP]
           GAS     = 1.9094e-02 [CP]
```

Point C

Model results

```
Density    WATER   = 992.0000 [KG/M3]
           GAS     = 36.8587 [KG/M3]
Viscosity  WATER   = 1.0000e+00 [CP]
           GAS     = 1.8279e-02 [CP]
```

Theoretical Value

Property	Value	Unit
Medium :	carbon dioxide	
state of aggregation :	gas	
Pressure :	44.87	[bar]
Temperature :	378.2	[K]
Density :	70.37987528	[kg / m^3]
Dynamic viscosity :	19.30391736	[10^{-6} (Pa s)]
Medium :	carbon dioxide	
state of aggregation :	gas	
Pressure :	33.55	[bar]
Temperature :	378.2	[K]
Density :	51.0565708	[kg / m^3]
Dynamic viscosity :	19.07684725	[10^{-6} (Pa s)]
Medium :	carbon dioxide	
state of aggregation :	gas	
Pressure :	27.22	[bar]
Temperature :	378.2	[K]
Density :	40.768306344	[kg / m^3]
Dynamic viscosity :	18.969453004	[10^{-6} (Pa s)]

Figure 4.11: Comparison of CO_2 fluid properties for three points: Model calculations versus theoretical values from (Wischnewski, 2007). $P - T$ phase diagram for CO_2 from (Finney & Jacobs, 2010).

4.2.2. Joule–Thomson Cooling Effect

The base model was subjected to testing through the simulation of two cases, based on parameters from Table 4.6. The results were compared with literature findings, and the model successfully reproduced the same outcomes as reported in the literature (Oldenburg, 2007). The base model successfully captured the J-T effect, which validates its usage as a foundation for the empirical model developed through this study.

Property	Unit	Case A	Case B
		Value	
Radius	[m]	1130	
Thickness	[m]	50	
Porosity	[-]	0.3	
Permeability	[mD]	1000	20
Rock heat capacity	[J/kg/K]	1000	
Rock density	[kg/m3]	2600	
Formation thermal conductivity	[W/m/K]	2.51	
Tres	[C]	75	75
Pres	[bar]	50	50
Injection Constraint		Constant injection pressure	Constant injection rate
Tinj	[C]	75	20
Pinj	[bar]	100	-
CO2 injection rate	[kg/s]	-	3

Table 4.6: Parameters for simulation cases A and B, from (Oldenburg, 2007).

Figure 4.12 displays the model results for Case A, for different times since the start of injection (i.e., $10\ days$, $20\ days$, $1\ month$, $3\ months$, $1\ year$, and $15\ years$). The model results are found to be in good agreement with the literature results presented in Figure 4.13. The J-T effect is more severe during the first periods of injection ($\Delta T = 20°C$), decreasing significantly after 15 years ($\Delta T = 10°C$).

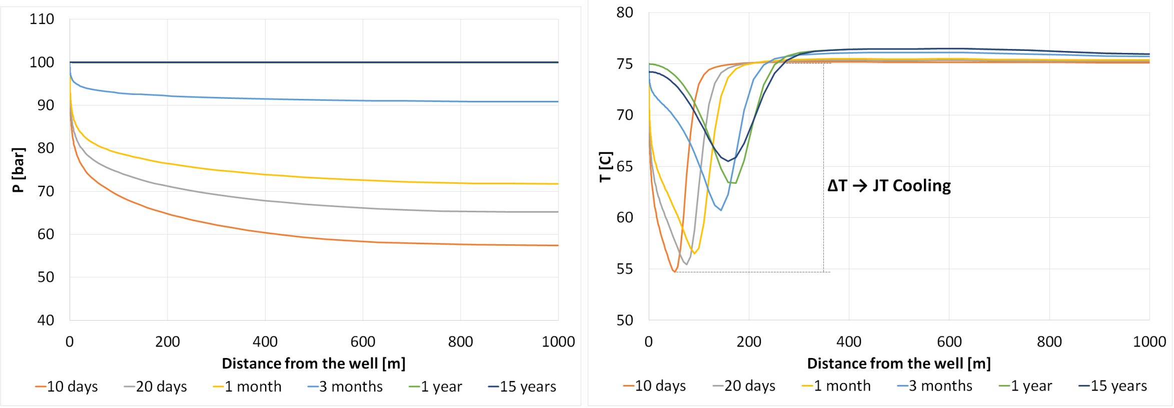

(a) Pressure profile.

(b) Temperature profile.

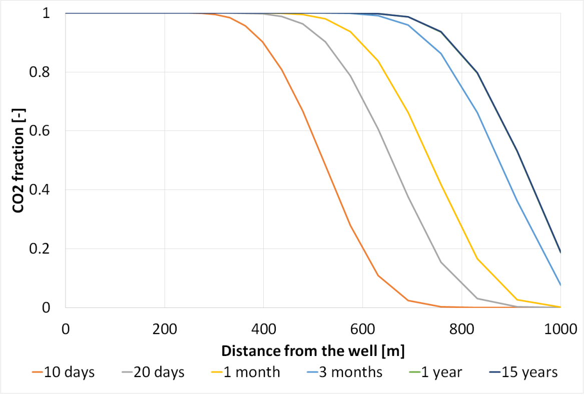

(c) CO_2 fraction profile.

Figure 4.12: Base model results for Case A.

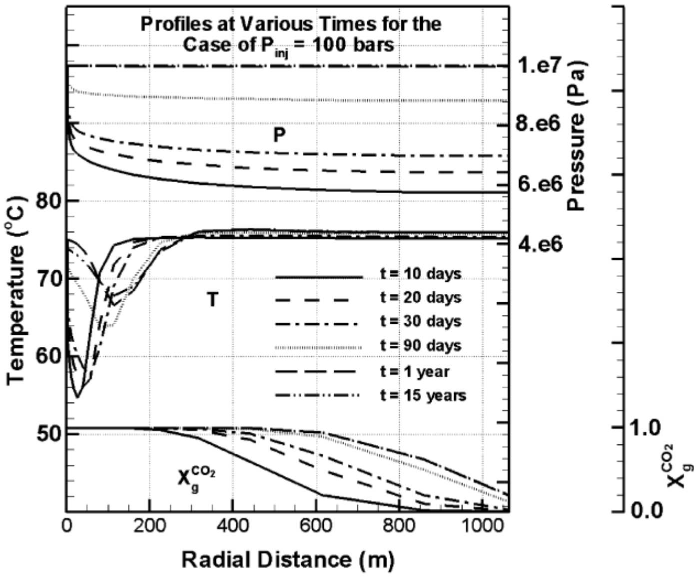

Figure 4.13: Case A: Pressure, temperature and CO_2 fraction results from (Oldenburg, 2007).

Figure 4.14 shows the model results for Case B, for different times since the start of injection (i.e., $10\ days$, $20\ days$, $1\ month$, $3\ months$, $1\ year$, and $15\ years$). The model results are consistent with the literature results presented in Figure 4.15. The J-T effect in Case B is small, creating a cooling of approximately $4°C$.

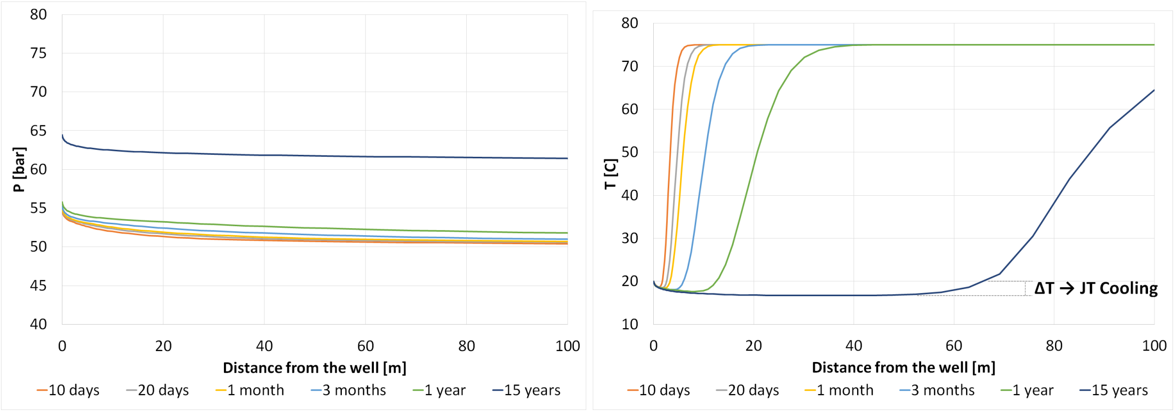

(a) Pressure profile.

(b) Temperature profile.

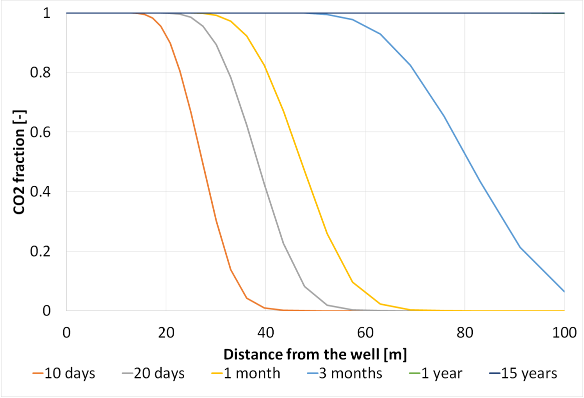

(c) CO_2 fraction profile.

Figure 4.14: Base model results for Case B.

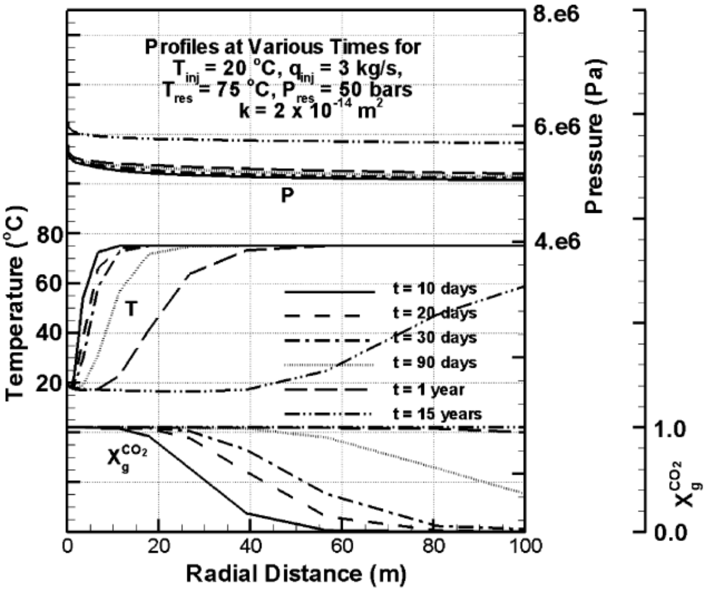

Figure 4.15: Case B: Pressure, temperature and CO_2 fraction results from (Oldenburg, 2007).

4.3. Empirical Model

This section will comprehensively discuss the additions made to the base model to simulate the processes of hydrate formation and dissociation. Additionally, it will explore the influence of these hydrates on injectivity decline within the reservoir.

4.3.1. Thermal mode

Since the model operates in thermal mode, it becomes essential to incorporate the heat capacity of CO_2 hydrates, which is equal to $3368\ J/kg/K$ according to the thermodynamic software HydraFlash.

4.3.2. Phases and Components

One additional phase, solid, is incorporated into the model to account for CO_2 hydrates. Subsequently, the corresponding component representing the solid phase is also added to the model, hydrate. This inclusion enables the model to account for the formation and dissociation of CO_2 hydrates.

4.3.3. CO_2 Hydrate Properties

The enthalpy values for CO_2 hydrates are obtained from the thermodynamic software HydraFlash and are defined as presented in Table 4.7.

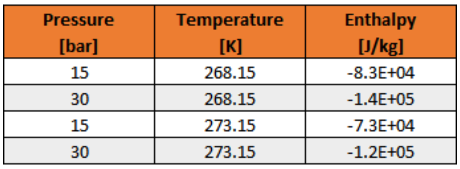

Pressure [bar]	Temperature [K]	Enthalpy [J/kg]
15	268.15	-8.3E+04
30	268.15	-1.4E+05
15	273.15	-7.3E+04
30	273.15	-1.2E+05

Table 4.7: Enthalpy values for CO_2 hydrates.

The density of a CO_2 hydrate is assumed to be constant at a value of $1040\ kg/m^3$, based on literature values (Ferdows & Ota, 2006). As hydrates are treated as solids in the model, the concept of viscosity is not applicable.

For the molecular weight of a CO_2 hydrate, it is calculated using the equation explained in Section 2.2, considering a hydration number of 7.7. As a result, the molecular weight of a CO_2 hydrate is determined to be $182.6\ g/mol$.

As there is no phase transition for a hydrate in the model, the K-value is defined as 1. This means that the hydrate component remains in a solid state throughout the simulation, and no partitioning between different phases is considered for hydrates. Table 4.8 presents the K-values for all the components in the model.

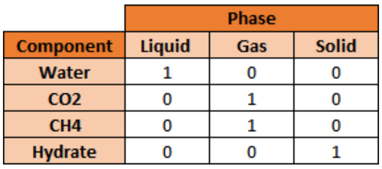

	Phase		
Component	**Liquid**	**Gas**	**Solid**
Water	1	0	0
CO2	0	1	0
CH4	0	1	0
Hydrate	0	0	1

Table 4.8: K-values for all the components in the model.

4.3.4. PT Phase Diagrams

The first significant addition to the model involves defining the hydrate equilibrium curve, which is dependent on the concentrations of various components, including NaCl, calcium chloride ($CaCl_2$), MeOH, and MEG. To accomplish this, the equilibrium curves were generated using the thermodynamic software HydraFlash, and subsequent curve fitting via equations was performed. The resulting curves are visually represented in Figure 4.16. In all the phase diagram, the equilibrium curve liquid-gas CO_2 has been omitted.

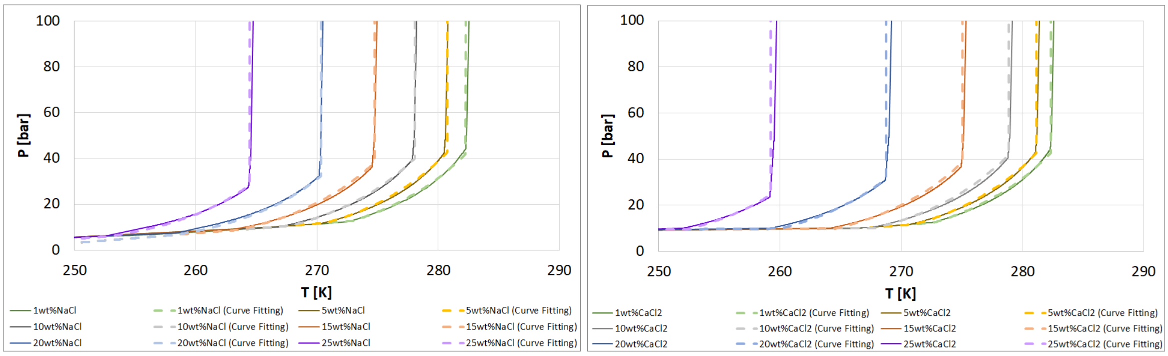

(a) NaCl **(b)** $CaCl_2$

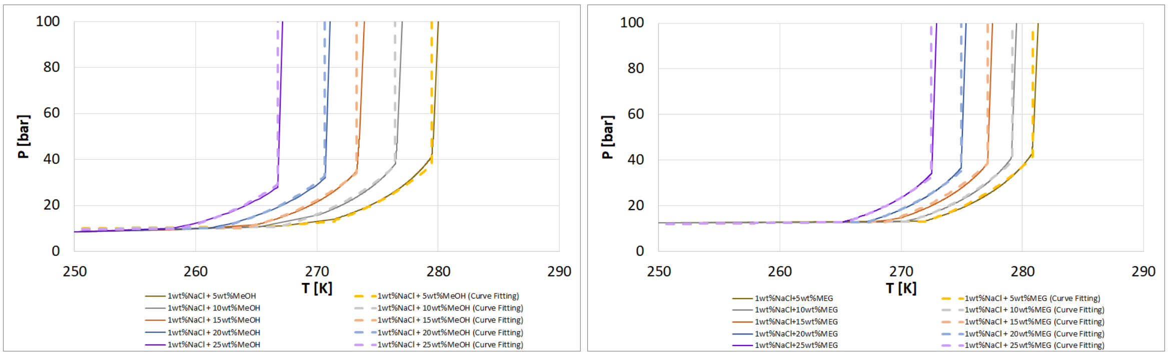

(c) $1wt\%$ NaCl + MeOH **(d)** $1wt\%$ NaCl + MEG

Figure 4.16: $P-T$ phase diagrams showing the hydrate equilibrium curve depending on the component and its concentration in the system. The solid lines in the diagrams represent the results obtained from HydraFlash, while the dashed lines depict the outcomes of the curve fitting process.

4.3.5. Hydrates Formation/Dissociation

In the model, the hydrate formation and dissociation processes are governed by the thermodynamic conditions defined according to the $P-T$ phase diagrams presented in Section 4.3.4. To exemplify this procedure, Figure 4.17 is provided.

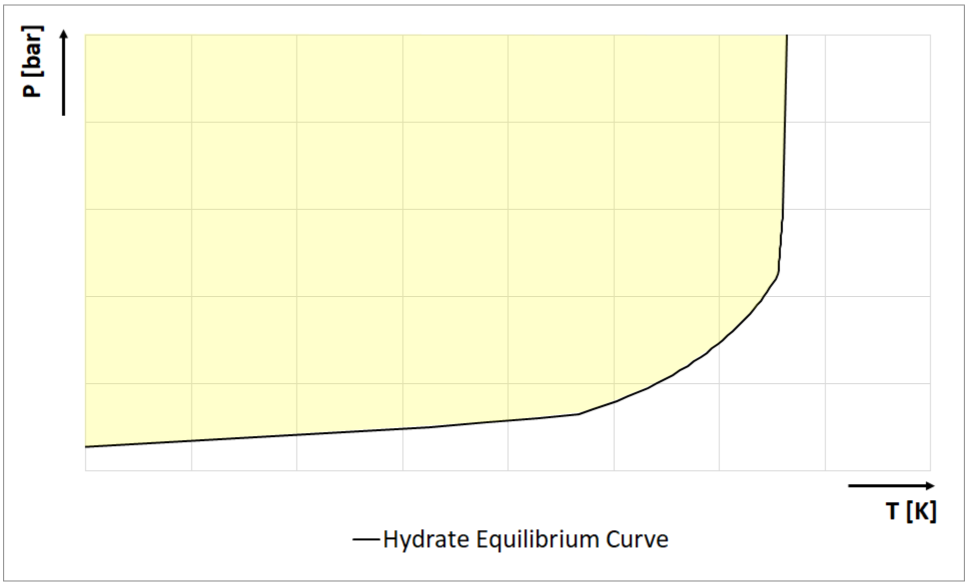

Figure 4.17: $P-T$ phase diagram defining the criteria for hydrate formation and dissociation processes. The yellow area represents the hydrate formation zone. The white area indicates the hydrate dissociation zone. The equilibrium curve liquid-gas CO_2 has been omitted in this phase diagram.

The code developed compares the pressure and temperature of each grid-block at each time step against the defined phase diagram, if the pressure and temperature conditions fall within the yellow area in the diagram, hydrate formation occurs. Once hydrates have formed, if the pressure and temperature conditions move outside the yellow area, hydrate dissociation takes place.

An additional criterion needs to be met for hydrate formation: there should be a non-zero CO_2 fraction and water saturation in the grid-block. Similarly, hydrate dissociation only occurs if the hydrate saturation is greater than zero.

Once the thermodynamic conditions for hydrate formation and dissociation are defined, it is necessary to define the kinetics associated to these processes. This is achieved based on Equation 4.1, where k_f and k_b are the reaction rate coefficients, and 7.7 corresponds to the hydration number, as explained in section 2.2.

$$7.7H_2O + CO_2 \underset{k_b}{\overset{k_f}{\rightleftharpoons}} Hydrate \tag{4.1}$$

Considering Equation 4.1, the forward reaction rate (r_f), representing the formation rate, is determined by Equation 4.2, and the backward reaction rate (r_b), indicating the dissociation rate, is determined by Equation 4.3. In both equations the square brackets ([ ]) denote the concentration of each component.

$$r_f = k_f \left[H_2O\right]^{7.7} \left[CO_2\right] \tag{4.2}$$

$$r_b = k_b \left[Hydrate\right] \tag{4.3}$$

Finally, this model assumes equilibrium, resulting in $k_f = k_b$. The initial value assumed for the reaction rate coefficients is 0.22, based on literature sources (Roosta et al., 2013). Nevertheless, it is crucial to consider that this parameter might require adjustment during the history match process, if conducted.

4.3.6. Hydrates Impact on Injectivity

To accurately model the reduction in permeability due to hydrate formation, it is crucial to ensure that the predicted hydrate saturation based on water saturation from the model aligns with the results obtained from HydraFlash. Figure 4.18 illustrates the validation process, confirming the consistency between the model's predictions and the outcomes from HydraFlash.

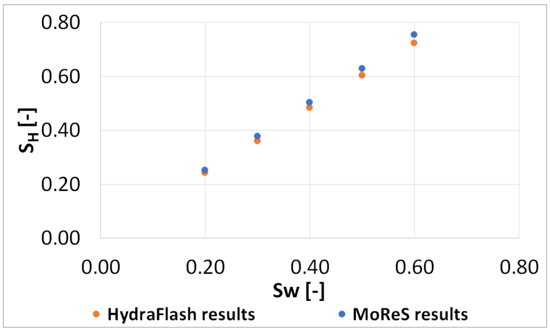

Figure 4.18: Validation of hydrate saturation versus water saturation.

Once the hydrate saturation is calculated, this value is utilized in the Pang-Sharma model, as defined in Section 2.5.1. In this empirical model, β is assumed to be 10; however, it is important to note that this parameter and the permeability reduction model to be used need to be adjusted when a history match process is performed.

4.4. One-Layer Model Results and Sensitivity Analysis

This section will present the results of the empirical model for the One-layer model, including a sensitivity analysis on various variables. The variables under investigation include the number of cells in the radial direction, injection temperature, capillary pressure, CO_2 injection rate, thermal conductivity, and reaction rate coefficients.

4.4.1. Base Case

Initially, the empirical model was run without including in the code the sections on hydrate formation/dissociation and their impact on injectivity. This enabled a comparison of the reservoir behavior with and without hydrates, specifically analyzing the effects on temperature and pressure distribution, as well as the advancement of the CO_2 front within the reservoir. Figure 4.19 displays the results for temperature, pressure, CO_2 fraction, water saturation, and hydrate saturation for different times since the start of injection (i.e., $1\ day$, $1\ month$, $1\ year$, and $5\ years$). Based on the results, it is observed that the J-T cooling effect increases proportionally with the injection time. However, as the pressure of the system increases, the impact of the J-T cooling effect becomes less pronounced. In the base case in the absence of hydrate formation, the water saturation remains constant over time.

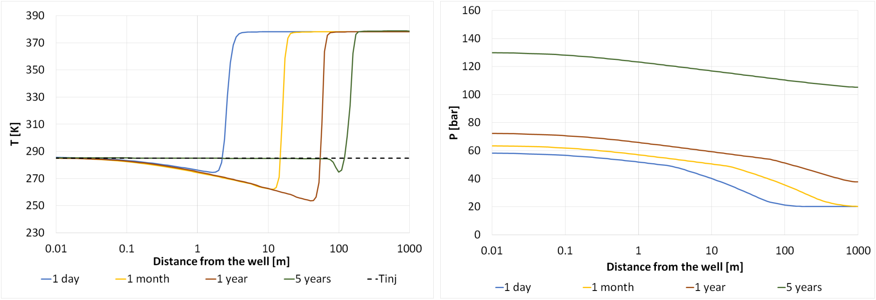

(a) Temperature profile.

(b) Pressure profile.

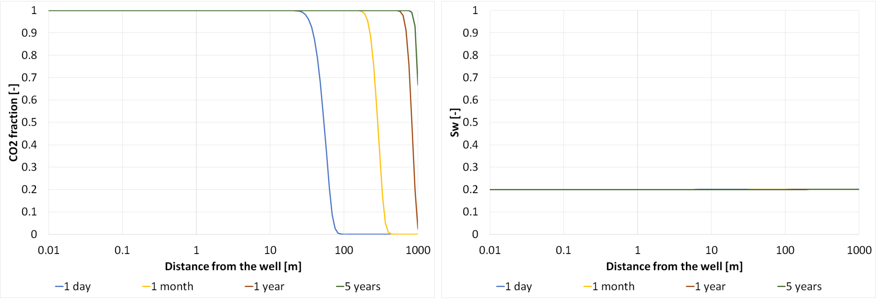

(c) CO_2 fraction profile.

(d) Water saturation profile.

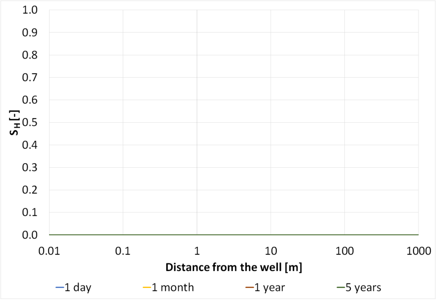

(e) Hydrate saturation profile.

Figure 4.19: Empirical model results without accounting for hydrates formation.

Next, the results for the empirical model considering hydrate formation/dissociation and their impact on injectivity are presented. Figure 4.20 displays the results for temperature, pressure, and CO_2 fraction. All the results are shown for different times since the start of injection (i.e., $1\ day$, $1\ month$, $1\ year$, and $5\ years$). According to the results, in the case that includes hydrate formation, minimal temperature changes were observed in the initial meters from the wellbore, attributable to the limited pressure drop in that zone, resulting in negligible to no J-T cooling effect. Further from the wellbore, the J-T cooling effect became more pronounced, due to the reduction in permeability consequence of hydrate formation. This reduction led to a higher pressure in the reservoir, that narrowed the J-T cooling effect in comparison to the scenario without hydrate formation. The advancement of the CO_2 front occurred similarly in both cases.

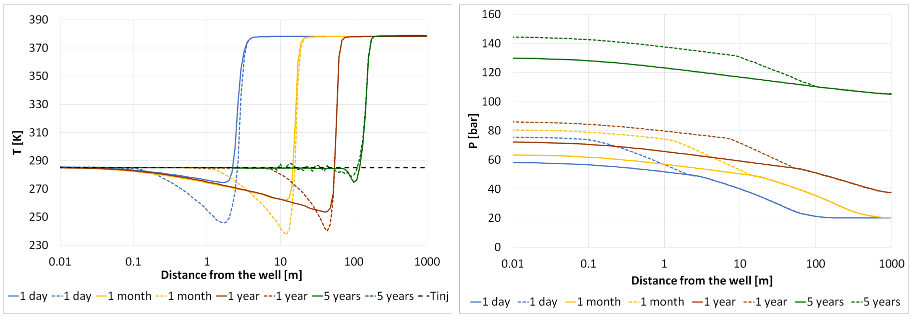

(a) Temperature profile. **(b)** Pressure profile.

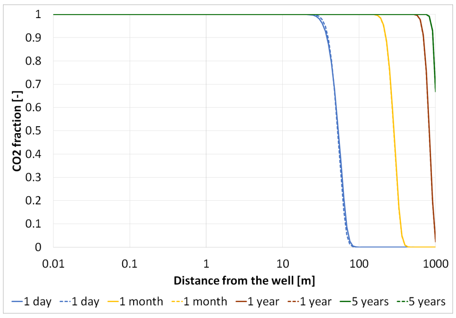

(c) CO_2 fraction profile.

Figure 4.20: Empirical model results including hydrates formation/dissociation and impact on injectivity. The solid lines correspond to the case without hydrate formation. The dashed lines represent the case with hydrate formation/dissociation.

Figures 4.21 and 4.22 show the results for water saturation and hydrate saturation, respectively. All the saturation curves are shown for different times since the start of injection (i.e., $1\ day$, $1\ month$, $1\ year$, and $5\ years$). Regarding the water saturation results, areas where hydrates have formed experience a decrease in water saturation, as water is one of the components involved in hydrate formation. Conversely, hydrate saturation values increase in zones that meet the thermodynamic conditions within the hydrate stability zone for hydrate formation. After 15 years of injection, areas where pressure and temperature fall outside the hydrate stability zone exhibit a reduction in hydrate saturation, meaning that in those areas hydrate dissociation has occurred.

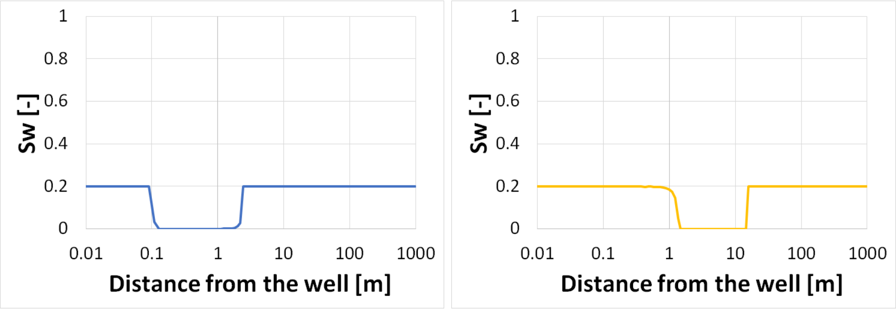

(a) Water saturation profile after $1\ day$ of injection. **(b)** Water saturation profile after $1\ month$ of injection.

Figure 4.21: Empirical model results for water saturation including hydrates formation/dissociation and impact on injectivity.

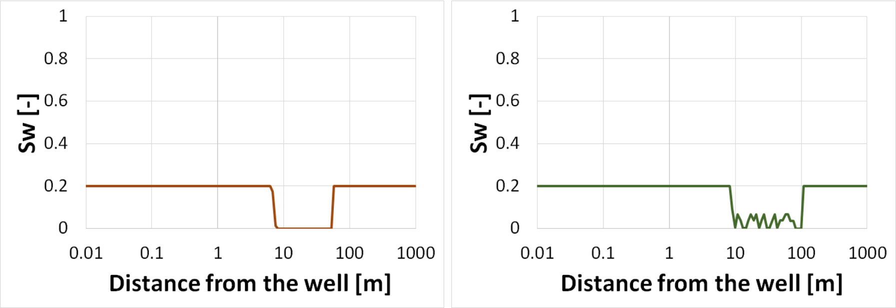

(c) Water saturation profile after $1\ year$ of injection. **(d)** Water saturation profile after $5\ years$ of injection.

Figure 4.21: Empirical model results for water saturation including hydrates formation/dissociation and impact on injectivity (cont.).

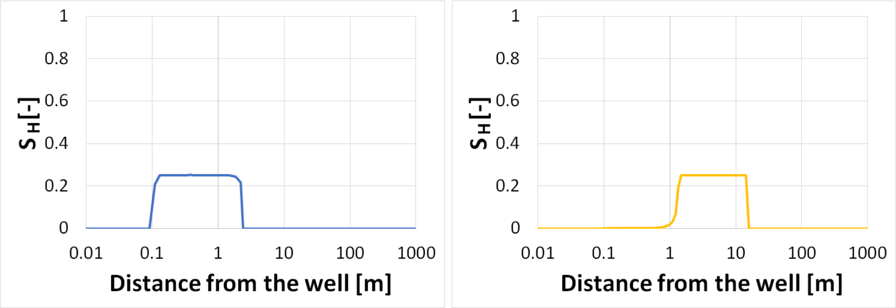

(a) Hydrate saturation profile after $1\ day$ of injection. **(b)** Hydrate saturation profile after $1\ month$ of injection.

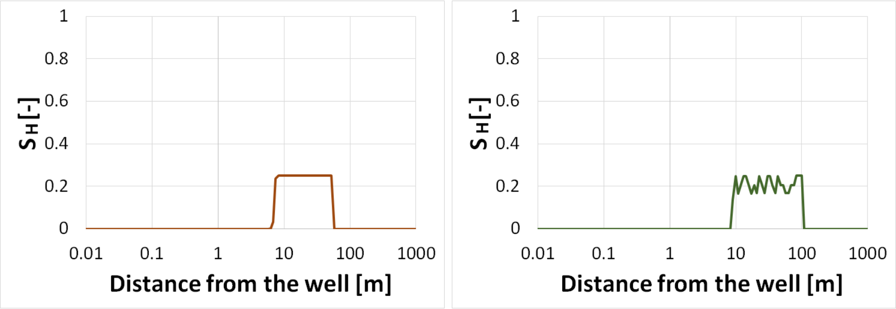

(c) Hydrate saturation profile after $1\ year$ of injection. **(d)** Hydrate saturation profile after $5\ years$ of injection.

Figure 4.22: Empirical model results for hydrate saturation including hydrates formation/dissociation and impact on injectivity.

Finally, a comparison of the injection Bottom Hole Pressure (BHP) is depicted in Figure 4.23. In the scenario with hydrate formation, the presence of hydrates in the porous space causes a reduction in permeability, leading to higher BHP compared to the case without hydrates.

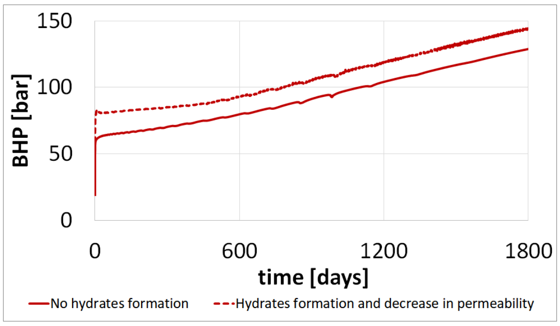

Figure 4.23: BHP comparison: Cases without hydrate formation versus hydrate formation/dissociation.

4.4.2. Number of Cells

A sensitivity analysis was conducted to explore the impact of varying the number of cells in the radial direction of the model comparing a case with 100 number of cells in the radial direction versus a case with 1000. The results for temperature, pressure, and CO_2 fraction are presented in Figure 4.24, considering different time intervals since the start of injection (i.e., $1\ day$, $1\ month$, $1\ year$, and $5\ years$). It is observed that as the radial resolution increases, the J-T cooling effect becomes more localized but also stronger. However, no significant variations are observed in the pressure and CO_2 fraction profiles. It is important to notice that the observed result on the J-T effect, as consequence of the increase in the resolution, reflects a reduction in the numerical dispersion.

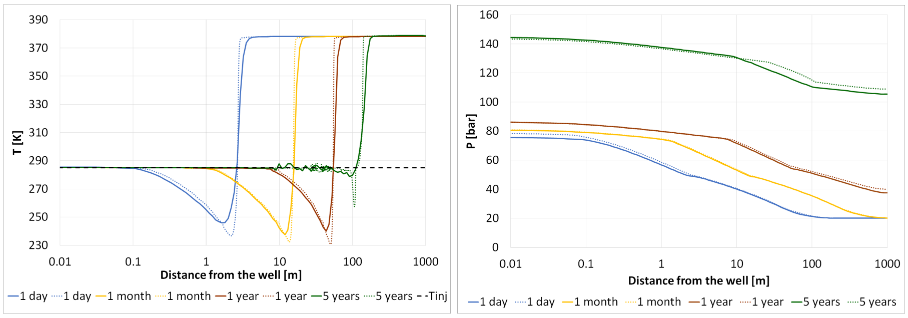

(a) Temperature profile. **(b)** Pressure profile.

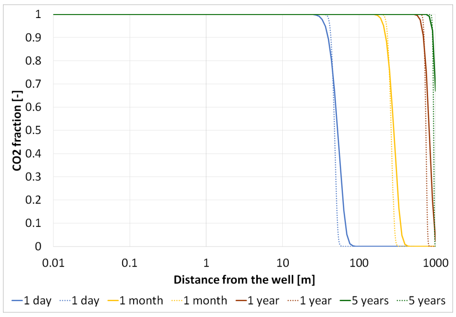

(c) CO_2 fraction profile.

Figure 4.24: Sensitivity of empirical model results depending on the number of cells in the radial direction. The solid lines correspond to the case with 100 cells. The dotted lines represent the case with 1000 cells.

Figure 4.25 shows the results for hydrate saturation for different times since the start of injection (i.e., $1\ day$, $1\ month$, $1\ year$, and $5\ years$). The higher radial resolution in the model results in the localization of the J-T effect, leading to a narrower distribution of hydrate saturation after $5\ years$.

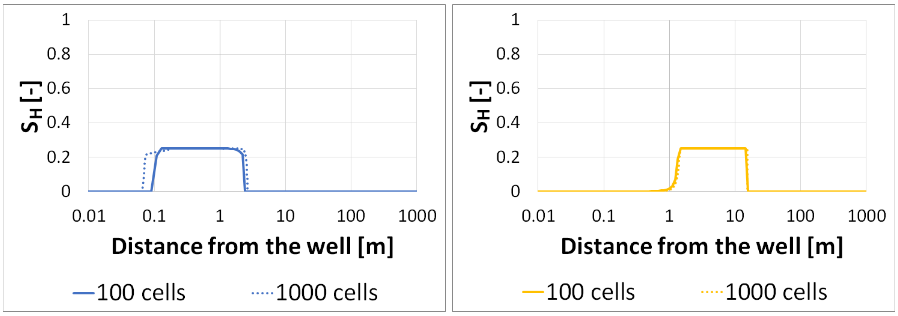

(a) Hydrate saturation profile after $1\ day$ of injection. **(b)** Hydrate saturation profile after $1\ month$ of injection.

Figure 4.25: Sensitivity of empirical model results for hydrate saturation depending on the number of cells in the radial direction.

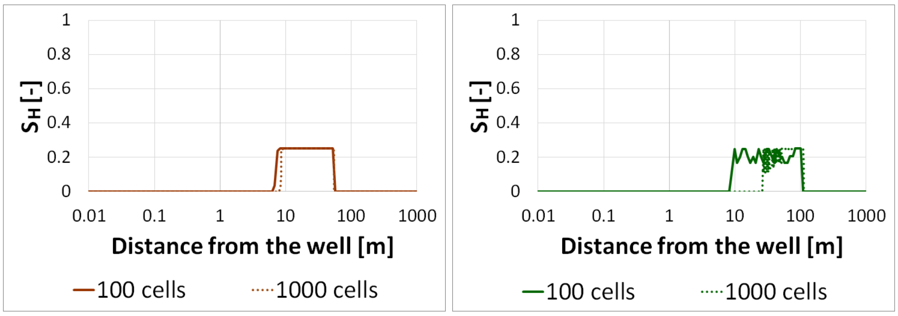

(c) Hydrate saturation profile after $1\ year$ of injection.

(d) Hydrate saturation profile after $5\ years$ of injection.

Figure 4.25: Sensitivity of empirical model results for hydrate saturation depending on the number of cells in the radial direction (cont.).

4.4.3. Capillary Pressure

To assess the influence of capillary pressure on hydrate formation, three cases were simulated. The first case, serving as the base case, omitted capillary pressure effects. In the second case, standard capillary pressure was incorporated, while the third case involved capillary pressure values ten times higher than the standard. Figure 4.26 illustrates the capillary pressure curves utilized in the simulations.

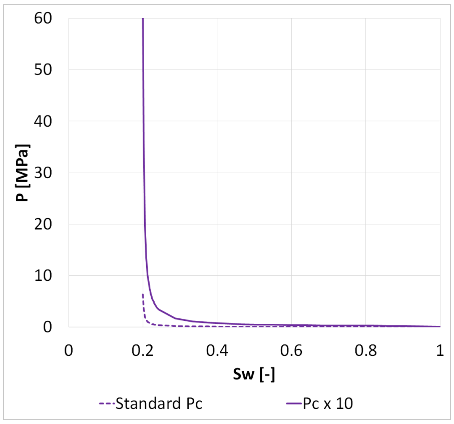

Figure 4.26: Capillary pressure curves used for the sensitivity analysis.

The results for temperature, pressure, and CO_2 fraction are presented in Figure 4.27, considering different time intervals since the start of injection (i.e., $1\ day$, $1\ month$, $1\ year$, and $5\ years$). The analysis revealed that capillary pressure had a minimal effect on the results, indicating that it did not significantly influence hydrate formation.

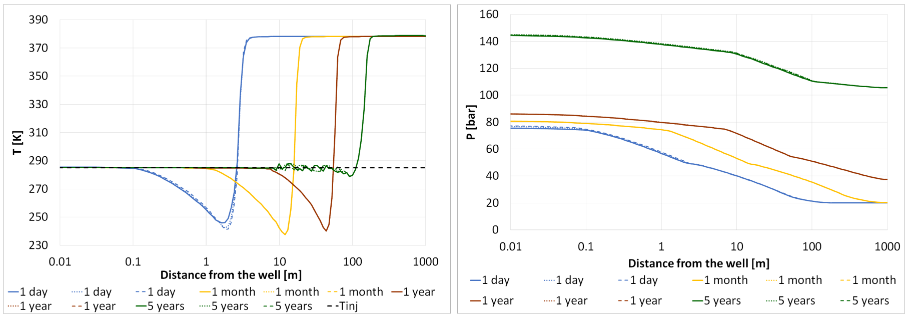

(a) Temperature profile.

(b) Pressure profile.

Figure 4.27: Sensitivity analysis of empirical model results varying capillary pressure. The solid lines correspond to the base case without capillary pressure. The dotted lines represent a case with standard capillary pressure. The dashed lines referred to a case with capillary pressure ten times bigger than standard.

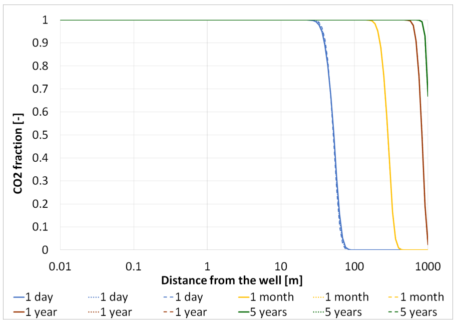

(c) CO_2 fraction profile.

Figure 4.27: Sensitivity analysis of empirical model results varying capillary pressure. The solid lines correspond to the base case without capillary pressure. The dotted lines represent a case with standard capillary pressure. The dashed lines referred to a case with capillary pressure ten times bigger than standard (cont.).

Figure 4.28 depicts the results for hydrate saturation at different times since the start of injection (i.e., $1\ day$, $1\ month$, $1\ year$, and $5\ years$). Consistent with previous findings, capillary pressure did not impact significantly the hydrate saturation.

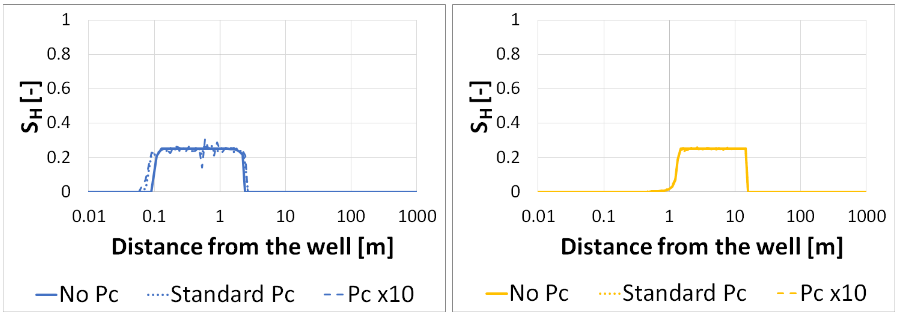

(a) Hydrate saturation profile after $1\ day$ of injection.

(b) Hydrate saturation profile after $1\ month$ of injection.

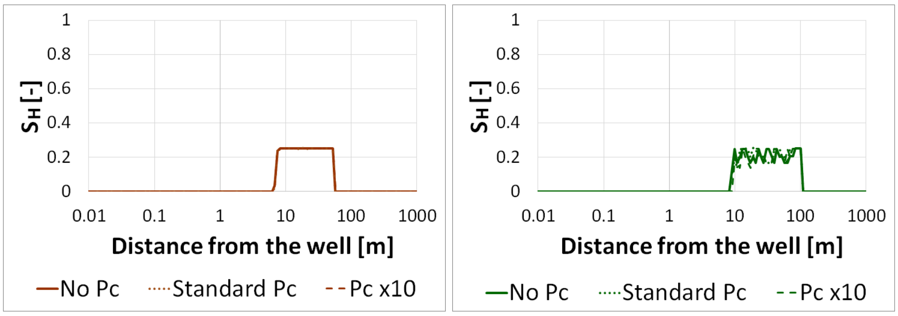

(c) Hydrate saturation profile after $1\ year$ of injection.

(d) Hydrate saturation profile after $5\ years$ of injection.

Figure 4.28: Sensitivity analysis of empirical model results for hydrate saturation varying capillary pressure.

4.4.4. Rock Thermal Conductivity

The influence of rock thermal conductivity (k) on the results was studied by comparing two cases: one with no rock thermal conductivity (base case) and another with rock thermal conductivity set to 2.5 $W/m/K$. The results, depicted in Figure 4.29, were assessed over various time intervals from the injection commencement (i.e., $1\ day$, $1\ month$, $1\ year$, and $5\ years$). The findings revealed that increasing rock thermal conductivity causes the surrounding rock near the wellbore to function as a heat source, leading to a reduction in the impact of the J-T cooling effect. Without considering rock thermal conductivity, heat transfer remains entirely convective, resulting in faster cooling of the wellbore's vicinity and a more prominent J-T cooling effect. The pressure and CO_2 fraction profiles displayed minimal variations due to the changes in rock thermal conductivity.

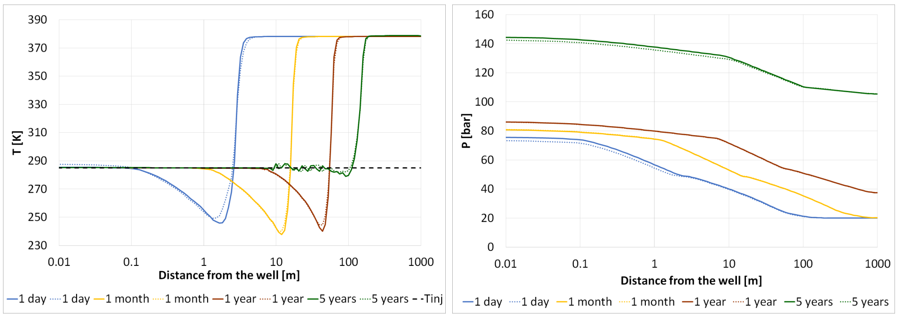

(a) Temperature profile. **(b)** Pressure profile.

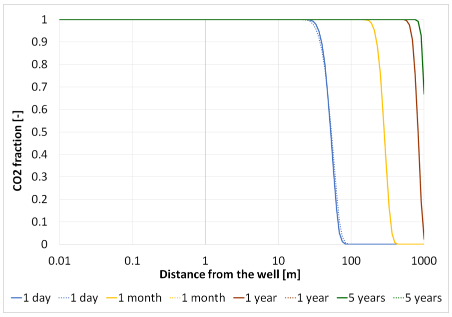

(c) CO_2 fraction profile.

Figure 4.29: Sensitivity analysis of empirical model results varying rock thermal conductivity. The solid lines correspond to the base case without rock thermal conductivity. The dotted lines represent a case with rock thermal conductivity equal to 2.5 $W/m/K$.

Concerning hydrate saturation, Figure 4.30 illustrates the outcomes for different time intervals since the injection initiation (i.e., $1\ day$, $1\ month$, $1\ year$, and $5\ years$). The findings indicate that in the absence of thermal conductivity consideration, the J-T effect becomes more prominent, resulting in a more extensive formation of hydrates within the reservoir.

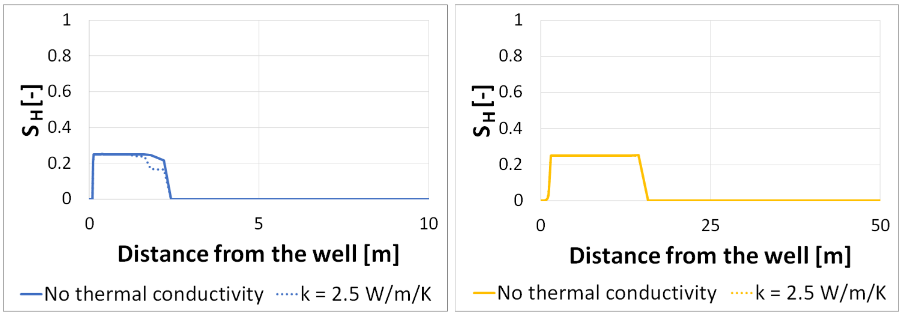

(a) Hydrate saturation profile after $1\ day$ of injection. **(b)** Hydrate saturation profile after $1\ month$ of injection.

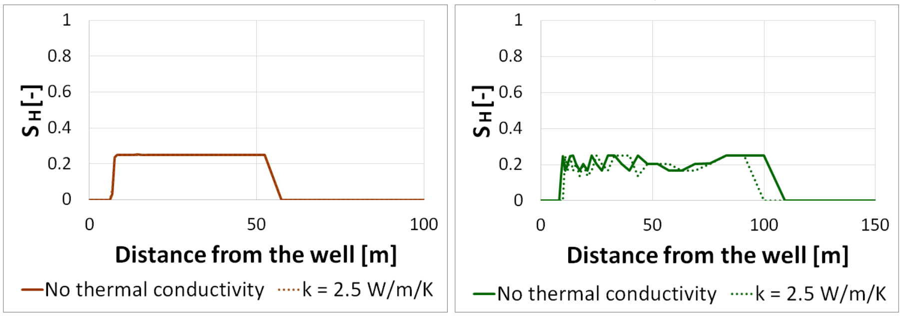

(c) Hydrate saturation profile after $1\ year$ of injection. **(d)** Hydrate saturation profile after $5\ years$ of injection.

Figure 4.30: Sensitivity analysis of empirical model results for hydrate saturation varying rock thermal conductivity.

4.4.5. Reaction Rate Coefficients

The influence of the reaction rate coefficients (kf, kb) on the results was investigated by comparing two cases: the base case with $kf, kb = 0.22$ and another case with $kf, kb = 2.2e-04$. The profiles for temperature, pressure, and CO_2 fraction, depicted in Figure 4.31, were evaluated over different time intervals from the injection initiation (i.e., $1\ day$, $1\ month$, $1\ year$, and $5\ years$). According to the results, decreasing the reaction rate coefficients slows down both hydrate formation and dissociation processes. This notably affects the J-T cooling effect, causing a reduction in its impact during the initial times ($t < 1y$). However, over extended periods, the pressure remains higher for smaller reaction rate coefficients due to the persistent hydrate saturation in the near wellbore, as hydrate dissociation is also slowed down. The movement of the CO_2 front remains unaffected by the reaction rate coefficients since it does not depend on their values.

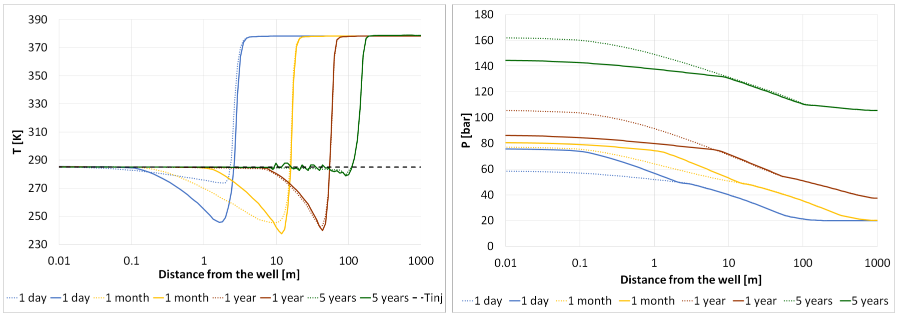

(a) Temperature profile. **(b)** Pressure profile.

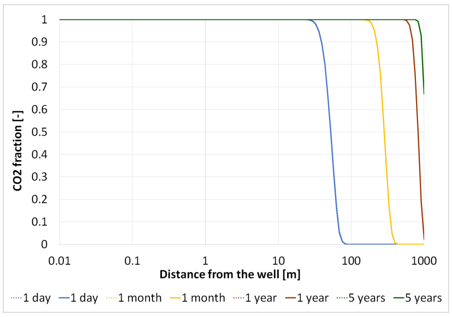

(c) CO_2 fraction profile.

Figure 4.31: Sensitivity analysis of empirical model results varying reaction rate coefficients. The solid lines correspond to the base case ($k_f, k_b = 0.22$). The dotted lines represent a case with reaction rate coefficients equal to $2.2e-04$.

Figures 4.32 and 4.33 illustrate the results for water saturation and hydrate saturation, respectively. All the saturation curves are shown for different times since the start of injection (i.e., $1\ day$, $1\ month$, $1\ year$, and $5\ years$). The findings demonstrated that reducing the reaction rate coefficients led to a decrease in the rate of water consumption, consequently resulting in a slower formation of hydrates. Moreover, since $k_f = k_b$ was assumed, the dissociation of hydrates also occurred at a slower pace when the reaction rate coefficients are smaller.

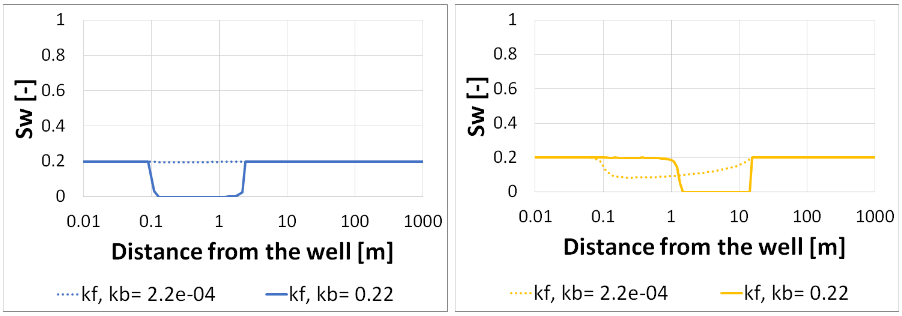

(a) Water saturation profile after $1\ day$ of injection. **(b)** Water saturation profile after $1\ month$ of injection.

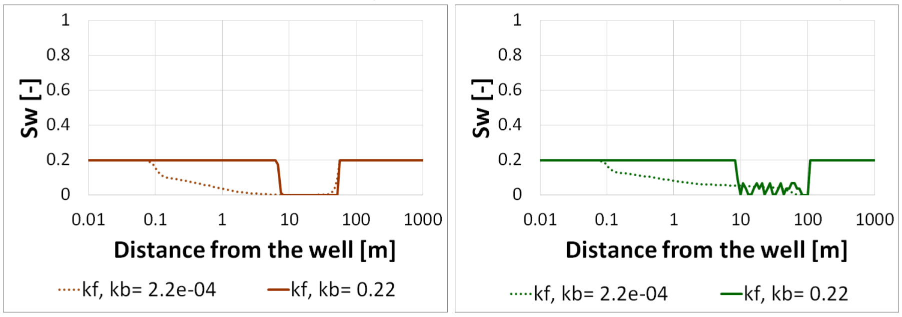

(c) Water saturation profile after $1\ year$ of injection. **(d)** Water saturation profile after $5\ years$ of injection.

Figure 4.32: Sensitivity analysis of empirical model results for water saturation varying reaction rate coefficients.

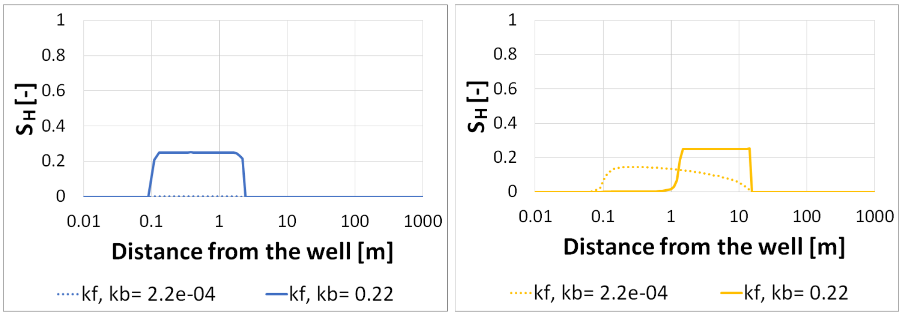

(a) Hydrate saturation profile after $1\ day$ of injection. **(b)** Hydrate saturation profile after $1\ month$ of injection.

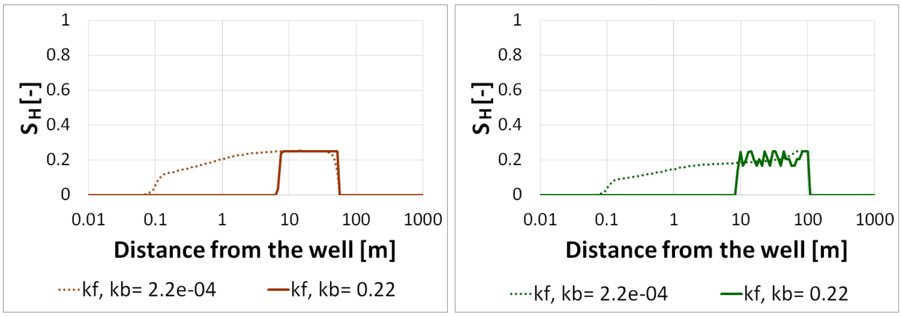

(c) Hydrate saturation profile after $1\ year$ of injection. **(d)** Hydrate saturation profile after $5\ years$ of injection.

Figure 4.33: Sensitivity analysis of empirical model results for hydrate saturation varying reaction rate coefficients.

4.4.6. CO_2 Injection Rate

To investigate the impact of CO_2 injection rate on hydrate formation, three different scenarios were modeled, where the injection rates of CO_2 were set at $15\ kg/s$ (low rate case), $30\ kg/s$ (medium rate case), and $60\ kg/s$ (high rate case), respectively. Temperature profiles at various time intervals (i.e., $1\ day$, $1\ month$, 1 $year$, and $5\ years$) since injection initiation were plotted in Figure 4.34. In general, the high rate injection scenario resulted in increased pressure buildup, which subsequently impacted the temperature and diminished the J-T cooling effect. Concerning the medium and low rate cases, the medium injection rate resulted in a more pronounced J-T cooling effect over shorter time frames, this is times shorter than one year. This phenomenon occurs due to the rapid injection of CO_2, causing a substantial pressure drop and expansion that intensifies the J-T cooling effect. However, as time extends beyond one year, the cumulative influence of the injection on the reservoir pressure reduced the overall impact of the J-T cooling effect. This led to a more pronounced J-T cooling effect for the low rate case over time frames longer than one year.

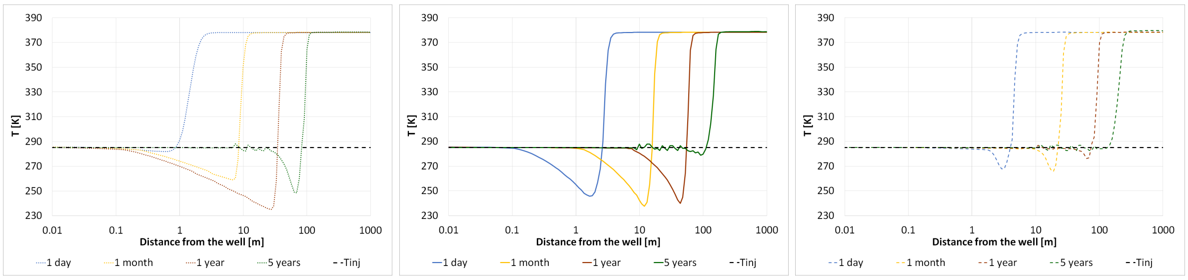

(a) Temperature profile for CO_2 injection rate of $15\ kg/s$.
(b) Temperature profile for CO_2 injection rate of $30\ kg/s$.
(c) Temperature profile for CO_2 injection rate of $60\ kg/s$.

Figure 4.34: Sensitivity analysis of empirical model results for temperature varying CO_2 injection rate.

Pressure profiles were plotted at different time intervals (i.e., $1\ day$, $1\ month$, 1 $year$, and $5\ years$) since the start of injection, as shown in Figure 4.35. The findings revealed a direct relationship between injection rate and the rate at which pressure built up around the wellbore. Specifically, higher injection rates led to a faster increase in pressure. This rising pressure directly impacted both the J-T cooling effect and the hydrate formation process, by reducing them.

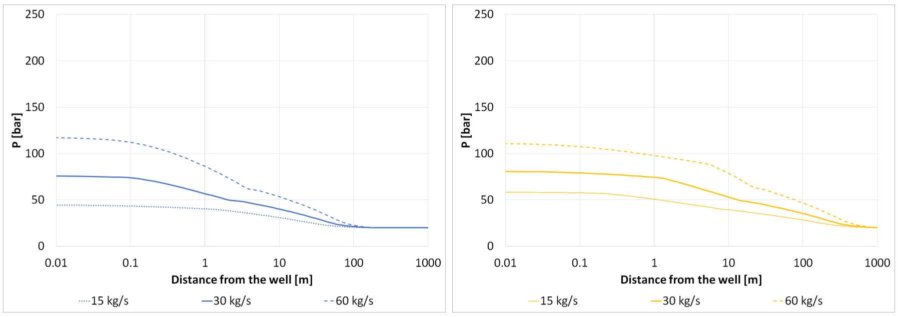

(a) Pressure profile after $1\ day$ of injection.
(b) Pressure profile after $1\ month$ of injection.

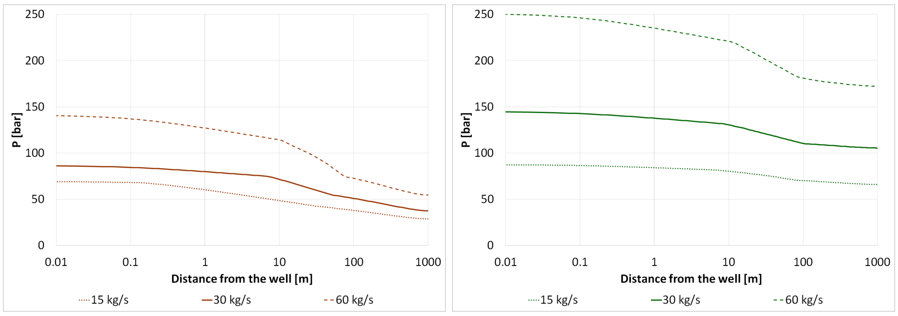

(c) Pressure profile after $1\ year$ of injection.
(d) Pressure profile after $5\ years$ of injection.

Figure 4.35: Sensitivity analysis of empirical model results for pressure varying CO_2 injection rate.

Figure 4.36 shows the CO_2 fraction profile over different times (i.e., $1\ day$, $1\ month$, 1 $year$, and $5\ years$) for different injection rates (i.e., $15\ kg/s$, $30\ kg/s$, and $60\ kg/s$). Based on the results, it was observed that the CO_2 front moves at a faster pace when the injection rate is higher.

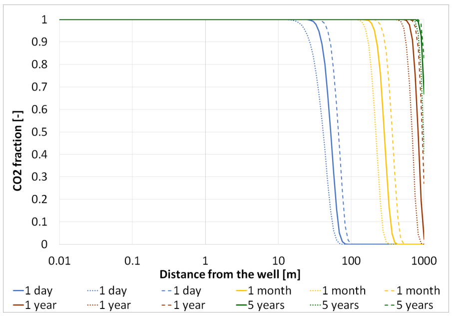

Figure 4.36: Sensitivity analysis of empirical model results for CO_2 fraction varying CO_2 injection rate. The dotted lines represent of CO_2 injection rate at $15\ kg/s$. The solid lines correspond to CO_2 injection rate of $30\ kg/s$. The dashed lines referred to a case of CO_2 injection rate of $60\ kg/s$.

Figure 4.37 depicts the results for hydrate saturation at different times since the start of injection (i.e., $1\ day$, $1\ month$, 1 $year$, and $5\ years$) for different injection rates (i.e., $15\ kg/s$, $30\ kg/s$, and $60\ kg/s$). Notably, with increasing injection rates, the near wellbore region experienced pressurization, resulting in a reduction of hydrate formation in that specific area. However, even after five years injection and consequently pressurization, hydrates were found to have formed in the reservoir for all the cases, except for a 10-meter region around the wellbore, which remained free from hydrates.

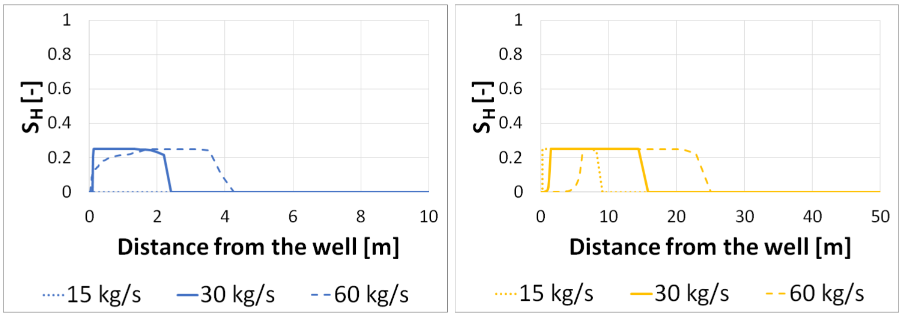

(a) Hydrate saturation profile after $1\ day$ of injection.

(b) Hydrate saturation profile after $1\ month$ of injection.

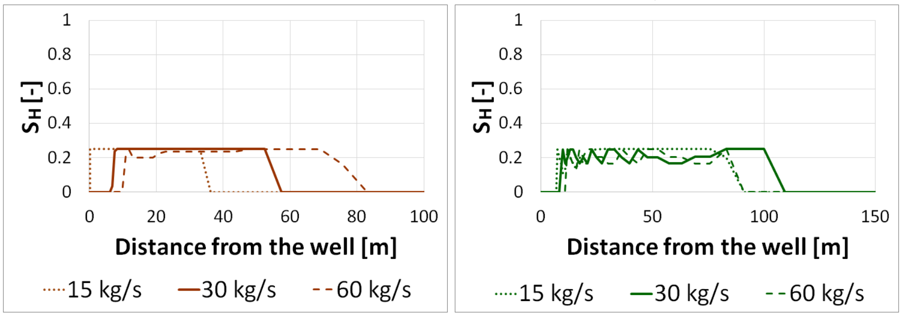

(c) Hydrate saturation profile after $1\ year$ of injection.

(d) Hydrate saturation profile after $5\ years$ of injection.

Figure 4.37: Sensitivity analysis of empirical model results for hydrate saturation varying CO_2 injection rate.

Finally, a comparison of the injection Bottom Hole Pressure (BHP) is presented in Figure 4.38. The findings indicated a direct correlation between the injection rate and the BHP achieved. Specifically, higher injection rates resulted in higher BHP values being reached.

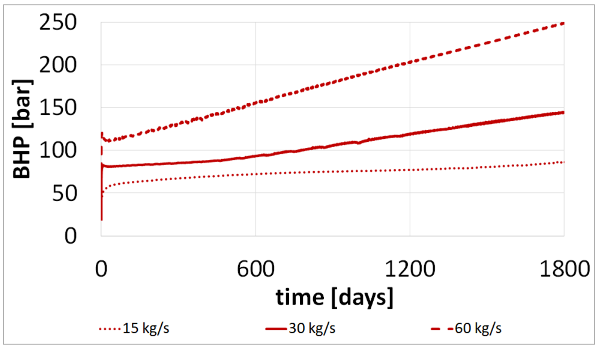

Figure 4.38: BHP comparison based on CO_2 injection rate, cases $15\ kg/s$, $30\ kg/s$, and $60\ kg/s$.

4.4.7. CO_2 Injection Temperature

An analysis on the impact of injection temperature on hydrate formation was conducted. Two cases were considered: one with CO_2 injection at $12°C$ (base case) and another with CO_2 injection at $20°C$. The results for temperature, pressure, and CO_2 fraction are displayed in Figure 4.39, considering different time intervals since the start of injection (i.e., $1\ day$, $1\ month$, $1\ year$, and $5\ years$). Based on the findings, it is evident that the warmer injection temperature leads to a reduced J-T cooling effect, resulting in less hydrate formation and, consequently, a lower increase in reservoir pressure during CO_2 injection.

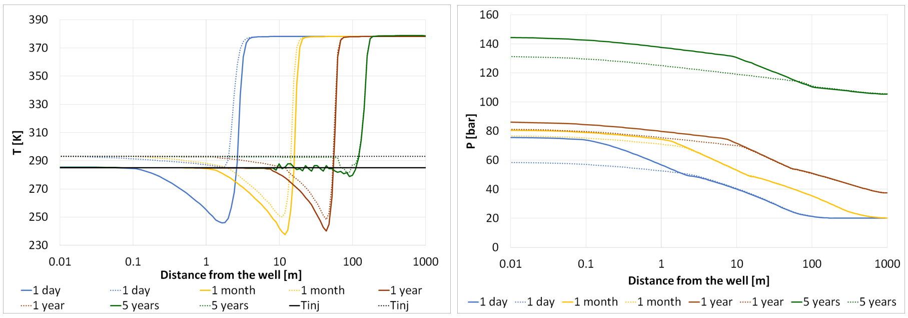

(a) Temperature profile.

(b) Pressure profile.

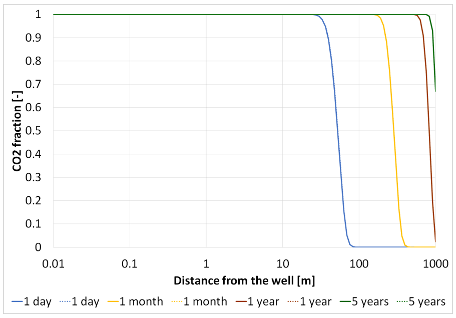

(c) CO_2 fraction profile.

Figure 4.39: Sensitivity of empirical model results depending on the CO_2 injection temperature. The solid lines correspond to the base case (CO_2 injected at $12°C$). The dotted lines represent the case of CO_2 injection at $20°C$.

Figure 4.40 illustrates the results for hydrate saturation at different times since the start of injection (i.e., $1\ day$, $1\ month$, $1\ year$, and $5\ years$). In the case with CO_2 injected at $20°C$, there is noticeably less hydrate formation over time compared to the case with CO_2 injected at $12°C$.

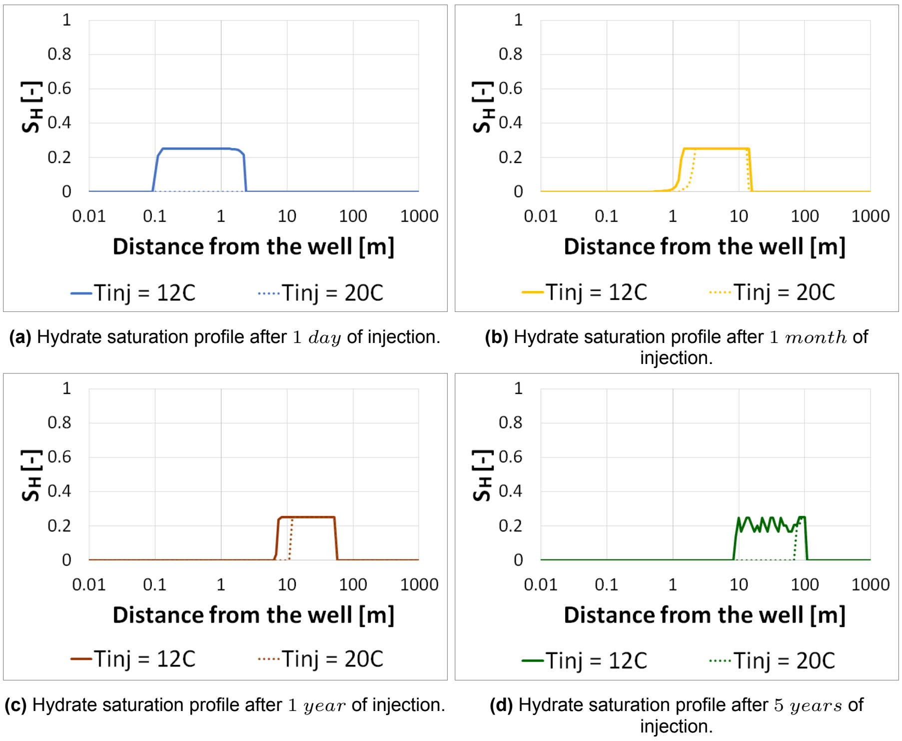

(a) Hydrate saturation profile after $1\ day$ of injection.

(b) Hydrate saturation profile after $1\ month$ of injection.

(c) Hydrate saturation profile after $1\ year$ of injection.

(d) Hydrate saturation profile after $5\ years$ of injection.

Figure 4.40: Sensitivity of empirical model results for hydrate saturation depending on the CO_2 injection temperature.

Ultimately, a comparison of the injection Bottom Hole Pressure (BHP) is depicted in Figure 4.41. The scenario with CO_2 injection at $20°C$ shows reduced hydrate formation, resulting in a lower BHP. Conversely, the scenario with CO_2 injection at $12°C$ exhibits higher hydrate formation, leading to a higher BHP.

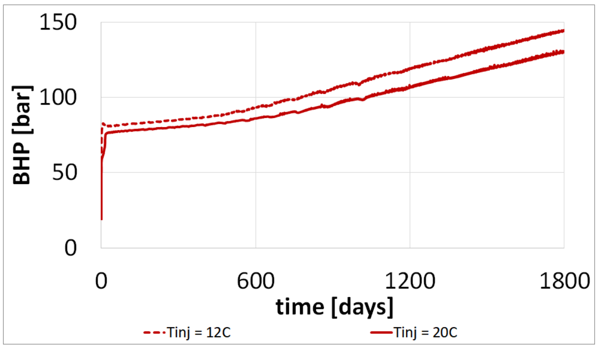

Figure 4.41: BHP comparison: Cases of CO_2 injection at $12°C$ versus CO_2 injection at $20°C$.

4.5. Two-Layer Model Results

To analyze the impact of vertical heterogeneity on the hydrate formation and dissociation processes, a simulation was conducted using a two-layer model with different permeabilities. The top layer was assigned a permeability of $50\ mD$, while the bottom layer had a permeability of $5\ mD$. Figure 4.42 illustrates the profiles for temperature, pressure, and CO_2 fraction, evaluated over various time intervals from the start of injection (i.e., $1\ day$, $1\ month$, $1\ year$, and $5\ years$). The results indicate that CO_2 moves faster in the layer with higher permeability, leading to a more pronounced and faster J-T cooling effect in that layer and slightly higher pressure as well.

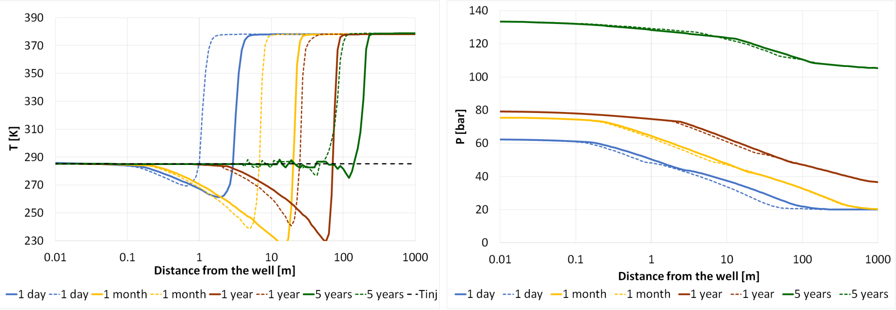

(a) Temperature profile. **(b)** Pressure profile.

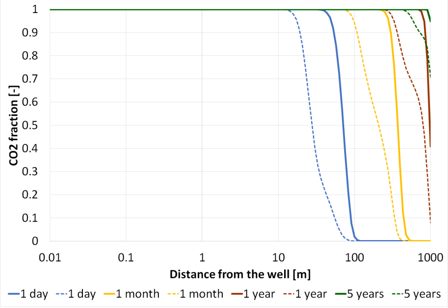

(c) CO_2 fraction profile.

Figure 4.42: Sensitivity analysis of empirical model results considering 2-layer model with different permeability. The solid lines correspond to the layer with high permeability ($K = 50\ mD$). The dashed lines represent the layer with low permeability ($K = 5\ mD$).

Figure 4.43 presents the hydrate saturation profile over different time intervals since the beginning of injection (i.e., $1\ day$, $1\ month$, $1\ year$, and $5\ years$). In line with the temperature, pressure, and CO_2 fraction profiles, hydrates have notably cover a longer length in the more permeable layer.

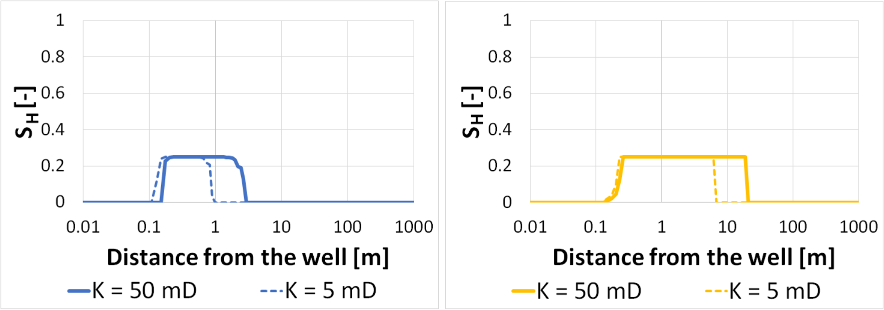

(a) Hydrate saturation profile after $1\ day$ of injection. **(b)** Hydrate saturation profile after $1\ month$ of injection.

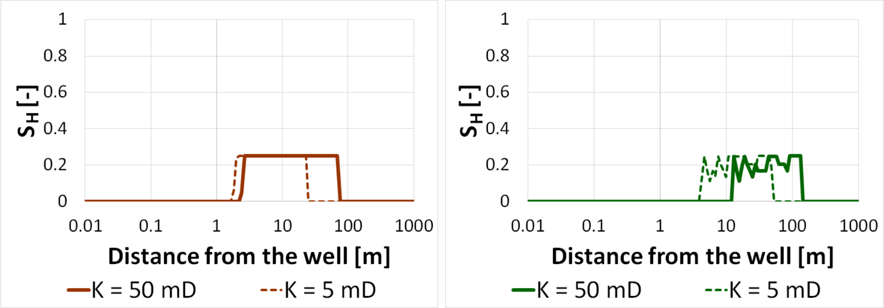

(c) Hydrate saturation profile after $1\ year$ of injection. **(d)** Hydrate saturation profile after $5\ years$ of injection.

Figure 4.43: Sensitivity analysis of empirical model results for hydrate saturation considering 2-layer model with different permeability.

4.6. Case Studies

This section presents the simulation results for two case studies involving multi-layering reservoirs with heterogeneous vertical properties, including variations in porosity, permeability, and thickness. For each case study, two CO$_2$ injection temperatures are evaluated: $-5°C$ and $12°C$.

4.6.1. Reservoir A

Reservoir A consists of 20 layers, each with specific properties as defined in Table 4.9. The initial conditions and simulation parameters for Reservoir A are provided in Table 4.10.

Layer	Permeability [mD]	Porosity [-]	Thickness [m]
1	6.73	0.119	5.63
2	43.70	0.124	5.48
3	9.63	0.127	5.63
4	49.76	0.156	5.48
5	7.33	0.119	5.63
6	5.69	0.120	5.48
7	6.43	0.121	5.63
8	4.71	0.118	5.48
9	0.63	0.083	5.63
10	3.58	0.112	5.48
11	4.85	0.122	5.63
12	1.78	0.104	5.48
13	5.37	0.115	5.63
14	6.26	0.127	5.48
15	2.82	0.102	5.63
16	5.44	0.119	5.48
17	5.48	0.110	5.63
18	12.17	0.126	5.48
19	4.41	0.102	5.63
20	5.10	0.100	5.33

Table 4.9: Properties Reservoir A.

Property	Unit	Value
Number of cells radial direction	[-]	100
Radius	[m]	1000
Thickness	[m]	111
Rock heat capacity	[J/kg/K]	1000
Rock density	[kg/m3]	2600
Formation thermal conductivity	[W/m/K]	0
Heat exchange with surronding rock		No
Tres	[C]	104
Pres	[bar]	20
Swi	[-]	0.20
Pc		No
Initial fluids in reservoir		CH4 and Water
Salinity		NaCl 20 wt%
kf,kb	[-]	0.22
Permeability reduction model		Chen et al.
Fitting parameter	[-]	3
Injection Constraint		Constant injection rate
Tinj	[C]	12
CO2 injection rate	[kg/s]	30

Table 4.10: Initial conditions and simulation parameters for Reservoir A.

Based on the model results, the injection rate was distributed among the layers according to Figure 4.44. In this distribution, layer 4 (the most permeable layer) received the highest injection rate, while layer 9 (the least permeable layer) received the lowest injection rate.

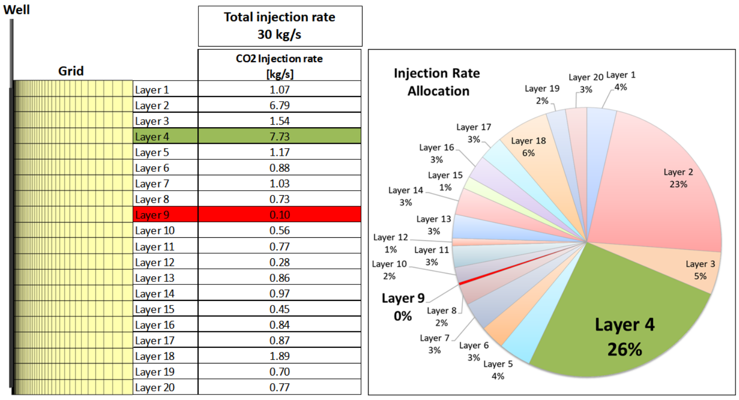

Total injection rate 30 kg/s

	CO2 Injection rate [kg/s]
Layer 1	1.07
Layer 2	6.79
Layer 3	1.54
Layer 4	7.73
Layer 5	1.17
Layer 6	0.88
Layer 7	1.03
Layer 8	0.73
Layer 9	0.10
Layer 10	0.56
Layer 11	0.77
Layer 12	0.28
Layer 13	0.86
Layer 14	0.97
Layer 15	0.45
Layer 16	0.84
Layer 17	0.87
Layer 18	1.89
Layer 19	0.70
Layer 20	0.77

Figure 4.44: Injection rate allocation for Reservoir A.

4.6.1.1. CO_2 Injection at $-5°C$

Figures 4.45, 4.46, 4.47, and 4.48 depict the profiles for temperature, pressure, CO_2 fraction, and hydrate saturation, respectively, evaluated over different time intervals since the start of injection (i.e., $1\ day$, $3\ years$, and $5\ years$) for Reservoir A when injecting CO_2 at $-5°C$.

The results indicate that the most permeable layer is rapidly swept by CO_2, leading to a highly pronounced J-T cooling effect in this layer compared to the other layers. Conversely, the least permeable layer is the last to be swept by CO_2, resulting in a slower temperature drop in that layer. The results clearly show the advancement of the thermal front, the increase in pressure, and the movement of the CO_2 front over time. Moreover, the reduction of the J-T cooling effect can be observed as pressure increases over time. However, due to the injection temperature being within the hydrate stability zone, continuous hydrate formation is promoted, as evident from the hydrate saturation profile.

One crucial effect of vertical heterogeneity is the occurrence of a secondary thermal front within the most permeable layers after 3 and $5\ years$. This phenomenon is evident in the temperature profile and can be directly linked to the movement of the CO_2 front seen in the CO_2 fraction profile. As a permeable layer detects its own thermal front, it also experiences the thermal front of the neighboring layers. This is a result of the varied permeability of each layer, leading to differential velocities of CO_2 movement.

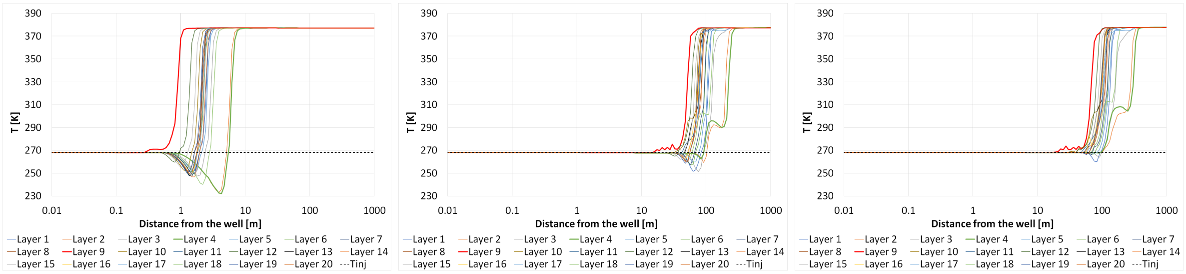

(a) Temperature profile after $1\ day$ of injection.

(b) Temperature profile after $3\ years$ of injection.

(c) Temperature profile after $5\ years$ of injection.

Figure 4.45: Temperature profile, case study Reservoir A, CO_2 injection at $-5°C$. The green bold line represents the most permeable layer. The red bold line shows the least permeable layer.

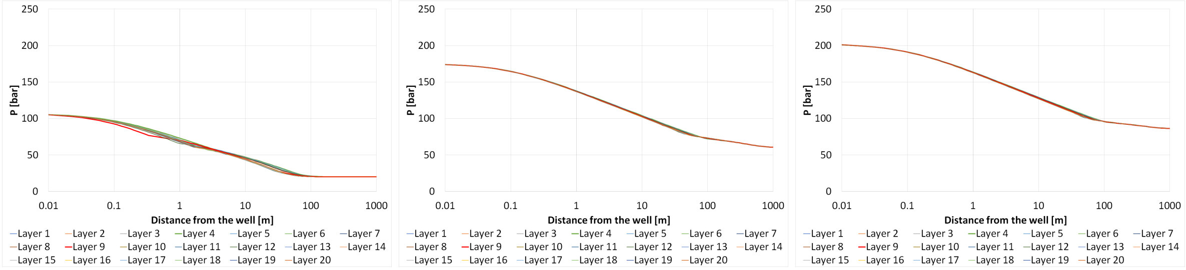

(a) Pressure profile after $1\ day$ of injection. **(b)** Pressure profile after $3\ years$ of injection. **(c)** Pressure profile after $5\ years$ of injection.

Figure 4.46: Pressure profile, case study Reservoir A, CO_2 injection at $-5°C$. The green bold line represents the most permeable layer. The red bold line shows the least permeable layer.

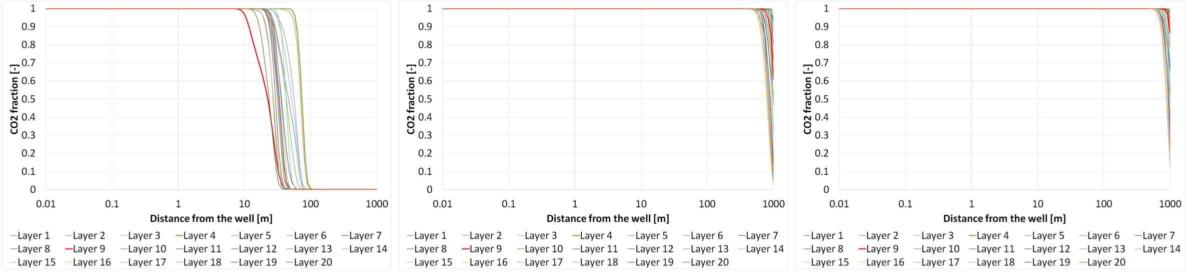

(a) CO_2 fraction profile after $1\ day$ of injection. **(b)** CO_2 fraction profile after $3\ years$ of injection. **(c)** CO_2 fraction profile after $5\ years$ of injection.

Figure 4.47: CO_2 fraction profile, case study Reservoir A, CO_2 injection at $-5°C$. The green bold line represents the most permeable layer. The red bold line shows the least permeable layer.

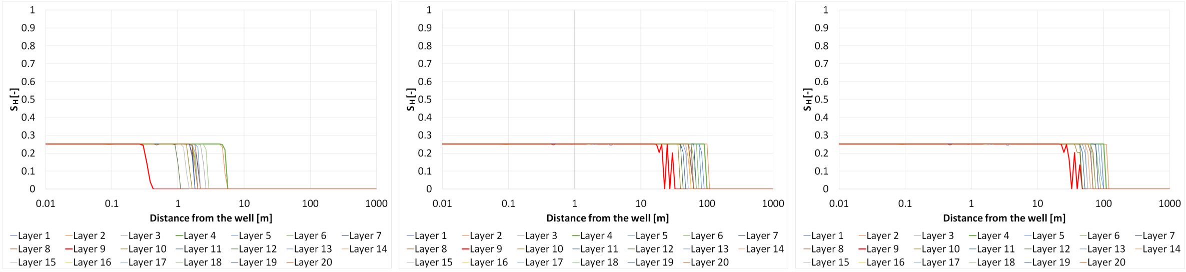

(a) Hydrate saturation profile after $1\ day$ of injection. **(b)** Hydrate saturation profile after $3\ years$ of injection. **(c)** Hydrate saturation profile after $5\ years$ of injection.

Figure 4.48: Hydrate saturation profile, case study Reservoir A, CO_2 injection at $-5°C$. The green bold line represents the most permeable layer. The red bold line shows the least permeable layer.

To provide a more comprehensive view of the profiles figures 4.49, 4.50, 4.51, 4.52, and 4.53 show two-dimensional (2D) plots of the reservoir for temperature, pressure, CO_2 fraction, hydrate saturation, and water saturation, respectively, after $5\ years$ of injection.

The results indicate that the thermal front travels at a faster rate through the most permeable layers. Generally, the near wellbore area exhibits a temperature close to the injection temperature. Areas that have not been affected by the thermal front retain warmer initial reservoir conditions. In the near wellbore, lower temperatures create the conditions for hydrate formation, leading to higher pressure in this zone as permeability gets reduced. Concerning the CO_2 front, areas with high permeability display a more rapid advancement of the CO_2 front. As for hydrate saturation, the near wellbore zone presents hydrate formation and nearly zero water saturation, as most of the water has been consumed during the hydrate formation process.

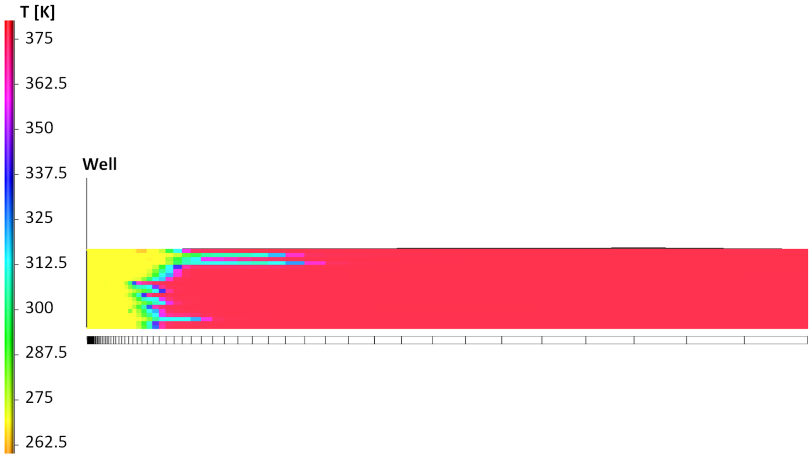

Figure 4.49: 2D plot for temperature after $5\ years$ of injection, case study Reservoir A, CO_2 injection at $-5°C$ $(268.15K)$.

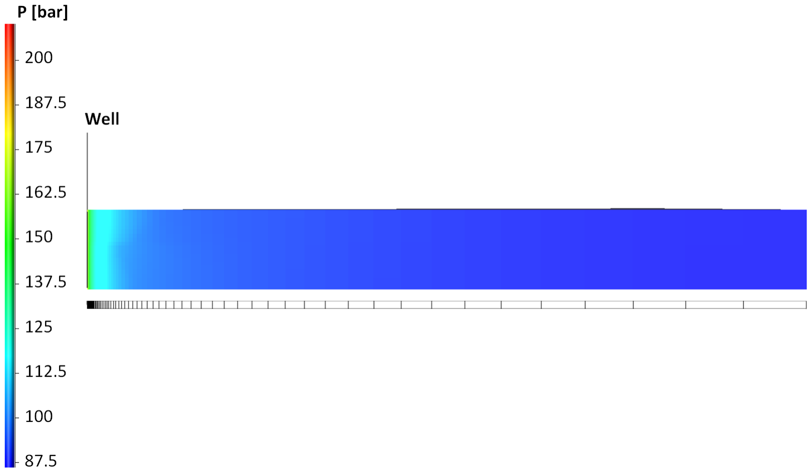

Figure 4.50: 2D plot for pressure after $5\ years$ of injection, case study Reservoir A, CO_2 injection at $-5°C$ $(268.15K)$.

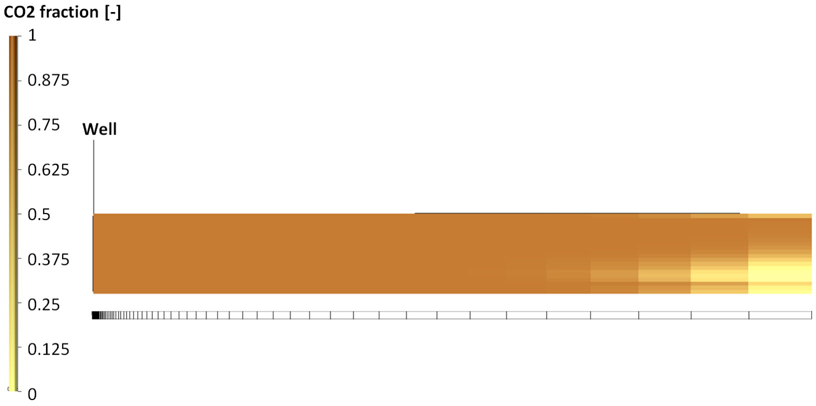

Figure 4.51: 2D plot for CO_2 fraction after $5\ years$ of injection, case study Reservoir A, CO_2 injection at $-5°C$ $(268.15K)$.

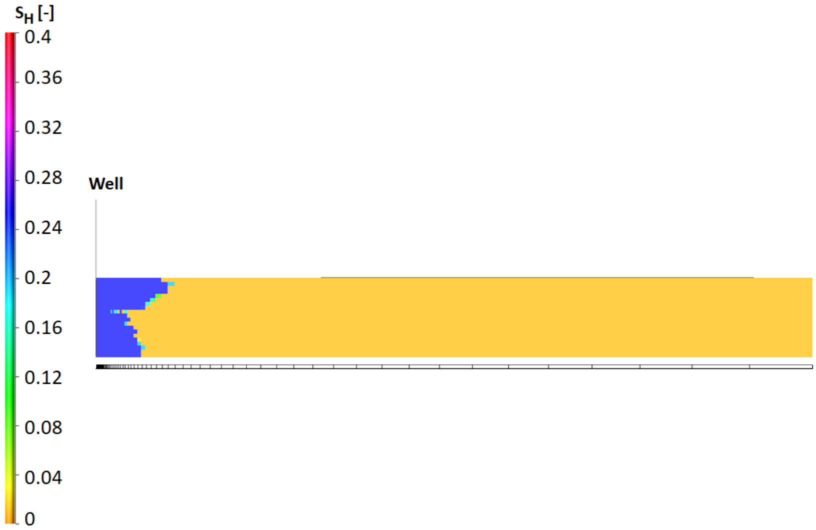

Figure 4.52: 2D plot for hydrate saturation after $5\ years$ of injection, case study Reservoir A, CO_2 injection at $-5°C$ $(268.15K)$.

Figure 4.53: 2D plot for water saturation after $5\ years$ of injection, case study Reservoir A, CO_2 injection at $-5°C$ $(268.15K)$.

Finally, Figure 4.54 displays a visualization of the permeability multiplier distribution throughout the reservoir. Notably, in the region where hydrates have formed, the permeability multiplier approaches zero, indicating that hydrate formation results in nearly a 100% reduction in permeability.

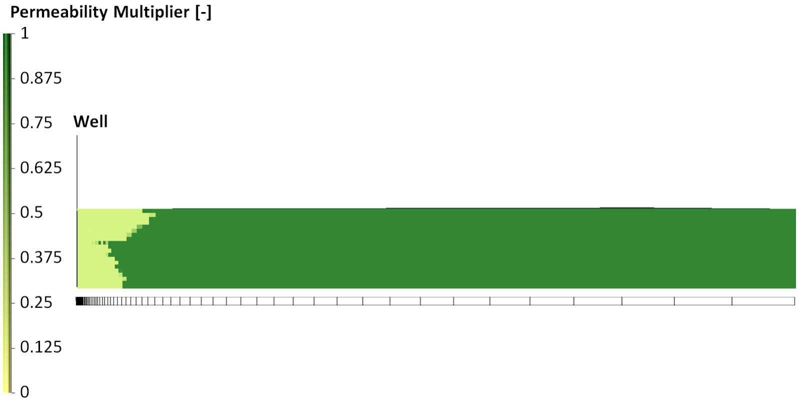

Figure 4.54: 2D plot for permeability multiplier after $5\ years$ of injection, case study Reservoir A, CO_2 injection at $-5°C$ $(268.15K)$.

4.6.1.2. CO_2 Injection at $12°C$

Figures 4.55, 4.56, 4.57, and 4.58 show the profiles for temperature, pressure, CO_2 fraction, and hydrate saturation, respectively, evaluated over different time intervals since the beginning of injection (i.e., $1\ day$, $3\ years$, and $5\ years$) for Reservoir A when injecting CO_2 at $12°C$.

The findings from this case study align with the results of CO_2 injection at $-5°C$, highlighting the preferential movement of CO_2 through the most permeable layer and the slower CO_2 sweep in the least permeable layer. Notably, in this scenario, the injection of CO_2 leads to an increase in pressure, which subsequently reduces the J-T cooling effect and triggers the dissociation of hydrates, as evident in the hydrate saturation profiles. This occurs due to the pressure and temperature conditions moving outside the hydrate stability zone, causing the dissociation of hydrates. As in the case of injection at $-5°C$, a second thermal front can be observed in the most permeable layers in the temperature profiles.

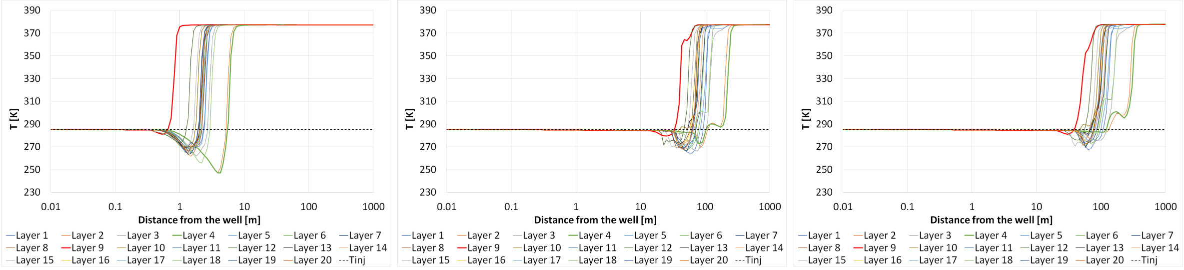

(a) Temperature profile after $1\ day$ of injection.

(b) Temperature profile after $3\ years$ of injection.

(c) Temperature profile after $5\ years$ of injection.

Figure 4.55: Temperature profile, case study Reservoir A, CO_2 injection at $12°C$. The green bold line represents the most permeable layer. The red bold line shows the least permeable layer.

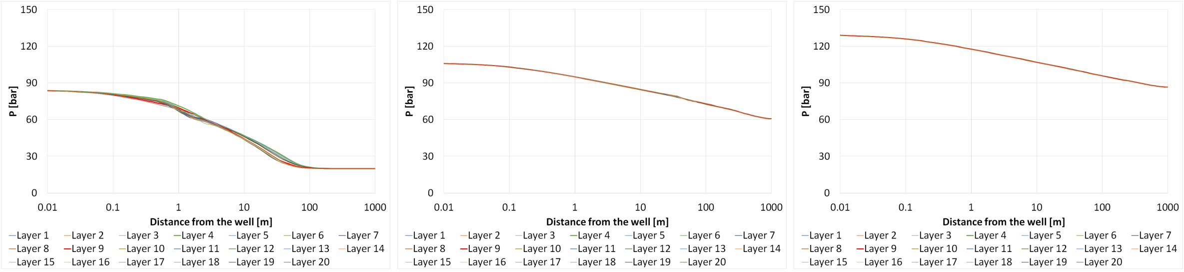

(a) Pressure profile after $1\ day$ of injection.

(b) Pressure profile after $3\ years$ of injection.

(c) Pressure profile after $5\ years$ of injection.

Figure 4.56: Pressure profile, case study Reservoir A, CO_2 injection at $12°C$. The green bold line represents the most permeable layer. The red bold line shows the least permeable layer.

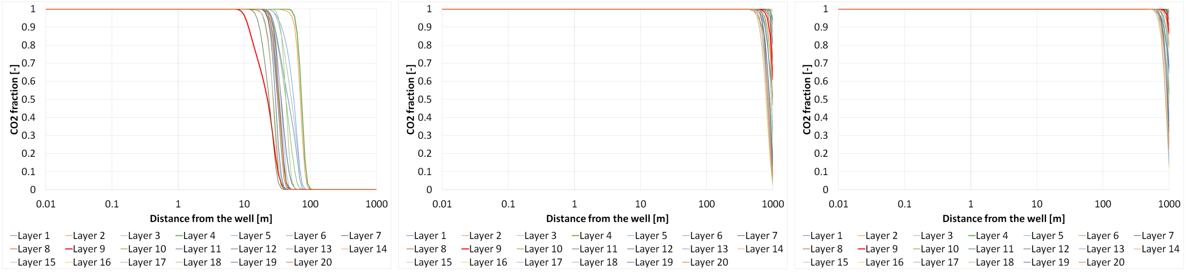

(a) CO_2 fraction profile after $1\ day$ of injection.

(b) CO_2 fraction profile after $3\ years$ of injection.

(c) CO_2 fraction profile after $5\ years$ of injection.

Figure 4.57: CO_2 fraction profile, case study Reservoir A, CO_2 injection at $12°C$. The green bold line represents the most permeable layer. The red bold line shows the least permeable layer.

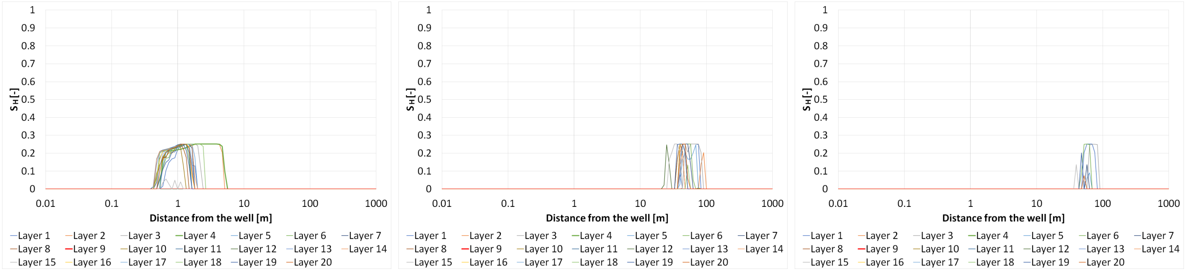

(a) Hydrate saturation profile after $1\ day$ of injection.

(b) Hydrate saturation profile after $3\ years$ of injection.

(c) Hydrate saturation profile after $5\ years$ of injection.

Figure 4.58: Hydrate saturation profile, case study Reservoir A, CO_2 injection at $12°C$. The green bold line represents the most permeable layer. The red bold line shows the least permeable layer.

To offer a more comprehensive perspective on the profiles, figures 4.59, 4.60, 4.61, 4.62, and 4.63 present two-dimensional (2D) representations of the reservoir depicting temperature, pressure, CO_2 fraction, hydrate saturation, and water saturation, respectively, following a 5-year injection period.

The results from this case align with the observations made in the scenario of CO_2 injection at $-5°C$. However, the increase in injection temperature brings about notable differences. First, only a few locations across the reservoir display temperatures below $275K$, and these specific areas experience hydrate formation. Second, the pressure in the near wellbore is lower compared to the case of injection at $-5°C$, primarily due to a smaller amount of hydrates formed in this region, resulting in a relatively lower impact on permeability. The regions exhibiting hydrate formation also demonstrate an almost zero water saturation, a consequence of water consumption during the hydrate formation process.

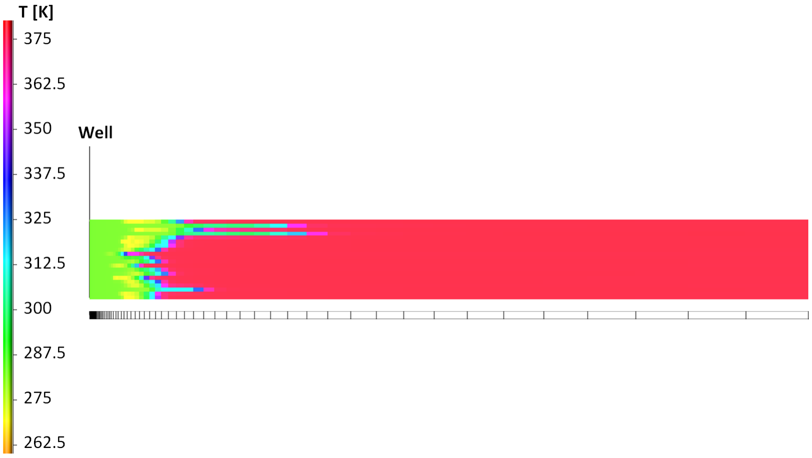

Figure 4.59: 2D plot for temperature after $5\ years$ of injection, case study Reservoir A, CO_2 injection at $12°C$ $(275.15K)$.

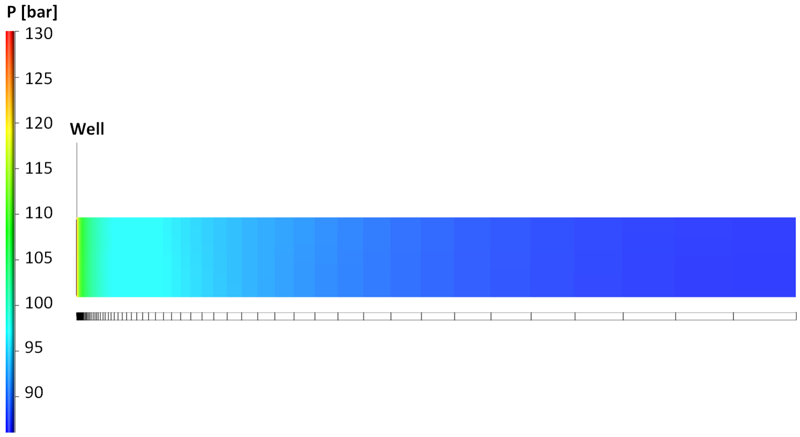

Figure 4.60: 2D plot for pressure after $5\ years$ of injection, case study Reservoir A, CO_2 injection at $12°C$ $(275.15K)$.

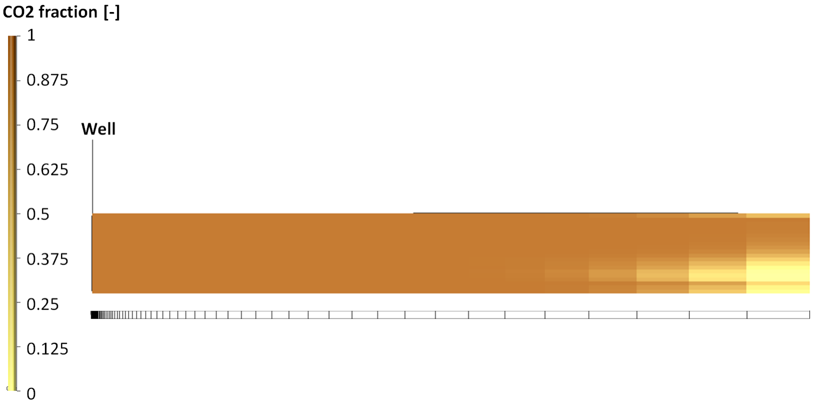

Figure 4.61: 2D plot for CO_2 fraction after $5\ years$ of injection, case study Reservoir A, CO_2 injection at $12°C$ $(275.15K)$.

Figure 4.62: 2D plot for hydrate saturation after $5\ years$ of injection, case study Reservoir A, CO_2 injection at $12°C$ $(275.15K)$.

Figure 4.63: 2D plot for water saturation after $5\ years$ of injection, case study Reservoir A, CO_2 injection at $12°C$ $(275.15K)$.

Lastly, Figure 4.64 presents a visualization of the permeability multiplier distribution across the reservoir. Over the course of the 5-year injection period, the majority of hydrates have dissociated due to the increased reservoir pressure resulting from the injection process. Consequently, only a few layers retain hydrates. In areas with persistent hydrate saturation, the small permeability multiplier indicates a significant reduction in permeability caused by hydrate formation.

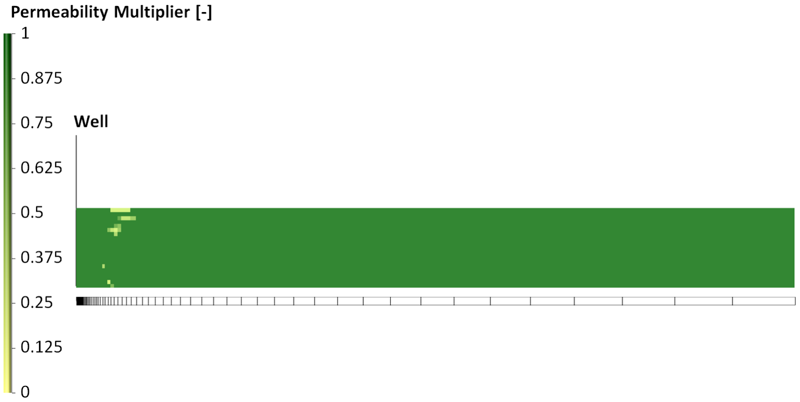

Figure 4.64: 2D plot for permeability multiplier after $5\ years$ of injection, case study Reservoir A, CO_2 injection at $12°C$ $(275.15K)$.

4.6.1.3. BHP Comparison for Reservoir A

A comparison of the injection Bottom Hole Pressure (BHP) is depicted in Figure 4.65. The scenario with CO_2 injection at $12°C$ shows reduced hydrate formation, resulting in a lower BHP. Conversely, the scenario with CO_2 injection at $-5°C$ exhibits higher hydrate formation, leading to a higher BHP as a consequence of the reduction in permeability.

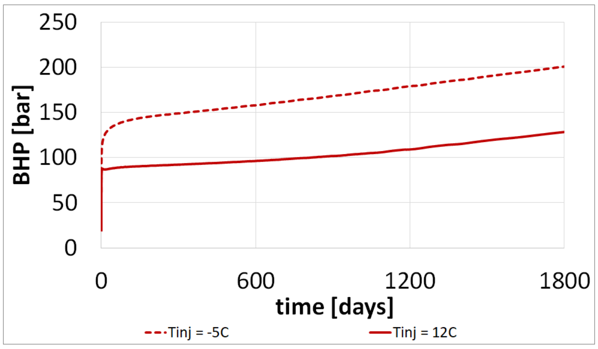

Figure 4.65: BHP comparison for Reservoir A: Cases of CO_2 injection at $-5°C$ versus CO_2 injection at $12°C$.

4.6.2. Reservoir B

Reservoir B is composed of 6 layers, each with specific properties as defined in Table 4.11. The initial conditions and simulation parameters for Reservoir B are provided in Table 4.12.

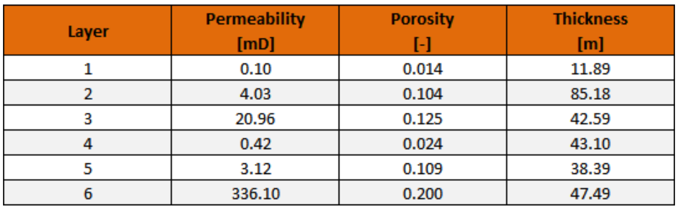

Layer	Permeability [mD]	Porosity [-]	Thickness [m]
1	0.10	0.014	11.89
2	4.03	0.104	85.18
3	20.96	0.125	42.59
4	0.42	0.024	43.10
5	3.12	0.109	38.39
6	336.10	0.200	47.49

Table 4.11: Properties Reservoir B.

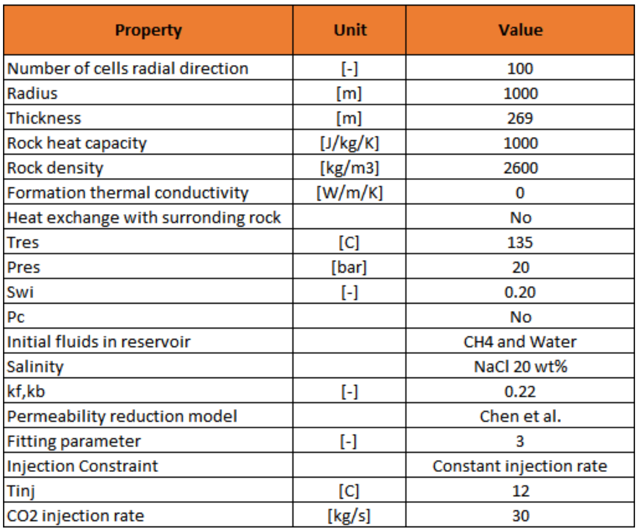

Property	Unit	Value
Number of cells radial direction	[-]	100
Radius	[m]	1000
Thickness	[m]	269
Rock heat capacity	[J/kg/K]	1000
Rock density	[kg/m3]	2600
Formation thermal conductivity	[W/m/K]	0
Heat exchange with surronding rock		No
Tres	[C]	135
Pres	[bar]	20
Swi	[-]	0.20
Pc		No
Initial fluids in reservoir		CH4 and Water
Salinity		NaCl 20 wt%
kf,kb	[-]	0.22
Permeability reduction model		Chen et al.
Fitting parameter	[-]	3
Injection Constraint		Constant injection rate
Tinj	[C]	12
CO2 injection rate	[kg/s]	30

Table 4.12: Initial conditions and simulation parameters for Reservoir B.

Based on the model results, the injection rate was distributed among the layers according to Figure 4.66. In this distribution, layer 6 (the most permeable layer) received the highest injection rate, while layer 1 (the least permeable layer) received the lowest injection rate.

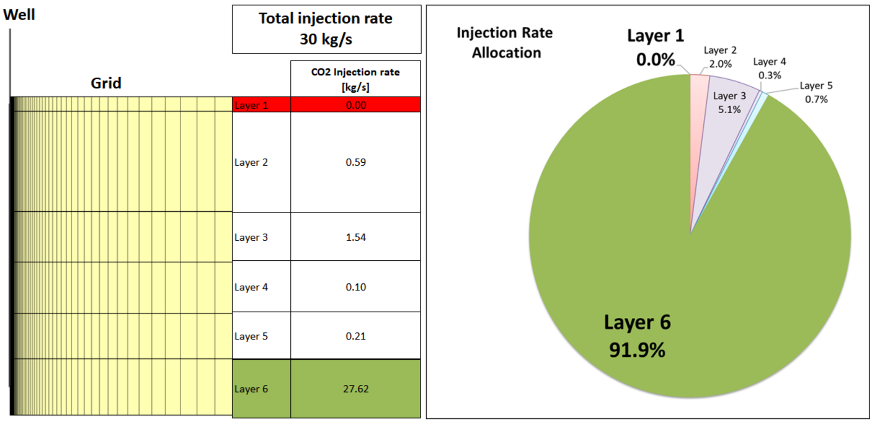

Figure 4.66: Injection rate allocation for Reservoir B.

4.6.2.1. CO_2 Injection at $-5°C$

Figures 4.67, 4.68, 4.69, and 4.70 depict the profiles for temperature, pressure, CO_2 fraction, and hydrate saturation, respectively, evaluated over different time intervals since the start of injection (i.e., $1\ day$, $3\ years$, and $5\ years$) for Reservoir B when injecting CO_2 at $-5°C$.

The results show a demonstrate a notable disparity in the impact of CO_2 sweeping through the different layers based on their permeability. The most permeable layer experiences a rapid and substantial J-T cooling effect compared to the other layers. On the other hand, the least permeable layer encounters CO_2 sweeping last, leading to a milder J-T cooling effect in that layer. The results clearly illustrate the progressive advancement of the thermal front, the rise in pressure, and the movement of the CO_2 front over time. Regarding hydrate saturation, the initial and pronounced J-T cooling effect in the most permeable layer accelerates the formation of hydrates in this specific layer. However, as time passes, hydrate formation is promoted steadily across all layers due to the ongoing injection of CO_2 at a temperature within the hydrate stability zone.

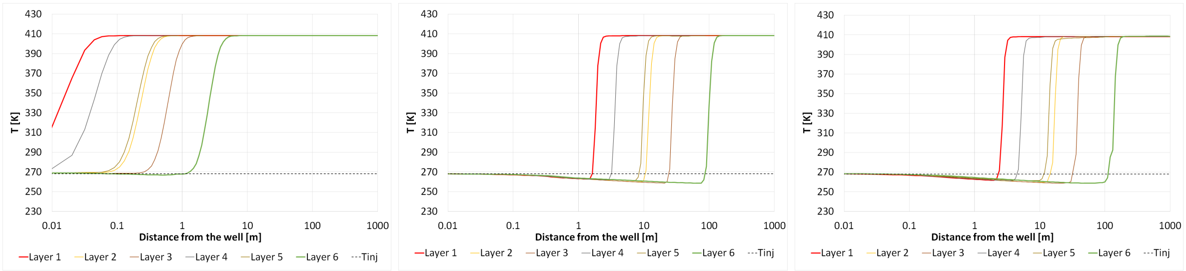

(a) Temperature profile after $1\ day$ of injection.

(b) Temperature profile after $3\ years$ of injection.

(c) Temperature profile after $5\ years$ of injection.

Figure 4.67: Temperature profile, case study Reservoir B, CO_2 injection at $-5°C$. The green bold line represents the most permeable layer. The red bold line shows the least permeable layer.

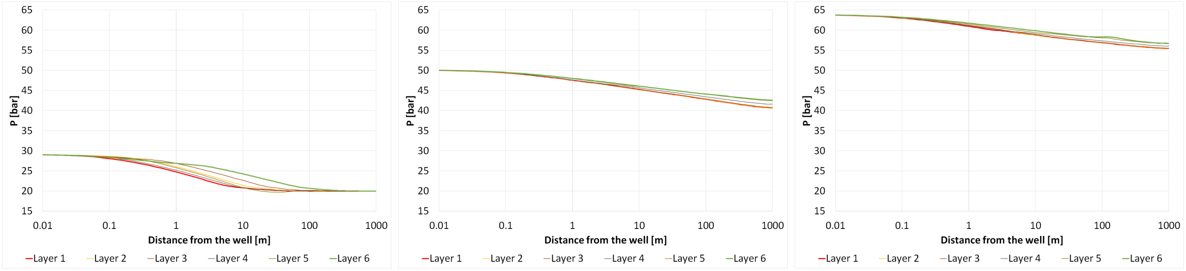

(a) Pressure profile after $1\ day$ of injection. **(b)** Pressure profile after $3\ years$ of injection. **(c)** Pressure profile after $5\ years$ of injection.

Figure 4.68: Pressure profile, case study Reservoir B, CO_2 injection at $-5°C$. The green bold line represents the most permeable layer. The red bold line shows the least permeable layer.

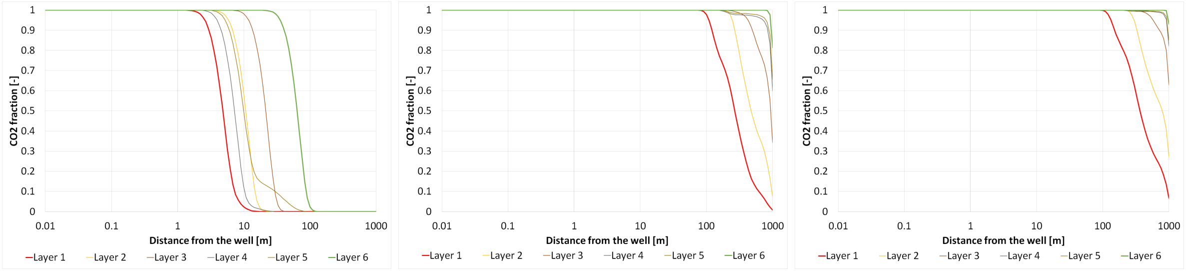

(a) CO_2 fraction profile after $1\ day$ of injection. **(b)** CO_2 fraction profile after $3\ years$ of injection. **(c)** CO_2 fraction profile after $5\ years$ of injection.

Figure 4.69: CO_2 fraction profile, case study Reservoir B, CO_2 injection at $-5°C$. The green bold line represents the most permeable layer. The red bold line shows the least permeable layer.

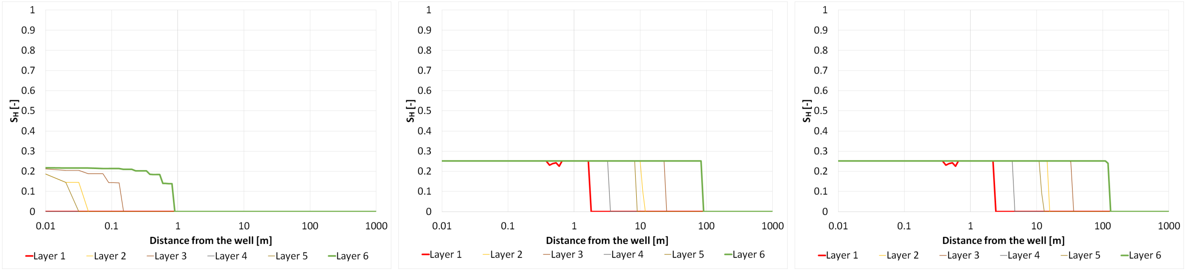

(a) Hydrate saturation profile after $1\ day$ of injection. **(b)** Hydrate saturation profile after $3\ years$ of injection. **(c)** Hydrate saturation profile after $5\ years$ of injection.

Figure 4.70: Hydrate saturation profile, case study Reservoir B, CO_2 injection at $-5°C$. The green bold line represents the most permeable layer. The red bold line shows the least permeable layer.

To gain a better understanding of the profiles after a 5-year injection period, figures 4.71, 4.72, 4.73, 4.74, and 4.75 show two-dimensional (2D) plots of the reservoir, presenting temperature, pressure, CO_2 fraction, hydrate saturation, and water saturation, respectively.

According to the results, after a 5-year injection period, it is observed that the most permeable layers exhibit the lowest temperature due to the more pronounced J-T effect on these layers. As a consequence of the lower temperature, hydrate formation occurs, leading to a reduction in permeability, which increases the pressure in the vicinity of the wellbore area. Moreover, the CO_2 front moves faster through the more permeable layers. In regions where hydrate formation has taken place, the available water has been nearly exhausted.

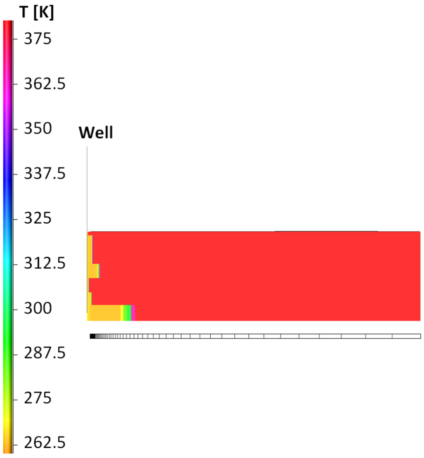

Figure 4.71: 2D plot for temperature after $5\ years$ of injection, case study Reservoir A, CO_2 injection at $-5°C$ $(268.15K)$.

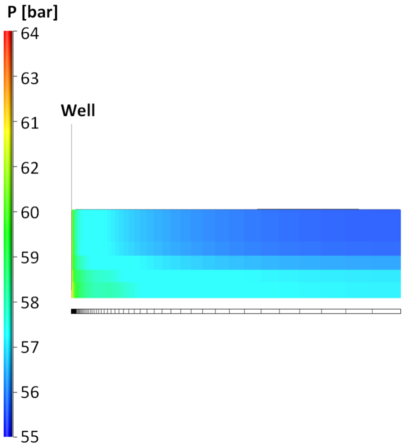

Figure 4.72: 2D plot for pressure after $5\ years$ of injection, case study Reservoir A, CO_2 injection at $-5°C$ $(268.15K)$.

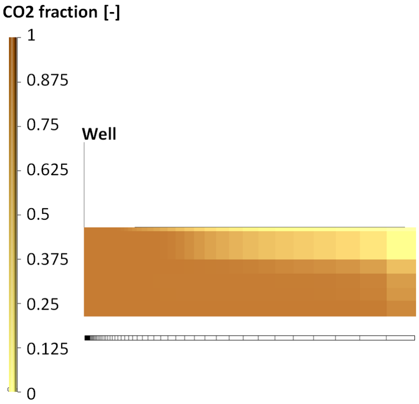

Figure 4.73: 2D plot for CO_2 fraction after $5\ years$ of injection, case study Reservoir A, CO_2 injection at $-5°C$ $(268.15K)$.

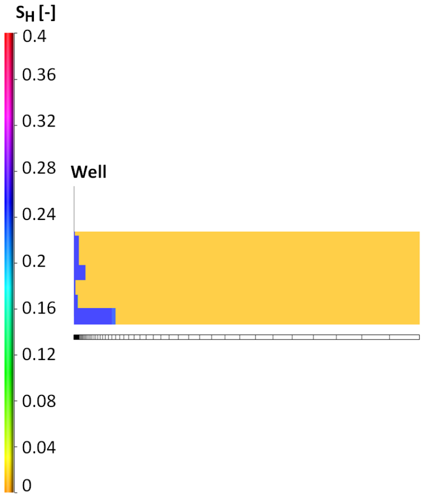

Figure 4.74: 2D plot for hydrate saturation after $5\ years$ of injection, case study Reservoir A, CO_2 injection at $-5°C$ $(268.15K)$.

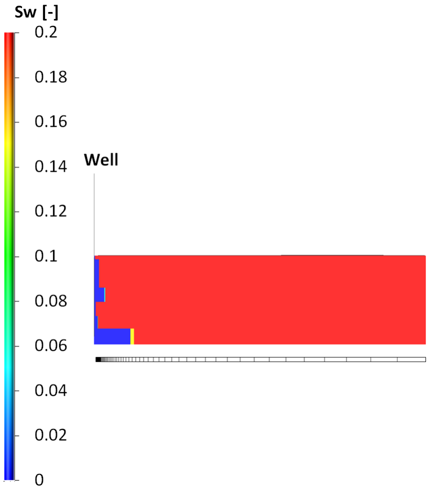

Figure 4.75: 2D plot for water saturation after $5\ years$ of injection, case study Reservoir A, CO_2 injection at $-5°C$ $(268.15K)$.

Finally, Figure 4.76 displays a visualization of the permeability multiplier distribution throughout the reservoir. Notably, in the region where hydrates have formed, the permeability multiplier approaches zero, indicating that hydrate formation results in nearly a 100% reduction in permeability.

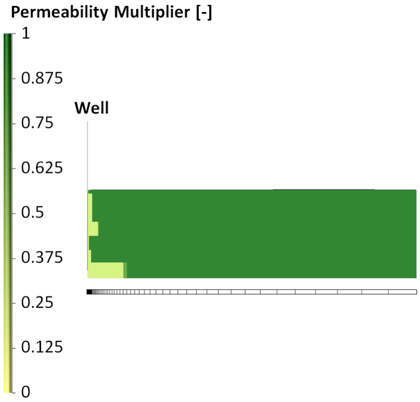

Figure 4.76: 2D plot for permeability multiplier after $5\ years$ of injection, case study Reservoir A, CO_2 injection at $-5°C$ $(268.15K)$.

4.6.2.2. CO_2 Injection at $12°C$

Figures 4.77, 4.78, 4.79, and 4.80 illustrate the profiles for temperature, pressure, CO_2 fraction, and hydrate saturation, respectively, evaluated over different time intervals since the start of injection (i.e., $1\ day$, $3\ years$, and $5\ years$) for Reservoir B when injecting CO_2 at $12°C$.

The findings demonstrate distinct variations in the movement of the thermal and CO_2 fronts within the layers, influenced by their permeability. The results provide a clear visualization of the gradual progression of the thermal front, the increase in pressure, and the advancement of the CO_2 front over time.

Due to the relatively mild J-T cooling effect observed over time, no hydrate saturation is detected in any of the layers. This absence of hydrate formation is attributed to the pressure and temperature conditions in the reservoir not reaching the hydrate stability zone over the injection time.

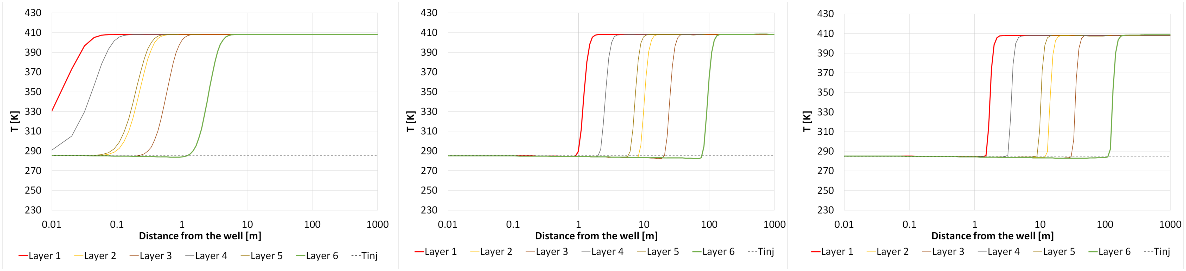

(a) Temperature profile after $1\ day$ of injection.

(b) Temperature profile after $3\ years$ of injection.

(c) Temperature profile after $5\ years$ of injection.

Figure 4.77: Temperature profile, case study Reservoir B, CO_2 injection at $12°C$. The green bold line represents the most permeable layer. The red bold line shows the least permeable layer.

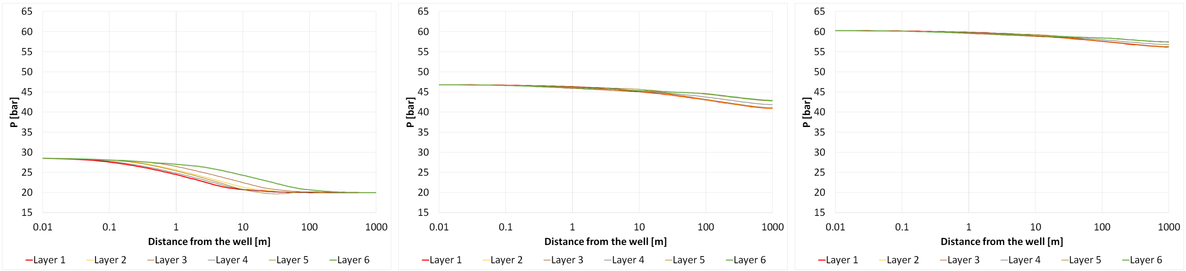

(a) Pressure profile after $1\ day$ of injection.

(b) Pressure profile after $3\ years$ of injection.

(c) Pressure profile after $5\ years$ of injection.

Figure 4.78: Pressure profile, case study Reservoir B, CO_2 injection at $12°C$. The green bold line represents the most permeable layer. The red bold line shows the least permeable layer.

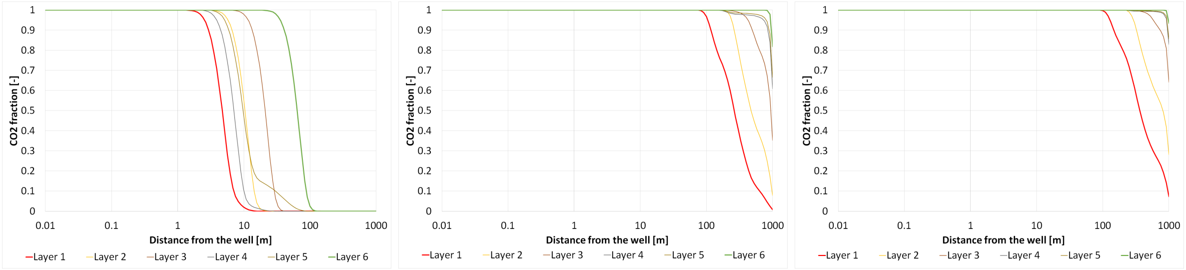

(a) CO_2 fraction profile after $1\ day$ of injection. **(b)** CO_2 fraction profile after $3\ years$ of injection. **(c)** CO_2 fraction profile after $5\ years$ of injection.

Figure 4.79: CO_2 fraction profile, case study Reservoir B, CO_2 injection at $12°C$. The green bold line represents the most permeable layer. The red bold line shows the least permeable layer.

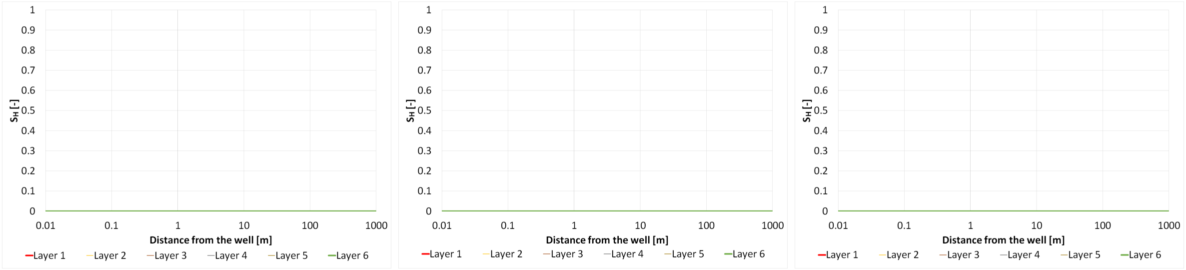

(a) Hydrate saturation profile after $1\ day$ of injection. **(b)** Hydrate saturation profile after $3\ years$ of injection. **(c)** Hydrate saturation profile after $5\ years$ of injection.

Figure 4.80: Hydrate saturation profile, case study Reservoir B, CO_2 injection at $12°C$. The green bold line represents the most permeable layer. The red bold line shows the least permeable layer.

4.6.2.3. BHP Comparison for Reservoir B

A comparison of the injection Bottom Hole Pressure (BHP) is depicted in Figure 4.81. The scenario with CO_2 injection at $12°C$ did not show hydrate formation, resulting in a lower BHP. Conversely, the scenario with CO_2 injection at $-5°C$ exhibits hydrate formation, which results in a reduction in the permeability of the reservoir leading to a higher BHP.

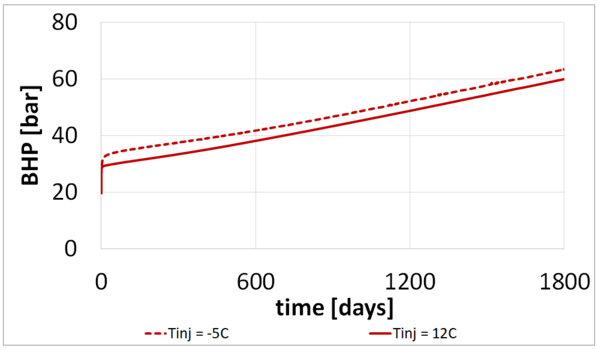

Figure 4.81: BHP comparison for Reservoir B: Cases of CO_2 injection at $-5°C$ versus CO_2 injection at $12°C$.

4.7. Hydrate Formation Prevention Strategy

In the preceding sections, a comprehensive study on the influence of various variables, such as injection rate and temperature, was presented and analyzed. The investigation revealed that the most effective approach for reducing hydrate formation in the reservoir involves injecting CO_2 at $20°C$. However, due to potential cost considerations associated with continuous CO_2 injection at this temperature, this section introduces an alternative prevention strategy based on a cyclic process of yearly alternating cold and warm CO_2 injection. This alternative can help to prevent hydrate formation for injection of CO_2 in depleted gas reservoirs.

4.7.1. Alternating Cold-Warm CO_2 Injection

To explore potential solutions for preventing hydrate formation in the reservoir, a case of yearly alternating cold and warm CO_2 injection was studied. Figure 4.82 presents the profiles for temperature, pressure, and CO_2 fraction, evaluated over different time intervals from the injection start (i.e., $1\ day$, $1\ month$, $1\ year$, and $5\ years$). The results indicate that the only significant variation observed over time was in the pressure profile after 5 years of injection.

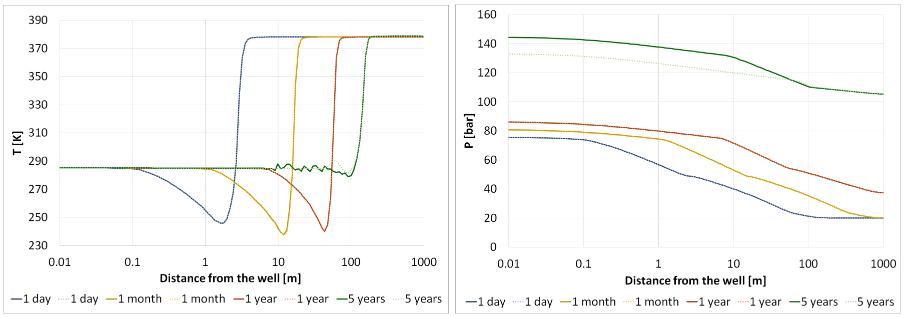

(a) Temperature profile.

(b) Pressure profile.

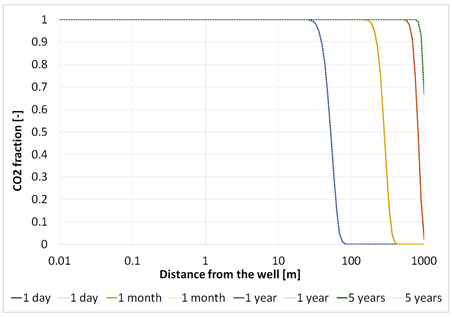

(c) CO_2 fraction profile.

Figure 4.82: Sensitivity analysis of empirical model results considering alternating cold $(12°C)$ warm $(24°C)$ CO_2 injection. The solid lines correspond to the case of CO_2 injection at $12°C$. The dashed lines represent the case of alternating cold $(12°C)$ and warm $(24°C)$ CO_2 injection.

Figure 4.83 presents the hydrate saturation profile over different time intervals since the beginning of injection (i.e., $1\ day$, $1\ month$, $1\ year$, and $5\ years$). Initially, the results exhibit no significant variation compared to the case of cold CO_2 injection. However, after 5 years of implementing the cyclic process of alternating cold and warm CO_2 injection, the hydrate saturation becomes more localized along the total length. This localization is advantageous as it helps preserve injectivity over time, making the alternating injection strategy beneficial for long-term operations.

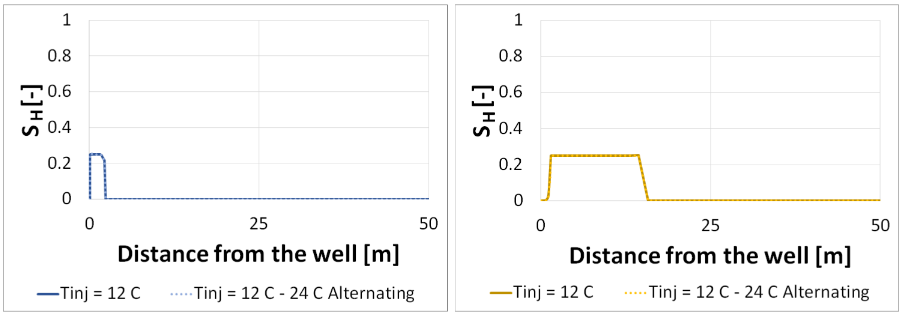

(a) Hydrate saturation profile after $1\ day$ of injection.

(b) Hydrate saturation profile after $1\ month$ of injection.

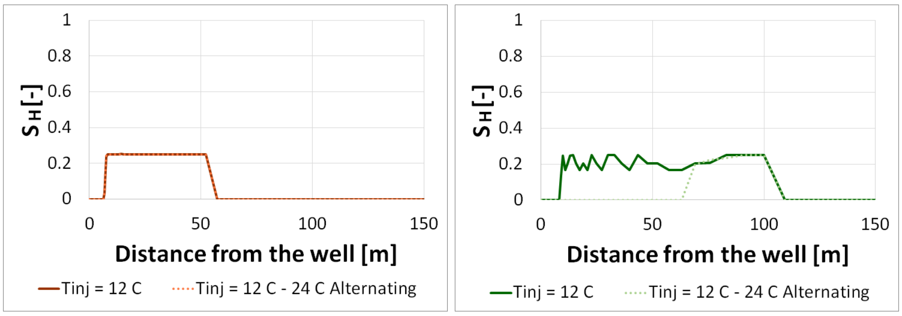

(c) Hydrate saturation profile after $1\ year$ of injection.

(d) Hydrate saturation profile after $5\ years$ of injection.

Figure 4.83: Sensitivity analysis of empirical model results for hydrate saturation considering alternating cold $(12°C)$ warm $(24°C)$ CO_2 injection.

Finally, Figure 4.84 illustrates a comparison of the injection Bottom Hole Pressure (BHP). The results demonstrate that by implementing a cyclic process of alternating cold and warm CO_2 injection, a reduction in the BHP can be achieved.

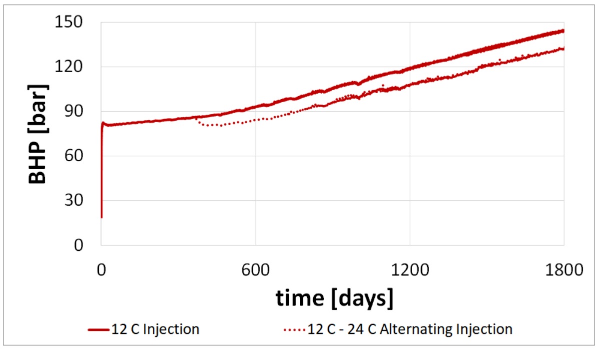

Figure 4.84: BHP comparison: Cold $(12°C)$ CO_2 injection versus cold $(12°C)$ warm $(24°C)$ alternating CO_2 injection.

5

History Matching

History matching is the process of adjusting key properties of a reservoir model to match the actual historic data (Okotie & Ikporo, 2019). This process is a crucial step to validate and enhance the model's accuracy and reliability for forecasting and decision-making. It also helps to understand and identify weaknesses of the available data and the model. Usually, after historic data has been successfully history matched, the model can be used to model future reservoir behavior with increased certainty (Schlumberger, n.d.).

Usually, history matching is a continuous and iterative process, which involves successive adjustments to the model. After each modification, a new prediction is made and its results are analyzed to see how the changed parameter affected the forecast and how accurate the outcomes were when compared to actual data. Through this iterative approach, the model is gradually improved, reducing discrepancies between the model results and the real data.

This chapter focuses on the history matching process for three experiments that were analyzed in Chapter 3, using the empirical model developed in Chapter 4. The objective of this history matching exercise is to validate the accuracy and reliability of the empirical model while also gaining insights into its limitations.

This chapter starts with an introduction to the model used for the history match, followed by a detailed description of the history matching process for three distinct experiments. Each history match will be described in detail, highlighting the specific adjustments made to the model to align it with the experimental data. The validation of the model through this process will ensure its suitability for future applications on CCS projects.

5.1. Model Description

The empirical model was carefully adjusted to accurately represent the experimental conditions conducted in the laboratory. To achieve this, a Cartesian grid was employed, and the volume was appropriately scaled to replicate the same PV of the core used in the experiments. The model properties and simulation parameters utilized for the history matching of the experiments are outlined in Table 5.1.

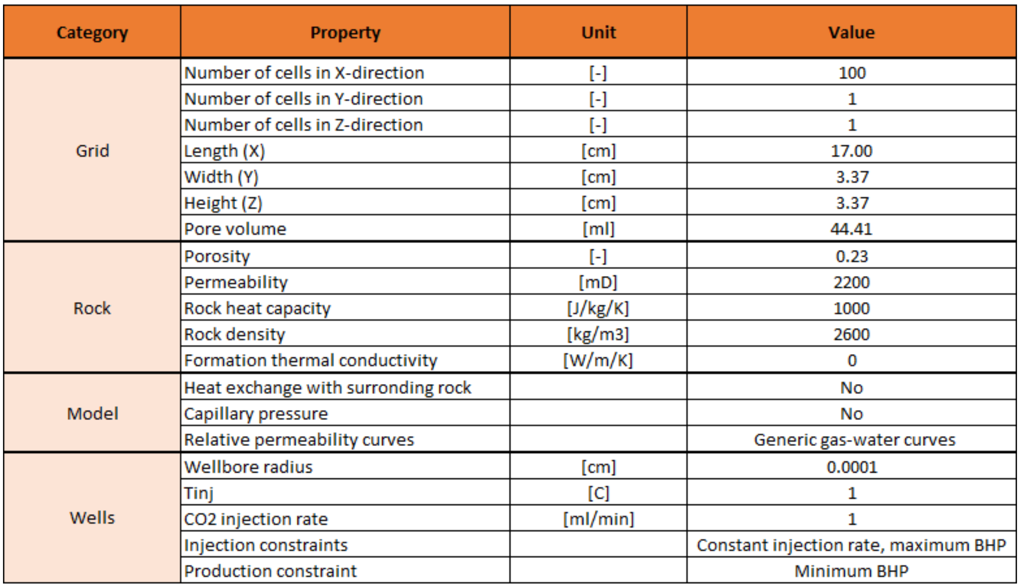

Category	Property	Unit	Value
Grid	Number of cells in X-direction	[-]	100
	Number of cells in Y-direction	[-]	1
	Number of cells in Z-direction	[-]	1
	Length (X)	[cm]	17.00
	Width (Y)	[cm]	3.37
	Height (Z)	[cm]	3.37
	Pore volume	[ml]	44.41
Rock	Porosity	[-]	0.23
	Permeability	[mD]	2200
	Rock heat capacity	[J/kg/K]	1000
	Rock density	[kg/m3]	2600
	Formation thermal conductivity	[W/m/K]	0
Model	Heat exchange with surronding rock		No
	Capillary pressure		No
	Relative permeability curves		Generic gas-water curves
Wells	Wellbore radius	[cm]	0.0001
	Tinj	[C]	1
	CO2 injection rate	[ml/min]	1
	Injection constraints		Constant injection rate, maximum BHP
	Production constraint		Minimum BHP

Table 5.1: Model properties and simulation parameters for history matching experimental data.

As per the laboratory setup, the core featured an inlet and outlet points, which were accurately replicated in the model by positioning two wells, one injector representing the inlet and one producer for the outlet. Figure 5.1 illustrates the placement of the wells in the grid.

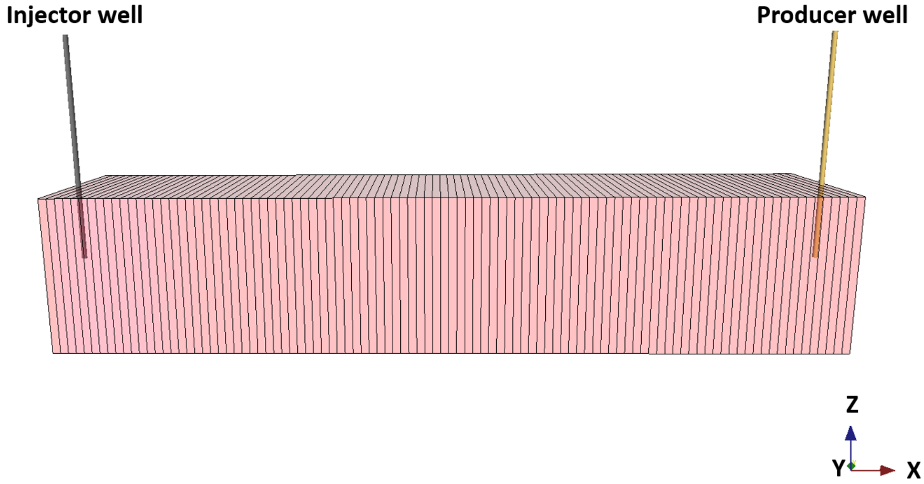

Figure 5.1: Grid and wells locations.

5.2. History Match Process

The experiments chosen for history matching were 16, 17, and 18. This selection was based on the criterion of having an initial water saturation of less than 50%, which is a realistic approach considering the objective of injecting CO_2 into a depleted gas reservoir.

It is crucial to note that the history matching process was focused only on the first cycle of CO_2 injection for each experiment. Three parameters were subject to adjustment during the history match process: the relative permeability curves, the reaction rate coefficients and the constant for the permeability reduction model. Regarding the relative permeability curves, the generic gas-water curves were replaced for CO_2-water curves obtained from a core flooding experiment conducted in a Bentheimer core (Eftekhari & Farajzadeh, 2017). The specific values used are detailed in Table 5.2.

Water			Gas (CO2)		
Swc [-]	Krw [-]	nw [-]	Sgr [-]	Krg [-]	ng [-]
0.05	0.720	4.423	0.03	0.587	0.938

Table 5.2: Corey parameters for the relative permeability model of a CO_2-water system, from (Eftekhari & Farajzadeh, 2017).

5.2.1. Experiment No. 16

The initial conditions for experiment No. 16 are defined in Table 5.3.

Property	Unit	Value
Tres	[C]	1.0
Pres	[bar]	30.3
Swi	[-]	0.258
Initial fluids in core		CH4 and Water
Salinity		NaCl 1 wt%

Table 5.3: Initial conditions experiment No. 16.

For experiment No. 16, five cases were conducted to get a match with the experimental data. The parameters used for each case are detailed in Table 5.4. The history match results are depicted in Figure 5.2. Based on the results, case 5 was identified as the best fit for the experimental data.

Case	Relative Permeability Curves	kf,kb	Permeability Reduction Model	Constant for Permeability Reduction Model
1	Generic gas-water curves	0.22	Pang-Sharma	12000.0
2	CO2-water curves	0.22	Pang-Sharma	12000.0
3	CO2-water curves	0.22	Pang-Sharma	13000.0
4	CO2-water curves	8.00	Chen et al.	26.5
5	CO2-water curves	0.04	Pang-Sharma	19000.0

Table 5.4: Cases evaluated for history match of experiment No. 16.

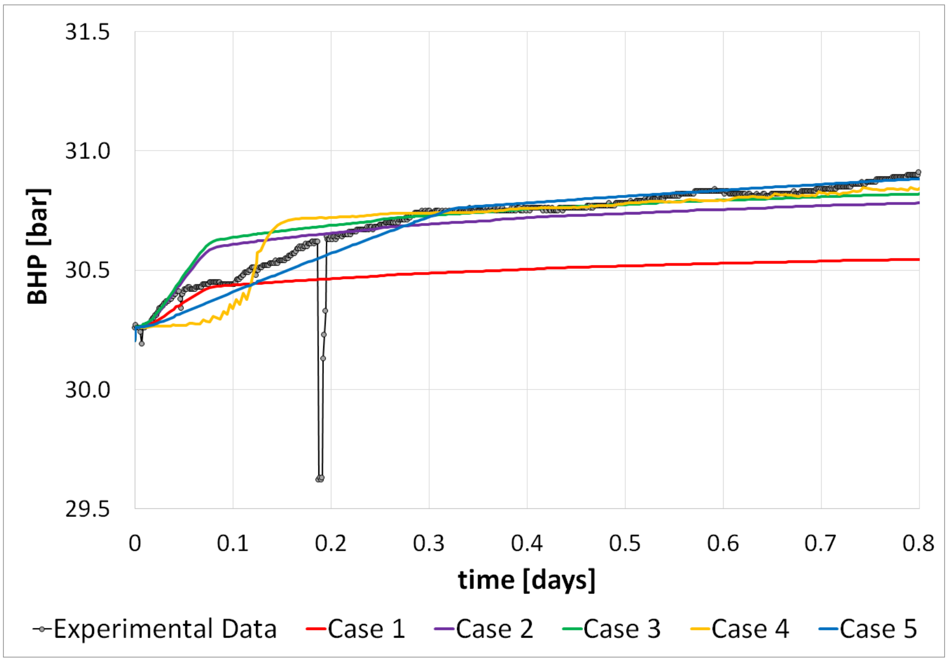

Figure 5.2: History match results for experiment No. 16.

5.2.2. Experiment No. 17

The initial conditions for experiment No. 17 are defined in Table 5.5.

Property	Unit	Value
Tres	[C]	1.0
Pres	[bar]	29.5
Swi	[-]	0.35
Initial fluids in core		CH4 and Water
Salinity		NaCl 1 wt%

Table 5.5: Initial conditions experiment No. 17.

For experiment No. 17, four cases were executed to achieve a match with the experimental data. The parameters employed for each case are outlined in Table 5.6. The history match results are illustrated in Figure 5.3. Based on the outcomes, case 4 was determined to be the best fit for the experimental data.

Case	Relative Permeability Curves	kf,kb	Permeability Reduction Model	Constant for Permeability Reduction Model
1	Generic gas-water curves	0.220	Pang-Sharma	13000.0
2	CO2-water curves	0.220	Pang-Sharma	13000.0
3	CO2-water curves	9.900	Chen et al.	20.5
4	CO2-water curves	0.045	Pang-Sharma	26000.0

Table 5.6: Cases evaluated for history match of experiment No. 17.

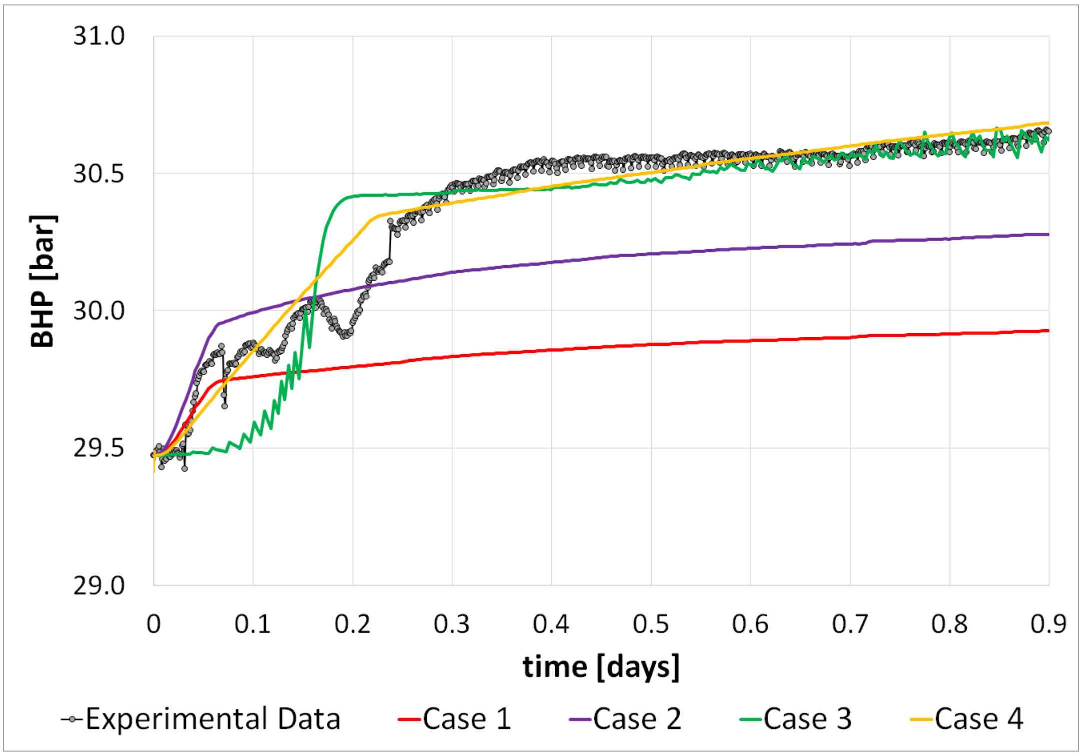

Figure 5.3: History match results for experiment No. 17.

5.2.3. Experiment No. 18

The initial conditions for experiment No. 18 are defined in Table 5.7.

Property	Unit	Value
Tres	[C]	1.0
Pres	[bar]	29.5
Swi	[-]	0.30
Initial fluids in core		CH4 and Water
Salinity		NaCl 1 wt%

Table 5.7: Initial conditions experiment No. 18.

For experiment No. 18, three cases were carried out to achieve a match with the experimental data. The parameters utilized for each case are provided in Table 5.8. The history match results are shown in Figure 5.4. From the outcomes, case 3 was found to be the best fit for the experimental data.

Case	Relative Permeability Curves	kf,kb	Permeability Reduction Model	Constant for Permeability Reduction Model
1	Generic gas-water curves	0.040	Pang-Sharma	19000.0
2	CO2-water curves	0.013	Pang-Sharma	48000.0
3	CO2-water curves	0.400	Chen et al.	26.0

Table 5.8: Cases evaluated for history match of experiment No. 18.

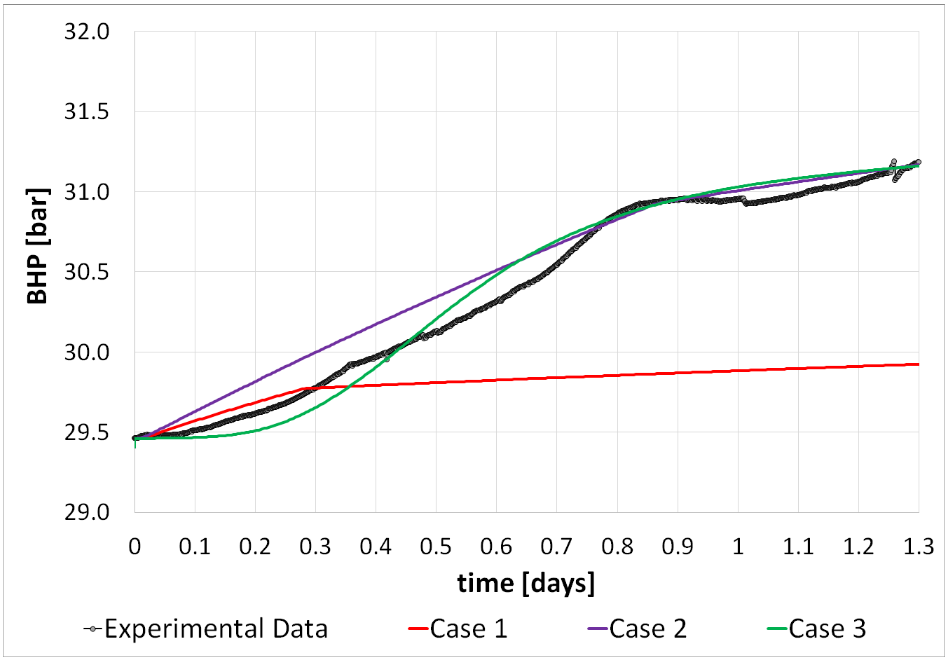

Figure 5.4: History match results for experiment No. 18.

5.3. History Match Review

To ensure that the history match aligns with the experimental conditions, profiles of temperature, pressure, water saturation, and hydrate saturation were carefully analyzed. Based on this analysis, modifications were made to represent laboratory conditions more accurately. This section will present a description of the specific adjustments made the final history match results for each experiment.

5.3.1. Experiment No. 16

Figure 5.7 presents profiles of temperature, pressure, water saturation, and hydrate saturation at different times since the start of the injection (i.e., $0.05\ day$, $0.1\ day$, $0.45\ day$, and $0.8\ day$) for experiment No. 16, based on the selected case after history match. The results indicate that the temperature increases by approximately $6K$ over time throughout the core, except for the first $2\ cm$. As time progresses, the pressure also rises, with the first $2\ cm$ showing a higher pressure due to a greater amount of hydrate formation in that region.

Over time, the water saturation decreases due to water consumption during the hydrate formation process. While hydrates are primarily formed in the inlet section, the entire core exhibits a hydrate saturation of 5%. The temperature increase prevents additional hydrate formation from occurring beyond $0.02\ cm$ along the core. This is because the rising temperature pushes the core's conditions to the boundary of the hydrate stability zone, as illustrated in Figure 5.6. As a result, the conditions in the region between $0.02 - 0.17\ cm$ are no longer conducive to sustaining hydrate formation.

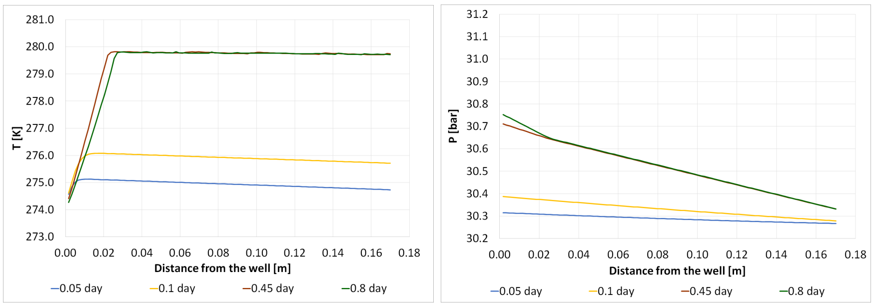

(a) Temperature profile.

(b) Pressure profile.

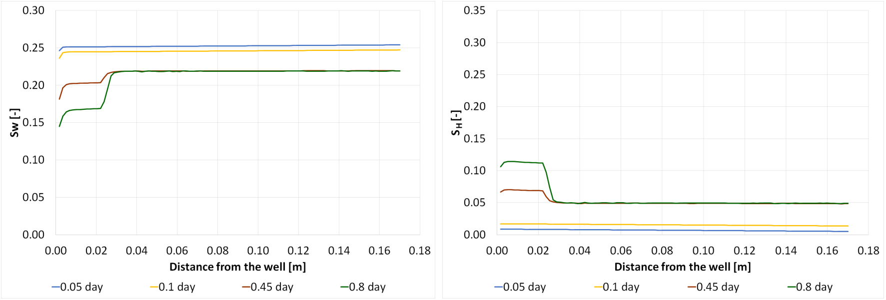

(c) Water saturation profile.

(d) Hydrate saturation profile.

Figure 5.5: Experiment No. 16: Results for case selected from history match process.

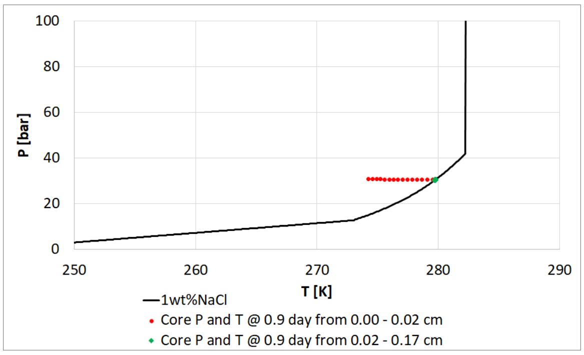

Figure 5.6: $P - T$ diagram for results of experiment No. 16 at $0.8\ day$ for case selected from history match process.

Considering that the temperature increase was not detected by the temperature sensors placed at the core's inlet and outlet, a revision of the hydrates' enthalpy definition was undertaken. The HydraFlash enthalpy values were replaced with a simpler definition, where the enthalpy of hydrates is computed as the product of their heat capacity and temperature. Subsequently, all the profiles were reconstructed using this modified enthalpy definition for the same time instances (Figure 5.7). This analysis was performed to assess whether the results are now more representative of the actual laboratory conditions. Based on the revised profiles, the temperature remains nearly constant along the core, as expected. The pressure shows a gradual increase over time due to the progressive formation of hydrates, resulting in a reduction of water saturation. The enthalpy adjustment contributes to a better match between the model and actual laboratory conditions, enhancing the reliability of the simulation results.

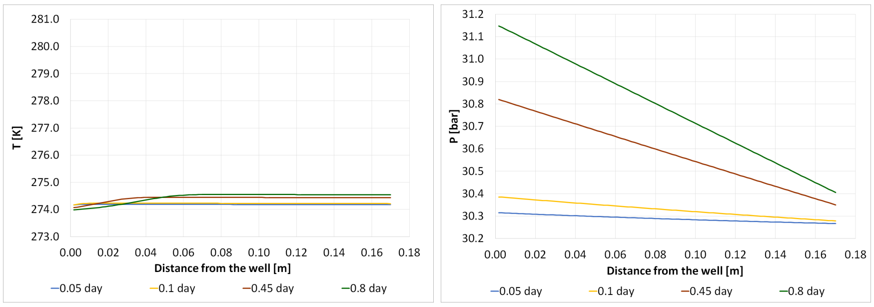

(a) Temperature profile. **(b)** Pressure profile.

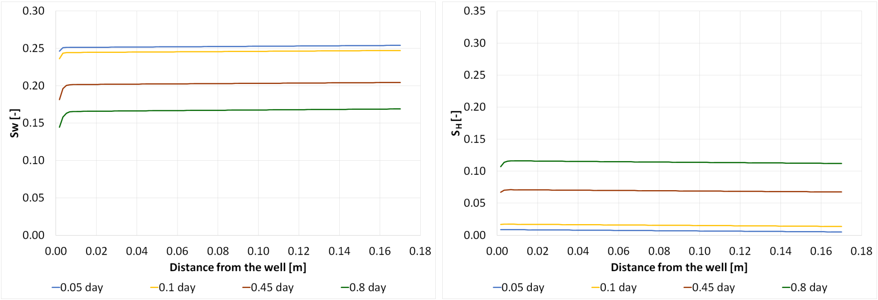

(c) Water saturation profile. **(d)** Hydrate saturation profile.

Figure 5.7: Experiment No. 16: Results for case selected from history match process after modifying hydrate enthalpy definition.

After updating the enthalpy definition as depicted in Figure 5.8, a new round of history matching was conducted. Case A, which corresponded to the case selected previous enthalpy definition change, no longer aligned with the experimental data. Consequently, several additional cases were evaluated until Case I was identified as the most suitable fit for the experimental results. The parameters from Case I are detailed in Table 5.9.

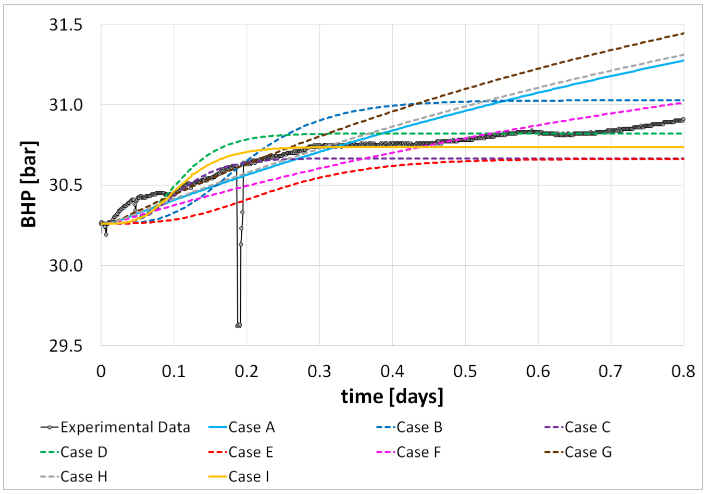

Figure 5.8: History match results after enthalpy adjustment for experiment No. 16.

Case	Relative Permeability Curves	kf,kb	Permeability Reduction Model	Constant for Permeability Reduction Model
I	CO2-water curves	2.00	Chen et al.	20.5

Table 5.9: Parameters of the final case selected for experiment No. 16.

Figure 5.9 presents the final profiles of temperature, pressure, water saturation, and hydrate saturation at different times since the start of the injection (i.e., $0.05\ day$, $0.1\ day$, $0.45\ day$, and $0.8\ day$) for experiment No. 16, based on the selected case after history match. Based on the results, there is an almost two-degree increase in temperature over time, which can be attributed to the exothermic nature of hydrate formation. As time progresses, pressure gradually rises due to the ongoing hydrate formation, initially higher near the inlet but later occurring throughout the entire core. The water saturation decreases as hydrates form over time, eventually reaching levels of zero after $0.8\ day$.

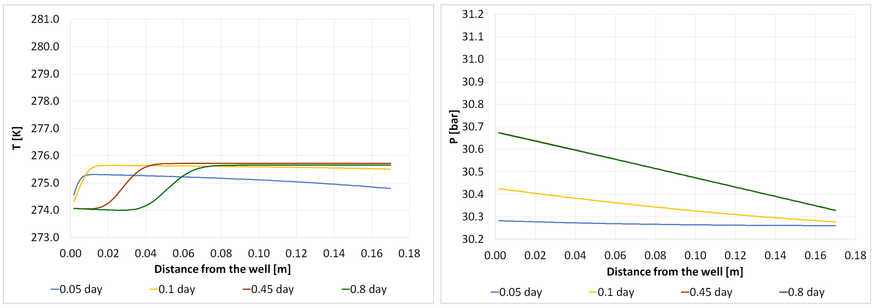

(a) Temperature profile. **(b)** Pressure profile.

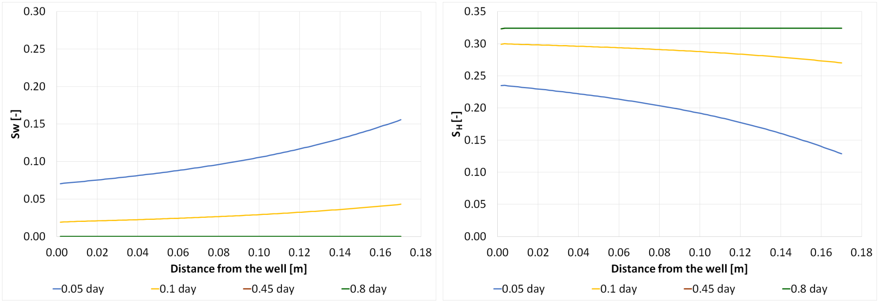

(c) Water saturation profile. **(d)** Hydrate saturation profile.

Figure 5.9: Experiment No. 16: Final results for case selected from history match process.

Table 5.10 displays the reduction in permeability resulting from hydrate formation, based on the selected case after history match for experiment No. 16. According to the permeability reduction model used, it is observed that the permeability decreases by nearly 100%, due to the high hydrate saturation levels, which reach values of approximately 35%. The significant decrease in permeability accounts for the observed rise in BHP from Figure 5.8.

Initial Permeability [mD]	Permeability after Hydrate Formation [mD]	Permeability reduction
2200	1.9	-99.91%

Table 5.10: Permeability reduction according to model results from experiment No. 16.

5.3.2. Experiment No. 17

Experiment No. 17 underwent a similar revision as Experiment No. 16, involving a careful review of the pressure, temperature, water saturation, and hydrate saturation profiles. An adjustment to the enthalpy definition was also necessary, followed by repeating the history matching process. The results are presented in Figure 5.10. Nevertheless, Case A, which represented the case selected before the enthalpy definition change, no longer matched the experimental data. As a result, multiple additional cases were evaluated to find the best fit, ultimately leading to the selection of Case F as the most appropriate representation of experimental data. The specific parameters used in Case F are detailed in Table 5.11.

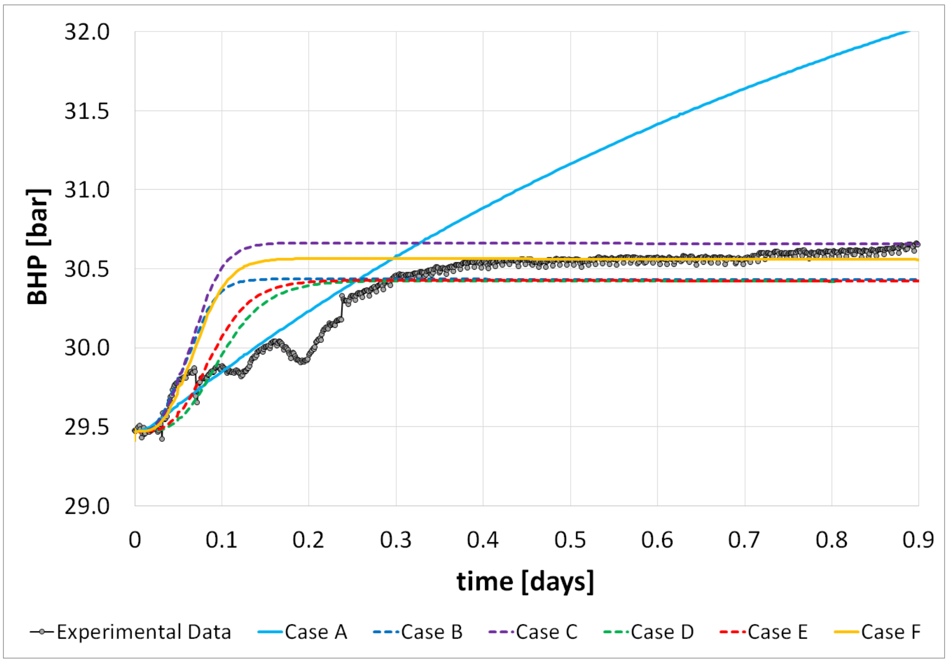

Figure 5.10: History match results after enthalpy adjustment for experiment No. 17.

Case	Relative Permeability Curves	kf,kb	Permeability Reduction Model	Constant for Permeability Reduction Model
F	CO2-water curves	4.50	Chen et al.	16.3

Table 5.11: Parameters of the final case selected for experiment No. 17.

Figure 5.11 presents the final profiles of temperature, pressure, water saturation, and hydrate saturation at different times since the start of the injection (i.e., $0.05\ day$, $0.1\ day$, $0.3\ day$, and $0.9\ day$) for experiment No. 17, based on the selected case after history match. According to the results, over the course of the injection, there is an approximately two-degree rise in temperature. As injection time advances, pressure steadily climbs due to the continuous development of hydrates, initially higher in proximity to the inlet but subsequently occurring throughout the entire core. The water saturation diminishes progressively as hydrates are formed, ultimately reaching zero levels after a period of $0.9\ day$.

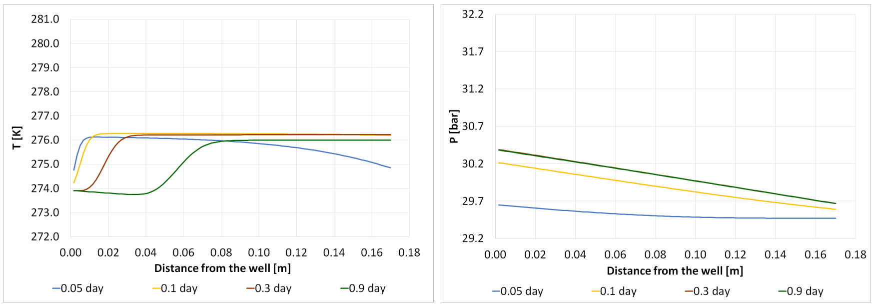

(a) Temperature profile. **(b)** Pressure profile.

Figure 5.11: Experiment No. 17: Final results for case selected from history match process.

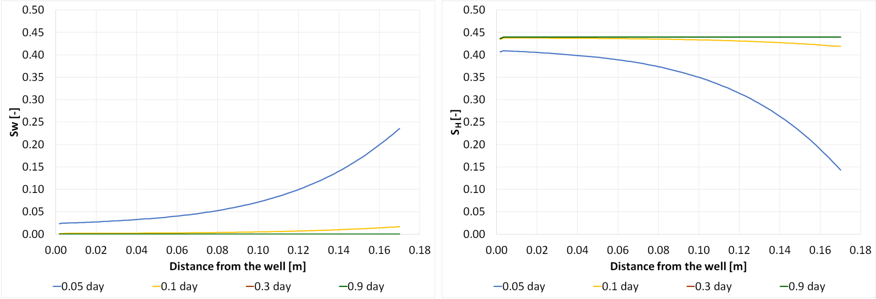

(c) Water saturation profile.

(d) Hydrate saturation profile.

Figure 5.11: Experiment No. 17: Final results for case selected from history match process (cont.).

Table 5.12 illustrates the decrease in permeability caused by hydrate formation, as determined from the selected case after history match for experiment No. 17. Utilizing the permeability reduction model, it becomes evident that the permeability experiences a near-complete reduction of almost 100%, attributable to the high levels of hydrate saturation, which reach approximately 45%. This substantial reduction in permeability explains the observed increase in BHP from Figure 5.10.

Initial Permeability [mD]	Permeability after Hydrate Formation [mD]	Permeability reduction
2200	0.9	-99.96%

Table 5.12: Permeability reduction according to model results from experiment No. 17.

5.3.3. Experiment No. 18

Similar to the preceding experiments, a thorough review of the temperature, pressure, water saturation, and hydrate saturation profiles was performed for experiment No. 18. An adjustment to the enthalpy definition was necessary, leading to the repetition of the history match process, as illustrated in Figure 5.12. Case A denotes the initial case chosen before the enthalpy adjustment was implemented. However, since the results no longer accurately represent the experimental data, multiple cases were evaluated until Case K was identified as the closest match for replicating the experimental observations. The parameters utilized for Case K are outlined in Table 5.13.

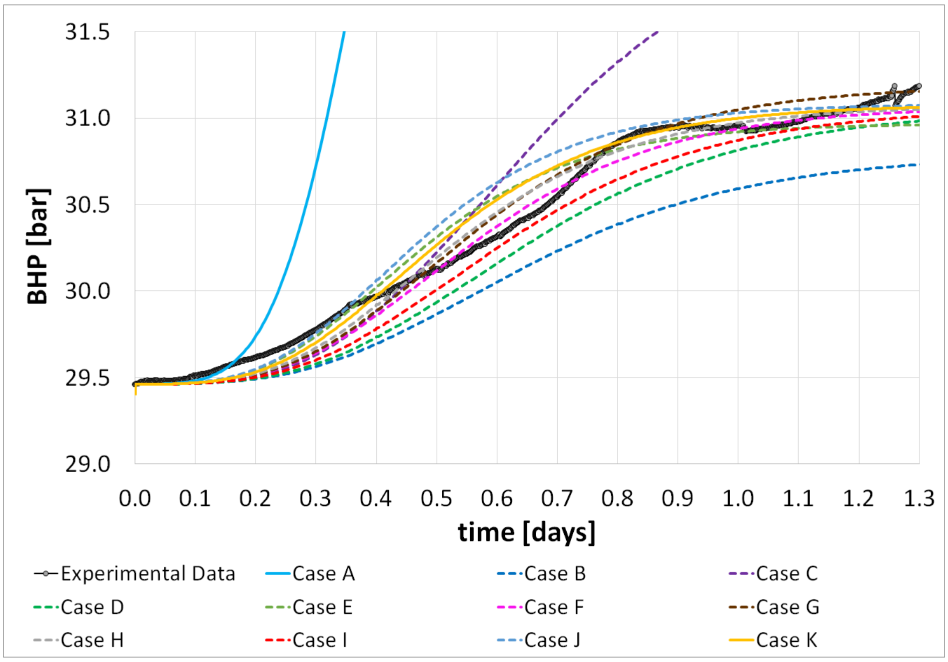

Figure 5.12: History match results after enthalpy adjustment for experiment No. 18.

Case	Relative Permeability Curves	kf,kb	Permeability Reduction Model	Constant for Permeability Reduction Model
K	CO2-water curves	0.39	Chen et al.	20.5

Table 5.13: Parameters of the final case selected for experiment No. 18.

Figure 5.13 presents the final profiles of temperature, pressure, water saturation, and hydrate saturation at different times since the start of the injection (i.e., $0.05\ day$, $0.4\ day$, $0.8\ day$, and $1.2\ days$) for experiment No. 18, based on the selected case after history match. Based on the findings, during the injection period, there is an increase in temperature of approximately two degrees. As the injection time progresses, the pressure gradually increases due to the ongoing formation of hydrates, initially slightly pronounced near the inlet but later occurring throughout the entire core. The water saturation decreases steadily as hydrates form, eventually reaching zero levels after a duration of $1.2\ days$.

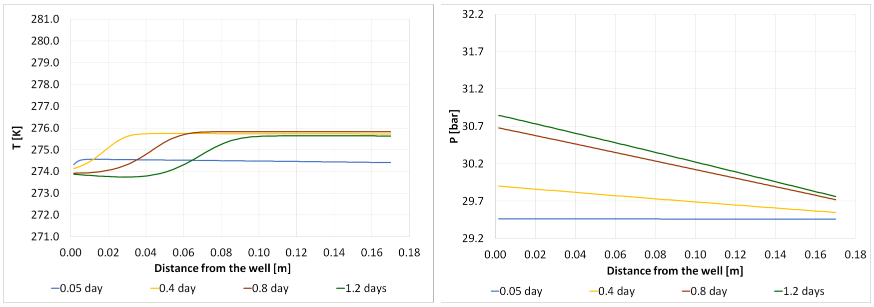

(a) Temperature profile. **(b)** Pressure profile.

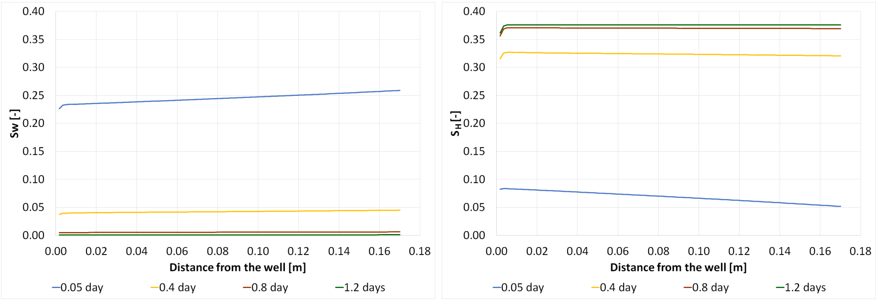

(c) Water saturation profile. **(d)** Hydrate saturation profile.

Figure 5.13: Experiment No. 18: Final results for case selected from history match process.

Table 5.14 displays the reduction in permeability resulting from hydrate formation, as determined from the case selected after the history match was conducted for experiment No. 18. The observed permeability reduction is approximately 100%, due to the substantial levels of hydrate saturation, which reach approximately 37%. This substantial decrease in permeability provides an explanation for the observed increase in BHP, as depicted in Figure 5.12.

Initial Permeability [mD]	Permeability after Hydrate Formation [mD]	Permeability reduction
2200	0.6	-99.97%

Table 5.14: Permeability reduction according to model results from experiment No. 18.

6

Discussion

An insightful examination of the obtained results becomes imperative to understand the underlying reasons behind observed results, comprehend their potential implications on a CCS (Carbon Capture and Storage) project, identify the constraints that might influence the outcomes, and find opportunities to improve both the methods and the models.

This chapter undertakes a comprehensive critical discussion of the results derived from the experiments outlined in Chapter 3, the empirical model introduced in Chapter 4, and the history match results presented in Chapter 5. It centers around the fundamental question: "*What is the impact on injectivity resulting from the formation of hydrates during CO_2 injection in depleted gas reservoirs?*". Through a comprehensive analysis of these results, the discussion seeks to provide insights into the consequences of hydrate formation during the development of CCS projects in depleted gas reservoirs.

6.1. Experimental Results

This section presents a comprehensive discussion of the experimental results, organized into relevant topics. It encompasses permeability measurements, pressure results, temperature findings, implications of THIs at pre-injection and mitigation stages, as well as general remarks.

6.1.1. Permeability Tests

Overall, in the permeability tests, it was observed that despite the core being composed of a homogeneous Bentheimer sandstone, different permeability values were reported for section one and two. Although in average the variation was minimal (less than 10%), it underscores the inherent natural heterogeneity in formations. In the case of significant variations arising, it becomes imperative to conduct uncertainty studies to capture the potential impact of permeability variations during CO_2 injection.

In general, heterogeneity in a reservoir can contribute to enhancing the structural and stratigraphic trapping of CO_2. Regarding injection pressure, high permeability reservoirs require lower injection pressures, while low permeability reservoirs demand higher injection pressures to allow the same injection rate. When examining the implications of high versus low permeability on hydrate formation during constant-rate injection, high permeability formations exhibit lower pressure drops, resulting in a reduced J-T cooling effect and a lesser tendency for hydrate formation. Conversely, low permeability formations experience higher pressure drops, leading to an increased J-T cooling effect and a higher risk of hydrate formation (Oldenburg, 2007).

6.1.2. Pressure Results

Regarding the pressure history obtained from the experiments, pressure increments above the base pressure line were attributed to blockage caused by hydrate formation. This can be explained by the fact that when the injection rate is kept constant, but hydrate formation impedes the flow of CO_2 through the core, the injected CO_2 will accumulate in the system, leading to a rise in pressure. As a result, the pressure readings above the base pressure line serve as a clear indication of hydrate-induced blockage, where the accumulated CO_2 creates pressure buildup in the system.

In general, in experiments where hydrate formation was observed, the pressure consistently rose above the base pressure line ($30\ bars$). This pressure behavior has been studied by other researchers as well (Gauteplass et al., 2020), and their findings show that the pressure gradient increases with hydrate formation and decreases in the absence of hydrates, as illustrated in Figure 6.1 where pressure gradient reached values of $140\ bar/m$ when hydrate-induced blockage occurred. This observation further supports the interpretation of pressure increments above the base pressure line as a reliable indicator of hydrate-induced blockage during the core flooding experiments.

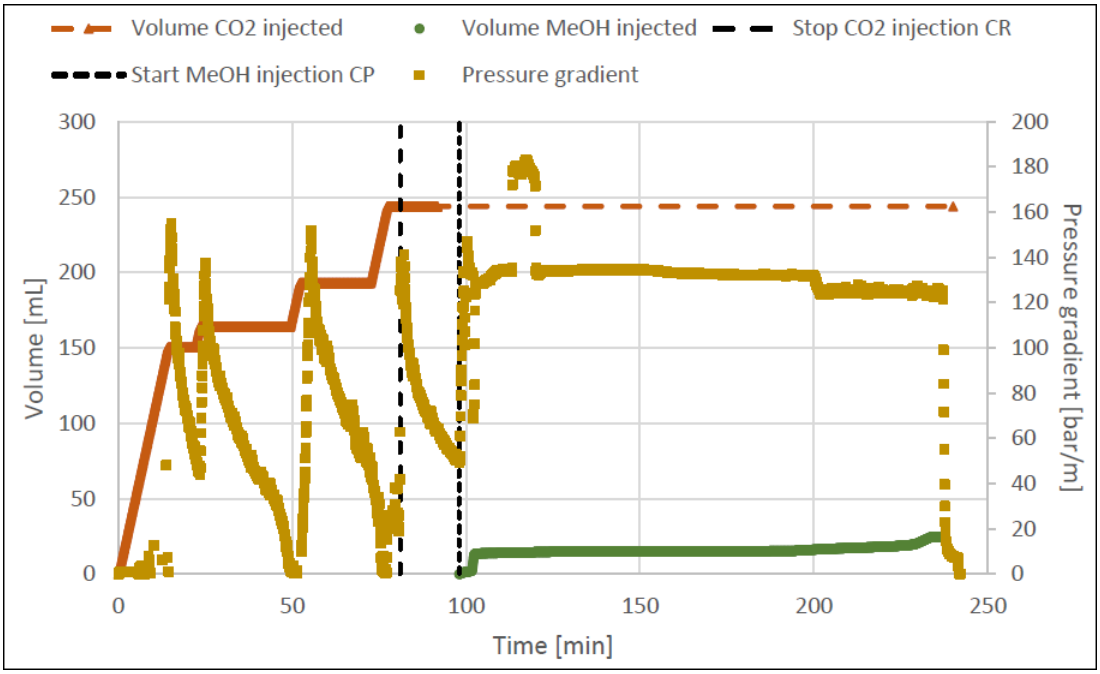

(a) Literature results from (Gauteplass et al., 2020).

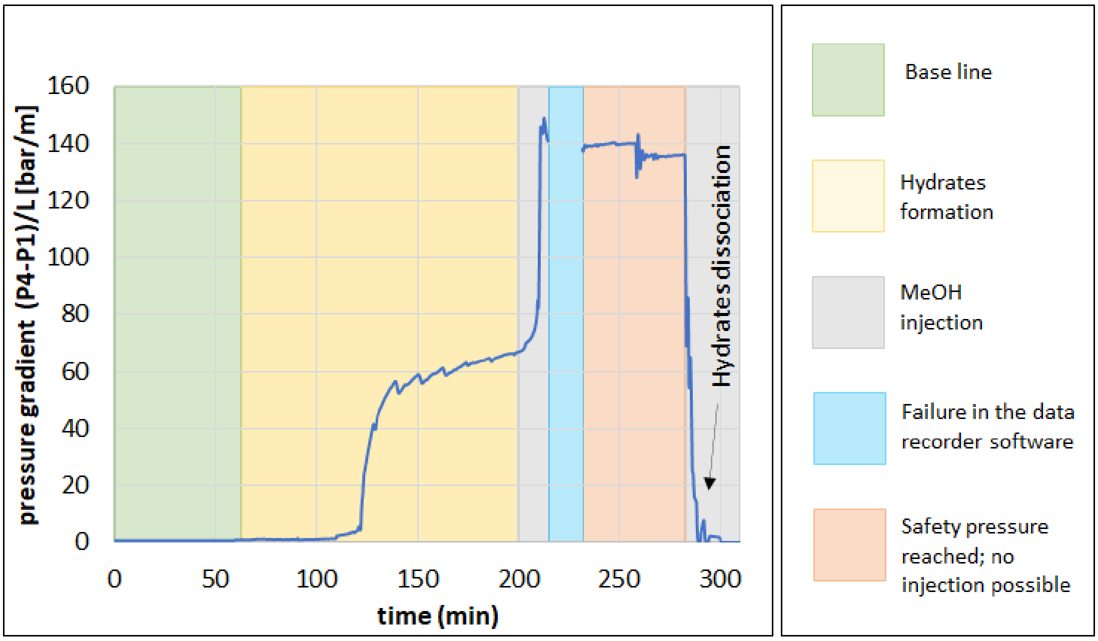

(b) Results experiment No. 6.

Figure 6.1: Analysis on the pressure gradient during hydrate formation and dissociation processes.

A distinct pressure behavior was consistently observed in most experiments where hydrate formation was detected, particularly noticeable in experiments 13, 16, 17, and 18, as shown in Figure 6.2. Despite maintaining a constant injection rate, the pressure exhibited a dip, attributed to the sudden increase in gas consumption during the initial stage of hydrate growth following the nucleation period. As gas consumption rises while the injection rate remains steady, the pressure decreases. Figure 6.3 provides a closer view of this phenomenon.

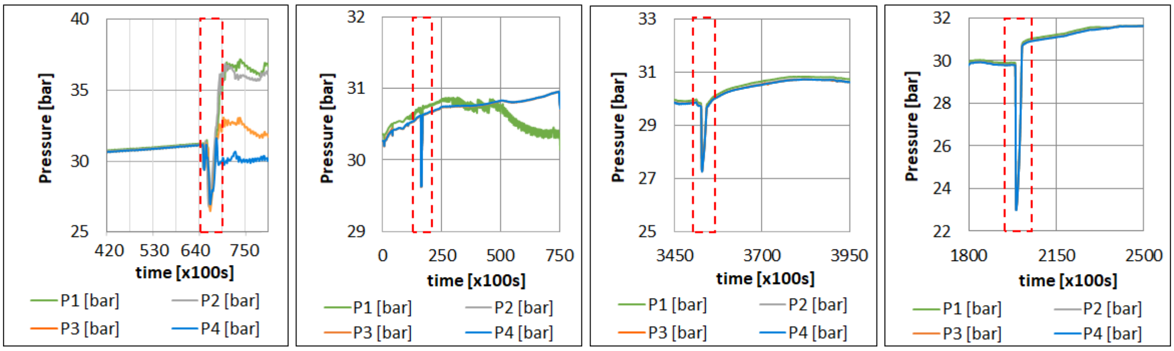

(a) Experiment No. 13.

(b) Experiment No. 16, first injection cycle.

(c) Experiment No. 17, third injection cycle.

(d) Experiment No. 18, second injection cycle.

Figure 6.2: Pressure dip observed in most experiments where hydrate formation was detected. The red dashed box indicates the moment when gas consumption increases and generates the pressure dip.

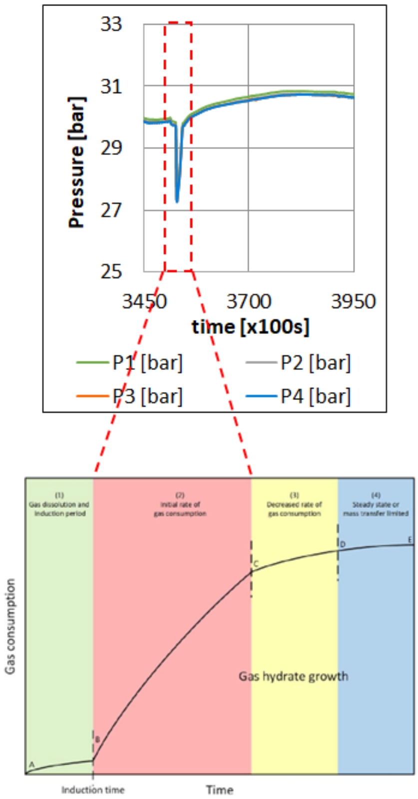

Figure 6.3: Graphic explanation of pressure dip generated by the increase in gas consumption during hydrate formation. Top plot, data from experiment No. 17. Bottom plot, gas consumption curve during gas hydrate formation from (Yin et al., 2018).

6.1.3. Temperature Results

To begin, it is noteworthy to highlight the absence of any J-T effect in the laboratory results. This is explained by the fact that the thermodynamic conditions needed to reach the hydrate stability zone were achieved by using a fridge and a back pressure regulator, as opposed to inducing a scenario of fluid expansion from high to low pressure.

Despite hydrate formation being an exothermic physical process, no significant temperature variation was observed in the experiment when hydrates formed. However, it is believed that the exothermic behavior might not have been adequately captured by the thermocouples installed at the inlet and outlet of the core holder. To improve accuracy, it is highly recommended to install temperature sensors inside the core to precisely measure the temperature change during hydrate formation.

The investigation of whether hydrate formation-induced temperature increase can lead to a self-healing process by moving the conditions out of the hydrate stability zone is pertinent. However, this self-healing phenomenon was not observed in the laboratory experiments.

6.1.4. THIs Utilization

As discussed in Section 2.6, the use of THIs can effectively hinder hydrate formation by shifting the hydrate equilibrium curve towards regions of lower-temperature and higher-pressure, thus preventing the system from entering the hydrate stability zone (Nagashima et al., 2020). Experimental results from tests No. 2 and 5 further validated this, as pre-injection of a $30wt$% MeOH successfully prevented hydrate formation at $30\ bar$ and $1°C$.

Furthermore, experiment No. 7 provided additional evidence supporting the influence of THIs on the shift of the hydrate equilibrium curve. In this case, hydrates formed only when the system's temperature was below $-3°C$ at $30\ bar$, due to the injection of brine with a salinity of $20wt$% NaCl. In contrast, when brine with a salinity of $1wt$% NaCl was used, hydrates formed at $1°C$ under the same pressure conditions of $30\ bar$. This comparison highlights the significant impact of THIs in shifting the hydrate equilibrium curve.

Given that THIs are high dosage hydrate inhibitors, it is crucial to acknowledge that while they can effectively prevent hydrate formation, their implementation at a field scale may result in significant quantities being required in case THIs pre-injection is chosen as the preventive hydrate formation strategy. Consequently, the cost of a CCS project incorporating THIs for hydrate prevention may noticeably exceed that of a CCS project without THIs. Careful consideration of the economic implications is essential when deciding on the most suitable approach to prevent hydrate formation in a CCS project.

Regarding the use of THIs, particularly MeOH, as a remediation technique for hydrate formation, laboratory experiments (No. 6, 8, 9, and 13) demonstrated its effectiveness in dissociating hydrates. This effectiveness was particularly notable when a soaking time was allowed for MeOH to interact with the porous media. Injection of MeOH as a remediation technique has been studied previously (Gauteplass et al., 2020); as MeOH is soluble in water, it can come into contact with formed hydrates and destabilize them by moving through preserved water channels in the water phase. The successful proof of MeOH's effect on hydrate dissociation suggests it as a recommended strategy to employ in the field when hydrates have formed and dissociation has not been achieved.

6.1.5. General Remarks

In relation to the influence of hydrate formation on injectivity during CO_2 injection, the pressure results unequivocally demonstrated that the formation of hydrates hinders the CO_2 injection process, leading to a reduction in injectivity. The presence of hydrates, occupying the porous space, constrains the available pathways for CO_2 flow, resulting in a reduction in permeability and, consequently, a negative impact on injectivity. This observation was further corroborated by the Mobility Reduction Factor (MRF) plots, which clearly indicated an increase in the MRF coinciding with the formation of hydrates within the core. In field applications, an increase in the bottom hole pressure (BHP) can be indicative of diminished injectivity resulting from the formation of hydrates.

Concerning the determination of blockage location, inference was drawn from pressure reading variations. However, as hydrates can also form around pressure gauges, the utilization of computed tomography (CT) scans or magnetic resonance imaging (MRI) would further enable accurate identification of blockage distribution across the core and precise localization of CO_2 hydrates. At the field scale, blockage identification is more intricate, given the impossibility of installing pressure gauges within the reservoir. As previously discussed, while bottom hole pressure (BHP) aids in identifying hydrate formation, it does not pinpoint the precise location of hydrates within the reservoir.

It was noted that water saturation significantly influences the induction time, with a longer induction period observed when water saturation was below 100%. This phenomenon can be attributed to the incomplete water saturation of the core, enabling injected CO_2 to flow through the core without immediately contacting water molecules. This delayed contact contributes to a slower initiation of hydrate formation. In the context of a depleted gas reservoir, where 100% water saturation is not anticipated within the formation, the extent of hydrate formation delay will be linked to the percentage of water saturation present in the reservoir.

An essential yet unmeasured parameter in the conducted experiments, critical for comprehending the kinetics of hydrate formation, was the quantity of injected gas. Hence, it becomes imperative to quantify the injected gas volume to establish correlations between the gas consumption and the different stages of hydrate formation, such as nucleation and hydrate growth, as presented in Section 2.4.2.

As outlined in existing literature, hydrate formation is inherently a stochastic process (Sloan & Koh, 2007). This stochastic nature of hydrate formation introduces challenges in achieving precise repeatability of experimental outcomes. Consequently, a preference is given to discerning general trends rather than focusing solely on exact values derived from the experimental data.

Finally, it is crucial to recognize that while the experimental results contributed to comprehending the underlying physical processes of hydrate formation and dissociation, these observations were conducted at a core-scale. In fact, injecting CO_2 into depleted gas reservoirs presents a multiscale challenge, necessitating a comprehensive study encompassing processes from the micro to field scale. This holistic approach aims to bridge the gap between scales and establish correlations between laboratory findings and their practical applications in the field. Therefore, further research is imperative to upscale the acquired data to a field scale.

6.2. Empirical Model

This section encompasses a comprehensive discussion of the empirical model, encompassing the model results, outcomes from case studies, proposed prevention strategies, and an exploration of the model's limitations.

6.2.1. Model Results

As indicated by the results, the empirical model effectively captures the J-T cooling effect and subsequently properly simulates hydrate formation and dissociation processes in the areas where P and T conditions enter into the hydrate stability zone.

As described in the results section, hydrates formation amplifies the J-T cooling effect, primarily due to its impact on permeability. However, over time, the reduction in permeability increases the pressure which reduces the pressure drop and diminishes the J-T cooling effect resulting in smaller areas over the reservoir with hydrates formation. This situation raises a crucial question: What is the permissible threshold for reservoir pressure as a result of the injection, considering its potential role in mitigating hydrate formation? The response to this question necessitates a comprehensive geomechanical assessment encompassing both the formation and the cap rock. The outcome of this assessment must ensure that the injection pressure remains within a safe limit, preventing any risk of fracturing the formations due to exceeding the fracture pressure of the rock.

Regarding water saturation and hydrate saturation, as explained in the results section, the presence of hydrate formation leads to a decrease in water saturation, consequently causing an increase in hydrate saturation. This is attributed to the consumption of water during hydrate formation since water is one of the essential components for hydrate development. It is important to note that the decrease in water saturation is not a result of a dry-out effect caused by CO_2 injection, where water is evaporated from its liquid phase. The empirical model exclusively considers liquid water; hence, the dry-out effect is neither simulated nor captured. This limitation is discussed in greater detail in Section 6.2.4.

When considering the sensitivity results, commonly accepted values for parameters like capillary pressure and rock thermal conductivity demonstrated minimal influence on the outcomes. However, the reaction rate coefficients are critical parameters that require precise quantification in laboratory settings to narrow down the uncertainties associated with their values. This is imperative since these coefficients can markedly accelerate or decelerate the pace of hydrate formation within the reservoir, directly impacting injectivity.

In relation to injection rate and temperature, these are operational settings that can affect hydrate formation and ultimately BHP, so carefully choosing these factors can help reducing hydrate formation and, in turn, avoiding adverse effects on injectivity. Typically, if feasible, opting for a higher injection temperature is preferable to prevent hydrate formation because the high temperature reduces the J-T cooling effect and consequently hydrate saturation.

Similar to temperature, the injection rate also influences the BHP. For instance, if the aim is to achieve the lowest BHP feasible without time constraints for injecting a certain CO_2 volume, a lower rate should be chosen. However, if the priority is minimizing the time to store a given CO_2 volume, without limiting BHP, then a higher rate could be considered. Figure 6.4 illustrates the options just mentioned.

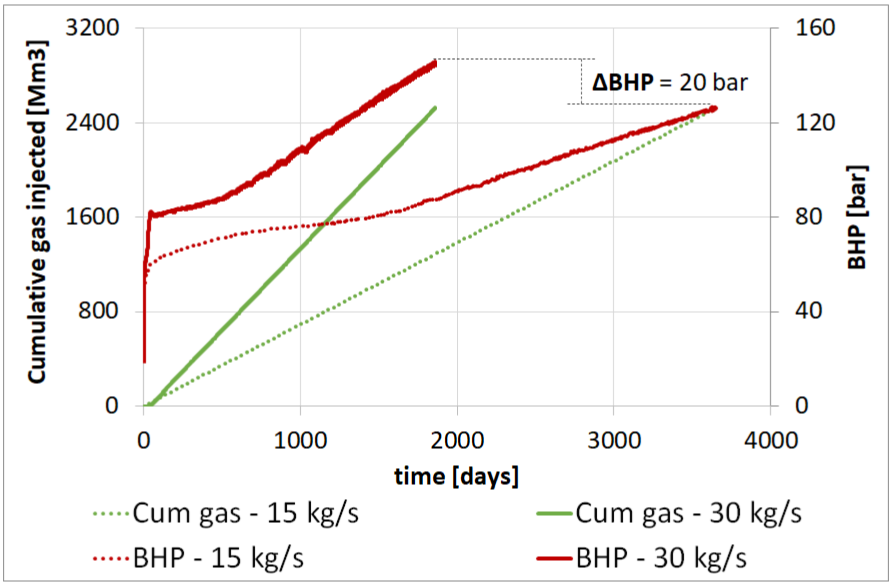

Figure 6.4: Cumulative gas and BHP for two scenarios: dotted lines injection rate of $15\ kg/s$, solid lines injection rate of $30\ kg/s$.

6.2.2. Case Studies Results

In the case of the two studied reservoirs, it was evident that the flow capacity (permeability times thickness) serves as the critical factor governing the movement of CO_2 within the reservoir. Consequently, zones characterized by higher flow capacity exhibit a greater capacity to take a larger portion of the injected CO_2, leading to an accelerated CO_2 propagation, progression of the thermal front, and pressurization.

Moreover, layers with higher permeability also displayed a more pronounced J-T cooling effect. This observation does not contradict the fact that the J-T cooling effect is accentuated in less permeable layers, as this fact holds true only when the injection rate is the same across all layers. However, if the injection rate varies, with a higher injection rate in the more permeable layer compared to the less permeable one, the J-T cooling effect will be more pronounced in the more permeable layer.

In relation to injection temperature, as previously discussed, an increase in injection temperature corresponds to a decrease in the potential for hydrate formation. This relationship was also evident in the scenarios that were examined for each reservoir.

Furthermore, in line with expectations, it was verified that areas where hydrate formation took place exhibited a reduction in water saturation, thereby confirming previously observed results.

6.2.3. Prevention Strategies

Based on the results, it is evident that elevating the injection temperature is an effective strategy for averting hydrate formation in the reservoir. However, maintaining a continuous injection of warm CO_2 $(T > 20°C)$ can incur substantial costs in a CCS project. Therefore, the proposed alternative of alternating yearly injections of cold $(12°C)$ and warm $(24°C)$ CO_2 becomes an appealing option. This approach minimizes hydrate formation within the reservoir, thereby preserving injectivity, as evidenced by the behavior of the BHP. An additional optimization of this approach should focus on reducing the duration of warm injection periods while simultaneously minimizing the formation of hydrates. Implementing this strategic adjustment would guarantee the preservation of injectivity while optimizing costs.

6.2.4. Model Limitations

It is important to remember that a model simplifies reality, making it crucial to understand the model's limitations in order to assess its relevance for real-world applications.

While it is established that hydrate formation is an exothermic process, it is important to note that the empirical model does not account for the temperature rise resulting from hydrate formation. Consequently, the assessment of the extent of temperature increase and its potential to shift pressure and temperature conditions out of the hydrate stability zone remains unaddressed.

Concerning the model's components and the potential phases in which each component may exist, CO_2 was assumed to consistently remain in the gas phase. Although this may not precisely mirror the actual conditions of CO_2 injection, it can be viewed as a pessimistic scenario. This is explained by the fact that the Joule-Thomson coefficient is larger for gaseous CO_2 compared to its liquid form (J. Wang et al., 2017). Consequently, if the liquid phase were considered, the actual J-T cooling effect would likely be reduced. In essence, this implies that the model results might lean more towards overestimation rather than underestimation.

In the empirical model used for sensitivity analysis and case studies assessment, a generic gas-water relative permeability curve was employed. This choice was influenced by the assumption that in those scenarios the initial water saturation equated to the connate water saturation. As a result, no displacement of water by gas was considered in those cases. Therefore, the choice of relative permeability curves had no impact on the results.

Concerning the permeability reduction models incorporated in the empirical model, only two models were included: Pang-Sharma and Chen et al. However, a multitude of models have been documented in the literature (Xu et al., 2022). Therefore, additional research can be pursued to identify the model that more accurately captures the nature of permeability reduction attributed to hydrate formation.

To capture the kinetics associated with hydrate formation and dissociation processes, the empirical model assumes an equilibrium condition where the forward reaction rate coefficient is considered equal to the backward reaction rate coefficient. However, entropy favors disorder over order, indicating that the reaction rate for hydrate dissociation should be faster than that for hydrate formation (Sloan & Koh, 2007). Based on this insight, a more accurate approach to address reaction rates would involve measuring these parameters in the laboratory. This adjustment would result in a model that better represents the actual dynamics of hydrate formation and dissociation.

Finally, to account for the dry-out effect observed during CO_2 injection into a reservoir, the model should incorporate an altered definition for the K-values. This new definition would enable the partitioning of each component into multiple phases, which could better approximate the dynamics of a CO_2 injection process. Another possible approach could involve incorporating an equation of state into the model to characterize fluid properties for any phase, in contrast to the empirical model where fluid properties were determined using predefined tables.

6.3. History Match

The history match was successfully achieved for experiments No. 16, 17, and 18 by making adjustments to various factors, including the relative permeability curves, reaction rate coefficients, the permeability reduction model, and the constant associated with the reduction permeability model. An additional parameter, enthalpy, was also modified to better represent the experimental data. The adjustments made have prompted the emergence of several intriguing questions.

When considering reaction rate coefficients, a pertinent question arises: How can the kinetics of hydrate formation and dissociation be accurately measured within a laboratory setting? The significance of kinetics lies in its role in determining the speed at which hydrates form, subsequently impacting the rapidity at which injectivity is influenced by hydrate formation. It is imperative to acknowledge that further research is essential in this domain, as the processes of hydrate formation and dissociation are complex. They encompass multiple components (water, gas, and hydrate) distributed across various phases (liquid, gas, and hydrate) at a multiscale level, ranging from molecular-scale to macroscopic-scale (Yin et al., 2018).

Regarding the permeability reduction model, two crucial questions persist: What is the distribution of hydrates within the core, and how does this affect permeability? As demonstrated, variations in both the permeability reduction model and the associated constant exert a substantial influence on the extent to which hydrates impede injectivity. Consequently, it becomes essential to incorporate either CT or MRI equipment into the laboratory setup, enabling an in-depth comprehension of the physical distribution of hydrates within the core and their consequential impact on permeability. Figure 6.5 provides an illustrative example of how the variability of the constant affects the permeability according to the Chen et al. permeability reduction model. Notably, the higher the constant's value, the more pronounced its impact on permeability. Given this insight, precise measurement of core permeability in the presence of hydrate formation becomes indispensable for an accurate representation of permeability reduction.

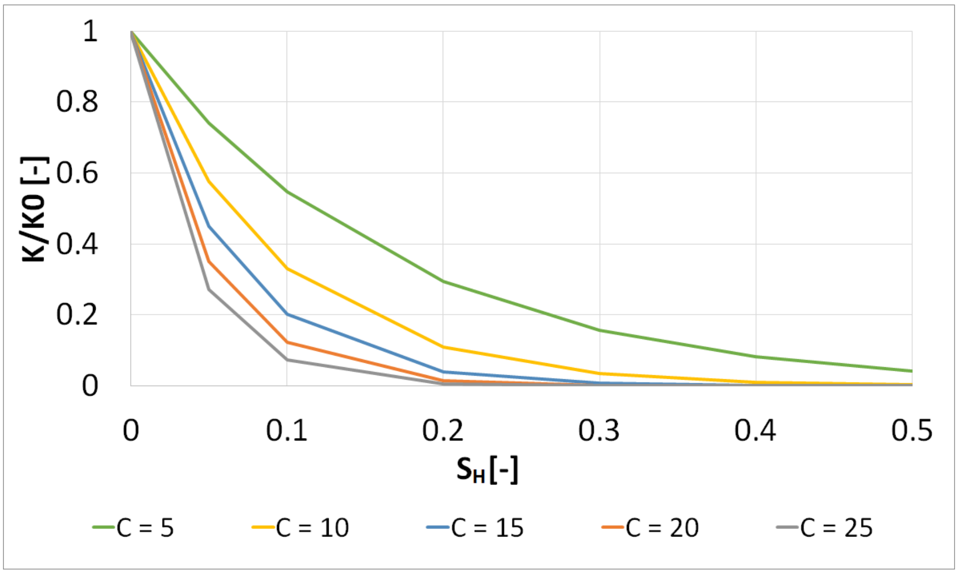

Figure 6.5: Sensitivity on the results of the Chen et al. permeability reduction model when varying the value of the constant C.

A final pertinent question remains: What is the enthalpy of the hydrate formation/dissociation reactions? The results showed that the definition of model enthalpy significantly influences temperature behavior. Consequently, addressing this question will not only enhance results accuracy but also reinforce the model's ability to faithfully represent the underlying physical processes of hydrate formation and dissociation.

7

Conclusions

The primary objective of this thesis was to investigate the impact of hydrate formation on injectivity during CO_2 injection within depleted gas reservoirs. This investigation was carried out through a comprehensive integration of experimental and numerical methodologies.

The experimental approach involved a core flooding experiment, based on the injection of CO_2 into sandstone. This experiment contributed to understand the complex physics underlying hydrate formation and dissociation processes. Accordingly, it was established that the formation of hydrates only occurs when both pressure and temperature are situated within the confines of the hydrate stability zone. Region that is delimited by the hydrate equilibrium curve, which can be shifted by inhibitors, including alcohols like MeOH or salts like NaCl. Furthermore, conducting experiments involving different water saturation allowed for the inference of how water saturation affects the time of hydrate formation. The experimental procedure also effectively enabled the testing of remediation mechanisms after hydrate formation, including thermal stimulation and THIs injection.

As for the numerical approach, an empirical model was formulated to simulate the process of hydrate formation and dissociation within depleted gas reservoirs. The model was employed to history match the experimental data. Through this process, it was determined that the main parameters that require further investigation in relation to hydrate formation and dissociation processes are the kinetics of the reactions, along with the distribution of the hydrates within the porous media. This distribution ultimately defines how hydrates affect permeability and subsequently diminish injectivity.

Through the utilization of the numerical model, it became evident that operational parameters, particularly the CO_2 injection rate and temperature, exert a big influence on increasing the risk of hydrate formation. Moreover, the model helped to investigate potential prevention strategies, including the examination of a yearly alternation between cold and warm CO_2 injection.

Ultimately, both experimental and numerical approaches showed that the formation of hydrates leads to a reduction in permeability, thereby diminishing injectivity and elevating injection pressure. This pressure increase may potentially trigger a self-healing phenomenon, contingent upon the threshold of maximum pressure that the reservoir and cap rock can endure before surpassing their fracture pressure.

While various challenges persist in both experimental and numerical domains, in order to enhance the understanding of hydrates formation within a reservoir and refine its representation through numerical models, this study has the potential to assist in evaluating CO_2 injection in depleted gas fields, which finally has the capacity to significantly mitigate CO_2 emissions in the atmosphere and contribute to the global effort of addressing climate change.

8

Recommendations

In light of the comprehensive analysis and insights gained from the preceding chapters, this recommendations section highlights potential refinements and considerations that can enhance and deepen the understanding of hydrate formation resulting from CO_2 injection in depleted gas reservoirs.

Experimental Section

- Installing temperature sensors within the core is strongly advised to accurately measure temperature changes during hydrate formation. This enables the quantification of temperature increases resulting from the exothermic reaction of hydrate formation.
- Integrating computed tomography (CT) scans or magnetic resonance imaging (MRI) into the experimental setup is crucial. This inclusion not only facilitates the precise identification of the distribution of hydrate-induced blockages throughout the core but also enables accurate characterization of permeability reduction.
- Conducting experiments to measure the formation and dissociation reaction rates is essential for gaining a deeper comprehension of the kinetics involved in hydrate formation and dissociation processes.
- A holistic approach that bridges the gap between scales (from micro to field scale) is required to apply the knowledge gained from lab results into effectively execution of field CCS projects.
- Following the implementation of the previous recommendations in a revised laboratory setup, when studying hydrate formation for a specific reservoir, it is advisable to conduct the experiment using actual core samples extracted from the field under investigation.

Empirical Model

- To address the dry-out effect noted during CO_2 injection into a reservoir, the model should incorporate an adjusted definition for the K-values or integrate an equation of state to define fluid properties. This enhancement would enable the partitioning of each component into multiple phases, offering a more accurate approximation of the complex dynamics during a CO_2 injection process.
- Incorporating hydrate equilibrium curves into the model that accurately capture the hysteresis of hydrate formation and dissociation processes is advisable. This addition aims to quantitatively assess the influence of this effect on the obtained results.
- It is suggested to revisit the assumption of considering equal the forward and backward reaction rate coefficients. This is based on the fact that entropy favors disorder over order, indicating that the reaction rate for hydrate dissociation should surpass that of its formation.
- Considering the variability in gas consumption over time, it is probable that the reaction rate may also fluctuate. Hence, an exploration of a kinetic model that accommodates the distinctive stages of the hydrate formation process is recommended.

- It is imperative to conduct further research to determine the enthalpy of the hydrate formation/dissociation reactions. This research would enhance the model's capacity to accurately represent the underlying physical processes of hydrate formation and dissociation.
- It is essential to incorporate the heat released during hydrate formation into the model. This addition aims to quantify the extent to which the resulting increase in temperature can potentially drive the system conditions away from the hydrate stability zone.
- Given the various permeability reduction models described in the literature, further research can be pursued to identify the model that most accurately captures the specific nature of permeability reduction associated with hydrate formation.
- Sensitivities that account for heat transfer to both the overburden and underburden should be addressed to comprehensively capture the impact of the surrounding layers on reservoir temperature and hydrates formation and dissociation processes.
- To further enhance the proposal of alternating cold and warm CO_2 injection as a method to prevent and mitigate hydrate formation, it is recommended to optimize the duration of warm injection periods. By implementing this strategic adjustment, both injectivity preservation and cost optimization could be assured.
- Considering the complexity of phase changes that CO_2 undergoes during a CCS project, it is advisable to couple the reservoir model with wellbore and surface facilities models. This would provide a more accurate representation of the entire CO_2 journey.
- Integrating the adjustments derived from the history match of the experiments into the empirical model is advised. This integration will improve the model's robustness and applicability, particularly in the evaluation of the case studies for reservoirs A and B.

References

Aghajanloo, M. (2023). A Review of CO2 Storage into depleted oil and gas reservoirs with a focus on reducing the impact of hydrate formation on CO2 injectivity [TU Delft internal report].

Anderson, R., Llamedo, M., Tohidi, B., & Burgass, R. W. (2003). Experimental measurement of methane and carbon dioxide clathrate hydrate equilibria in mesoporous silica. *The Journal of Physical Chemistry B*, *107*(15), 3507–3514.

Baklid, A., Korbol, R., & Owren, G. (1996). Sleipner Vest CO2 disposal, CO2 injection into a shallow underground aquifer.

Buchanan, P., Soper, A., Thompson, H., Westacott, R., Creek, J., Hobson, G., & Koh, C. (2005). Search for memory effects in methane hydrate: Structure of water before hydrate formation and after hydrate decomposition. *Journal of Chemical Physics*, *123*(16), 1–7. https://doi.org/10.1063/1.2074927

Circone, S., Stern, L., Kirby, S., Durham, W., Chakoumakos, B., Rawn, C., Rondinone, A., & Ishii, Y. (2003). CO2 Hydrate: Synthesis, Composition, Structure, Dissociation Behavior, and a Comparison to Structure I CH 4 Hydrate. *Journal of Physical Chemistry B*, *107*. https://doi.org/10.1021/jp027391j

Clennell, M. B., Hovland, M., Booth, J. S., Henry, P., & Winters, W. J. (1999). Formation of natural gas hydrates in marine sediments: 1. Conceptual model of gas hydrate growth conditioned by host sediment properties. *Journal of Geophysical Research: Solid Earth*, *104*(B10), 22985–23003. https://doi.org/https://doi.org/10.1029/1999JB900175

Corey, A. T. (1954). The interrelation between gas and oil relative permeabilities. *Prod. Month.*, *19*, 38–41.

Eftekhari, A. A., & Farajzadeh, R. (2017). Effect of Foam on Liquid Phase Mobility in Porous Media. *Scientific Reports*, *7*. https://doi.org/10.1038/srep43870

Eiken, O., Ringrose, P., Hermanrud, C., Nazarian, B., Torp, T., & Høier, L. (2011). Lessons learned from 14 years of CCS operations: Sleipner, In Salah and Snøhvit. *Energy Procedia*, *4*, 5541–5548. https://doi.org/10.1016/j.egypro.2011.02.541

English, J. M., & English, K. L. (2022). An Overview of Carbon Capture and Storage and its Potential Role in the Energy Transition. *First Break*, *40*(4), 35–40. https://doi.org/https://doi.org/10.3997/1365-2397.fb2022028

EPA, U. (2023). Global greenhouse gas emissions data. *Greenhouse Gas Emissions*. Retrieved June 27, 2023, from https://www.epa.gov/ghgemissions/global-greenhouse-gas-emissions-data

Fegley, B. (Ed.). (2013). Chapter 7 - Phase Equilibria of Pure Materials. In *Practical Chemical Thermodynamics for Geoscientists* (pp. 225–286). Academic Press. https://doi.org/https://doi.org/10.1016/B978-0-12-251100-4.00007-9

Ferdows, M., & Ota, M. (2006). Density of CO2 Hydrate by Monte Carlo Simulation. *Proceedings of the Institution of Mechanical Engineers, Part C: Journal of Mechanical Engineering Science*, *220*(5), 691–696. https://doi.org/10.1243/09544062C13104

Finney, B., & Jacobs, M. (2010). Carbon dioxide pressure-temperature phase diagram.

Gabitto, J., & Tsouris, C. (2010). Physical Properties of Gas Hydrates: A Review. *Journal of Thermodynamics*, *2010*. https://doi.org/10.1155/2010/271291

Gaidukova, O., Misyura, S., & Strizhak, P. (2022). Key Areas of Gas Hydrates Study: Review. *Energies*, *15*(5). https://doi.org/10.3390/en15051799

Gasunie. (2022). Transport and storage of CO2 – how does it work? Retrieved July 9, 2023, from https://www.gasunie.nl/en/news/transport-and-storage-of-co2---how-does-it-work

Gauteplass, J., Almenningen, S., Barth, T., & Ersland, G. (2020). Hydrate Plugging and Flow Remediation during CO2 Injection in Sediments. *Energies*, *13*(17). https://doi.org/10.3390/en13174511

Gibbs, J. W. (1961). The Scientific Papers. *Vol I*.

Hassanpouryouzband, A., Joonaki, E., Vasheghani Farahani, M., Takeya, S., Ruppel, C., Yang, J., English, N. J., Schicks, J. M., Edlmann, K., Mehrabian, H., Aman, Z. M., & Tohidi, B. (2020).

Gas hydrates in sustainable chemistry. *Chem. Soc. Rev.*, *49*, 5225–5309. https://doi.org/10.1039/C8CS00989A

Haszeldine, R. (2009). Carbon capture and storage: how green can black be? *Science*, *325*, 1647–1652. https://doi.org/10.1126/science.1172246

Henry, P., Thomas, M., & Clennell, M. B. (1999). Formation of natural gas hydrates in marine sediments—part 2: thermodynamic calculations of stability conditions in porous sediments. *Journal of Geophysical Research B*, *104*(B10), 23005–23022.

Hubbert, M. K. (1957). Darcy's law and the field equations of the flow of underground fluids. *Hydrological Sciences Journal*, *2*(1), 23–59.

IEA. (2020). The Netherlands 2020 – Analysis. Retrieved June 29, 2023, from https://www.iea.org/reports/the-netherlands-2020

IEA. (2022). Netherlands climate resilience policy indicator. Retrieved June 29, 2023, from https://www.iea.org/articles/netherlands-climate-resilience-policy-indicator

IPCC. (2005). Carbon Dioxide Capture And Storage [Working Group III of the Intergovernmental Panel on Climate Change].

IPCC. (2023). *Climate Change 2023: Synthesis Report. A Report of the Intergovernmental Panel on Climate Change. Contribution of Working Groups I, II and III to the Sixth Assessment Report of the Intergovernmental Panel on Climate Change* (Core Writing Team, H. Lee and J. Romero, Ed.; tech. rep.). IPCC. Geneva, Switzerland.

Jenkins, C. R., Cook, P. J., Ennis-King, J., Undershultz, J., Boreham, C., Dance, T., de Caritat, P., Etheridge, D. M., Freifeld, B. M., Hortle, A., Kirste, D., Paterson, L., Pevzner, R., Schacht, U., Sharma, S., Stalker, L., & Urosevic, M. (2012). Safe storage and effective monitoring of CO2 in depleted gas fields. *Proceedings of the National Academy of Sciences of the United States of America*, *109*(2), E35–E41. https://doi.org/10.1073/pnas.1107255108

Jensen, L. (2010). Experimental investigation and molecular simulation of gas hydrates.

Kahrobaei, S., & Farajzadeh, R. (2022). Modelling JT Effect in CO2 injection [MoReS deck].

Kang, S.-P., Lee, J.-W., & Ryu, H.-J. (2008). Phase behavior of methane and carbon dioxide hydrates in meso- and macro-sized porous media. *Fluid Phase Equilibria*, *274*, 68–72. https://doi.org/10.1016/j.fluid.2008.09.003

Kang, S.-P., Ryu, H.-J., & Seo, Y. (2007). Phase Behavior of CO2 and CH4 Hydrate in Porous Media. *International Journal of Chemical and Molecular Engineering*, *1*(9), 77–82. https://publications.waset.org/vol/9

Khan, M. S., Lal, B., & Bustam, M. A. (2020). Gas Hydrate Inhibitors. In *Chemical Additives for Gas Hydrates* (pp. 27–46). Springer International Publishing. https://doi.org/10.1007/978-3-030-30750-9_2

Kingston, E., Clayton, C., & Priest, J. (2008). Gas hydrate growth morphologies and their effect on the stiffness and damping of a hydrate bearing sand, 8.

Kirchin, A. (2023). The pros & cons of depleted vs saline reservoirs in CCS [publisher: RPS]. *Insights: Carbon Capture and Storage*. Retrieved June 28, 2023, from https://www.rpsgroup.com/insights/carbon-capture-and-storage/the-pros-and-cons-of-depleted-versus-saline-reservoirs-in-carbon-capture-and-storage-ccs/

Kumar, A., Maini, B., P.R. Bishnoi, Clarke, M., Zatsepina, O., & Srinivasan, S. (2010). Experimental determination of permeability in the presence of hydrates and its effect on the dissociation characteristics of gas hydrates in porous media. *Journal of Petroleum Science and Engineering*, *70*(1), 114–122. https://doi.org/https://doi.org/10.1016/j.petrol.2009.10.005

Li, G., Weng, Y.-F., Li, X.-S., Xu, Z.-L., Lv, Q.-N., & Xu, C.-G. (2023). Studies on micromorphology and permeability of hydrate-bearing porous media. *Fuel*, *334*, 126647. https://doi.org/https://doi.org/10.1016/j.fuel.2022.126647

Lirio, C., & Pessoa, F. (2013). Enthalpy of Dissociation of Simple and Mixed Carbon Dioxide Clathrate Hydrate. *Chemical Engineering Transactions*, *32*, 577–582. https://doi.org/10.3303/CET1332097

Liu, F.-P., Li, A.-R., Qing, S.-L., Luo, Z.-D., & Ma, Y.-L. (2022). Formation kinetics, mechanism of CO2 hydrate and its applications. *Renewable and Sustainable Energy Reviews*, *159*, 112221. https://doi.org/https://doi.org/10.1016/j.rser.2022.112221

Llamedo, M., Anderson, R., & Tohidi, B. (2004). Thermodynamic prediction of clathrate hydrate dissociation conditions in mesoporous media. *American Mineralogist*, *89*(8-9), 1264–1270.

Loizzo, M., Lecampion, B., Bérard, T., Harichandran, A., & Jammes, L. (2010). Reusing o&g-depleted reservoirs for co2 storage: pros and cons. *SPE Projects, Facilities & Construction*, *5*(03), 166–172. https://doi.org/10.2118/124317-PA

Manjunath, G. (2022). Chapter 9 - Formation damage in oil reservoirs during CO2 injection. In T. Sharma, K. R. Chaturvedi, & J. J. Trivedi (Eds.), *Nanotechnology for CO2 Utilization in Oilfield Applications* (pp. 147–166). Gulf Professional Publishing. https://doi.org/https://doi.org/10.1016/B978-0-323-90540-4.00001-6

Masson-Delmotte, V., Zhai, P., Pörtner, H.-O., Roberts, D., Skea, J., Shukla, P., Pirani, A., Moufouma-Okia, W., Péan, C., Pidcock, R., Connors, S., Matthews, J., Chen, Y., Zhou, X., Gomis, M., Lonnoy, E., Maycock, T., Tignor, M., & Waterfield, T. (2018). Global Warming of 1.5°C. An IPCC Special Report.

Ministry of Economic Affairs and Climate Policy. (2019). National Climate Agreement [publisher: Ministry of Economic Affairs and Climate Policy]. Retrieved June 29, 2023, from https://www.klimaatakkoord.nl/documenten/publicaties/2019/06/28/national-climate-agreement-the-netherlands

Nagashima, H. D., Miyagi, T., Yasuda, K., & Ohmura, R. (2020). Clathrate hydrates at temperatures below the freezing point of water: A review. *Fluid Phase Equilibria*, *517*, 112610. https://doi.org/https://doi.org/10.1016/j.fluid.2020.112610

NETL. (2010). Carbon Dioxide Enhanced Oil Recovery [National Energy Technology Laboratory, U.S. Department of Energy].

OEC. (2022). Netherlands: Exports, imports, and trade partners. Retrieved June 29, 2023, from https://oec.world/en/profile/country/nld

Okotie, S., & Ikporo, B. (2019). History Matching: Fundamentals and Applications. https://doi.org/10.1007/978-3-030-02393-5_10

Oldenburg, C. M. (2007). Joule-Thomson cooling due to CO2 injection into natural gas reservoirs. *Energy Conversion and Management*, *48*(6), 1808–1815. https://doi.org/10.1016/j.enconman.2007.01.010

Ott, J. B., & Boerio-Goates, J. (2000). Chapter 3 - Thermodynamic Relationships and Applications. In J. B. Ott & J. Boerio-Goates (Eds.), *Chemical Thermodynamics: Principles and Applications* (pp. 105–153). Academic Press. https://doi.org/https://doi.org/10.1016/B978-012530990-5/50004-3

Pang, S., & Sharma, M. M. (1997). A Model for Predicting Injectivity Decline in Water-Injection Wells. *SPE Formation Evaluation*, *12*(03), 194–201. https://doi.org/10.2118/28489-PA

PBL. (2013). The effects of climate change in the netherlands: 2012 [publisher: PBL Netherlands Environmental Assessment Agency]. Retrieved June 29, 2023, from https://www.pbl.nl/en/publications/the-effects-of-climate-change-in-the-netherlands-2012

Peksa, A. E., Wolf, K.-H. A., & Zitha, P. L. (2015). Bentheimer sandstone revisited for experimental purposes. *Marine and Petroleum Geology*, *67*, 701–719. https://doi.org/https://doi.org/10.1016/j.marpetgeo.2015.06.001

Porthos. (2023). Project. Retrieved June 29, 2023, from https://www.porthosco2.nl/en/project/

Qorbani, K., Kvamme, B., & Kuznetsova, T. (2017). Simulation of CO2 Storage into Methane Hydrate Reservoirs, Non-equilibrium Thermodynamic Approach [13th International Conference on Greenhouse Gas Control Technologies, GHGT-13, 14-18 November 2016, Lausanne, Switzerland]. *Energy Procedia*, *114*, 5451–5459. https://doi.org/https://doi.org/10.1016/j.egypro.2017.03.1689

Raza, A., Gholami, R., Rezaee, R., Bing, C. H., Nagarajan, R., & Hamid, M. A. (2018). CO2 storage in depleted gas reservoirs: A study on the effect of residual gas saturation. *Petroleum*, *4*(1), 95–107. https://doi.org/https://doi.org/10.1016/j.petlm.2017.05.005

Ren, X., Guo, Z., Ning, F., & Ma, S. (2020). Permeability of hydrate-bearing sediments. *Earth-Science Reviews*, *202*, 103100. https://doi.org/https://doi.org/10.1016/j.earscirev.2020.103100

Ritchie, H., Roser, M., & Rosado, P. (2020). CO2 and Greenhouse Gas Emissions. *Our World in Data*. Retrieved June 22, 2023, from https://ourworldindata.org/co2-and-greenhouse-gas-emissions

RKTZ. (n.d.). Joule-Thomson cooling effect.

Rochelle, C. A., Camps, A., Long, D., Milodowski, A. E., Bateman, K., Gunn, D., Jackson, P. D., Lovell, M. A., & Rees, J. G. (2009). Can CO2 hydrate assist in the underground storage of carbon dioxide?

Rodger, M. (2000). Proc. Gas Hydrates: Challenges for the Future. *Ann. N.Y. Acad. Sci.*, 474.

Roosta, H., Varaminian, F., & Khosharay, S. (2013). Experimental study of CO 2 hydrate formation kinetics with and without kinetic and thermodynamic promoters. *Scientia Iranica*, *21*.

Rossi, F., Li, Y., & Gambelli, A. M. (2021). Thermodynamic and Kinetic Description of the Main Effects Related to the Memory Effect during Carbon Dioxide Hydrates Formation in a Confined Environment. *Sustainability*, *13*(24). https://doi.org/10.3390/su132413797

Sa, J. H., Kwak, G. H., Lee, B. R., Han, K., Cho, S. J., Lee, J. D., & Lee, K. H. (2017). Phase equilibria and characterization of CO2 and SF6 binary hydrates for CO2 sequestration. *Energy*, *126*, 306–311. https://doi.org/https://doi.org/10.1016/j.energy.2017.03.039

SCCS. (2023). Going underground [publisher: Scottish Carbon Capture and Storage, School of Geosciences, University of Edinburgh]. *Edinburgh Impact*. Retrieved June 28, 2023, from https://www.ed.ac.uk/impact/research/futureproofing-societies-planet/going-underground

Schlumberger. (n.d.). History matching. Retrieved July 31, 2023, from https://glossary.slb.com/en/terms/h/history_matching

Shaftel, H., Callery, S., Jackson, R., Bailey, D., & Callery, S. (2023). Global Warming vs. Climate Change. *Global Climate Change: Vital Signs of the Planet*. Retrieved June 22, 2023, from https://climate.nasa.gov/global-warming-vs-climate-change

Sloan, E., & Koh, C. (2007). *Clathrate Hydrates of Natural Gases* (3rd). CRC Press. https://doi.org/10.1201/9781420008494

Span, R., & Wagner, W. (1996). A New Equation of State for Carbon Dioxide Covering the Fluid Region from the Triple-Point Temperature to 1100 K at Pressures up to 800 MPa. *Journal of Physical and Chemical Reference Data*, *25*, 1509–1596.

Takeya, S., Hori, A., Hondoh, T., & Uchida, T. (2000). Freezing-Memory Effect of Water on Nucleation of CO2 Hydrate Crystals. *Journal of Physical Chemistry B*, *104*(17), 4164–4168. https://doi.org/10.1021/jp993759+

Tohidi, B., Anderson, R., Clennell, M. B., Burgass, R. W., & Biderkab, A. B. (2001). Visual observation of gas-hydrate formation and dissociation in synthetic porous media by means of glass micromodels. *Geology*, *29*(9), 867–870.

Tosun, İ. (2021). Chapter 2 - Thermodynamic property relations. In *The Thermodynamics of Phase and Reaction Equilibria (Second Edition)* (pp. 17–51). Elsevier. https://doi.org/10.1016/B978-0-12-820530-3.00010-6

TotalEnergies, Shell, Nederland, E. B., & Gasunie. (2023). About. *Aramis CCS*. Retrieved June 22, 2023, from https://www.aramis-ccs.com/project

Uchida, T. (1998). Physical property measurements on CO2 clathrate hydrates. Review of crystallography, hydration number, and mechanical properties. *Waste Management*, *17*(5), 343–352. https://doi.org/https://doi.org/10.1016/S0956-053X(97)10047-2

United Nations. (2015). Paris Agreement [UNFCCC document]. United Nations Framework Convention on Climate Change. https://unfccc.int/process-and-meetings/the-paris-agreement

United Nations. (n.d.). What is climate change?, *Climate Action*. Retrieved June 2, 2023, from https://www.un.org/en/climatechange/what-is-climate-change

Voronov, V., Gorodetskii, E., Podnek, V., & Grigoriev, B. (2016). Properties of equilibrium carbon dioxide hydrate in porous medium. *Chemical Physics*, *476*, 61–68. https://doi.org/https://doi.org/10.1016/j.chemphys.2016.05.031

Wang, Dou, M., Wang, Y., Xu, Y., Li, Y., Chen, Y., & Li, L. (2022). A Review of the Effect of Porous Media on Gas Hydrate Formation. *ACS Omega*, *7*(38), 33666–33679. https://doi.org/10.1021/acsomega.2c03048

Wang, J., Wang, Z., & Sun, B. (2017). Improved equation of CO2 Joule–Thomson coefficient. *Journal of CO2 Utilization*, *19*, 296–307. https://doi.org/https://doi.org/10.1016/j.jcou.2017.04.007

Wen, Z., Yao, Y., Luo, W., & Lei, X. (2021). Memory effect of CO2-hydrate formation in porous media. *Fuel*, *299*, 120922. https://doi.org/https://doi.org/10.1016/j.fuel.2021.120922

Winterbone, D. E., & Turan, A. (2015). Chapter 18 - liquefaction of gases. In D. E. Winterbone & A. Turan (Eds.), *Advanced Thermodynamics for Engineers (Second Edition)* (pp. 423–445). Butterworth-Heinemann. https://doi.org/10.1016/B978-0-444-63373-6.00018-6

Wischnewski, B. (2007). Peace Software. https://www.peacesoftware.de/einigewerte/co2_e.html

World Steel Association. (2023). World steel in figures 2023. Retrieved June 29, 2023, from https://worldsteel.org/steel-topics/statistics/world-steel-in-figures-2023/

Xu, J., Bu, Z., Li, H., Wang, X., & Liu, S. (2022). Permeability Models of Hydrate-Bearing Sediments: A Comprehensive Review with Focus on Normalized Permeability. *Energies*, *15*(13). https://doi.org/10.3390/en15134524

Yin, Z., Khurana, M., Tan, H. K., & Linga, P. (2018). A review of gas hydrate growth kinetic models. *Chemical Engineering Journal*, *342*, 9–29. https://doi.org/https://doi.org/10.1016/j.cej.2018.01.120

Zandalinas, S. I., Fritschi, F. B., & Mittler, R. (2021). Global Warming, Climate Change, and Environmental Pollution: Recipe for a Multifactorial Stress Combination Disaster [Special Issue: Feeding the World: The Future of Plant Breeding]. *Trends in Plant Science*, *26*(6), 588–599. https://doi.org/https://doi.org/10.1016/j.tplants.2021.02.011

Zhao, Y., Lei, X., Zheng, J.-n., Li, M., Johns, M. L., Huang, M., & Song, Y. (2021). High resolution MRI studies of CO2 hydrate formation and dissociation near the gas-water interface. *Chemical Engineering Journal*, *425*, 131426. https://doi.org/https://doi.org/10.1016/j.cej.2021.131426

A

Experimental Results

A.1. Experiment No. 1: $S_w = 100\%$, brine salinity $1wt\%$ NaCl

The conditions for experiment No. 1 considered an initial water saturation of 100% with brine salinity of $1wt\%$ NaCl.

Figure A.1 presents the hydrate equilibrium curve and the experimental conditions for experiment No. 1. According to the $P-T$ phase diagram shown, hydrate formation was expected since the experimental conditions were in the hydrate stability zone. In this phase diagram, the equilibrium curve liquid-gas CO_2 was omitted.

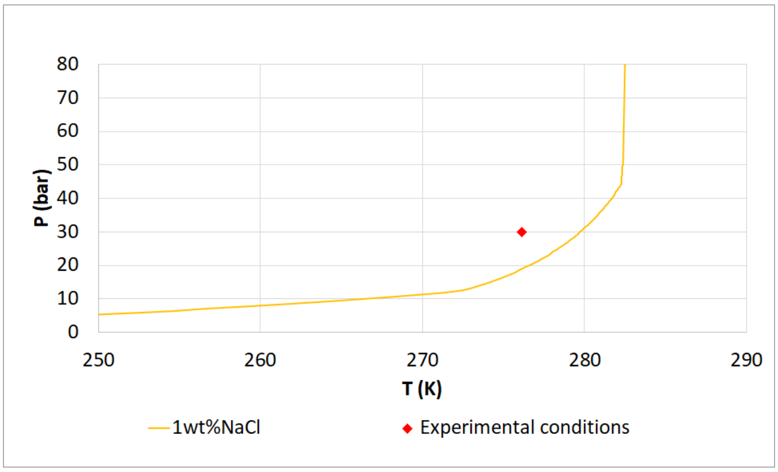

Figure A.1: $P-T$ phase diagram depicting pressure-temperature conditions for experiment No. 1 and hydrate equilibrium curve for a binary system brine (salinity $1wt\%$ NaCl) and CO_2, made with data from HydraFlash (thermodynamic software).

Figure A.2 shows the P and T results for experiment No. 1. The first area (shown in green) corresponds to the base line of brine injection at $1\ ml/min$. CO_2 injection started at $106 \times 20\ s$ and extended until $368 \times 20\ s$ (illustrated in yellow). Hydrate-induced blockage was observed during CO_2 injection as pressure increased from $30\ bar$ to $36\ bar$. The hydrate-induced blockage was identified between $P3$ and $P4$, as $P4$ did not continue registering the same increase in pressure observed in the other pressure gauges.

Subsequently, $30wt\%$ MeOH injection began immediately after CO_2 injections was stopped (displayed in grey). Since the flow paths were already blocked inside the core, when MeOH was injected, the safety pressure was reached at $50\ bar$ (presented in orange), impeding further MeOH injection. When P decreased MeOH injection continued. Since the pressure again started to rise, it was assumed that hydrate dissociation was not effective. Therefore, thermal dissociation was conducted (shown in blue). Finally, after temperature increased, pressure decreased to base line values. Hydrates were assumed to be dissociated at that point.

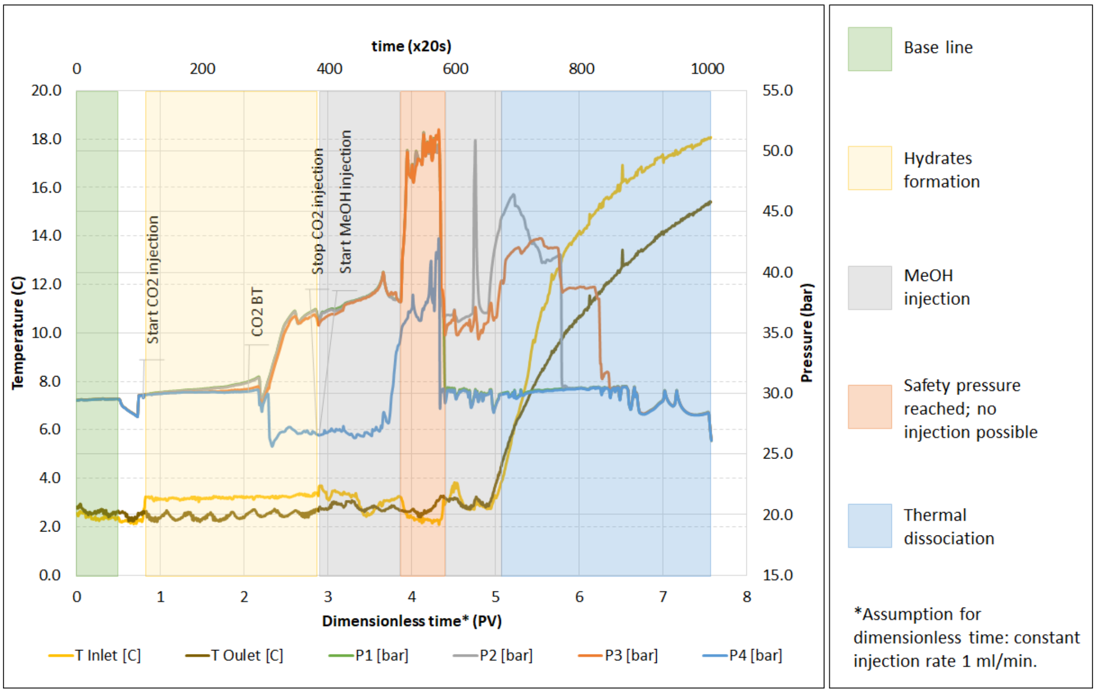

Figure A.2: P and T history for experiment No. 1.

According to the P measurements for experiment No. 1, the MRF is plotted in Figure A.3 to address the injectivity decline due to hydrate formation. The MRF between $P3$ and $P4$ rose up to approximately 600, which corroborated the location of the hydrate-induced blockage identified in Figure A.2.

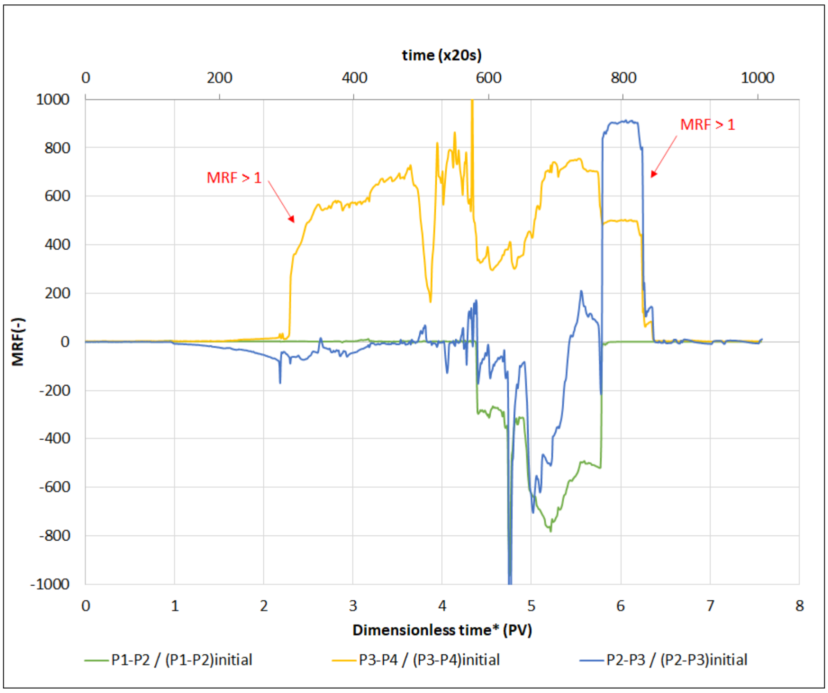

Figure A.3: MRF for experiment No. 1.

A.2. Experiment No. 3: $S_w = 100\%$, brine salinity $1wt\%$ NaCl

The conditions for experiment No. 3 considered an initial water saturation of 100% with brine salinity of $1wt\%$ NaCl.

Figure A.4 presents the hydrate equilibrium curve and the experimental conditions for experiment No. 3. According to the $P-T$ phase diagram shown, hydrate formation was expected since the experimental conditions were in the hydrate stability zone. In this phase diagram, the equilibrium curve liquid-gas CO_2 was omitted.

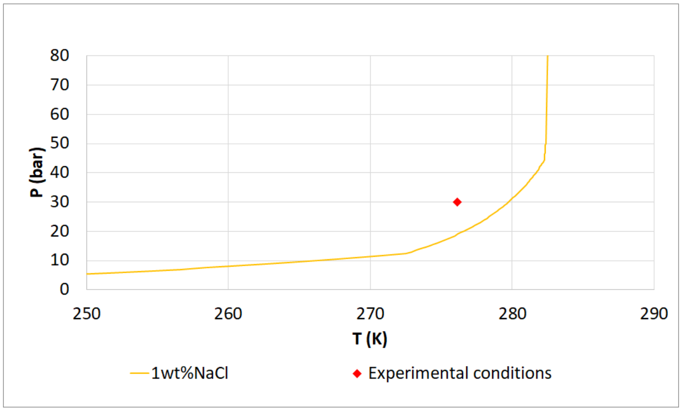

Figure A.4: $P-T$ phase diagram depicting pressure-temperature conditions for experiment No. 3 and hydrate equilibrium curve for a binary system brine (salinity $1wt\%$ NaCl) and CO_2, made with data from HydraFlash (thermodynamic software).

Figure A.5 shows the P and T results for experiment No. 3. The first area (shown in green) corresponds to the base line of brine injection at $1\ ml/min$. CO_2 injection started at $85 \times 20\ s$ and extended until $525 \times 20\ s$ (illustrated in yellow). Hydrate-induced blockage was observed during CO_2 injection as pressure increased from $30\ bar$ to $35\ bar$. The hydrate-induced blockage was identified between $P2$ and $P3$, as $P3$ and $P4$ did not continue registering the same increase in pressure observed in the other pressure gauges.

Subsequently, $30wt\%$ MeOH injection began immediately after CO_2 injections was stopped (displayed in grey). Since the flow paths were already blocked inside the core, when MeOH was injected, the safety pressure was reached (presented in orange), impeding further MeOH injection. Since pressure did not decrease, thermal dissociation was started by turning off the fridge (shown in blue). Finally, after temperature increased, pressure decreased to base line values. Hydrates were assumed to be dissociated at that point.

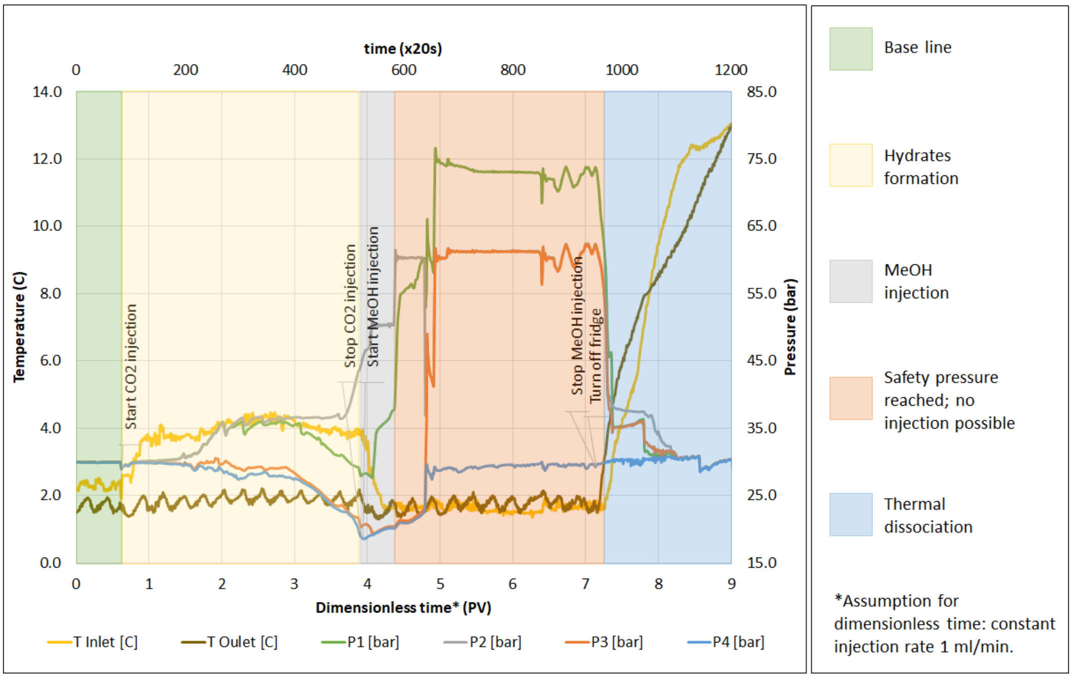

Figure A.5: P and T history for experiment No. 3.

According to the P measurements for experiment No. 3, the MRF is plotted in Figure A.3 to address the injectivity decline due to hydrate formation. The MRF between $P2$ and $P3$ rose at values higher than 1000, which corroborated the location of the hydrate-induced blockage identified in Figure A.5.

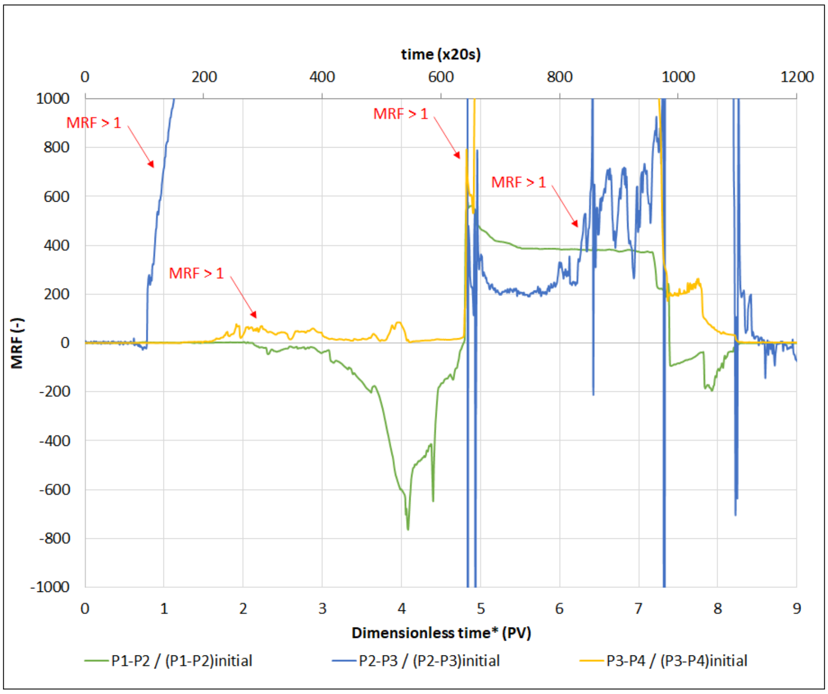

Figure A.6: MRF for experiment No. 3.

A.3. Experiment No. 4: $S_w = 100\%$, brine salinity $1wt\%$ NaCl

The conditions for experiment No. 4 considered an initial water saturation of 100% with brine salinity of $1wt\%$ NaCl.

Figure A.7 presents the hydrate equilibrium curve and the experimental conditions for experiment No. 4. According to the $P-T$ phase diagram shown, hydrate formation was expected since the experimental conditions were in the hydrate stability zone. In this phase diagram, the equilibrium curve liquid-gas CO_2 was omitted.

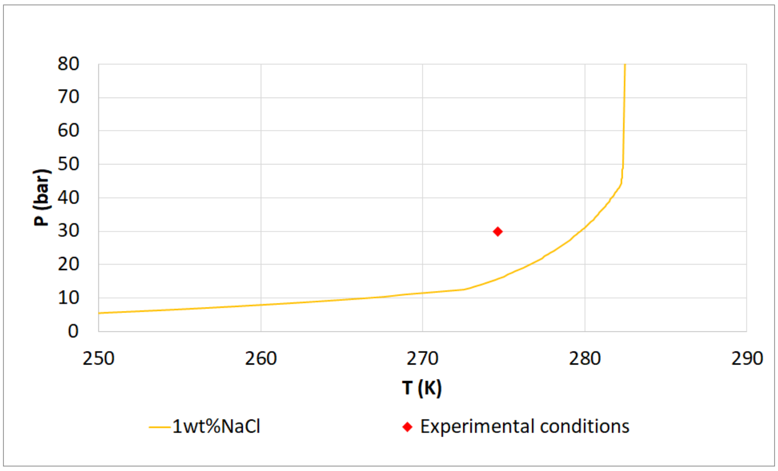

Figure A.7: $P-T$ phase diagram depicting pressure-temperature conditions for experiment No. 4 and hydrate equilibrium curve for a binary system brine (salinity $1wt\%$ NaCl) and CO_2, made with data from HydraFlash (thermodynamic software).

Figure A.8 shows the P and T results for experiment No. 4. The first area (shown in green) corresponds to the base line of brine injection at $1\ ml/min$. CO_2 injection started at $36 \times 20\ s$ and extended until $408 \times 20\ s$ (illustrated in yellow). Hydrate-induced blockage was observed during CO_2 injection as pressure increased from $30\ bar$ to $35\ bar$. The hydrate-induced blockage was identified $P3$ onward, as $P3$ and $P4$ did not continue registering the same increase in pressure observed in the other pressure gauges.

Subsequently, $30wt\%$ MeOH injection began immediately after CO_2 injections was stopped (displayed in grey). Since the flow paths were already blocked inside the core, when MeOH was injected, the safety pressure was reached (presented in orange), impeding further MeOH injection. Since pressure did not decrease, thermal dissociation was started by turning off the fridge (shown in blue). Finally, after temperature increased, pressure decreased to base line values. Hydrates were assumed to be dissociated at that point.

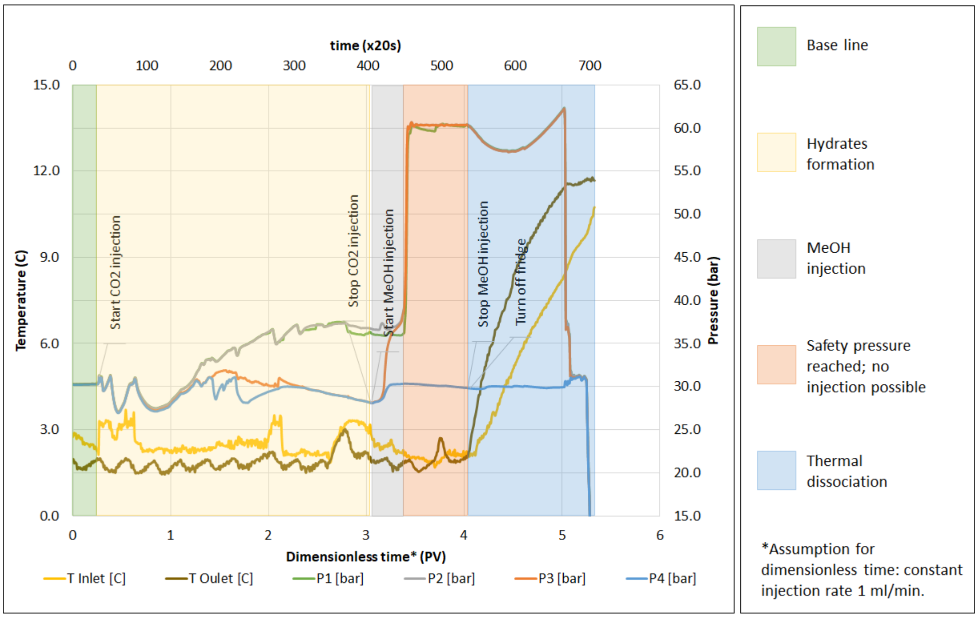

Figure A.8: P and T history for experiment No. 4.

According to the P measurements for experiment No. 4, the MRF is plotted in Figure A.9 to address the injectivity decline due to hydrate formation. The MRF between $P2$ and $P3$ rose up to values higher than 1500, which corroborated the location of the hydrate-induced blockage identified in Figure A.8.

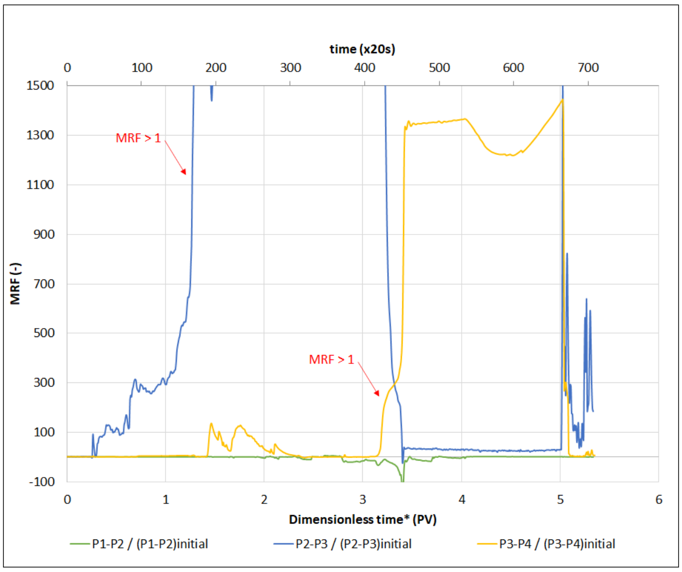

Figure A.9: MRF for experiment No. 4.

A.4. Experiment No. 7: $S_w = 100\%$, brine salinity $20wt\%$ NaCl

The conditions for experiment No. 7 considered an initial water saturation of 100% with brine salinity of $20wt\%$ NaCl.

Figure A.10 presents the hydrate equilibrium curve and the experimental conditions for experiment No. 7. The hydrate equilibrium curve was shifted to the left due to the concentration of $20wt\%$ NaCl in the brine. In order to achieve hydrate formation, the experimental condition (P and T) was adjusted to be within the hydrate stability zone. In this phase diagram, the equilibrium curve liquid-gas CO_2 was omitted.

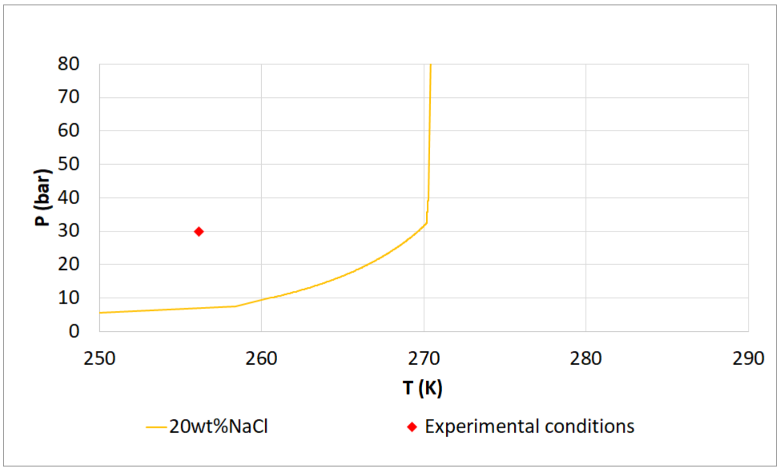

Figure A.10: $P - T$ phase diagram depicting pressure-temperature conditions for experiment No. 7 and hydrate equilibrium curve for a binary system brine (salinity $20wt\%$ NaCl) and CO_2, made with data from HydraFlash (thermodynamic software).

Figure A.11 shows the P and T results for experiment No. 7. The first area (shown in green) corresponds to the base line of brine injection at $1\ ml/min$. CO_2 injection started at $60 \times 100\ s$ and extended until $440 \times 100\ s$ (illustrated in yellow). Hydrate-induced blockage was observed during CO_2 injection as pressure increased from $30\ bar$ to $50\ bar$. The hydrate-induced blockage was identified at the outlet, as all the pressures increased with almost the same trend.

The next day, $30wt\%$ MeOH injection began at $809 \times 100\ s$ (displayed in grey). Since the flow paths were already blocked inside the core, when MeOH was injected, the safety pressure was reached (presented in orange), impeding further MeOH injection. Since pressure did not decrease to the base line, thermal dissociation was started by turning off the fridge on the next day (shown in blue). Finally, after temperature increased, pressure decreased. Hydrates were assumed to be dissociated at that point.

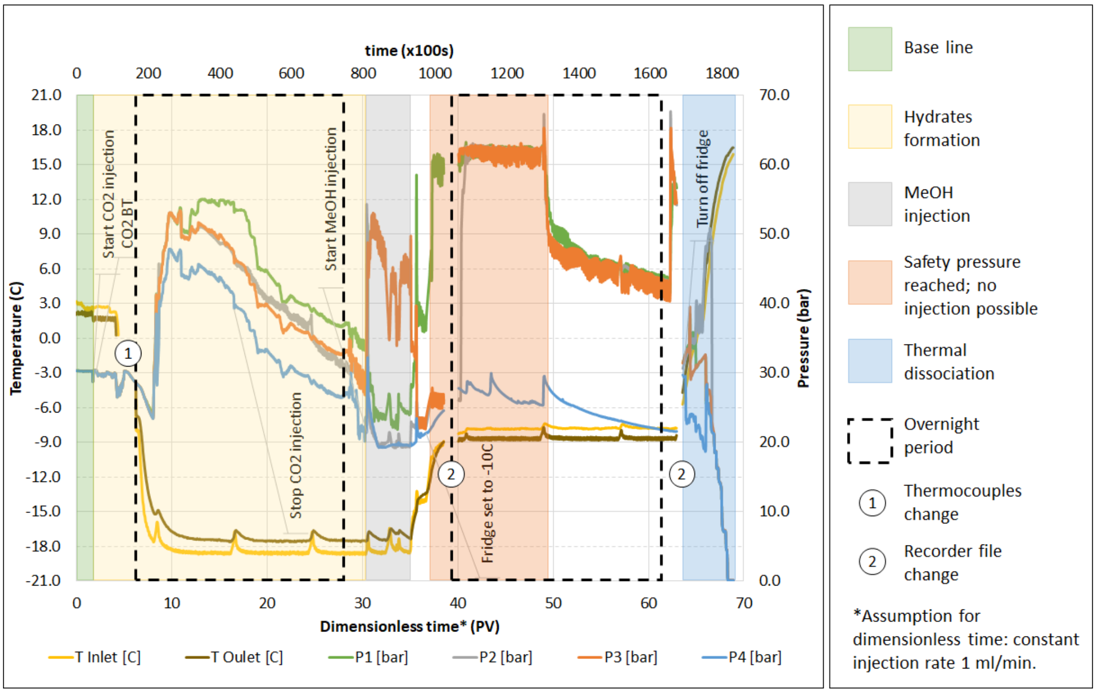

Figure A.11: P and T history for experiment No. 7.

According to the P measurements for experiment No. 7, the MRF is plotted in Figure A.12 to address the injectivity decline due to hydrate formation. The MRF between $P2$ and $P3$ rose up to approximately 300, which corroborated the location of the hydrate-induced blockage identified in Figure A.11.

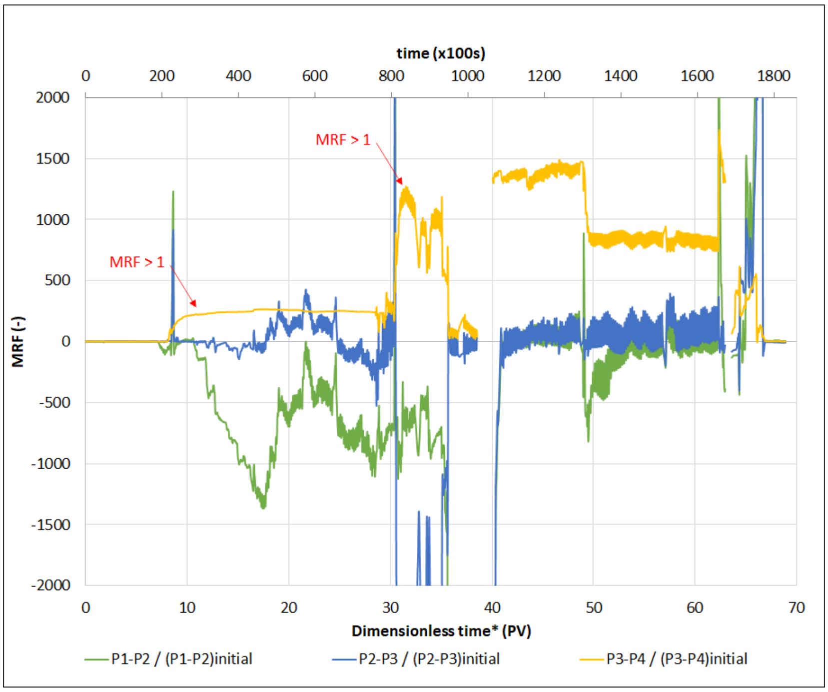

Figure A.12: MRF for experiment No. 7.

A.5. Experiment No. 2: $S_w = 100\%$, brine salinity $1wt\%$ NaCl, pre-injection $30wt\%$ MeOH

The conditions for experiment No. 2 considered an initial water saturation of 100% with brine salinity of $1wt\%$ NaCl. Before starting this experiment, the core was not cleaned under vacuum conditions, resulting in the presence of $30wt\%$ MeOH in the core.

Figure A.13 presents the hydrate equilibrium curve and the experimental conditions for experiment No. 2. According to the $P-T$ phase diagram shown, hydrate formation was not expected since the experimental conditions were outside the hydrate stability zone due to the shift created by MeOH in the hydrate equilibrium curve. In this phase diagram, the equilibrium curve liquid-gas CO_2 was omitted.

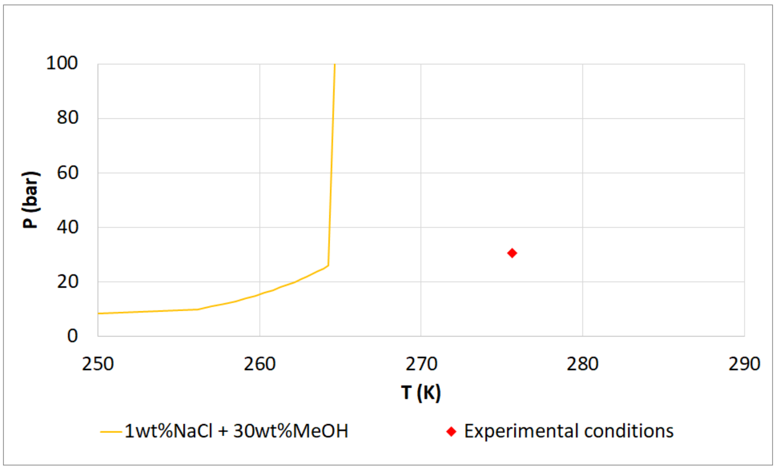

Figure A.13: $P - T$ phase diagram depicting pressure-temperature conditions for experiment No. 2 and hydrate equilibrium curve for a binary system brine (salinity $1wt\%$ NaCl) and CO_2 with pre-injection of THIs, made with data from HydraFlash (thermodynamic software).

Figure A.14 shows the P and T results for experiment No. 2. The first area (shown in green) corresponds to the base line of brine injection at $1\ ml/min$. CO_2 injection started at $37 \times 20\ s$ and extended until $586 \times 20\ s$. However, hydrate-induced blockage was not observed during CO_2 injection as pressure did not increase dramatically from the base line. As expected, the experimental conditions were outside of the hydrate stability zone, so hydrate formation was not possible.

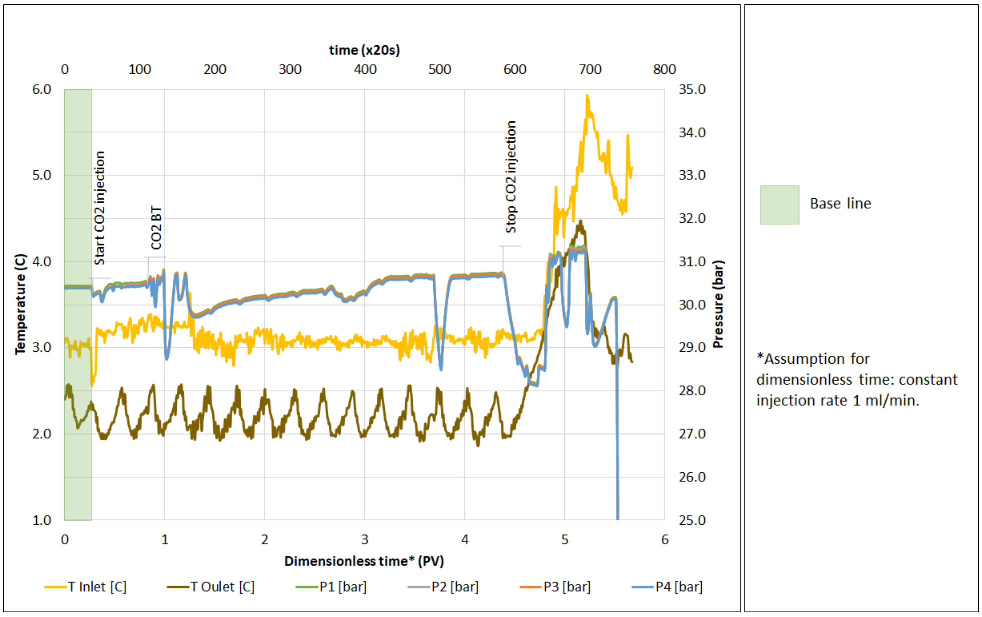

Figure A.14: P and T history for experiment No. 2.

There was no hydrate formation in experiment No. 2; therefore, MRF was not plotted.

A.6. Experiment No. 5: $S_w = 100\%$, brine salinity $1wt\%$ NaCl, pre-injection $30wt\%$ MeOH

The conditions for experiment No. 5 considered an initial water saturation of 100% with brine salinity of $1wt\%$ NaCl and pre-injection of $30wt\%$ MeOH.

Figure A.15 presents the hydrate equilibrium curve and the experimental conditions for experiment No. 5. According to the $P - T$ phase diagram shown, hydrate formation was not expected since the experimental conditions were outside the hydrate stability zone due to the shift created by MeOH in the hydrate equilibrium curve. In this phase diagram, the equilibrium curve liquid-gas CO_2 was omitted.

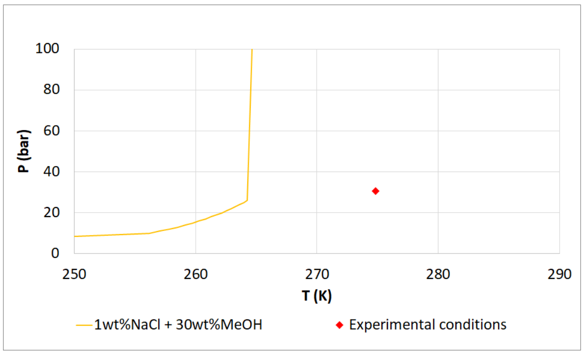

Figure A.15: $P - T$ phase diagram depicting pressure-temperature conditions for experiment No. 5 and hydrate equilibrium curve for a binary system brine (salinity $1wt\%$ NaCl) and CO_2 with pre-injection of THIs, made with data from HydraFlash (thermodynamic software).

Figure A.16 shows the P and T results for experiment No. 5. The first area (shown in green) corresponds to the base line of $30wt\%$ MeOH injection at $1\ ml/min$. CO_2 injection started at 207×20 s and extended until $780 \times 20\ s$. However, hydrate-induced blockage was not observed during CO_2 injection as pressure did not increase from the base line. As expected, the experimental conditions were outside of the hydrate stability zone, so hydrate formation was not possible.

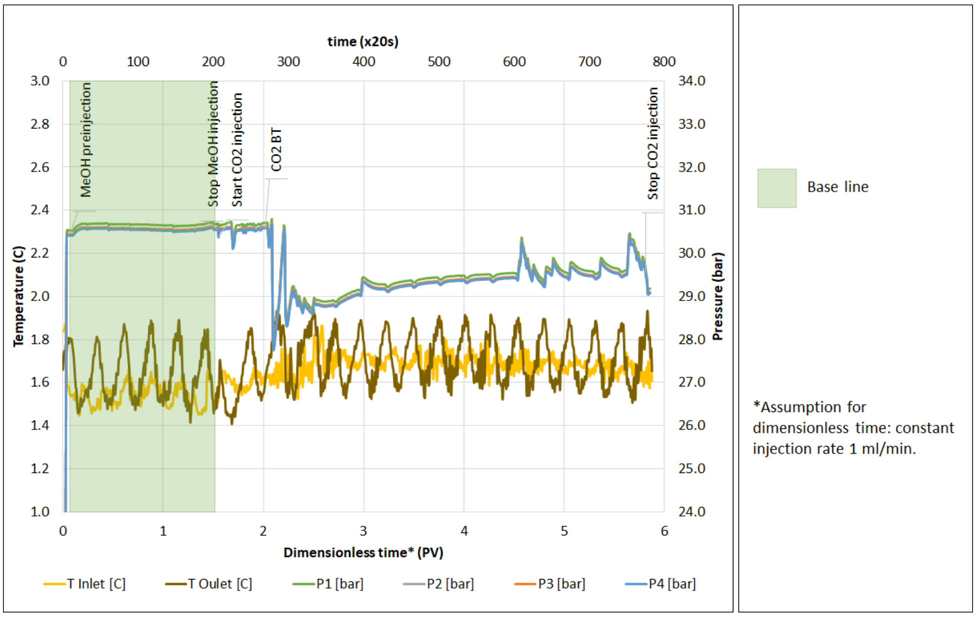

Figure A.16: P and T history for experiment No. 5.

There was no hydrate formation in experiment No. 5; therefore, MRF was not plotted.

A.7. Experiment No. 8: $S_w = 62.8\%$, brine salinity $1wt\%$ NaCl

For experiment No. 8, the specified conditions involved an initial water saturation of 62.8% using brine with salinity of $1wt\%$ NaCl. To reduce the initial water saturation from 100%, CO_2 was injected into the core in a vertical position at room temperature until breakthrough was reached, the volume of brine displaced was noted. Subsequently, the core was repositioned horizontally in the cooler to initiate CO_2 injection.

Figure A.17 presents the hydrate equilibrium curve and the experimental conditions for experiment No. 8. According to the $P - T$ phase diagram shown, hydrate formation was expected since the experimental conditions were in the hydrate stability zone. In this phase diagram, the equilibrium curve liquid-gas CO_2 was omitted.

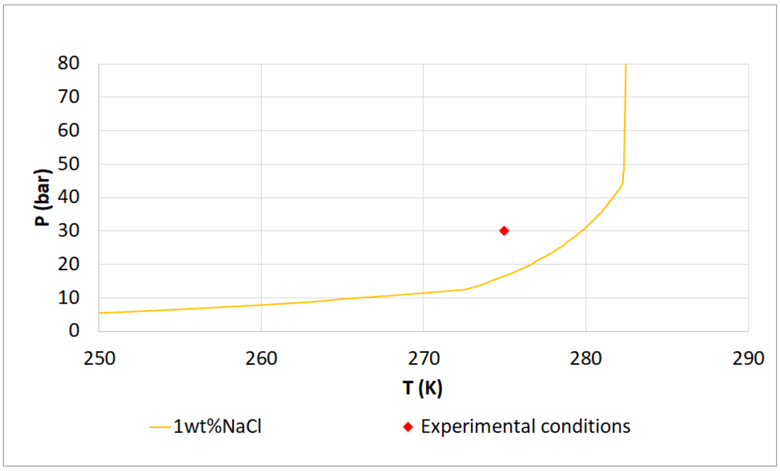

Figure A.17: $P - T$ phase diagram depicting pressure-temperature conditions for experiment No. 8 and hydrate equilibrium curve for a binary system brine (salinity $1wt\%$ NaCl) and CO_2, made with data from HydraFlash (thermodynamic software).

Figure A.18 shows the P and T results for experiment No. 8. The first area (shown in green) corresponds to the base line of CO_2 injection at $1\ ml/min$. Over the weekend the CO_2 injection was conducted at a very low rate. After the weekend, the CO_2 injection was restored and hydrate-induced blockage was observed as pressure increased from $30\ bar$ to $35\ bar$. The hydrate-induced blockage was identified between $P3$ and $P4$, as $P4$ did not continue registering the same increase in pressure observed in the other pressure gauges.

Remediation started when $30wt\%$ MeOH injection began at $2725 \times 100\ s$ (displayed in grey). Since some of the flow paths were already blocked inside the core, when MeOH was injected pressure reached $50\ bar$. MeOH injection continued on constant pressure mode, until pressure started to decrease reaching the base line. Hydrates were assumed to be dissociated at that point.

Figure A.18: P and T history for experiment No. 8.

Figure A.19 provides a closer view of the P and T results for experiment No. 8, specifically focusing on the stages of hydrate-induced blockage and subsequent remediation.

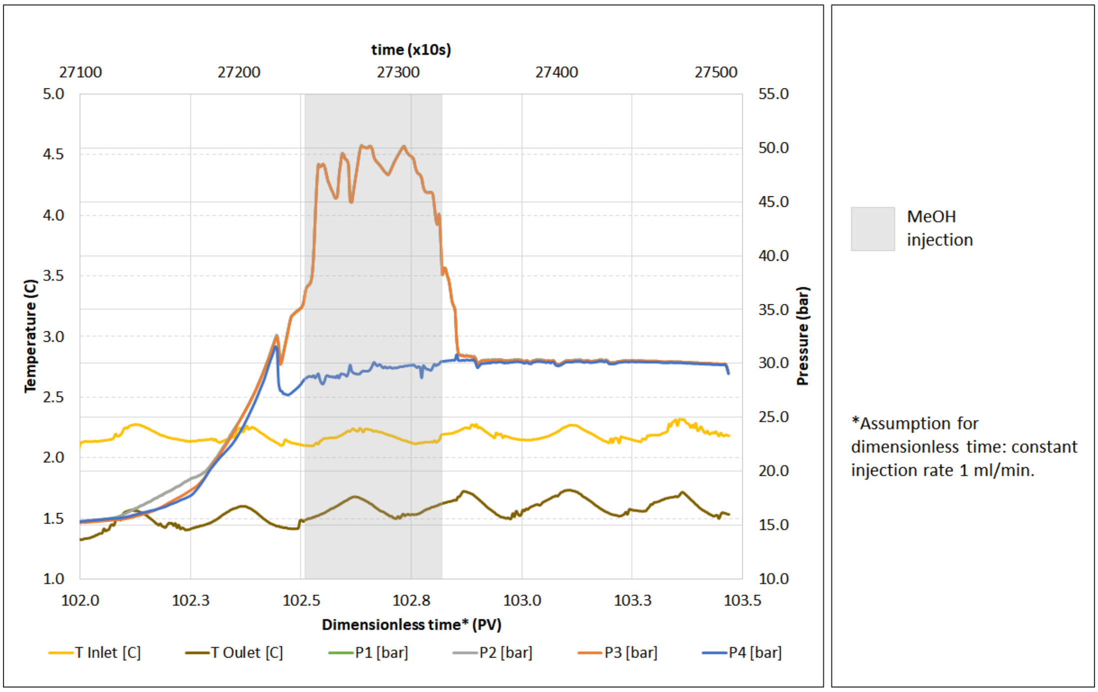

Figure A.19: P and T history for experiment No. 8 (zoom in).

According to the P measurements for experiment No. 8, the MRF is plotted in Figure A.20 to address the injectivity decline due to hydrate formation. The MRF between $P3$ and $P4$ rose up to approximately 800, which corroborated the location of the hydrate-induced blockage identified in Figure A.18.

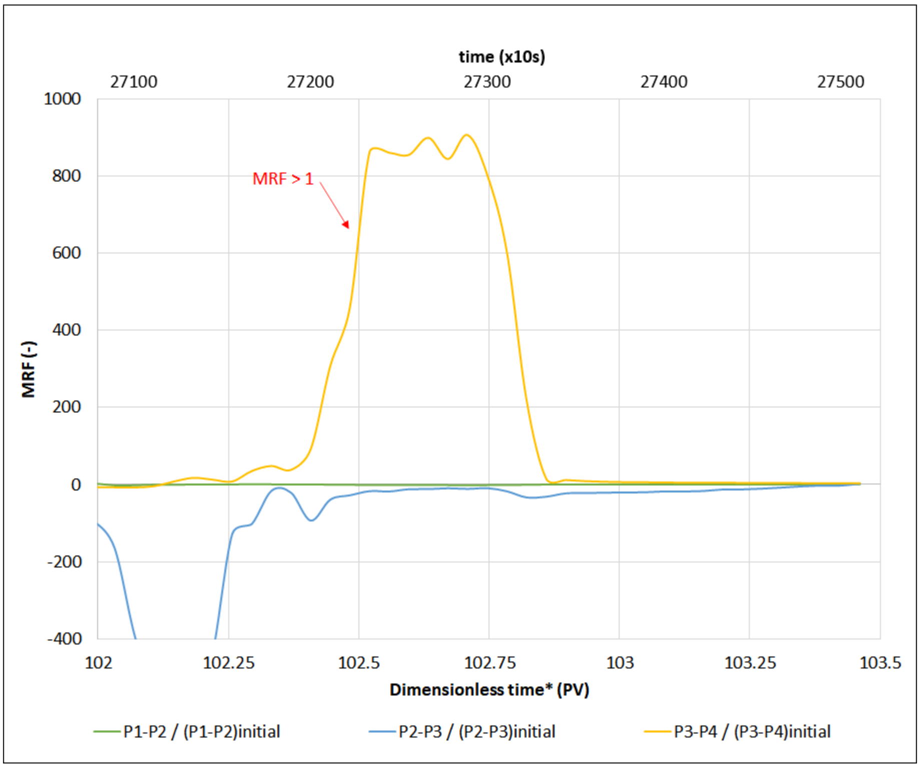

Figure A.20: MRF for experiment No. 8 (zoom in).

A.8. Experiment No. 9: $S_w = 62.3\%$, brine salinity $1wt\%$ NaCl

For experiment No. 9, the specified conditions involved an initial water saturation of 62.3% using brine with salinity of $1wt\%$ NaCl. To reduce the initial water saturation from 100%, N_2 was injected into the core in a vertical position until breakthrough was reached, the volume of brine displaced was noted. Subsequently, the core was repositioned horizontally in the cooler to initiate CO_2 injection.

Figure A.21 presents the hydrate equilibrium curve and the experimental conditions for experiment No. 9. According to the $P-T$ phase diagram shown, hydrate formation was expected since the experimental conditions were in the hydrate stability zone. In this phase diagram, the equilibrium curve liquid-gas CO_2 was omitted.

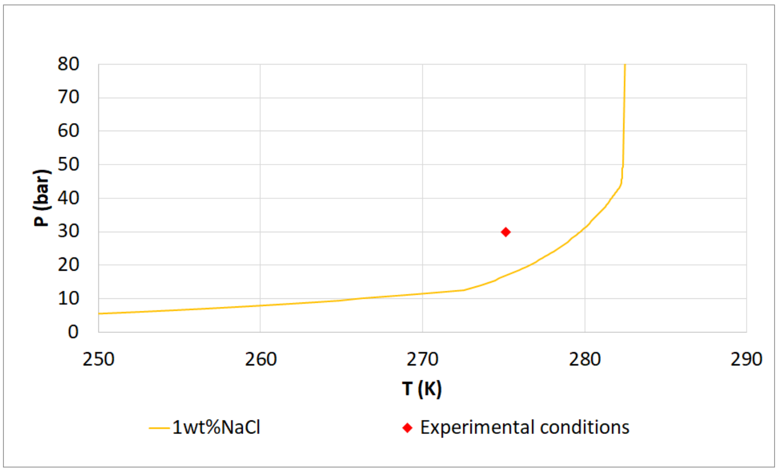

Figure A.21: $P-T$ phase diagram depicting pressure-temperature conditions for experiment No. 9 and hydrate equilibrium curve for a binary system brine (salinity $1wt\%$ NaCl) and CO_2, made with data from HydraFlash (thermodynamic software).

Figure A.22 shows the P and T results for experiment No. 9. The first area (shown in green) corresponds to the base line of N_2 injection at $1\ ml/min$. Then, CO_2 injection was conducted at $1\ ml/min$ (illustrated in yellow). At $2390 \times 20\ s$ pressure started to decrease abruptly, which suggested hydrate formation. CO_2 injection continued until $4243 \times 20\ s$, moment at which pressure abruptly increased from $30\ bar$ to $35\ bar$. At that point, CO_2 injection was stopped and $30wt\%$ MeOH injection started. MeOH injection was performed at constant pressure mode (depicted in grey). The hydrate-induced blockage was identified between $P1$ and $P2$, as $P2$, $P3$, and $P4$ did not continue registering the same increase in pressure observed in $P1$. Finally, hydrates were assumed to be dissociated when pressure started to decrease reaching the base line.

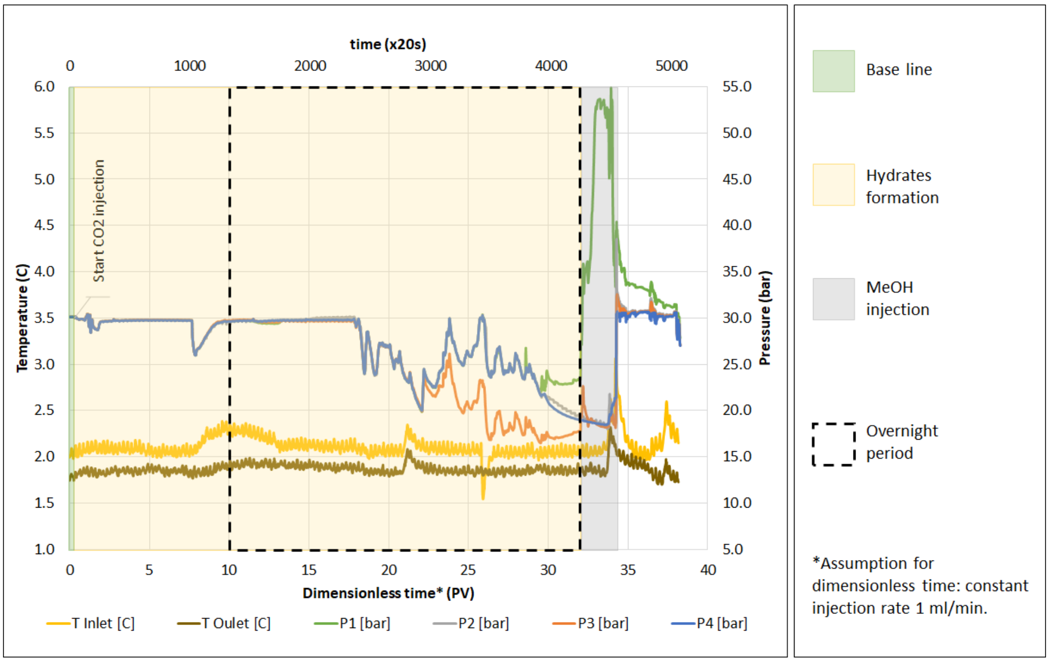

Figure A.22: P and T history for experiment No. 9.

According to the P measurements for experiment No. 9, the MRF is plotted in Figure A.23 to address the injectivity decline due to hydrate formation. The MRF between $P2$ and $P3$ rose up to approximately 300, which corroborated the location of the hydrate-induced blockage identified in Figure A.22.

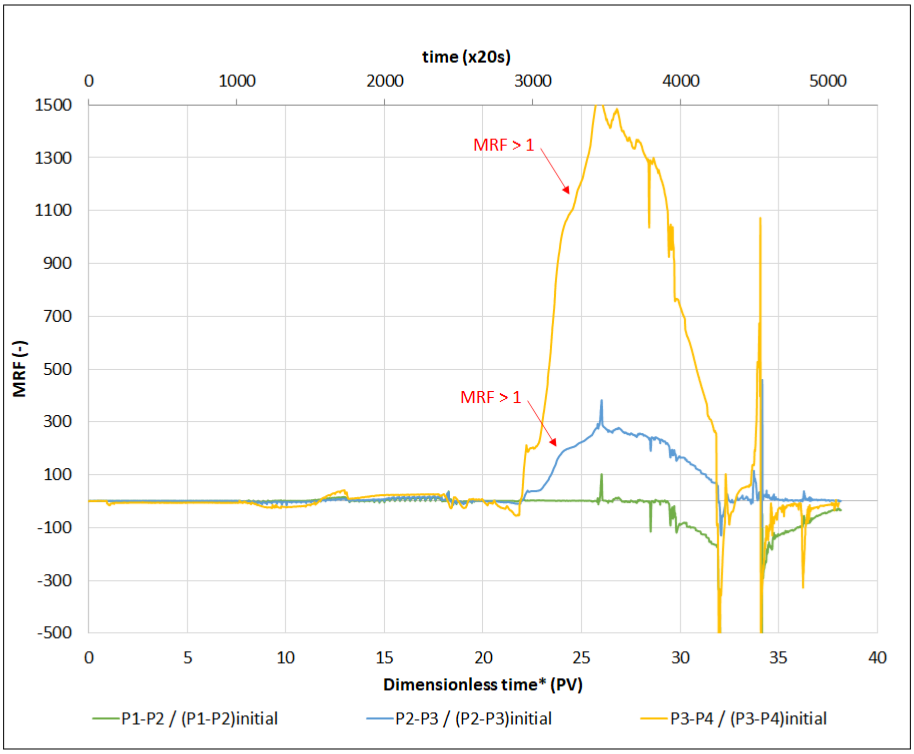

Figure A.23: MRF for experiment No. 9.